January 2015

A Comparison of Functionally Divergent Forms of the Purine Biosynthesis Enzyme PurE.

Kelly L. Sullivan
Purdue University

Recommended Citation

Sullivan, Kelly L., "A Comparison of Functionally Divergent Forms of the Purine Biosynthesis Enzyme PurE." (2015). *Open Access Dissertations*. 1190.
https://docs.lib.purdue.edu/open_access_dissertations/1190

Graduate School Form 30
Updated 1/15/2015

PURDUE UNIVERSITY
GRADUATE SCHOOL
Thesis/Dissertation Acceptance

This is to certify that the thesis/dissertation prepared

By Kelly L. Sullivan

Entitled
A Comparison of Functionally Divergent Forms of the Purine Biosynthesis Enzyme PurE.

For the degree of Doctor of Philosophy

Is approved by the final examining committee:

T. J. Kappock
Co-chair

Clint Chapple
Co-chair

Barbara Golden
Co-chair

Laurie Parker

To the best of my knowledge and as understood by the student in the Thesis/Dissertation Agreement, Publication Delay, and Certification Disclaimer (Graduate School Form 32), this thesis/dissertation adheres to the provisions of Purdue University's "Policy of Integrity in Research" and the use of copyright material.

Approved by Major Professor(s): T. J. Kappock

Approved by: Clint Chapple 04/17/2015
Head of the Departmental Graduate Program Date

A COMPARISON OF FUNCTIONALLY DIVERGENT FORMS OF THE PURINE BIOSYNTHESIS ENZYME PURE

A Dissertation

Submitted to the Faculty

of

Purdue University

by

Kelly L. Sullivan

In Partial Fulfillment of the

Requirements for the Degree

of

Doctor of Philosophy

May 2015

Purdue University

West Lafayette, Indiana

For My Parents

ACKNOWLEDGEMENTS

I would like to thank my research advisor Professor T. Joseph Kappock and the members of my research advisory committee Professors Clint Chapple, Barbara L. Golden and Laurie L. Parker.

I would also like to thank the many people who contributed to this study. T. Joseph Kappock created the plasmids encoding the AaPurE1-Y154X mutants. Sylvain Tranchimand isolated EcPurE1-W20F, EcPurE-W151F, and AaPurE1-W34F,W165F. Elwood A. Mullins crystallized and collected the crystallographic data for AaPurE1-W34F,165F. Jesse R. Murphy purified H6PurK and H6PurC. Professor Ronald L. Somerville generously furnished the P1 lysate and provided invaluable guidance with P1 phage transduction. Professor James G. Bann generously furnished the DL41 strain. Barbara L. Golden, Elwood A. Mullins and the staff of LS-CAT and provided assistance with crystallographic data collection and refinement. Professor Jeffery T. Bolin for generously providing access to an anaerobic chamber. Connie C. Bonham, Christie L. Eissler and Tzu-Yi Yang performed mass analysis of intact proteins and small molecules. The Purdue University Genomics Core Facility sequenced PCR products and plasmids.

In addition to the people who contributed scientifically to this study, I want to thank the people who got me here and for their unwavering support throughout the years. Thank you to my parents for making sure I got the best education I possibly could. Especially thank you to my mother for making sure science was always a big part of my life. Thank you to my father for being there when I needed encouragement. Thank you to my partner Leland Thurman for supporting me through these past seven years more than he could ever know. Finally thank you to my friends Kayla Harmeyer, Jesse Murphy, Kayleigh Nyffeler, and Elwood Mullins. Without you all, graduate school would not have been as memorable or as fun.

TABLE OF CONTENTS

Page

LIST OF FIGURES

Figure Page

Figure Page

Figure Page

Figure Page

LIST OF TABLES

Table Page

Table Page

ABSTRACT

Sullivan, Kelly L. Ph.D, Purdue University, May 2015. A Comparison of Functionally Divergent Forms of the Purine Biosynthesis Enzyme PurE. Major Professor: T.J. Kappock.

Purines are the basic building block for essential biomolecules such as DNA, RNA, NADH, CoA, and several essential vitamin cofactors. Most organisms have the ability to synthesize purines through the *de novo* purine biosynthesis pathway.

The *de novo* purine biosynthesis pathway contains a rare metabolic divergence within the eukaryotes. Animals convert CO_2 and aminoimidazole ribonucleotide (AIR) to carboxyaminoimidazole ribonucleotide (CAIR) using the enzyme aminoimidazole ribonucleotide carboxylase (PurE2), while other eukaryotes, archaea, and bacteria use two enzymes, N^5-carboxyaminoimidazole ribonucleotide synthetase (PurK) and N^5-carboxyaminoimidazole ribonucleotide (NCAIR) mutase, PurE (PurE1). PurE catalyzes formation of the sole carbon-carbon bond formed during purine biosynthesis.

Both PurE classes are proposed to generate a carbon-carbon bond using similar chemistry. We can monitor the carbon-carbon bond forming reaction in real-time using changes in intrinsic fluorescence that report upon electrostatic changes within the active site. To simplify fluorescence responses, we generated mutants of PurE1 from *Acetobacter aceti* (AaPurE1-W34F,W165F) and PurE2 from *Treponema denticola* (TdPurE2-F79W) that have a single tryptophan fluorophore, which responds to changes upon ligand addition as assessed by fluorescence titrations. Surprisingly, a Tyr residue,

with ambiguous electron density in a 1.35 Å AaPurE1-W34F,W165F structure, contributes to fluorescence.

Both PurE1 and PurE2 have similar structures and active sites. A universally conserved serine is the sole polar contact with the substrate aminoimidazole ring and any PurE side chain. Serine donates a hydrogen bond to the aminoimidazole N3 but may flip polarity in PurE2 at low pH. We generated a series of serine mutants in AaPurE1 and TdPurE2, which confirm a hydrogen-bonding role for serine, as the mutants with the highest detectable activity are able to donate (or accept, at low pH) a hydrogen bond. Serine is more important for PurE2 function and its role appears to be different between the two classes.

The PurE2 active site contains a strictly conserved, class-specific lysine. Due to the difficult task of acquiring CO_2 from solution, the lysine was proposed to form a carboxylated intermediate in PurE2 catalysis. We generated the TdPurE2-K41R mutant, which retained both AIR carboxylase and CAIR decarboxylase activity, indicating that formation of a lysine-carbamate is not an obligatory intermediate for PurE2 function.

PurE2 catalyzes the formation of CAIR from AIR and CO_2 without any detectable side reaction. Functional complementation assays and a crystal structure both indicated the "inactive" TdPurE2-H40N mutant may destroy AIR, CAIR, or both. We demonstrated that this "inactive" mutant does indeed destroy AIR in a slow O_2-dependent oxygenase activity reaction.

Due to the unusual divergence in purine biosynthesis, PurE1 is a potential antimicrobial target; however, no enzyme activity assay is suitable for high throughput screening. We developed a simple chemical quench that fixes the PurE1 substrate/product ratio for 24 h, as assessed by the Bratton-Marshall assay (BMA) for diazotizable amines. The $ZnSO_4$ stopping reagent is proposed to chelate CAIR, allowing later analysis of this acid-labile product by BMA or a high throughput screening methods.

CHAPTER 1 INTRODUCTION

1.1 Background and Significance

Purines are Essential in Biological Systems. Purine biosynthesis supplies the precursors for RNA, DNA, and coenzymes like NADH and CoA. In addition, purines serve as starting materials for vitamins like folic acid, B_{12}, and riboflavin[1] and for the universal methylating agent and radical initiator S-adenosylmethionine.[2]

Prebiotic Purine Synthesis. Organic compounds of biochemical significance, such as amino acids, can be synthesized from simple inorganic precursors under conditions thought to be resemble those on primitive Earth.[3] Prebiotic syntheses precede evolution. Purine synthesis requires an activated ribose and a base, each of which could have been formed in a prebiotic era. Adenine can be formed from the oligomerization of hydrogen cyanide and sugars can be produced from formaldehyde by the formose reaction.[4,5] Biological evolution produces customized molecular interfaces, enzymes, and ultimately multistep biochemical pathways.[6,7]

Purine Biosynthesis. Contemporary purine synthesis occurs by two routes, a salvage pathway and the *de novo* purine biosynthetic pathway. The purine salvage pathway couples an activated ribose, phosphoribosyl pyrophosphate (PRPP), with bases recovered from the degradation of nucleic acids and nucleotides.[8] While energy efficient, purine salvage requires a ready source of purine heterocycles. When purine bases are not available, purines are biosynthesized from PRPP and various small molecules, with considerable energy input from ATP, by the *de novo* purine pathway (Figure 1.1).

Purine Biosynthesis May Have Evolved from Preexisting Pathways. New metabolic pathways are composed of enzymes that acquire new functions or biochemical roles[8] in the context of existing metabolic pathways. New enzymes evolve from gene duplication and functional diversification of ancestral genes. The extant purine biosynthetic pathway appears to have been assembled from two older pathways, histidine and thiamine biosynthesis, which unlike purine biosynthesis, have no alternative biosynthetic pathways.

Histidine biosynthesis generates 5-aminoimidazole-4-carboxamide ribonucleotide (AICAR) as a byproduct.[9] Ancient microbes may have evolved PurP and PurO enzymes as a way to recycle AICAR from IMP.[10] Thiamine contains a pyrimidine derived in all organisms from aminoimidazole ribonucleotide (AIR).[11,12] Cells require very little thiamine, meaning the AIR demand for this biosynthesis is very low.[13] Excess AIR is an intrinsically reactive molecule and is actively eliminated from cells. This may have spurred the evolution of PurE, PurK, PurC, and PurB as a "biosynthetic bridge" to convert any excess AIR to AICAR. PurB was already necessary to convert adenylosuccinate to AMP; it appears to have acquired a promiscuous function and an additional role, in AICAR biosynthesis.[14]

Only a few molecules of thiamine are required for cell viability, which yields a very low flux pathway (purines are required in a 1000:1 ratio over thiamine for growth).[15] The evolution of PurF, PurD, PurT, PurL (or its multiprotein equivalent PurSQL), and PurM would provide a high flux route for AIR production well in excess of thiamine demand.

Finally, the folate-dependent enzymes (PurN and PurH) would have only evolved after folate appeared. The formate dependent alternatives PurT and PurP would have been available first, and some are still used, since archaea lack folates.[10,16]

In summary, the purine pathway likely "evolved backwards" from AICAR to AIR to PRPP and was very clearly driven by the high demand for adequate purines for growth.

The de novo Purine Biosynthesis Pathway Contains a Rare Metabolic Divergence. The modern *de novo* purine biosynthetic pathway requires either 10 or 11 enzymatic steps. The additional step is catalyzed by PurK and represents a rare metabolic divergence in the carboxylation of AIR to form 4-carboxy-5-aminoimidazole ribonucleotide (CAIR). Animals convert CO_2 and AIR to CAIR using a class II PurE (PurE2; AIR carboxylase, EC 4.1.1.21) while other eukaryotes, archaea, and bacteria use two enzymes, PurK and class I PurE (PurE1; N^5-carboxy-AIR [NCAIR] mutase, EC 5.4.99.18) (Figure 1.2).[17,18] PurE1 and PurE2 catalyze the formation of the sole carbon-carbon (C−C) bond installed during purine biosynthesis. Other pathway steps build up the purine base by forming C−N bonds.

Carbon-Carbon Bond Chemistry. Biochemistry is the study of the molecular basis of biology. C−C bond formation is of central importance to all life. These covalent bonds are generally formed by a complex process that requires the intermediate formation of a negatively charged carbon atom (carbanion), which then functions as a nucleophile in a subsequent condensation reaction. Carbanions are typically formed by either decarboxylation or deprotonation of a carbon acid, which is difficult for both thermodynamic (e.g., high pK_a values) and kinetic reasons.[19,20] Removal of the proton is challenging, however, the key difficulty in carbanion generation may be controlling the reactivity for this highly unstable species.

Decarboxylases. Decarboxylases catalyze the general reaction shown in equation 1.1, which is almost always irreversible due to the entropy gain associated with the loss of gaseous CO_2. Decarboxylases lower the barrier to carbanion cleavage of a C−C bond, an easier task than the one confronted by carboxylases (see below). Decarboxylations are involved in many different biological processes: isocitrate dehydrogenase (TCA cycle), thiolase (fatty acid synthesis), glycine cleavage system (glycine catabolism), orotidine 5′-monophosphate decarboxylase (pyrimidine biosynthesis), acetoacetate decarboxylase (ketone body metabolism), and pyruvate decarboxylase (fermentation).

$$R\text{-}CO_2^{\ominus} + H^+ \rightarrow R\text{-}H^+ + CO_2 \qquad \text{Equation 1.1}$$

Several decarboxylases have carbanion stabilization strategies similar to both PurE1 and PurE2. Acetoacetate decarboxylase proceeds through a Schiff base intermediate that stabilizes the carbanion formed by decarboxylation. The Schiff base stabilizes a carbanion on the α-carbon (Figure 1.2A). Thiamine-dependent decarboxylases, like pyruvate decarboxylase, stabilize the carbanion produced by loss of CO_2 from α-keto acids (Figure 1.2B). Again the carbanion is stabilized by resonance with an "electron sink" a positively charged nitrogen adjacent to the decarboxylated carbon. PurE1 and PurE2 both decarboxylate CAIR to form a similar resonance-stabilized carbanion β-iminium zwitterion, from which CO_2 does not immediately separate. Unlike most decarboxylases, PurE1 and PurE2 are *both* a decarboxylase and a carboxylase.

Carboxylases. Carboxylases catalyze the general reaction shown in equation 1.2. They solve two difficult challenges: forming carbanions and trapping CO_2. Like decarboxylases, carboxylases are involved in many different biological processes: acetyl-CoA carboxylase (fatty acid synthesis), pyruvate carboxylase (gluconeogenesis), phosphoenolpyruvate carboxylase (TCA cycle), and Rubisco (photosynthesis).

$$R\text{-}H + CO_2 \rightarrow R\text{-}CO_2^{\ominus} + H^+ \qquad \text{Equation 1.2}$$

Several other carbanion-forming enzymes share similarities to the C−C bond formation catalyzed by PurE. The citrate synthase mechanism has been extensively studied and serves as a model for enzymatic C−C bond formation. The reaction proceeds by formation of an acetyl-CoA carbanion (enolate), which then attacks a highly polarized carbonyl in enzyme-bound oxaloacetate (OAA). The polarization of OAA can be directly observed by infrared and ^{13}C NMR spectroscopy.[21,22] The subsequent steps in C−C bond formation can be monitored by changes in pre-steady state fluorescence.[23]

Unlike citrate synthase, PurE1 and PurE2 have a single substrate and it is challenging to detect carbonyl polarization by PurE. The C−C bond forming steps, however, are amenable to study by the same fluorescence-based approach used for citrate synthase.

Citrate synthase highlights an additional difficulty C−C forming enzymes encounter; it is not enough to simply generate a carbanion, a suitably reactive acceptor must also be present to avoid quenching by protonation. PurE1 and PurE2 may use hydrogen bonds to further polarize AIR and promote the reaction between the AIR carbanion and bound CO_2 (Figure 1.3).

PurE2 and Rubisco share the rare ability to fix CO_2 directly, without the need for additional energy input or other enzymes.[23–25] Rubisco cleaves ribulose 1,5-bisphosphate in competing irreversible carboxylase and oxygenase reactions. The Rubisco oxygenase reaction saps photosynthetic productivity.[24–26] The chemistry of initial attack on CO_2 shared by PurE2 and Rubisco is fundamentally different from all other known enzymes. However, neither PurE2 nor PurE1 has any known oxygenase activity. We speculate that the reason for this substrate specificity is PurE2 flips the sequence of steps in C−C bond formation relative to Rubisco: AIR reacts with CO_2 *before* carbon deprotonation (Figure 1.2). This chemical strategy may account for the vastly improved selectivity of PurE2•AIR for CO_2 over O_2.

PurE1 and PurE2 Acquire CO_2 Differently. PurE1 and PurE2 are thought to break and form C−C bonds through a common ternary complex, PurE•AIR•CO_2.[26–28] One absolute, class-specific difference is the source of CO_2: PurE1 produces it by the decarboxylation of bound NCAIR, while PurE2•AIR acquires CO_2 directly from solution (Figure 1.2).

Subtle Structural Differences in PurE1 and PurE2 Regulate Substrate Specificity. Minor structural differences in PurE1 and PurE2 must encode the divergent substrate specificity. First, PurE2 cannot use NCAIR[26] as a substrate and appears structurally unable to accommodate the “flipped” ring of NCAIR.[29] Second, the PurE2•AIR•CO_2 ternary complex reversibly dissociates CO_2, unlike the corresponding PurE1 complex, which quantitatively retains CO_2.[30] Polarization of PurE1 or PurE2-bound AIR forms the zwitterionic form, which electrostatically attracts CO_2 and helps to retain it. Confining

CO_2 in PurE1 preserves the investment made by PurK, which uses ATP to activate bicarbonate (Figure 1.1).

PurE2•AIR contains a 6 Å long portal leading to the carboxylate/CO_2-binding site that is not present in “closed” PurE1•AIR structures. [26,28] The portal may allow CO_2 to enter the active site after AIR and bind underneath it while allowing protons to exit. The portal also creates a polar, solvent accessible active site in PurE2. It is unclear how these class specific differences in PurE sequence, structure, and CO_2 acquisition evolved while still maintaining similar C−C bond forming chemistry though a common PurE•AIR•CO_2 ternary complex.

The 40s Loop Residues May Have Different Roles in Each PurE Class. Both PurE1 and PurE2 have similar structures, apart from two active site loops (Figure 1.3).[31,32] The 40s loop, SAH[R/K], contains a conserved His that functions as a general acid/base that is necessary for activity in both classes.[26,28,29] The 40s loop Ser is the sole polar contact with the substrate aminoimidazole ring and any PurE1 or PurE2 side chain (Figure 1.3). An earlier study of PurE2 suggests that the hydrogen bond between Ser and aminoimidazole N3 might flip polarity as a function of pH.[26] No similar function is expected for PurE1. In contrast, its first protonation equilibrium (pK_1) is associated with *inhibition* of activity.[28] Ser may have a different role in PurE1 and PurE2, producing subtle mechanistic differences between them.

The differentially conserved 40s loop basic residue, Arg in PurE1 and Lys in PurE2, contacts the phosphate moiety of the nucleotide (Figure 1.3). The challenging acquisition of CO_2 by PurE2 has been suggested to involve intermediate formation of an N-carboxylated species on this Lys, which is strictly conserved in PurE2.[30] Lys-carbamates are produced in Rubisco and urease [25,33,34] active sites, and a N-terminus carbamate is formed in hemoglobin to carry CO_2.[34] While this could serve to accumulate a CO_2 equivalent near the active site, carbamate formation *decreases* electrophilic reactivity, relative to free CO_2, making it seem unlikely that this would be useful in PurE2 catalysis.

Ancestral PurEs were single proteins. Several purine biosynthesis enzymes exist as fusion proteins containing two or more independent enzyme active sites in distinct domains.[31,35] As a general rule, bacteria have monofunctional single enzyme purine biosynthesis proteins. Bacteria contain a single domain, monofunctional PurE1.[28,36] Yeast and plants have a bifunctional PurE1-PurK fusion protein and vertebrates have a bifunctional PurE2—PurC fusion protein.[32,37] The fusion proteins in higher eukaryotes suggest the possibility of metabolite channeling or other regulatory phenomena added to the essential pathway architecture not necessarily used in the ancestral monofunctional proteins.

It is considerably more difficult to study an enzyme within a bifunctional complex especially where the same substrate compound binds to both active sites. Until recently, it was not possible to study PurE unless it was fused to PurK (PurK—PurE fusion ADE2 in yeast)[37] or PurC (PurE2—PurC fusion in *Gallus gallus* and PAICS in humans)[32,38]. A monofunctional PurE2 from the spirochete *Treponema denticola* (TdPurE2) was discovered and verified to be a bona fide PurE2 by our laboratory.[26] This allowed the characterization of a monofunctional PurE2, without interference from a separate active site that also binds CAIR, for the close comparison to PurE1 needed for mechanistic studies.

Which PurE Class was First? In many cases, enzyme divergence can be traced back to a common ancestor (or ancestral form) by phylogenetic analyses. When it comes to PurE, an unambiguous hypothesis about its evolutionary history has proven elusive. Phylogenic analyses do not provide a clear hypothesis that can account for the contemporary distribution of PurE classes or reveal how they many have diverged.[26] One might presume that, enzymes in higher eukaryotes (e.g. PurE2) are the more modern form, diverged from ancestral forms in microbes (PurE1). However, PurE2 is found throughout all kingdoms of life and eukaryotes have PurE1 and PurE2 in about equal numbers.[26] PurE2 is used by animals (many of which have readily available CO_2 via the bloodstream); but PurE2 is also found in a small number of bacteria, pathogenic protozoa (primitive eukaryotes), and archaea (Figure 1.4).[39–46] Lateral gene transfer may have happened from an animal host in all but the last case. In addition, *de novo* purine biosynthesis is not present in many parasites, the simpler eukaryotes that might help reconstruct the evolutionary history of eukaryotic PurE.

Does an Ambidextrous PurE1/PurE2 Exist? Evolutionary analysis is extremely problematic to perform with current forms of PurE1 and PurE2. Like PurE, mammalian paraoxonases were a family of enzymes with poorly understood evolutionary origins. The discovery of structurally similar bacterial enzymes with similar activity was used in the reconstruction of a phylogenetic tree, which established evolutionary origin and revealed the sequence divergences that led to the modern family of paraoxonases. Going one step further, the authors designed and characterized an ancestral paraoxonase with ambidextrous activity.[47,48]

Phylogenic analysis similar to those discussed above might require the discovery (or design) of an ambidextrous PurE1/PurE2. Characterization of an ambidextrous PurE1/PurE2 could help to pinpoint the key residue differences associated with PurE sequence and structure that occurred during the divergence of one PurE class from the other.

Does CO_2 Availability Dictate the Selection of a Particular PurE Class? CO_2 availability is the leading candidate to explain the "choice" of PurE class: bicarbonate is abundant in air-exposed water, charged, easy to bind, and unreactive; CO_2 is the opposite.[49]

PurE2 can directly use CO_2, while, PurE1 requires NCAIR as a ready source of CO_2. NCAIR is formed either from bicarbonate and ATP by PurK (Figure 1.1) or by the spontaneous carboxylation of AIR N6 under high CO_2 and high pH. NCAIR is highly labile with a half–life of only 0.9 min^{-1} at 37 °C and pH 7.8.[18]

Environmental pH also influences CO_2 availably. At low pH, NCAIR is less stable and CO_2 is favored over bicarbonate. The PurE equilibria are also influenced by pH: CAIR formation is favored over decarboxylation at high pH in PurE1 and PurE2. PurE2 favors CAIR decarboxylation in acid or at low pCO_2.[26,27,36]

We will consider the four environmental conditions presented in Figure 1.5.

1) High CO_2 and high pH, such as the bloodstream or the gastrointestinal tract in animals and deep-sea hydrothermal fields,[50,51] may support any PurE configuration.

2) High CO_2 and low pH**,** such as sediments and the deep sea surrounding deep-sea hydrothermal vents,[51,52] may support organisms possessing PurE2 since NCAIR formation is disfavored.

3) Low CO_2 and high pH, such as atmospheric conditions or shallow fresh water like tide pools and the littoral zone of lakes and rivers,[53,54] would require PurE1+PurK. PurK would be necessary to incorporate bicarbonate into NCAIR, as a ready source of CO_2.

4) Low CO_2 and low pH, such as deep-sea hydrothermal vents,[55] could support organisms possessing either PurE2 or PurE1+PurK (potential reasons for PurE2 are discussed further in Chapter 5).

We hypothesize that CO_2 availability could influence the presence of a certain PurE class within an organism. However, the possibility of random inheritance cannot be ruled out.

Newly Identified Microbial pure2 Genes are Found in Organisms from Predicted Environments. Prior to the work done with *T. denticola* PurE2, only a single other microbial *purE2* gene had been identified.[26] With the abundance of new genome sequences available, a BLAST search revealed six new microbial PurE2s from thermophilic and green sulfur bacteria (*D. thermophilum, O. profundus, D. orientale, M.*

salmonicolor, B. graminisolvens) and pathogenic protozoa (*B. hominis*) that inhabit the niches we would predict, deep sea environments and the gastrointestinal tract in animals, which have high CO_2 availability and high pH (Figure 1.4-1.5).[39–46]

PurE1 is an Unexploited Antibiotic Target. The "magic bullet" concept put forth by Paul Ehrlich is the basis for all chemotherapies.[56–58] Current antibiotics halt essential microbial functions such as cell wall, DNA and protein synthesis and lead to cell stasis or death.[59–61] An emerging focus in anti-infective agents is to target virulence factors rather than essential targets, which are under greater selective pressure that leads to the inevitable acquisition of drug resistance.[62–64] PurE1 has been validated as an anti-infective target with inhibitor studies currently underway.[65–67] The PurE-associated chemical divergence in purine biosynthesis nicely fits the "magic bullet" model: if PurE1 can be selectively inhibited, PurE2 should be unaffected. Achieving this challenging level of targeted specificity may require a detailed knowledge of the chemical mechanism used by PurE1 and PurE2.

Characteristics of PurE1 and PurE2 Examined in this Work. PurE1 from *Acetobacter aceti* PurE1 and *Treponema denticola* PurE2 are used here to explore the chemistry of C−C bond cleavage and CO_2 acquisition.

Chapter 2 details published work on metal stopping reagents for the PurE1 reaction.

Chapter 3 reports on the characterization of single-tryptophan AaPurE1 forms and the fluorescence changes associated with ligand binding. The results allowed the identification of the primary fluorophore (the molecule responsible for observed emission intensity upon excitation) and characterization of its fluorescence responses to ligand binding, which further studies can use to elucidate the chemistry of C−C bond formation.

Chapter 4 details the structural and kinetic characterization of 40s loop Ser mutants in AaPurE1 and TdPurE2. We found that this universally conserved Ser is important but not necessary for activity in both classes, interestingly it may have different roles in PurE1 and in PurE2.

Chapter 5 is a short description of the role associated with the 40s loop Lys in TdPurE2 mutants. The results rule out the possibility that a Lys carbamate is an obligatory intermediate in catalysis.

Chapter 6 is a short description of oxygenase activity in the "inactive" TdPurE2-H40N mutant. The detection of oxygenase activity in the highly CO_2 specific PurE2 may further the understanding of specificity in CO_2 fixing enzymes.

1.2 References

1. Plaut, G. W. E. Water-Soluble Vitamins, Part II (Folic Acid, Riboflavin, Thiamine, Vitamin B_{12}). *Annu. Rev. Biochem.* **30,** 409–444 (1961).

2. Roth, J. R., Lawrence, J. G. and Bobik, T. A. Cobalamin (Coenzyme B_{12}): Synthesis and Biological Significance. *Annu. Rev. Microbiol.* **50,** 137–181 (1996).

3. Miller, S. L. A Production of Amino Acids Under Possible Primitive Earth Conditions. *Science (80).* **117,** 528–529 (1953).

4. Zubay, G. and Mui, T. Prebiotic Synthesis of Nucleotides. *Orig. life Evol. Biosph.* **31,** 87–102

5. Oró, J. Synthesis of Adenine from Ammonium Cyanide. *Biochem. Biophys. Res. Commun.* **2,** 407–412 (1960).

6. Wächtershäuser, G. Before Enzymes and Templates: Theory of Surface Metabolism. *Microbiol. Rev.* **52,** 452–484 (1988).

7. Wächtershäuser, G. Groundworks for an Evolutionary Biochemistry: the Iron-Sulphur World. *Prog. Biophys. Mol. Biol.* **58,** 85–201 (1992).

8. Nyhan, W. L. Nucleotide Synthesis via Salvage Pathway. *eLS* (2014).

9. Alifano, P., Fani, R., Liò, P., Lazcano, A., Bazzicalupo, M., Carlomagno, M S. and Bruni, C B., Histidine Biosynthetic Pathway and Genes: Structure, Regulation, and Evolution. *Microbiol. Rev.* **60,** 44–69 (1996).

10. Ownby, K., Xu, H. and White, R. H. A *Methanocaldococcus Jannaschii* Archaeal Signature Gene Encodes for a 5-Formaminoimidazole-4-Carboxamide-1-Beta-D-Ribofuranosyl 5'-Monophosphate Synthetase. A New Enzyme in Purine Biosynthesis. *J. Biol. Chem.* **280,** 10881–10887 (2005).

11. Settembre, E., Begley, T. P. and Ealick, S. E. Structural Biology of Enzymes of the Thiamin Biosynthesis Pathway. *Curr. Opin. Struct. Biol.* **13,** 739–747 (2003).

12. Bazurto, J. V and Downs, D. M. Plasticity In the Purine-Thiamine Metabolic Network of *Salmonella. Genetics* **187,** 623–631 (2011).

13. Roepke, R. R., Libby, R. L. and Small, M. H. Mutation or Variation of *Escherichia coli* with Respect to Growth Requirements. *J. Bacteriol.* **48,** 401–412 (1944).

14. Toth, E. A., Worby, C., Dixon, J. E., Goedken, E. R., Marqusee, S. and Yeates, T.O. The Crystal Structure of Adenylosuccinate Lyase from *Pyrobaculum Aerophilum* Reveals an Intracellular Protein with Three Disulfide Bonds. *J. Mol. Biol.* **301,** 433–450 (2000).

15. Allen, S., Zilles, J. L. and Downs, D. M. Metabolic Flux in Both the Purine Mononucleotide and Histidine Biosynthetic Pathways Can Influence Synthesis of the Hydroxymethyl Pyrimidine Moiety of Thiamine in *Salmonella enterica. J. Bacteriol.* **184,** 6130–6137 (2002).

16. White, R. H. Purine Biosynthesis in the Domain Archaea Without Folates or Modified Folates. *J. Bacteriol.* **179,** 3374–3377 (1997).

17. Firestine, S. M., Poon, S. W. W., Mueller, E. J., Stubbe, J. and Davisson, V. J. Reactions Catalyzed by 5-Aminoimidazole Ribonucleotide Carboxylases from *Escherichia coli* and *Gallus gallus*: A Case for Divergent Catalytic Mechanisms? *Biochemistry* **33,** 11927–11934 (1994).

18. Mueller, E. J., Meyer, E., Rudolph, J., Davisson, V. J. and Stubbe, J. N^5-Carboxyaminoimidazole Ribonucleotide: Evidence for a New Intermediate and Two New Enzymatic Activities in the *de novo* Purine Biosynthetic Pathway of *Escherichia Coli*. *Biochemistry* **33,** 2269–2278 (1994).

19. Richard, J. P. and Amyes, T. L. Proton Transfer at Carbon. *Curr. Opin. Chem. Biol.* **5,** 626–33 (2001).

20. Gerlt, J. A. *Hydrogen-Transfer Reactions*. (Wiley, 2006).

21. Kurz, L. C. and Drysdale, G. R. Evidence From Fourier Transform Infrared Spectroscopy for Polarization of the Carbonyl of Oxaloacetate in the Active Site of Citrate Synthase. *Biochemistry* **26,** 2623–2627 (1987).

22. Kurz, L. C., Ackerman, J. J. H. and Drysdale, G. R. Evidence from ^{13}C NMR for Polarization of the Carbonyl of Oxaloacetate in the Active Site of Citrate Synthase. *Biochemistry* **24,** 452–457 (1985).

23. Kurz, L. C., Fite, B., Jean, J., Park, J., Erpelding, T. and Callis, P. Photophysics of Tryptophan Fluorescence: Link with the Catalytic Strategy of the Citrate Synthase from *Thermoplasma acidophilum*. *Biochemistry* **44,** 1394–1413 (2005)

24. Stec, B. Structural mechanism of Rubisco Activation by Carbamylation of the Active Site Lysine. *Proc. Natl. Acad. Sci. U. S. A.* **109,** 18785–18790 (2012).

25. Cleland, W. W., Andrews, T. J., Gutteridge, S., Hartman, F. C. and Lorimer, G. H. Mechanism of Rubisco: The Carbamate as General Base. *Chem. Rev.* **98,** 549–562 (1998).

26. Tranchimand, S., Starks, C. M., Mathews, I. I., Hockings, S. C. and Kappock, T. J. *Treponema denticola* PurE is a Bacterial AIR Carboxylase. *Biochemistry* **50,** 4623–4637 (2011).

27. Meyer, E., Kappock, T. J., Osuji, C. and Stubbe, J. Evidence for the Direct Transfer of the Carboxylate of N^5-Carboxyaminoimidazole Ribonucleotide (N^5-CAIR) to Generate 4-Carboxy-5-Aminoimidazole Ribonucleotide Catalyzed by *Escherichia Coli* PurE, an N^5-CAIR Mutase. *Biochemistry* **38,** 3012–3018 (1999).

28. Constantine, C. Z., Starks, C. M., Mill, C.P., Ransome, A. E., Karpowicz, S.J., Francois, J.A., Goodman, R.A. and Kappock, T. J. Biochemical and Structural Studies of N^5 -Carboxyaminoimidazole Ribonucleotide Mutase from the Acidophilic Bacterium *Acetobacter aceti. Biochemistry* **45,** 8193–8208 (2006).

29. Hoskins, A. A., Morar, M., Kappock, T. J., Mathews, I. I., Zaugg, J. B., Barder, T. E., Peng, P., Okamoto, A., Ealick, S. E. and Stubbe, J. N^5-CAIR Mutase: Role of a CO_2 Binding Site and Substrate Movement in Catalysis. *Biochemistry* **46,** 2842–2855 (2007).

30. Schaefer, J., Jiang, H., Ransome, A. E. and Kappock, T. J. Multiple Active Site Histidine Protonation States in *Acetobacter aceti* N^5-Carboxyaminoimidazole Ribonucleotide Mutase Detected by REDOR NMR. *Biochemistry* **46,** 9507–9512 (2007).

31. Mathews, I. I., Kappock, T. J., Stubbe, J. and Ealick, S. E. Crystal structure of *Escherichia coli* PurE, an Unusual Mutase in the Purine Biosynthetic Pathway. *Structure* **7,** 1395–1406 (1999).

32. Li, S. Tong, Y., Xie, X., Wang, Q., Zhou, H., Han, Y., Zhang, Z., Gao, W., Li, S., Zhang, X. and Bi, R. Octameric Structure of the Human Bifunctional Enzyme PAICS in Purine Biosynthesis. *J. Mol. Biol.* **366,** 1603–1614 (2007).

33. Jabri, E., Carr, M. B., Hausinger, R. P. and Karplus, P. A. The Crystal Structure of Urease from *Klebsiella aerogenes*. *Science* **268,** 998–1004 (1995).

34. Lorimer, G. H. Carbon Dioxide and Carbamate Formation: the Makings of a Biochemical Control System. *Trends Biochem. Sci.* **8,** 65–68 (1983).

35. Zhang, Y., Morar, M. and Ealick, S. E. Structural Biology of the Purine Biosynthetic Pathway. *Cell. Mol. Life Sci.* **65,** 3699–3724 (2008).

36. Meyer, E., Leonard, N. J., Bhat, B., Stubbe, J. and Smith, J. M. Purification and Characterization of the *purE, purK*, and *purC* Gene Products: Identification of a Previously Unrecognized Energy Requirement in the Purine Biosynthetic Pathway. *Biochemistry* **31,** 5022–5032 (1992).

37. Firestine, S. M., Misialek, S., Toffaletti, D.L., Klem, T. J., Perfect, J. R. and Davisson, V. J. Biochemical Role of the *Cryptococcus neoformans* ADE2 Protein in Fungal *de novo* Purine Biosynthesis. *Arch. Biochem.* **351,** 123–134 (1998).

38. Firestine, S. M. and Davisson, V. J. Carboxylases in *de novo* Purine Biosynthesis. Characterization of the *Gallus gallus* Bifunctional Enzyme. *Biochemistry* **33,** 11917–11926 (1994).

39. Estelmann, S., Ramos-Vera, W.H., Gad'on, N., Huber, H., Berg, I. A. and Fuchs, George. Carbon Dioxide Fixation in *Archaeoglobus lithotrophicus*: are There Multiple Autotrophic Pathways? *FEMS Microbiol. Lett.* **319,** 65–72 (2011).

40. Dashper, S. G., Seers, C. A., Tan, K. H. and Reynolds, E. C. Virulence Factors of the Oral Spirochete *Treponema denticola*. *J. Dent. Res.* **90,** 691–703 (2011).

41. Kumar, S., Subramanian, S., Raghava, G. P. S. and Pinnaka, A. K. Genome Sequence of the Marine Macterium *Marinilabilia salmonicolor.* JCM 21150T. *J. Bacteriol.* **194,** 3746 (2012).

42. Nishiyama, T., Ueki, A., Kaku, N., Watanabe, K. and Ueki, K. *Bacteroides graminisolvens* sp. nov., a Xylanolytic Anaerobe Isolated from a Methanogenic Reactor Treating Cattle Waste. *Int. J. Syst. Evol. Microbiol.* **59,** 1901–1907 (2009).

43. Miroshnichenko, M. L. *Oceanithermus profundus* gen. nov., sp. nov., a Thermophilic, Microaerophilic, Facultatively Chemolithoheterotrophic Bacterium from a Deep-sea Hydrothermal Vent. *Int. J. Syst. Evol. Microbiol.* **53,** 747–752 (2003).

44. Du, Z. J., Wang, Y., Dunlap, C., Rooney, A. P. and Chen, G.-J. *Draconibacterium orientale* gen. nov., sp. nov., Isolated from Two Distinct Marine Environments, and Proposal of *Draconibacteriaceae* fam. nov. *Int. J. Syst. Evol. Microbiol.* **64,** 1690–1696 (2014).

45. Coil, D. Coil, Badger, J. H., Forberger, H. C., Riggs, F., Madupu, R., Fedorova, N., Ward, N., Robb, F. T. and Eisen, J. A. Complete Genome Sequence of the Extreme Thermophile *Dictyoglomus thermophilum* H-6-12. *Genome Announc.* **2,** 12–13 (2014).

46. Denoeud, F., Roussel, M., Noel, B., Wawrzyniak, I., Da Silva, C., Diogon, M., Viscogliosi, E., Brochier-Armanet, C., Couloux, A., Poulain, J., Segurens, B., Anthouard, V., Texier, C., Blot, N., Poirier, P., Ng, G. C., Tan, K. Artiguenave, F., Jaillon, O., Aury, J., Delbac, F., Wincker, P., Vivarès, C. P. and El Alaoui, H. Genome sequence of the stramenopile *Blastocystis*, a Human Anaerobic Parasite. **12,** R29 (2011).

47. Elias, M. and Tawfik, D. S. Divergence and Convergence in Enzyme Evolution: Parallel Evolution of Paraoxonases from Quorum-Quenching Lactonases. *J. Biol. Chem.* **287,** 11–20 (2012).

48. Bar-Rogovsky, H., Hugenmatter, A. and Tawfik, D. S. The Evolutionary Origins of Detoxifying Enzymes: the Mammalian Serum Paraoxonases (PONs) Relate to Bacterial Homoserine Lactonases. *J. Biol. Chem.* **288,** 23914–23927 (2013).

49. Casey, J. R. Why Bicarbonate? *Biochem. Cell Biol.* **84,** 930–939 (2006).

50. Cummings, J. H. and Macfarlane, G. T. The Control and Consequences of Bacterial Fermentation in the Human Colon. *J. Appl. Bacteriol.* **70,** 443–459 (1991).

51. Kelley, D. S., Karson, J. A., Blackman, D. K., Früh-Green, G. L., Butterfield, D. A., Lilley, M. D., Olson, E. J., Schrenk, M. O., Roe, K. K., Lebon, G. T. and Rivizzigno, P. An Off-Axis Hydrothermal Vent Field Near the Mid-Atlantic Ridge at 30 ° N. *Nature* **412,** 145–149 (2001).

52. Yanagawa, K., Morono, Y., de Beer, D., Haeckel, M., Sunamura, M., Futagami, T., Hoshino, T., Terada, T., Nakamura, K., Urabe, T., Rehder, G., Boetius, A. and Inagaki, F. Metabolically Active Microbial Communities in Marine Sediment Under High-CO_2 and Low-pH Extremes. *ISME J.* **7,** 555–567 (2013).

53. Kempe, S. *Transport of Carbon and Minerals in Major World Rivers* (ed. Degens, E. T.) 91–332 (SCOPE/UNEP, 1982).

54. Neal, C., House, W., Jarvie, H. and Eatherall, A. The Significance of Dissolved Carbon Dioxide in Major Lowland Rivers Entering the North Sea. *Sci. Total Environ.* **210-211,** 187–203 (1998).

55. Jannasch, H. W. and Mottl, M. J. Geomicrobiology of Deep-Sea Hydrothermal Vents. *Science* **229,** 717–25 (1985).

56. Strebhardt, K. and Ullrich, A. Paul Ehrlich's Magic Bullet Concept: 100 Years of Progress. *Nat. Rev. Cancer* **8,** 473–480 (2008).

57. Gensini, G. F., Conti, A. A. and Lippi, D. The contributions of Paul Ehrlich to infectious disease. *J. Infect.* **54,** 221–224 (2007).

58. Ehrlich, P. *Die Schutzstoffe des Blutes*. (Verlag von Georg Thieme, 1901).

59. Davies, J. and Davies, D. Origins and Evolution of Antibiotic Resistance. *Microbiol. Mol. Biol. Rev.* **74,** 417–433 (2010).

60. Walsh, C. Antibiotics: Actions, Origins, Resistance. (2003).

61. Chadegani, F., Lovell, S., Mullangi, V., Miyagi, Masaru. and Bann, J. G. ^{19}F Nuclear Magnetic Resonance and Crystallographic Studies of 5-Fluorotryptophan-labeled Anthrax Protective Antigen and Effects of the Receptor on Stability. *Biochemistry* **53,** 690–701 (2014).

62. Clatworthy, A. E., Pierson, E. and Hung, D. T. Targeting Virulence: a New Paradigm for Antimicrobial Therapy. *Nat. Chem. Biol.* **3,** 541–548 (2007).

63. Allen, R. C., Popat, R., Diggle, S. P. and Brown, S. P. Targeting Virulence: Can We Make Evolution-Proof Drugs? *Nat. Rev. Microbiol.* **12,** 300–308 (2014).

64. Ruer, S., Pinotsis, N., Steadman, D., Waksman, G. and Remaut, H. Virulence-Targeted Antibacterials: Concept, Promise, and Susceptibility to Resistance Mechanisms. *Chem. Biol. Drug Des.* 1-21 (2015).

65. Samant, S., Lee, H., Ghassemi, M., Chen, J., Cook, J. L., Mankin, A. S. and Neyfakh, A. A. Nucleotide Biosynthesis is Critical for Growth of Bacteria in Human Blood. *PLoS Pathog.* **4,** e37 (2008).

66. Kim, A., Wolf, N. M., Zhu, T., Johnson, M. E., Deng, J., Cook, J. L. and Fung, Leslie W.M. Identification of *Bacillus anthracis* PurE Inhibitors with Antimicrobial Activity. *Bioorg. Med. Chem.*1492-1499 (2015).

67. Zhu, T., Lee, H., Lei, H., Jones, C., Patel, K., Johnson, M. E. and Hevener, K. E. Fragment-Based Drug Discovery Using a Multidomain, Parallel MD-MM/PBSA Screening Protocol. *J. Chem. Inf. Model.* **53,** 560–572 (2013).

1.3 Figures and Tables

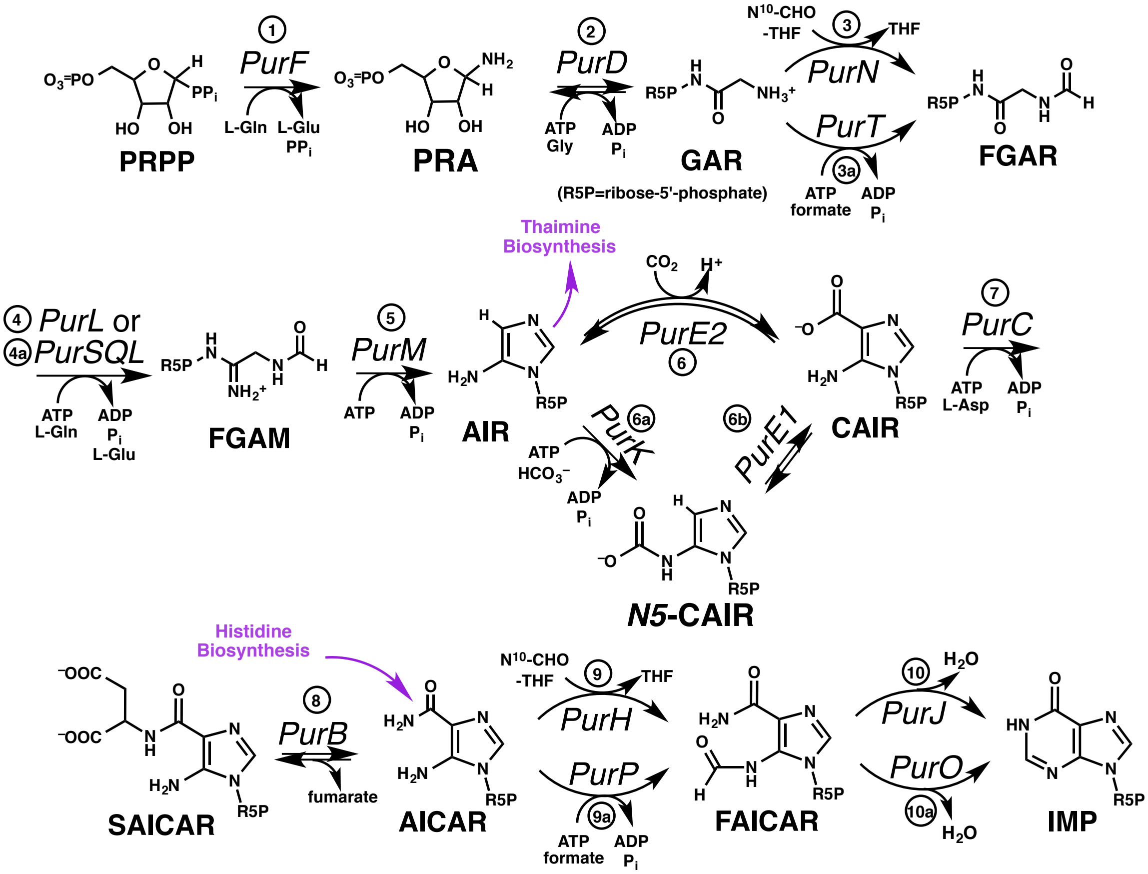

Figure 1.1 The *de novo* purine biosynthesis pathway. Steps 1–10 define the pathway in animals. Steps 3a, 4a, 6a, 6b, 9a and 10a represent variations of the pathway found in microbes, plants, or fungi. Thiamine biosynthesis requires AIR and histidine biosynthesis supplies AICAR.

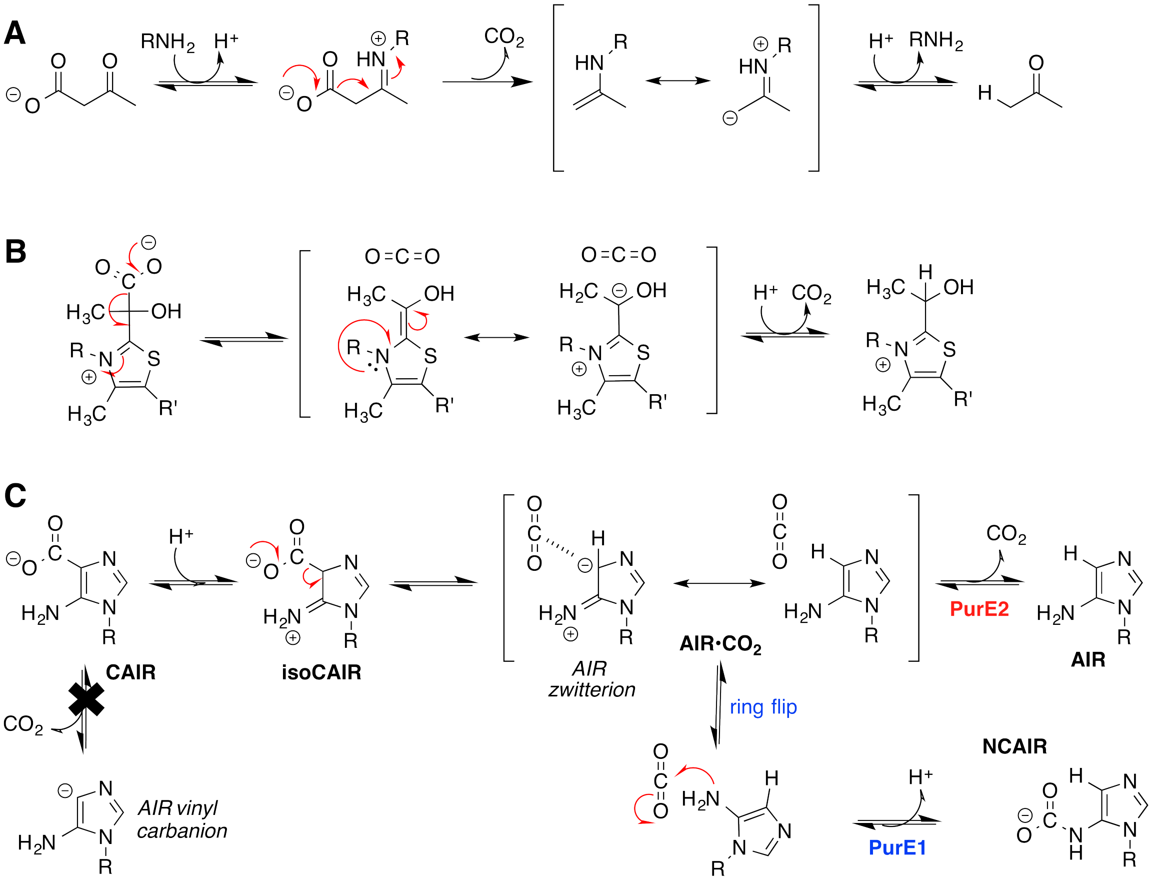

Figure 1.2 Decarboxylase reactions. (A) Acetoacetate decarboxylase forms a stabilized carbanion. (R = Lys) (B) Thiamine-dependent pyruvate decarboxylase forms a stabilized carbanion (R = aminopyrimidine ring and R' = hydroxyethyl side chain of the thiamine cofactor). (C) CAIR decarboxylation (R= ribose 5'-phosphate) begins with protonation, avoiding a non-stabilized vinyl carbanion, then decarboxylation. Both PurE1 and PurE2 form a ternary PurE•AIR•CO_2 complex. The conversion of NCAIR→CAIR by PurE1 requires an aminoimidazole ring flip and the qualitative retention of CO_2 and AIR.

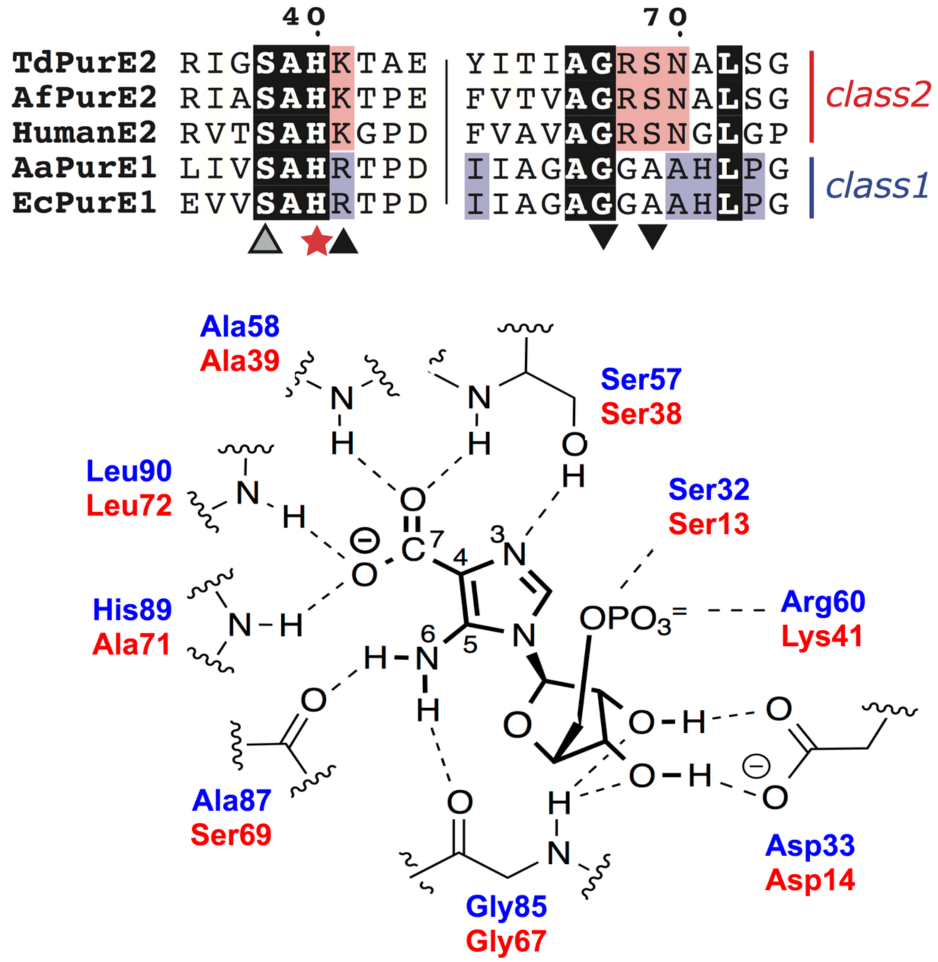

Figure 1.3 Sequence alignments and active site contacts in PurE1 and PurE2. (A) The 40s and 70s loops contain universal (black background) and class-specific (colored background) residues. The critical His is indicated with a star. Triangles denote other polar contacts with bound nucleotides (hydrogen bond donor, ▲; acceptor, ▼). The universally conserved Ser is denoted by a grey triangle, it may flip polarity in PurE2 at low pH. *Treponema denticola* PurE2 (TdPurE2) residue numbers are given. (B) PurE1 and PurE2 active site contacts with CAIR (*A. aceti* PurE1 residues shown in blue and *T. denticola* PurE2 residues shown in red).

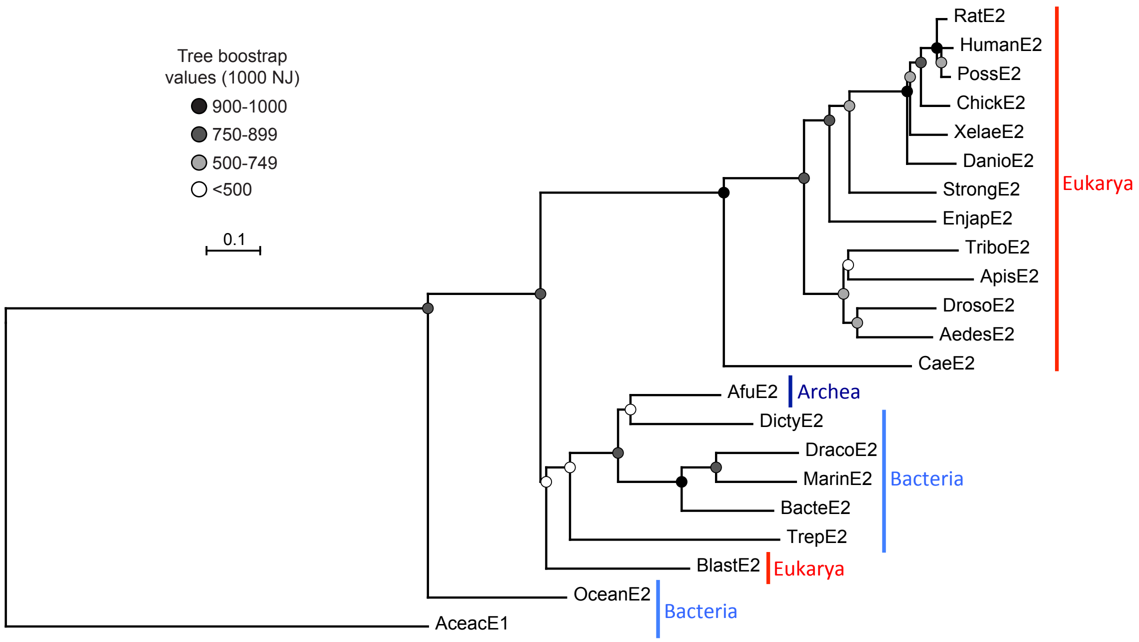

Figure 1.4 Phylogenetic tree illustrating PurE2 exists in diverse organisms throughout all three kingdoms. The newly identified PurE2s from green sulfur and thermophilic bacteria and pathogenic protozoa from (Figure 1.5) are included.

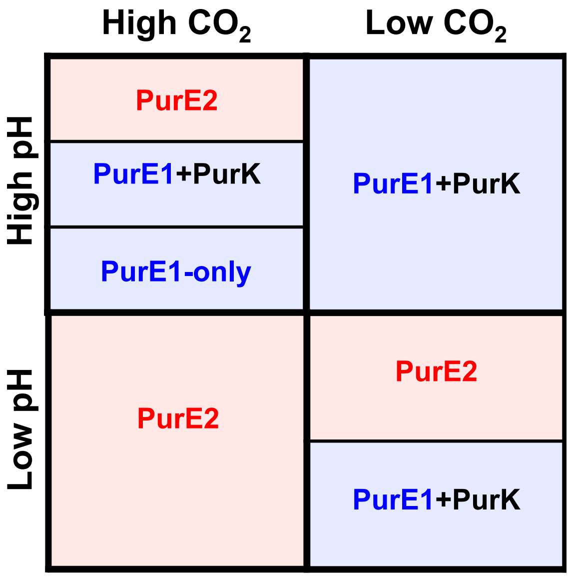

Figure 1.5 Possible PurE combinations in different environmental conditions. There are three known PurE combinations to consider: PurE2, PurE1+PurK, or PurE1-only without a recognizable PurK.[31] No known organisms have both a PurE1 and PurE2, this may be due to controlling metabolic flux of CO_2 and bicarbonate.

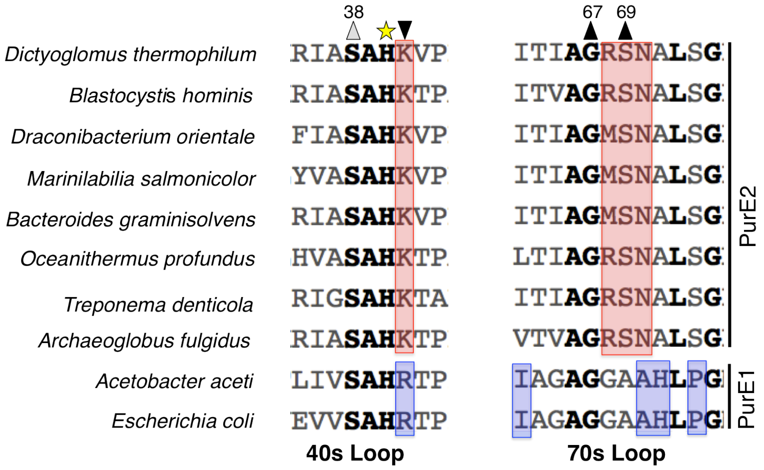

Figure 1.6 Diagnostic regions in newly identified *purE2* genes. (A) The 40s and 70s loops contain universal (bold letters) and class-specific (colored background) residues. The critical His is indicated with a star. Triangles denote other polar contacts with bound nucleotides (hydrogen bond donor, ▲; acceptor, ▼). The universally conserved Ser is denoted by a grey triangle, it may flip polarity in PurE2 at low pH. *Treponema denticola* PurE2 (TdPurE2) residue numbers are given. All PurEs shown are microbial, with the exception of *B. hominis.*

CHAPTER 2 METAL STOPPING REAGENTS FACILITATE DISCONTINUOUS ACTIVITY ASSAYS OF PURE1

2.1 Introduction

De novo purine biosynthesis harbors an unusual divergence in a ubiquitous biosynthetic pathway.[1] In most microbes and nonmetazoan eukaryotes, a class I PurE [PurE1, *N*-carboxyaminoimidazole ribonucleotide (NCAIR) mutase, EC 5.4.99.18] reversibly converts NCAIR to 4-carboxy-5-aminoimidazole ribonucleotide (CAIR) (Figure 2.1).[2] Animals produce CAIR by a different route, using a class II PurE (PurE2, 5-aminoimidazole ribonucleotide (AIR) carboxylase, EC 4.1.1.21)[3–5]. Microbial pathogenesis relies upon purine biosynthesis[6] particularly *purE1*, which is therefore a promising but unexploited antibiotic target.[7,8] Inhibitors selective for PurE1 could have antibacterial, antifungal, or herbicidal activity.[9] In this work, we describe a functional assay for PurE that is compatible with inhibitor identification by high-throughput screening (HTS) methods.

Currently available PurE1 functional assays are not amenable to HTS methods. A continuous ultraviolet (UV) assay that monitors the absorbance decrease due to CAIR decarboxylation[2,10,11] is subject to spectral interference by many candidate inhibitors.

*The text within this chapter is taken from the manuscript written in October 2013 by T.J. Kappock, K.L. Sullivan, and E.A. Mullins, with the exception of Figure 2.8 and Figures 2.10-2.12 and the text shown in italics throughout. T. J. Kappock performed the experiments with NiNTA and NiIDA columns and the nickel stopping experiments with EcPurE1. E. A. Mullins performed all HPLC analyses

CAIR synthesis assays are complicated by the acid lability of the NCAIR substrate[2,12,13], the need for multiple coupling enzymes,[9,14] and, for discontinuous assays detecting inorganic phosphate production, handling of malachite green reagent[15] and a background due to formation of phosphate by the coupling enzymes. The Bratton-Marshall assay (BMA)[16] was used in early studies of PurE2,[3] but seldom thereafter. The BMA yields intensely colored AIR and CAIR derivatives, AIR-BM and CAIR-BM (Figure 2.1), which possess characteristic visible absorbance spectra,17 are relatively stable, and might be suitable for HTS methods. The BMA, however, requires multiple, timed reagent additions that would be difficult to implement during parallel screens. An alternative would be to stop the PurE1 reaction prior to BMA workup using a reagent that does not alter product yields.

2.2 Materials and Methods

AICAR (>98% purity) was purchased from Sigma (St. Louis, MO) or Toronto Research Chemicals (Toronto, Canada). Other chemicals were purchased from Sigma; all were used without further purification. AIR was synthesized by enzyme-mediated decarboxylation.1 4-Carboxy-5-aminoimidazole ribonucleoside (CAIRs) was synthesized by saponification of 5-aminoimidazole-4-carboxamide ribonucleoside (AICARs).[18]

NiNTA agarose (Qiagen; Valencia, CA) was placed in a Micro Bio-Spin column (BioRad; Hercules, CA). NiIDA was prepared by saturating Chelex 100 (BioRad) with $NiSO_4$, followed by extensive water washing to rinse off unbound metal, and a portion was transferred to a Micro Bio-Spin column. A 3 mL disposable syringe plugged with cotton (cosmetic 100% cotton, 0.5 mL) was washed three times with H_2O to remove soluble fibers. Another 3 mL disposable syringe containing a layer of sand (0.5 mL) sandwiched between cotton layers (0.5 mL each) was washed with H_2O and then absolute ethanol (200 proof).

PurE1 from *Acetobacter aceti* and PurE2 from *Treponema denticola* were isolated as described previously.[5,19] Protein concentrations were determined by the method of Bradford using bovine serum albumin as the standard.[20]

Absorbance spectra were recorded on a Cary 100 UV-vis spectrophotometer or an Agilent 8453 diode-array spectrophotometer. Absorbance spectra were vertically shifted (by less than 0.001 A) to set the absorbance value at 800 nm at zero. ^{1}H NMR spectra were recorded on a Bruker 500 MHz NMR spectrometer, using 5 mm o.d. tubes and sample concentrations of ~25% (w/v) in D_2O.

Synthesis of CAIR. AICAR (50 mg, 0.15 mmol) was placed in a 25 mL round bottom flask containing LiOH (8 mL of a 1 M aqueous solution, 8 mmol). The flask was sealed with a septum and the mixture was stirred at 125 °C under a N_2 atmosphere. A positive pressure of N_2 was maintained using a balloon, with a small vent needle inserted to allow slow solvent evaporation. After ~2 h, the reaction mixture volume was ~2 mL. The reaction vessel was then sealed under a N_2 atmosphere and held for another 2.5 h at 125 °C. The reaction mixture was cooled to room temperature and deionized H_2O (2 mL) was added with stirring. The mixture was cooled to 0 °C and HCl (2 N) was added to adjust the pH to ~7, as judged by spotting on pH test strips. The solution was forced by air pressure through a column packed with cotton to remove particulates. The filtered solution was then lyophilized to dryness. The resulting solid was resuspended in cold absolute ethanol (3 x 15 mL) and transferred as a suspension to a column packed with cotton and sand. Air pressure was used to blow out residual ethanol. Cold deionized H_2O (20 mL) was applied to the cotton/sand column to dissolve CAIR, which was recovered and lyophilized to furnish a white powder (42.5 mg, 85% yield). ^{1}H NMR (500 MHz, D2O 4.84): δ 8.03 (s, 1H), 5.73 (d, J = 6.4 Hz, 1H), 4.63 (m, 1H), 4.42 (m, 1H), 4.32 (m, 1H), 4.03 (m, 2H).

Fluorescence Emission Spectra. Spectra were recorded on a Horiba Fluoromax-3 fluorometer thermostated with a Peltier Accessory and a Wavelength Electronics temperature controller using a 1 cm pathlength fluorometer cell that contained 2.0 mL of

AIR (0-23.8 μM), CAIR (0-23.8 μM), or AICAR (0-33 μM) in 50 mM Tris-HCl, pH 8. The excitation wavelength was 295 nm (2 nm slit width) and emission spectra were collected from 305 to 450 nm (5 nm slit width). A buffer only-spectrum was subtracted from as the background from all spectra.

LiOH Titrations. LiOH titrations (0-6.7 mM, neutralized to pH 8 with HCl, from 100 mM stock) were performed in 50 mM Tris-HCl, pH 8, with CAIR (10.5 μM) at 30 °C. CAIR fluorescence emission spectra were recorded as described above.

CAIR Synthesis Without Plastic Vessels. CAIR synthesis was carried out according to the above protocol with a single exception: no plastic vessels were used during synthesis. Instead only glassware soaked overnight in concentrated nitric acid was used. Fluorescence emission spectra of CAIR from this synthesis were recorded as described above.

CAIR Synthesis with Extensive EtOH Washes. CAIR synthesis was carried out according to the above protocol with a single exception: the lyophilized CAIR was resuspended in cold absolute ethanol (10 x 25 mL) and transferred as a suspension to a column packed with cotton and sand. Fluorescence emission spectra of CAIR from this synthesis were recorded as described above.

Metal Content of CAIR. CAIR titrations (0-50 μM CAIR, from 600 μM stock) were performed in 50 mM Tris-HCl, pH 8, with 8-Hydroxyquinoline-5-sulfonic acid (HQS; 1 mM) at 30 °C. CAIR fluorescence emission spectra were recorded as described above.

Removal of Metals from CAIR. EDTA titrations (0-20 mM, from a 200 mM stock) were performed in 50 mM Tris-HCl, pH 8, with CAIR (33 μM) at 30 °C. CAIR fluorescence emission spectra were recorded as described above.

CAIR (0.5 mL, 1 mM) in 50 mM Tris-HCl, pH 8 was incubated with Chelex-100 resin (0.5 mg of the sodium form prepared as in Bio-Rad manual) rocking, for 1 h at 4 °C. The CAIR solution was centrifuged (max speed, 30 s), the supernatant transferred, and diluted to 33 μM in the same buffer and CAIR fluorescence emission spectra were recorded as described above.

CAIR Separation from the Fluorescent Species. CAIR (235 nmoles) was applied to a silica column (0.6 cm x 2.2 cm) equilibrated in the one of the following solvents: water, 25% EtOH, 50% EtOH, 75% EtOH, or 100 % EtOH. A single CV of the same solvent was applied, the flow-thru collected, analyzed by BMA for the presence of CAIR, and fluorescence emission spectra were recorded as described above

CAIR (490 nmoles) in 50 mM Tris-HCl pH, 8 was mixed with 27 mg of C18 media (activated with MeOH and washed with 50 mM Tris-HCl pH, 8) and incubated rocking, for 4 h at 4 °C. The C18 mixture was transferred to a mini spin column (Qiagen) and eluted by centrifugation at (1000 g for 30 s). The elution was analyzed for the presence of CAIR by UV-endpoint assay and fluorescence emission spectra were recorded as described above.

CAIR (490 nmoles) in 50 mM Tris-HCl, pH 8 was applied to a ZnIDA (1.5 x 1 cm) column equilibrated in the same buffer. Buffer was applied (6 CV) and the flow-thru collected. The fractions were analyzed for the presence of CAIR by BMA and $ZnSO_4$ by the addition HQS (0.5 mM final concentration). HQS fluorescence was detected using a handheld UV lamp.

CAIR Quantitation Assays. CAIR samples (0.5 mL) were mixed 1:1 with orcinol reagent, heated to 100 °C for 30 min, cooled to ambient temperature, and quantitated at 670 nm. A blank spectrum was recorded from a solution containing a 1:1 orcinol reagent to water that was processed at described above. CAIR samples were referenced to an AMP calibration curve, AMP standards (5-250 μM, 10 mM stock solution standardized at 260 nm, ε_{260} = 15.4 mM^{-1} cm^{-1}) were mixed with orcinol reagent and processed as described above. Orcinol reagent [0.1% (w/v) orcinol acid and 0.1% (w/v) iron (III) chloride hexahydrate in concentrated HCl] was freshly prepared before use.

Phosphate ashing assays of CAIR were performed using a published method.[21] The CAIR sample (0.05 mL, 1 mM) in a 13 x 100 mm Pyrex test tube was mixed with and equal volume of 10%. $Mg(NO_3)_2$•$6H_2O$ in ethanol; the mixture was evaporated to dryness over a flame with rapid shaking and further heated in the flame until brown fumes were no longer observed. The mixture cooled to ambient temperature, 0.3 mL of 1 M HCl was added, the tube was capped, and heated at 100 °C for 15 min. An ascorbic acid mixture (0.7 mL) (1 part 10% ascorbic acid to 6 parts of 0.42% ammonium molybdate•$4H_2O$ in 1 M H_2SO_4) was then added and heated at 45 °C for 20 min. The solution was then read at 820 nm against a blank containing water in place of the CAIR solution.

Enzyme Activity Assays. A unit is defined as the amount of enzyme that produces 1 µmol product per min.

Continuous assays of PurE1-mediated CAIR decarboxylation were performed using a published method.[11] A final volume of 0.6 mL in a masked, 1 cm path length cuvette containing 50 mM Tris·HCl, pH 8.0, and CAIR (4–80 µM) was incubated at 30 °C for at least 3 min. Reactions were initiated by the addition of *Acetobacter aceti* PurE1 (27 ng; 2.4 nM subunits). The initial velocity of CAIR decomposition ($\Delta\varepsilon_{260}$ = 8930 M^{-1} cm^{-1}) was recorded at 260 nm, with a correction for a small background slope. CAIR was quantitated by endpoint assay using the same method, except that 50 µg mL^{-1} *Treponema denticola* PurE2 was the enzyme.

Discontinuous reaction mixtures (V_{rxn}, 0.15–2.0 mL final volume) contained 50 mM Tris·HCl, pH 8, 6-80 µM CAIR (12 nmol total), and 26–320 ng (M_{PurE1}) *Acetobacter aceti* PurE1 (10 nM subunits). After incubation at 30 °C for a period Δt ranging from 1–6 min, $ZnSO_4$ (V_{Zn}, 6 µL, of a 5 mM stock; equivalent to a three-fold molar excess over the amount of CAIR initially present) was added to stop the reaction and the mixture was vortexed briefly. An aliquot (V_{rxn}/1.2 mL) of each quenched mixture was withdrawn, adjusted to either 0.5 or 2.0 mL with buffer, and subjected to BMA analysis as described in the caption to Figure 6.7, except that the sample volume was larger.

The final analyte volume (V_a) was either 0.9 or 3.6 mL, depending on the cuvette used for analysis. A dilution correction factor C_{dil} was computed using equation 1.

$$C_{dil} = \frac{6}{5} \times \frac{V_{\mathrm{rxn}} + V_{\mathrm{Zn}}}{V_{\mathrm{rxn}}} \qquad \text{Equation 1}$$

The amount of AIR formed was determined from absorbance readings of the BMA reaction mixture, containing AIR-BM and CAIR-BM in varying ratios, for both the quenched reaction mixtures (A_{500}^{t}) and a no-enzyme control, processed in otherwise identical fashion ($A_{500}^{\mathrm{control}}$). The differential extinction coefficient for AIR formation was $\Delta\varepsilon_{500}$ = 13,600 M^{-1} cm^{-1}. The cuvette pathlength (ℓ) was 1 or 4 cm for V_a of 0.9 and 3.6 mL, respectively. Three replicate assays were performed at each [CAIR]. Reaction velocities (v) for AIR formation were computed using equation 2.

$$v = \left(\frac{A_{500}^{t} - A_{500}^{control}}{\Delta\varepsilon_{500}}\right) \times \frac{V_a C_{dil}}{\ell M_{PurE} \Delta t} \qquad \text{Equation 2}$$

One set of reaction mixtures (containing 40 µM CAIR) was quenched with $ZnSO_4$ as above, then incubated at room temperature for 24 h prior to BMA workup. Kinetic constants were obtained by non-linear least-squares fitting to the Michaelis-Menten equation with gnuplot (version 4.4).

Matrix-assisted Laser Desorption/Ionization (MALDI) Mass Spectrometry. BMA reaction mixtures containing 25 nmol of nucleotide or nucleoside were prepared as described in the caption to Fig. 2. Mass spectra were recorded on an ABI 4800 MALDI time-of-flight (TOF)/time-delayed fragmentation (TDF) instrument (AB SCIEX; Framingham, MA). The matrix was α-cyano-4-hydroxycinnamic acid in 50% acetonitrile and 0.1% trifluoroacetic acid.

High-Pressure Liquid Chromatography (HPLC) Analysis of BM Derivatives. HPLC analysis was performed using a Waters (Milford, MA) Breeze system equipped with a Waters 717plus autosampler. A ZORBAX Eclipse XDB-C18 column (4.6 × 150 mm, 5 µM; Agilent, Santa Clara, CA) with a C18 guard column (4.6 × 12.5 mm, 5 µM) was developed at 0.5 mL/min with dual- wavelength monitoring (260 nm / 500 nm). Buffer A was 150 mM sodium acetate, 200 mM sodium phosphate, pH 4.6. Buffer B was buffer A containing 30% methanol. The gradient program was: 0–5 min, 0% B; 5–25 min, 0 to 100% B; 25–30 min, 100% B, 35–55 min, 100 to 0% B; 55–60 min, 0% B.

Immobilized-Metal Affinity Chromatography (IMAC). NiIDA and NiNTA columns (0.4 mL bed volume) were equilibrated in 25 mM (N-morpholino)propanesulfonic acid (MOPS), pH 7.4. All operations were carried out under gravity flow at room temperature. A 1:1 mixture of AIR:CAIR (15 nmol combined, in 0.6 mL MOPS buffer) was applied to each column, which were then developed by the adding more MOPS buffer one bed volume at a time. Column fractions were analyzed by the BMA. CAIR adhering to the washed NiNTA column was completely displaced by the addition of excess $NiSO_4$ solution (data not shown).

Molecular model construction. A CAIR model (residue type C2R) was obtained from the HIC- Up server[22] and positioned using the Pymol[23] Pair Fitting “wizard” onto the organic ligands in a template crystal structure. The templates were 5-coordinate, distorted square pyramidal complexes [Zn(picH)(pic)Cl] (pic = picolinate, picH = picolinic acid)[24] and $[CuL_2(H_2O)]$ (L = 5-amino-1-tolylimidazole-4-carboxylate).[25] The second complex contains the same heterocycle that is present in CAIR.

2.3 Results

A New Synthesis Produces Highly Pure CAIR. The first task was to determine an extinction coefficient for CAIR-BM at 500 nm, a goal that requires pure CAIR. A new CAIR synthesis, which uses LiOH to saponify aminoimidazole-4-carboxamide ribonucleotide (AICAR) and thereby facilitates salt removal (see materials and methods), furnished CAIR in high yield (85%) and purity (99%). No peak corresponding to AIR H2 peak was observed in ^{1}H NMR spectra (Figure 2.2). Mass spectrometry (MS) analysis of BMA reaction mixtures revealed only the expected molecular ions for single BM adducts and ions present in control mixtures (Table 2.1). HPLC analysis of CAIR subjected to BMA workup showed 97% CAIR-BM / 3% AIR-BM (Figure 2.3); a small amount of AIR evidently forms during the BMA acid quench step. CAIR-BM appears to consist of a mixture of species that cannot be resolved by HPLC but that possess the same molecular formula. An isobaric mixture might also account for the complex shape of the CAIR-BM visible spectrum (Figure 2.4). Aliquots of a solution containing pure CAIR were (1) used to determine an accurate CAIR concentration, by complete conversion to AIR followed by BMA analysis, and (2) used to obtain a spectrum of CAIR-BM, which gave $\varepsilon_{500}^{\mathrm{CAIR-BM}}$ = 11,200 M^{-1} cm^{-1} (for comparison $\varepsilon_{500}^{\mathrm{AIR-BM}}$= 24,800 M^{-1} cm^{-1}. [17]

ZnSO$_4$ or NiSO$_4$ are Sufficient to Quench the PurE1 Reaction. The second task was to identify an enzyme quenching method that is compatible with BMA workup and product analysis. CAIR and analogues form stable complexes in which aminoimidazole N3 and O7 atoms (Figure 2.1) coordinate a transition metal ion. [25] (CAIR)-metal (n = 2 or 3) complexes (Figure 2.5) do not bind to or inhibit chicken PurE2 in the presence of excess free CAIR [26–28] Mg^{2+} inhibits PurE2-mediated CAIR decarboxylation but not AIR carboxylation, consistent with the formation of a low-affinity metal-CAIR complex.[1,10] To determine if transition metals can rapidly and reversibly form CAIR-metal complexes, a ten-fold molar excess (relative to the initial CAIR concentration) of $NiSO_4$ or $ZnSO_4$ was added to UV-monitored CAIR decarboxylation reaction mixtures. CAIR decarboxylation stopped immediately, but could be restarted by the addition of EDTA (Fig. 2.6). EDTA had no effect on BMA workup; the initial acidification step apparently dissociates CAIR complexes formed with either Ni^{2+} or Zn^{2+}.

ZnSO$_4$ is a Better Stopping Reagent than NiSO$_4$. Zn^{2+} appeared to form a CAIR complex with higher kinetic stability than Ni^{2+}, and to pose fewer concerns with regard to toxicity, spectral overlap with (C)AIR-BM, and redox chemistry. A CAIR decarboxylation reaction mixture incubated at 30 °C was stopped at ~30% completion by the addition of ~3 molar equivalents of $ZnSO_4$ (Figure 2.7). Equivalent yields of CAIR-BM were obtained if the BMA workup was delayed by up to 4 h. In contrast, Ni^{2+}-stopped reactions lost CAIR at the rate of about 10% per h at 30 °C (data not shown). A saturation curve employing $ZnSO_4$ quenching gave kinetic constants similar to the standard continuous UV assay (Figure 2.8). Indistinguishable velocities were obtained at 40 μM CAIR for a quenched reaction worked up promptly or after a 24 h delay. Therefore $ZnSO_4$ is a suitable stopping reagent for PurE1 reaction mixtures.

Formation of the *Ni^{2+}-CAIR Complex is Reversible*. Metal stopping reagents are proposed to work by rapid substrate depletion, an uncommon mode of enzyme inhibition (e.g., vancomycin).[29,30] Immobilized metal affinity chromatography (IMAC) was used to test if CAIR binds to Ni^{2+}, immobilized on a nitrilotriacetic acid (NTA) column. An equimolar mixture of CAIR and AIR was applied to the NiNTA column. The first column fraction contained pure AIR, consistent with selective retention of CAIR on the column as a CAIR-Ni^{2+} complex (Figures 2.9 and 2.10). Subsequent fractions contained CAIR, indicating that the Ni^{2+}-CAIR interaction was reversible (data not shown). While these results do not exclude the possibility that PurE1 is inhibited by direct protein-metal interactions, they indicate that the rapid formation of a stable CAIR-transition metal complex is sufficient to account for $ZnSO_4$-mediated arrest of CAIR decarboxylation.

CAIR Synthesized by the New Method Contains a Fluorescent Species. We observed that CAIR, synthesized by the new method reported in this chapter, contains a fluorescent species with a λ_{max} = 405 nm (Figure 2.11). No such signal has been reported for AIR/CAIR synthesized by previous methods that use different reaction conditions. Therefore, we attempted to identify the source of the fluorescent species.

1.1 We first turned our attention to the synthesis of CAIR. Could the staring materials themselves be fluorescent?

1.1a Fluorescence emission spectra were obtained for the starting materials LiOH and AICAR (data not shown). Neither of these compounds is fluorescent, therefore we decided to check the synthesis conditions.

1.2 We considered the fluorescent species could be leached from plastic vessels used during CAIR synthesis.

1.2a To ensure fluorescent contaminants could not come from the reaction vessels, CAIR was synthesized using only nitric acid washed glassware. However, the fluorescent species was still observed (data not shown). The fluorescent species does not appear to be a consequence of the plastic vessels or the starting materials.

2.1 We then wanted to know if the fluorescent species could be separated from CAIR.

2.1a . The last step of synthesis involves washing CAIR in ice cold EtOH (45 mL total) we attempted to remove the fluorescent species by extensive washing of CAIR in ice cold EtOH (250 mL total). The fluorescence emission spectra had slightly diminished intensity, but the additional washes sacrificed the yield of CAIR (data not shown), indicating removal of the fluorescent species also removes CAIR. Therefore, we attempted several other separation techniques.

2.1b Zn^{2+} tightly chelates CAIR and we exploited this property to purify CAIR. CAIR was applied to a ZnIDA column. However, CAIR strips the metal off the column and co-elutes with fluorescent species (data not shown).

2.1c CAIR may absorb to silica. Therefore, silica columns were used to separate CAIR from the fluorescent species. Again, CAIR co-elutes with fluorescent species (data not shown).

2.1d CAIR should not absorb to hydrophobic C18 media. Therefore, C18 media was used to purify CAIR. Again, CAIR co-elutes with fluorescent species (Figure 2.12). The fluorescent species has a linear correlation to CAIR concentration (before and after C18 separation), indicating that the fluorescent species is associated with CAIR and was not separated by any of the methods attempted.

3.1 We then considered that the fluorescent species could be due to a metal contaminant.

3.1a Metal chelates of HQS fluoresce intensely and the addition of HQS to a solution allows one to determine if metals are present. Titration of CAIR into HQS confirmed the presence of metals in the solution (data not shown). If these metals are responsible for the observed fluorescent species, we may be able to remove them and see a decrease in fluorescence intensity.

3.1b Metals were removed from CAIR solution by the addition of EDTA or by treatment with chelex. Removal of metals did not alleviate the intensity of the fluorescent species, indicating it is not sensitive to the presence of metals.

4.1 All attempts to purify the fluorescent species failed and in each case the fluorescent species co-elutes with CAIR. The fluorescent species could be CAIR itself or a derivative of CAIR

4.1a CAIR was the only species detected by ^{1}H-NMR (Figure 2.2) and MS analysis (data not shown). Therefore, we wanted to confirm that the only species in solution is intact CAIR. We performed multiple assays (orcinol-ribose, phosphate, BMA-N6 of CAIR, UV endpoint-CAIR β-anomer) to ensure only intact CAIR was present in solution. The values from these assays agree (CAIR 1.0 ± 0.3 mM) and demonstrate that we have only intact CAIR in solution. The use of multiple analytical techniques has not been successful in detecting any species other than CAIR.

The results presented above indicate that only CAIR is present in solution and always co-partitions with the fluorescent species. We were therefore forced to conclude that the fluorescent species could be CAIR.

2.4 Discussion

We Have Developed a PurE1 Assay that is Specific and Suitable for HTS. The method can be used to screen candidate inhibitors that absorb UV light, a common practical concern for detecting initial hits, which often have low potency and therefore require high compound concentrations that cause significant spectral interference. PurE1-mediated CAIR decarboxylation can be stopped by a single liquid addition, of a $ZnSO_4$ solution, and subjected to the BMA workup hours later. BMA-detected PurE1 screens require no other enzymes and can be used to screen candidate inhibitors that do not contain diazotizable amines or strong metal chelators. A related method might be employed for functional assays of the other enzyme known to use CAIR as a substrate, 5-aminoimidazole-4-*N*-succinylcarboxamide ribonucleotide (SAICAR) synthetase (PurC, EC 6.3.2.6) the other enzyme known to use CAIR as a substrate. SAICAR has recently been shown to activate cancer metabolism via pyruvate kinase isoform M2.[31]

CAIR Synthesized by the New Method Contains a Fluorescent Species. AIR and CAIR synthesized by an earlier method involving KOH have no intrinsic fluorescence. KOH saponified CAIR is less pure, with more AIR present (in as-isolated CAIR), forms more dark polymeric decay products (and a greater tendency to form them), and potentially quenchers that might mask the intrinsic fluorescence of CAIR. The new CAIR synthesis produces a very pure, apparently fluorescent product. This could be an unrecognized property of aminoimidazoles that was previously not observed due to older synthesis methods.

The Fluorescent Species Cannot be Removed from CAIR. All attempts to remove the fluorescent species failed; therefore, to minimize the contribution of the fluorescent species (λ_{max} at 405 nm) to fluorescence titration data, emission for all AIR and CAIR spectra were monitored at 320 nm. There is less contribution of the fluorescent species at 320 nm then at the AaPurE1 λ_{max} at 338 nm (Figure 6.12).

2.5 References

1. Firestine, S. M., Poon, S. W. W., Mueller, E. J., Stubbe, J. and Davisson, V. J. Reactions Catalyzed by 5-Aminoimidazole Ribonucleotide Carboxylases from *Escherichia coli* and *Gallus gallus:* A Case for Divergent Catalytic Mechanisms? *Biochemistry* **33,** 11927–11934 (1994).

2. Mueller, E. J., Meyer, E., Rudolph, J., Davisson, V. J. and Stubbe, J. N^5-Carboxyaminoimidazole Ribonucleotide: Evidence for a New Intermediate and Two New Enzymatic Activities in the *de novo* Purine Biosynthetic Pathway of *Escherichia coli*. *Biochemistry* **33,** 2269–2278 (1994).

3. Lukens, L. N. and Buchanan, J. M. Biosynthesis of the Purines. XXIV. The Enzymatic Synthesis of 5-Amino-1-Ribosyl-4-Imidazolecarboxylic Acid 5'-Phosphate from 5-Amino-1-Ribosylimidazole 5'-Phosphate and Carbon Dioxide. *J. Biol. Chem.* **234,** 1799–1805 (1959).

4. Firestine, S. M. and Davisson, V. J. Carboxylases in *de novo* Purine Biosynthesis. Characterization of the *Gallus gallus* Bifunctional Enzyme. *Biochemistry* **33,** 11917–11926 (1994).

5. Tranchimand, S., Starks, C. M., Mathews, I. I., Hockings, S. C. and Kappock, T. J. *Treponema denticola* PurE is a Bacterial AIR Carboxylase. *Biochemistry* **50,** 4623–4637 (2011).

6. Bacon, G. A., Burrows, T. W. and Yates, M. The Effects of Biochemical Mutation on the Virulence of Bacterium. *Br. J. Exp. Pathol.* **32,** 85–96 (1951).

7. Perfect, J. R., Toffaletti, D. L. and Rude, T. H. The Gene Encoding Phosphoribosylaminoimidazole Carboxylase (ADE2) is Essential for Growth of *Cryptococcus neoformans* in Cerebrospinal Fluid. *Infect. Immun.* **61,** 4446–4451 (1993).

8. Samant, S., Lee, H., Ghassemi, M., Chen, J., Cook, J. L., Mankin, A. S. and Neyfakh, A. A. Nucleotide Biosynthesis is Critical for Growth of Bacteria in Human Blood. *PLoS Pathog.* **4,** e37 (2008).

9. Firestine, S. M., Paritala, H., Mcdonnell, J. E., Thoden, J. B. and Holden, H. M. Identification of Inhibitors of N^5-Carboxyaminoimidazole Ribonucleotide Synthetase by High-Throughput Screening. *Bioorganic Med. Chem.* **17,** 3317–3323 (2009).

10. Patey, C. A. H. and Shaw, G. Purification and Properties of an Enzyme Duet, Phosphoribosylaminoimidazole Carboxylase and Phosphoribosyl Aminoimidazole Succinocarboxamide Synthetase, Involved in the Biosynthesis of Purine Nucleotides *de novo*. *Biochem. J.* **135,** 543–545 (1973).

11. Meyer, E., Leonard, N. J., Bhat, B., Stubbe, J. and Smith, J. M. Purification and Characterization of the purE, purK, and purC Gene Products: Identification of a Previously Unrecognized Energy Requirement in the Purine Biosynthetic Pathway. *Biochemistry* **31,** 5022–5032 (1992).

12. Groziak, M. P., Bhat, B. and Leonard, N. J. Nonenzymatic Synthesis of 5-Aminoimidazole Ribonucleoside and Recognition of its Facile Rearrangement. *Proc. Natl. Acad. Sci.* **85,** 7174–7176 (1988).

13. Bhat, B., Groziak, M. P. and Leonard, N. J. Nonenzymatic Synthesis and Properties of 5-Aminoimidazole Ribonucleotide (AIR). Synthesis of Specifically ^{15}N-Labeled 5-Aminoimidazole Ribonucleoside (AIRs) Derivatives. *J. Am. Chem. Soc.* **112,** 4891–4897 (1990).

14. Firestine, S. M., Misialek, S., Toffaletti, D.L., Klem, T. J., Perfect, J. R. and Davisson, V. J. Biochemical Role of the *Cryptococcus neoformans* ADE2 Protein in Fungal *de novo* Purine Biosynthesis. *Arch. Biochem.* **351,** 123–134 (1998).

15. Carter, S. G. and Karl, D. W. Inorganic Phosphate Assay with Malachite Green: an Improvement and Evaluation. *J. Biochem. Biophys. Methods* **7,** 7–13 (1982).

16. Bratton, A. C. and Marshall, E. K., J. A New Coupling Component for Sulfanilamide Determination. *J. Biol. Chem.* **128,** 537–550 (1939).

17. Schrimsher, J. L., Schendel, F. J. and Stubbe, J. Isolation of a Multifunctional Protein with Aminoimidazole Ribonucleotide Synthetase, Glycinamide Ribonucleotide Synthetase and Glycinamide Ribonucleotide Transformylase Activities: Characterization of the Aminoimidazole Ribonucleotide Synthetase. *Biochemistry* **25,** 4356–4365 (1986).

18. Srivastava, P., Mancuso, R., Rousseau, R. and Robins, R. Nucleoside Peptides. 6. Synthesis of Certain N-[5-Amino-1-(β-D-Ribofuranosyl)Imidazole-4-Carbonyl]Amino Acids Related to Naturally Occurring Intermediates in the Purine Biosynthetic Pathway. *J. Med. Chem.* **17,** 1207–1211 (1974).

19. Constantine, C. Z., Starks, C. M., Mill, C.P., Ransome, A. E., Karpowicz, S.J., Francois, J.A., Goodman, R.A. and Kappock, T. J. Biochemical and Structural Studies of N^5-Carboxyaminoimidazole Ribonucleotide Mutase from the Acidophilic Bacterium *Acetobacter aceti. Biochemistry* **45,** 8193–8208 (2006).

20. Bradford, M. M. A Rapid and Sensitive Method for the Quantitation of Microgram Quantities of Protein Utilizing the Principle of Protein-Dye Binding. *Anal. Biochem.* **72,** 248–254 (1976).

21. Ames, B. N. and Dubin, D. T. The Role of Polyamines in the Neutralization of Bacteriophage Deoxyribonucleic Acid. *J. Biol. Chem.* **235,** 769–775 (1960).

22. Kleywegt, G. J. and Jones, T. A. Databases in Protein Crystallography. *Acta Crystallogr. D. Biol. Crystallogr.* **54,** 1119–11131 (1998).

23. DeLano, W. L. The PyMOL Molecular Graphics System. (2002). http://www.pymol.org

24. Goher, M. A. S., Abu-Youssef, M. A. M. and Mautner, F. A. Synthesis, Spectral and Structural Characterization of a Monomeric Chloro Complex of Zinc(II) with Picolinic Acid, $[Zn(C_5H_4NCO_2H)(C_5H_4NCO_2)Cl]$. *Polyhedron* **15,** 453–457 (1996).

25. Collins, M. Ewing, D., Mackenzie, G., Sinn, E. Sandbhor, U., Padhye, S. and Padhye, S. Metal Complexes as Anticancer Agents: 2. Synthesis, Spectroscopy, Magnetism, Electrochemistry, X-Ray Crystal Structure and Antimelanomal Activity of the Copper (II) Complex of 5-Amino-1-Tolylimidazole-4-Carboxylate in B16F10 Mouse Melanoma Cells. *Inorg. Chem. Commun.* **3,** 453–457 (2000).

26. Cusack, N. J., Shaw, G. and Litchfield, G. J. Purines, Pyrimidines, and Imidazoles. XXXVI. Carboxylation of Some 5-Aminoimidazoles and Related Compounds, Including Nucleosides and Nucleotides, with Potassium Hydrogen Carbonate in Aqueous Solution. *J. Chem. Soc. Perkin 1* **8,** 1501–1507 (1971).

27. Chipperfield, J. R., Humble, R. W., Iveson, G., Kadir, K., Mackenzie, G. and Shaw, G. Transition Metal Complexes of 5-Amino-1-β-D-Ribofuranosylimidazole-4-Carboxylic Acid 5′-Phosphate, an Intermediate in the *de novo* Biosynthesis of Purine Nucleotides: Synthesis and Effects on Enzyme Activity. *Nucleosides and Nucleotides* **6,** 353–358 (1987).

28. Chipperfield, J. R., Humble, R. W., Iveson, G., Kadir, K., Mackenzie, G. and Shaw, G. Effects on the Activity of the Enzyme Phosphoribosyl-Aminoimidazole Carboxylase, Involved in the Biosynthesis of Purine Nucleotides De Novo by Bi-Valent Metal Complexes of the Natural Substrate 5-Amino-1-β-D-Ribofuranosylimidazole-4-Carboxylic Acid 5′-Phophosphate. *Nucleosides and Nucleotides* **7,** 571–576 (1988).

29. Perkins, H. R. Vancomycin and Related Antibiotics. *Pharmacol. Ther.* **16,** 181–197 (1982).

30. Kodadek, T. Biochemistry: Molecular Cloaking Devices. *Nature* **453,** 861–862 (2008).

31. Keller, K. E., Tan, I. S. and Lee, Y.-S. SAICAR Stimulates Pyruvate Kinase Isoform M2 and Promotes Cancer Cell Survival in Glucose-Limited Conditions. *Science (80).* **338,** 1069–1072 (2012).

2.6 Figures

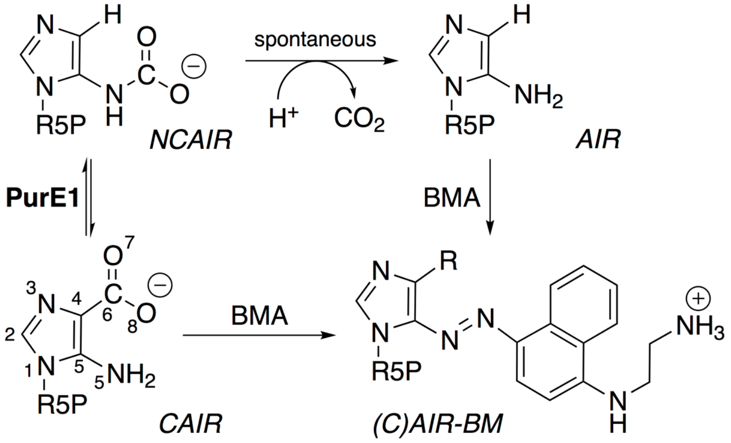

Figure 2.1 PurE1 reaction and CAIR/AIR detection by Bratton–Marshall assay (BMA). NCAIR decarboxylates to AIR (half-life of 0.9 min at pH 7.8 and 30 °C) during the enzyme assay,[2] an acid-dependent process that goes to completion during the BMA. R5P = ribosyl 5’-phosphate, R = H (AIR-BM) or COO^- (CAIR-BM). CAIR aminoimidazole atoms are numbered as in PDB residue type C2R.

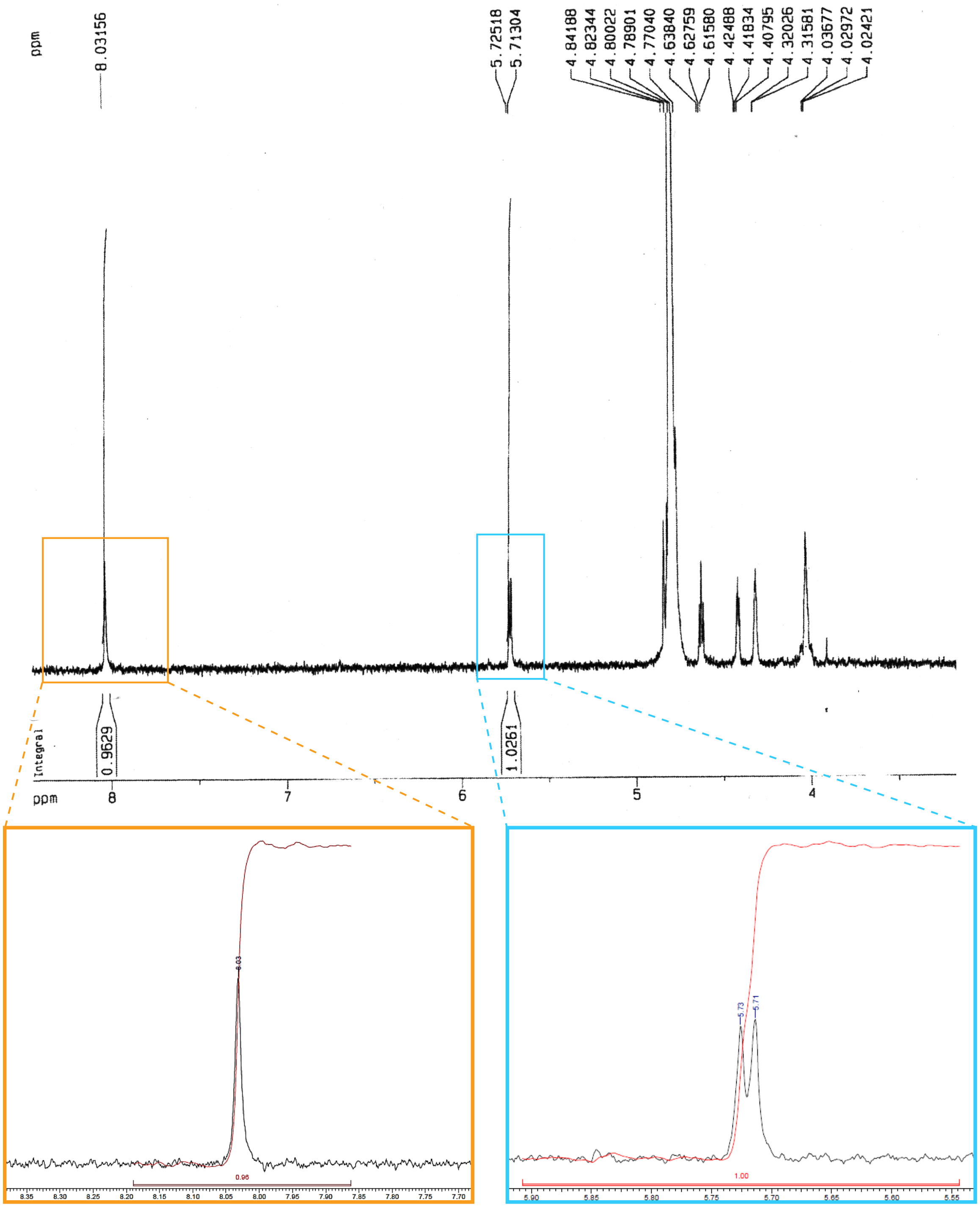

Figure 2.2 ^{1}H NMR spectrum of CAIR (500 MHz) in D_2O. AIR H2 would give a singlet with δ ~ 8.3 ppm; only the CAIR H2 signal is observed in this region (orange box). AIR H1′ would give a doublet with δ ~ 5.80 ppm; only the CAIR H1′ signal is observed in this region (blue box). Due to facile solvent exchange, AIR H4 (δ ~ 6.3 ppm) is typically not detected under these conditions.[17]

Table 2.1 MALDI-TOF MS analysis of selected BM derivatives. [a]

	[M+H+] (m/z)		[M+K+] (m/z)	
BM derivative	obs	exp	obs	exp
AIR-BM	493.09	493.16	none	531.12
CAIR-BM	537.11	537.15	575.06	575.11
CAIRs-BM	457.14	457.18	495.10	495.14
AICAR-BM	536.09	536.17	574.05	574.12
AICARs-BM	456.13	456.20	494.09	494.15

[a] Observed peaks (obs) were the most abundant molecular ions that were not observed in control spectra. BMA controls were prepared without a diazotizable amine. Exact masses (exp) were computed using ChemBioDraw 12.0 (CambridgeSoft).

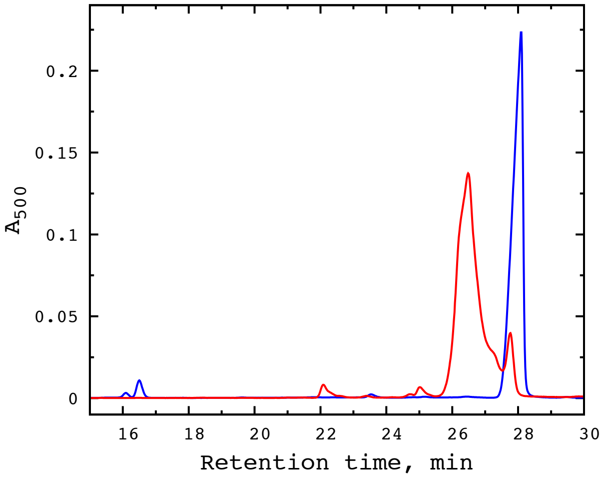

Figure 2.3 HPLC analysis of BMA reaction mixtures containing CAIR-BM (red trace, 26.4 min) or AIR-BM (blue trace, 28.1 min). Contaminating AIR-BM can be seen in the CAIR-BM trace as a peak at 27.8 min, as confirmed by co-injection with authentic AIR-BM (data not shown). The AIR chromatogram has been scaled by 45%.

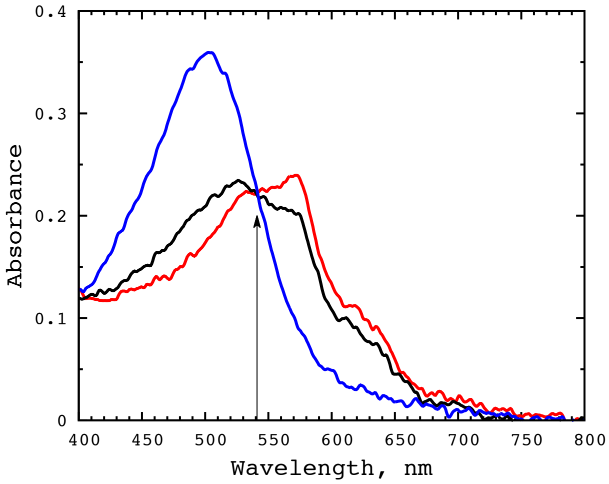

Figure 2.4 Visible absorbance spectra for CAIR-BM (red trace), AIR-BM (blue trace), and a 30:70 mixture of AIR-BM:CAIR-BM (black trace). Spectra of AIR-BM and CAIR-BM consistently cross at a single wavelength, 541 nm (vertical arrow). Spectra were recorded on a Cary 100 spectrophotometer.

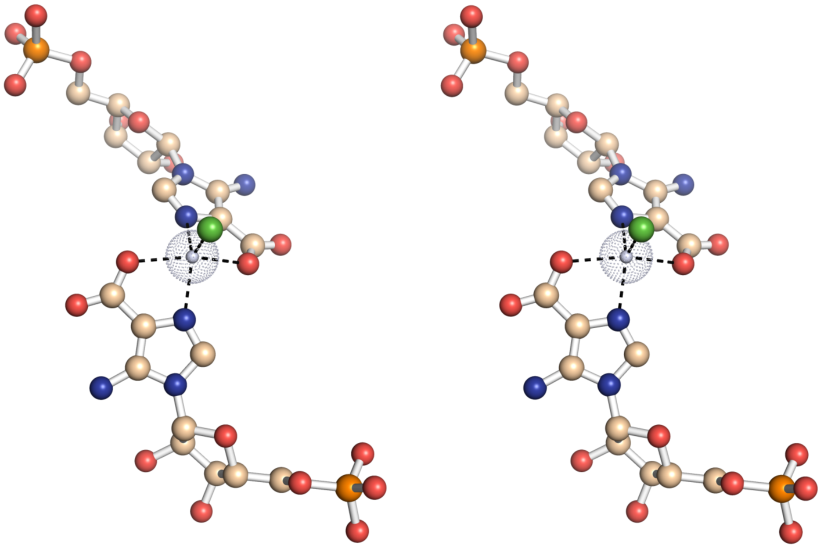

Figure 2.5 Wall-eyed stereodiagram depicting a speculative model of a $[Zn(CAIR)_2Cl]$ complex. The model was built as described above, using a [Zn(picH)(pic)Cl] complex[24] as the template. All atoms are presented in ball-and-stick depictions, in which each sphere radius is one-quarter of the van der Waals radius. The dotted sphere depicts the full van der Waals radius for Zn^{2+}. In this view, the Zn atom and the front aminoimidazole ring are approximately coplanar in the plane of the page. The Zn−Cl bond, which is tilted towards the viewer and to the right, defines the tetragonal axis, which has approximate twofold symmetry in these complexes.

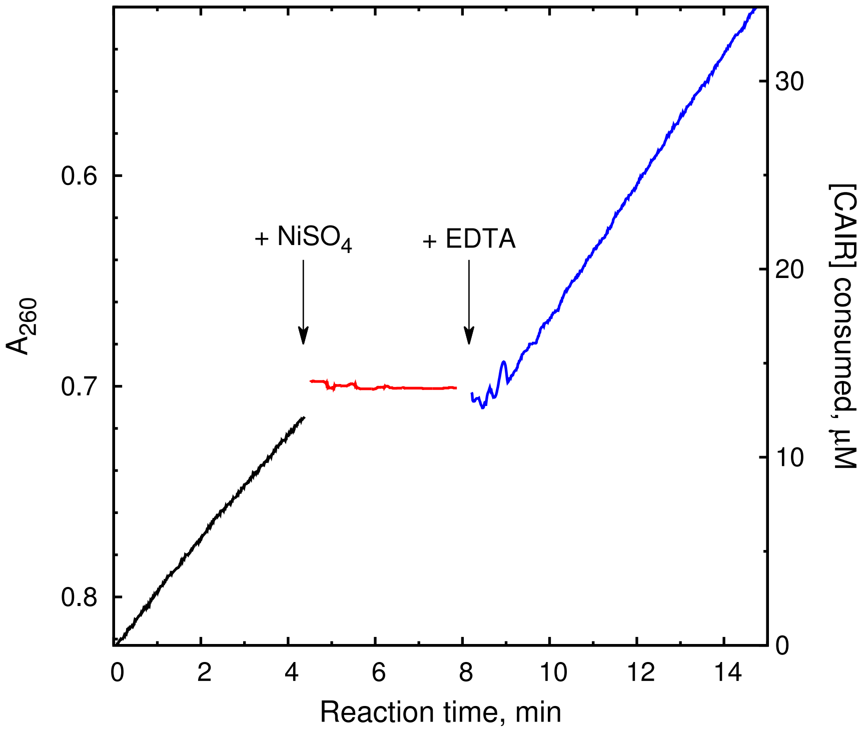

Figure 2.6 Nickel stops CAIR decarboxylation by *E. coli* PurE1. The reaction mixture (0.7 mL) initially contained 100 µM CAIR in 50 mM Tris·HCl, pH 8.0 (37 °C). CAIR decarboxylation was initiated by the addition of PurE1 at $t = 0$. A unit is defined as the amount of PurE1 that catalyzes 1 µmol CAIR decarboxylation per min. Absorbance changes at 260 nm (black trace, 0.0021 units) were converted to [CAIR] using the differential extinction coefficient $\Delta\varepsilon_{260}^{\mathrm{CAIR}\rightarrow\mathrm{AIR}} = 8930\ \mathrm{M}^{-1}\ \mathrm{cm}^{-1}$. The addition of 1 mM $NiSO_4$ stops CAIR decarboxylation (red trace, ~0 units). Full activity (blue trace, 0.0024 units) was restored upon the addition of 5 mM EDTA. $ZnSO_4$ also immediately stops CAIR decarboxylation but enzyme activity was not restored as quickly after the addition of EDTA (data not shown). These data have been digitized from a strip-chart recording.

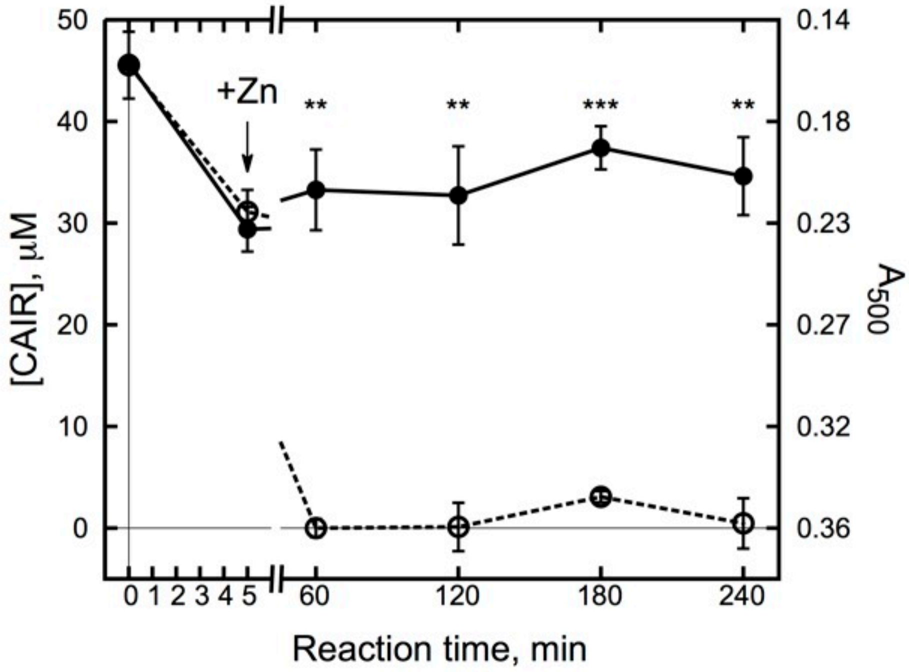

Figure 2.7 Zn^{2+} ions stop CAIR decarboxylation. Reaction mixtures (1.26 mL final volume) at 30 °C contained 50 mM Tris-HCl, pH 8.0, 42 μM CAIR, and 0.13 μg *Acetobacter aceti* PurE1 (0.005 units).[19] At 5 min, $ZnSO_4$ (0.1 mM) was added to one reaction. Aliquots (0.2 mL) were removed prior to the addition of enzyme (zero time point) and at indicated intervals, and immediately added to a 1.7 mL centrifuge tube containing a freshly prepared mixture of 20% (w/v) trichloroacetic acid / 1.33 M potassium phosphate, pH 1.4, (0.1 mL) and 0.1% (w/v) sodium nitrite (0.1 mL). After 3 min, 0.5% (w/v) ammonium sulfamate (0.1 mL) was added to destroy excess nitrite. After an additional min, Bratton–Marshall reagent [0.1 mL of 0.1% (w/v) N-(1-naphthyl)ethylenediamine dihydrochloride] was added. After 10 min, the solution (0.6 mL) was centrifuged (16,000g, 30 s) to eliminate bubbles and the absorbance at 500 nm (A_{500}) was recorded. CAIR consumption was quantitated using a differential extinction coefficient for CAIR to AIR conversion, $\Delta\varepsilon_{500} = \varepsilon_{500}^{\mathrm{AIR-BM}} - \varepsilon_{500}^{\mathrm{CAIR-BM}}$ =13,600 ± 1600 M^{-1} cm^{-1}. [CAIR] values at time t were determined using $(A_{500}^{\mathrm{AIR-BM}} - A_{500}^{t})/\Delta\varepsilon_{500}$, where $A_{500}^{\mathrm{AIR-BM}}$ was from a control reaction in which CAIR was completely converted to AIR. The symbols and error bars represent the mean and standard deviation, respectively, for at least three independent replicates of $ZnSO_4$-quenched (filled circles) and unquenched control (open circles) reactions. Concentrations determined at t > 5 min were significantly different in quenched and control reaction mixtures [one-tailed t-test, P-value <0.01 (**) or <0.001 (***)]. The slope of the line connecting the first two points corresponds to 0.003 units of enzyme activity, comparable to the 0.004 units expected under the reaction conditions. [19]

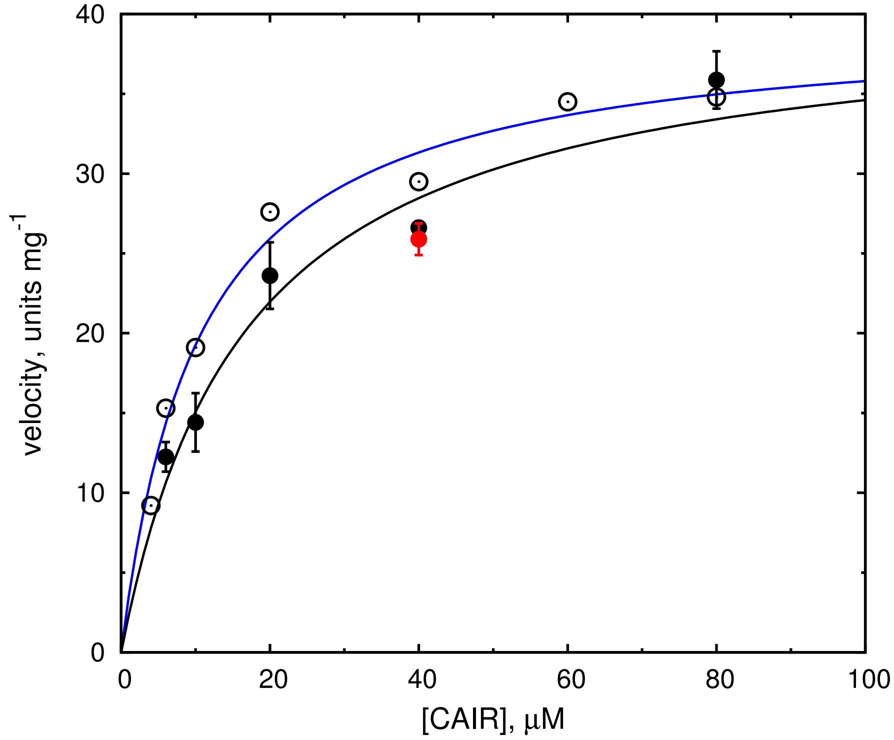

Figure 2.8 PurE1 saturation curves for continuous assays (open circles and blue trace) and discontinuous $ZnSO_4$-quenched, BMA-detected assays (filled circles, black trace). The symbols and error bars shown for the discontinuous assays represent the mean and standard deviation of three replicate measurements at each [CAIR]. One triplicate assay was subjected to BMA analysis 24 h after the quenching step (red symbol). Each solid line is a non-linear least-squares fit to the Michaelis-Menten equation: continuous assay, $V_{max} = 40 \pm 2$ units mg^{-1} and $K_m = 11 \pm 1$ μM; discontinuous, $V_{max} = 40 \pm 2$ units mg^{-1} and $K_\mathrm{m} = 17 \pm 3$ μM.

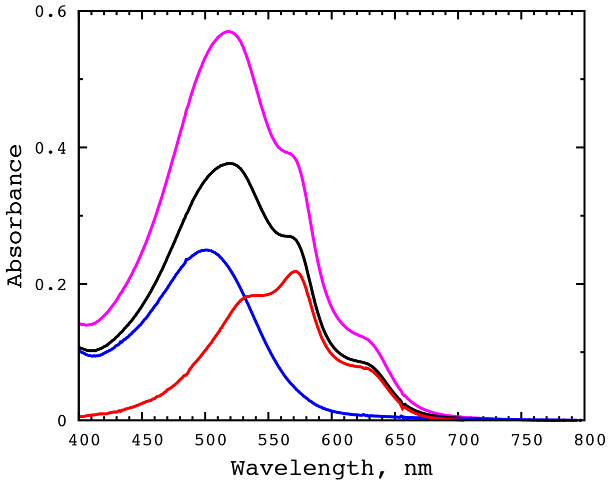

Figure 2.9 CAIR reversibly binds Ni^{2+}. A 1:1 mixture of AIR:CAIR was applied to IMAC columns developed in MOPS buffer (pH 7.4). BMA derivatives were prepared from the fractions emerging from Ni^{2+}-loaded nitrilotriacetic acid (NTA) and iminodiacetic (IDA) columns. Spectra correspond to BMA derivatives of the first fractions recovered from NiIDA (black trace) or NiNTA (blue trace) columns of equal volume. A NiIDA–NiNTA difference spectrum (red trace) is consistent with the spectrum of pure CAIR-BM (Figure 6.4). A reference spectrum (purple trace) obtained using the undiluted 1:1 AIR:CAIR mixture applied to both columns shows the same proportion of BMA derivatives present in the NiIDA fraction. Spectra were recorded on an Agilent 8453 spectrophotometer.

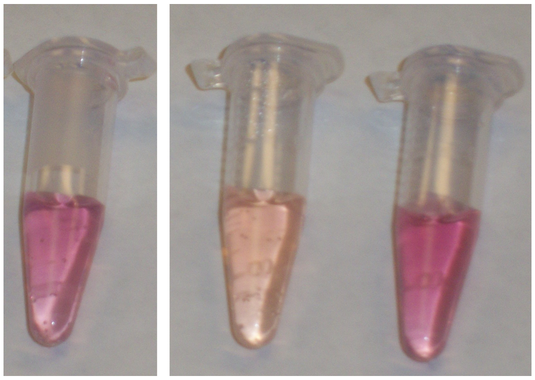

Figure 2.10 Fractions from IMAC columns loaded with a 1:1 mixture of CAIR:AIR then derivatized by the BMA. A NiNTA fraction (center tube) contains mainly the orange-colored AIR-BM. A NiIDA fraction (left tube) resembles a standard (15 nmol total AIR+CAIR) containing BM derivatives of the mixture applied to each column (right tube). The images are derived from a single photograph, trimmed at the gap.

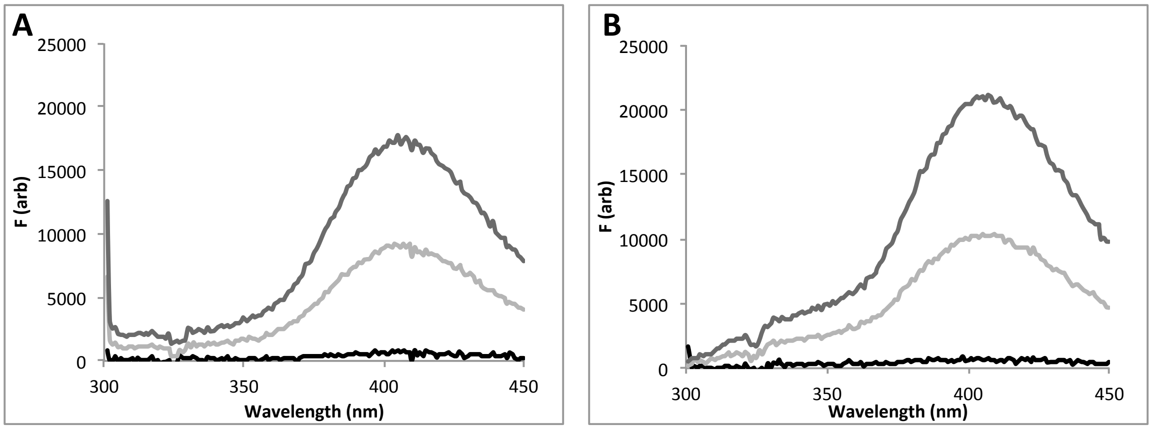

Figure 2.11 CAIR and AIR fluoresence emission spectra. CAIR and AIR (0 µM-23.8 µM, 0.6 mM stocks) were added to 50 mM Tris-HCl, pH 8.0. (A) CAIR emission spectra. (B) AIR emission spectra. Black line- no nucleotide present, light gray line- 12.8 µM CAIR/AIR added, and dark gray line- 23.8 µM CAIR/AIR added.

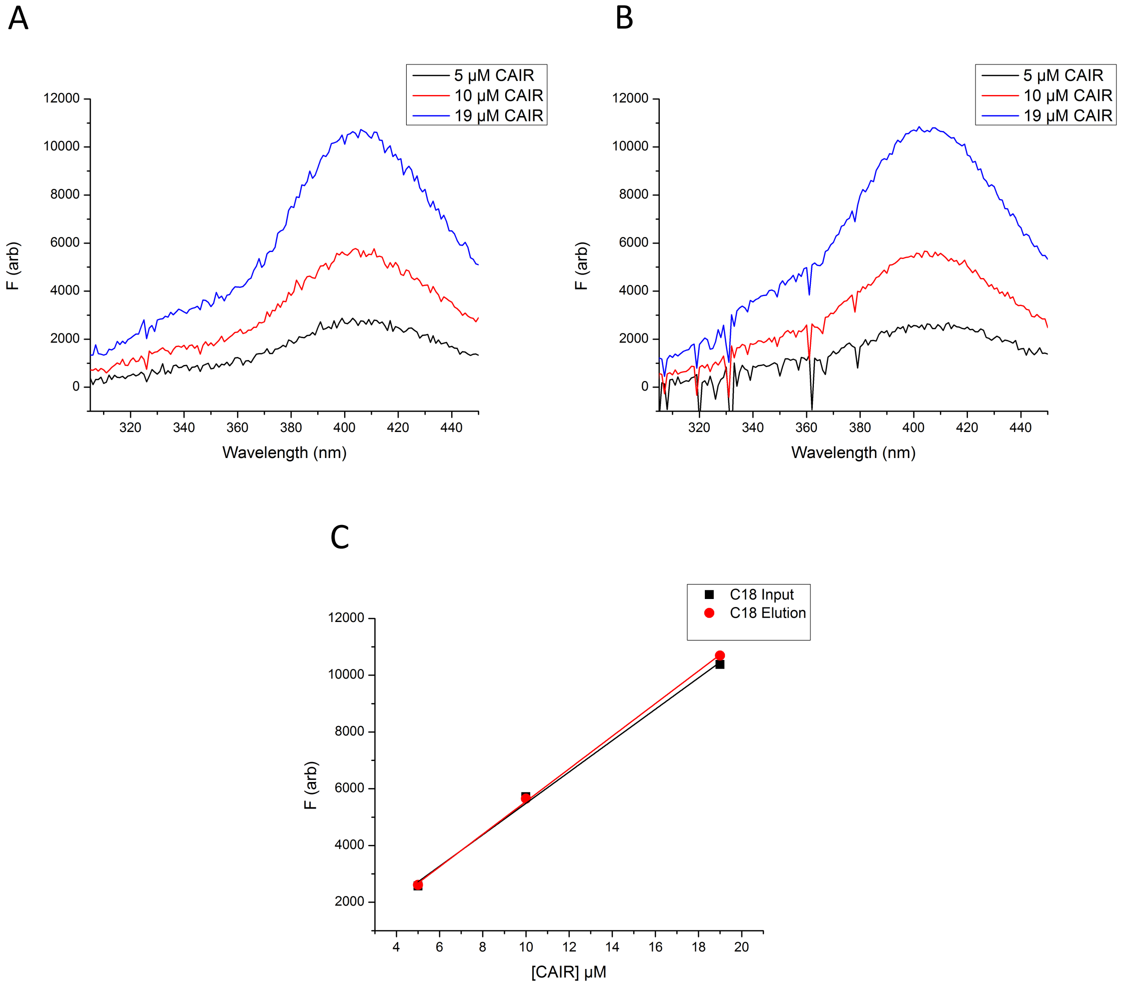

Figure 2.12 Fluorescence emission spectra of C18 separation of fluorescent species. (A) Emission spectra of the CAIR solution prior to the C18 cleanup. (B) Emission spectra of the CAIR solution after cleanup by C18 media. (C) F at λ_{max} (405 nm) is plotted vs. [CAIR]. The fluorescent species has F with a linear correlation to [CAIR] concentration.

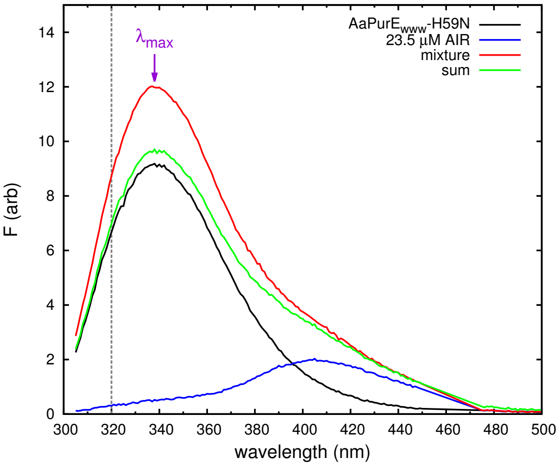

Figure 2.13 Selection of a wavelength to monitor AIR/CAIR titrations. Florescence emission spectra were recorded in 50 mM Tris-HCl, pH 8.0 at 25 °C with and excitation wavelength of 295 nm. Emission spectra with 0.4 µM AaPurE1-H59N (black line), 23.5 µM AIR (blue line), and both AaPurE1-H59N and AIR at the concentrations given (red line). The green line represents the sum of individual AaPurE1-H59N and AIR spectra. An increase due the impurity in AIR is obvious at the λ_{max} of AaPurE1-H59N (~338 nm). The contribution of the impurity is smaller at 320 nm, where the titrations were recorded.

CHAPTER 3 FLUORESCENCE CHANGES ASSOCIATED WITH LIGAND BINDING TO SINGLE-TRYPTOPHAN FORMS OF PURE1 AND PURE2

3.1 Introduction

Monitoring intrinsic protein fluorescence changes can be a powerful tool to study ligand binding, catalysis, conformational changes, and protein folding.[1–3] The use of intrinsic fluorescence requires the aromatic amino acids tryptophan (Trp), or tyrosine (Tyr), and occasionally phenylalanine (Phe). Protein fluorescence is dominated by the Trp fluorophore. The number and position of Trp residues is of particular importance. If we have a detailed understanding of the photophysical basis of Trp fluorescence changes, then one can go beyond using them as empirical reporter groups to understanding something about the enzyme chemistry.

Monitoring C—C bond Formation by Intrinsic Fluorescence. Changes in intrinsic fluorescence can be used to monitor an enzymatic reaction in real time. In particular, fluorescence is sensitive to the charge distribution within the active site that occur as an intact enzyme reacts with its natural substrate. This method has been successfully used to detect C—C bond formation by citrate synthase (Chapter 1).[4]

Our long-term goal is to learn how the mechanism of C—C bond formation differs in PurE1 and PurE2 using fluorescence changes as a real time reporter. As a prerequisite, we must first determine how fluorescence due to each Trp residue responds to ligand binding in both PurE1 and *A. aceti.* (AaPurE1) and PurE2 from *T. denticola* (TdPurE2).

Single-Trp Proteins Simplify Fluorescence Changes. The fluorescence properties of Trp and its parent indole have been extensively studied and are sensitive to changes within the environment within a given protein.[3–5] Environmental changes can be monitored by changes in emission wavelength (maximum at λ_{max}), fluorescence quantum yield (Φ, the ratio of photons emitted by the fluorophore to the number absorbed), fluorescence decay rates, accessibility to quenchers (Stern-Volmer interactions), resonance-energy transfer (FRET), and other phenomena. Some of these properties are not variable and are useless; however, the λ_{max} and Φ are highly variable among proteins and rely on the environment of the Trp(s).

For proteins, like AaPurE1, containing multiple Trps (Figure 3.1), changes in fluorescence or shift of the λ_{max} could result from a single-Trp fluorophore or could be due to contributions from several fluorophores. Single-Trp proteins, whether naturally occurring or engineered, are used to simplify the photophysics of an enzyme and allow one to link changes in intrinsic fluorescence to changes in the protein.[4,6–12]

Fluorescence Responses are Difficult to Predict. Upon ligand addition, the intrinsic fluorescence of a protein may be enhanced, quenched, or remain unchanged. It is easy to measure fluorescence changes, but it is challenging to understand the photophysical origin of a particular fluorescence change. For instance Trp fluorescence quenching by an acceptor quencher can occur by electron transfer or nonradiative energy transfer.[3,13] Differentiation between the two types of quenching is important because we need to know what intermediates are in catalysis and how these could relate to Trp fluorescence quenching.

Photo-excited indoles and indole derivatives such as Trp can be transiently oxidized leading to rapid quenching of fluorescence.[14,15] The addition of an electron-withdrawing fluorine to the indole ring raises the ionization potential which makes oxidation difficult and should suppress quenching due to electron transfer.[16]

Trp Analogs. Trp analogs can be incorporated into a protein of interest by recombinant expression in a bacterial strain that is auxotrophic for Trp (Table 3.1 and Figure 3.2).[17] Fluorinated Trp analogs are often used as ^{19}F NMR probes,[18,19] but are also useful as fluorescence probes.[20–24] If fluorescence changes occur due to electron transfer from the Trp indole, these should be diminished upon replacement by 5-fluorotryptophan (5FW).

E. coli PurE1 and A. aceti PurE1 Have Opposite Fluorescence Responses to CAIR Binding. Mutation of the conserved active site His to a neutral amino acid eliminates PurE1 decarboxylase activity, allowing for the determination of CAIR dissociation constants (K_ds) by fluorescence titrations. The fluorescence of EcPurE1-H45N or H45Q is strongly quenched by the addition of CAIR, but the fluorescence of AaPurE1-H59N or H59Q is moderately enhanced.[25,26]

A. aceti (AaPurE1) and *E. coli* PurE1 (EcPurE1) have a 58% sequence identity and similar 3D structures.[27] Each PurE1 contains multiple Trps, but AaPurE1 contains a Trp (Trp97) that has no equivalent in EcPurE1.

This divergent effect of CAIR binding on fluorescence may be due to the additional Trp in AaPurE1 or a different nucleotide complex bound within the active site. EcPurE1-H45N forms a complex containing CAIR (PDB codes 2nsl; H45Q is 2nsj), but AaPurE1-H59N (PDB code 2fwp) contains the AIR•CO_2 ternary complex (Figure 3.2). The different fates of CAIR suggest a difference between the two similar proteins. A variation in a polar side chain could explain the difference in bound nucleotide; however, no changes were observed within 10 Å of CAIR or AIR•CO_2.

Our working hypothesis is that the difference in fluorescence responses between the two forms of PurE1 is due to the presence of Trp97 in AaPurE1.

This chapter examines how each Trp fluorophore responds to ligand binding in both PurE1 and *A. aceti.* (AaPurE1) and PurE2 from *T. denticola* (TdPurE2). Once we understand the photophysical basis of Trp fluorescence changes of PurE1 and PurE2, we are positioned to use these fluorescence changes as a real time reporter of C—C bond formation.

3.2 Materials and Methods

Materials. Chemicals were obtained from Sigma or Fisher in the highest purity available unless otherwise noted. CAIR was prepared as described in Chapter 1.[28] AIR was synthesized from CAIR using *Treponema denticola* PurE2 (TdPurE2) and quantitated by Bratton-Marshall assay as described previously.[29] Oligodeoxynucleotides (ODNs) were obtained from Integrated DNA Technologies and used without further purification. Restriction endonucleases, Q5 DNA polymerase, CIP, and T4 DNA ligase were obtained from New England Biolabs. Mutagenesis was accomplished using Quikchange Mutagenesis using kits (Agilent). Phenyl Sepharose CL-6B was obtained from Sigma Hydroxyapatite (Bio-Gel® HT) and Bradford reagent were obtained from Bio-Rad. PD-10 desalting columns were obtained from GE Health Care.

Methods. Protein concentrations were determined by the method of Bradford with bovine serum albumin as the standard.[30] Protein concentrations of 5-fluorotryptophan containing proteins were determined by the method of Scopes by measuring protein concentrations at 205 nm in 0.1 M potassium sulfate, 5 mM potassium phosphate, adjusted to pH 7 with potassium hydroxide.[31] Small-scale centrifugation steps were performed using an Eppendorf 5424 centrifuge. All other centrifugation steps were performed using a Beckman Avanti J-E centrifuge with a JLA-10.5 or JA-20 rotor. Cell disruption was performed by sonication using a Fisher Scientific Dismembrator 550 at 25% output, (1 min each separated by 1 min cooling intervals) at 4 °C. Spectroscopic measurements were recorded on a Varian CARY-100 UV/Vis spectrophotometer thermostated by a Cary Dual Peltier Accessory temperature controller. Steady state fluorescence measurements were recorded on a Horiba Fluoromax-3 fluorometer thermostated with a Peltier Accessory and a Wavelength Electronics temperature controller. Data were analyzed using Origin (OriginLab, Northampton, MA) or using gnuplot 4.4 by T. J. Kappock. Plasmid DNA was sequenced by the staff of the Purdue University Genomics Core Facility. Full-length protein masses were determined by matrix-assisted laser desorption/ionization mass spectrometry (MALDI-MS) on a Voyager-DE PRO mass spectrometer (Applied Biosystems, Framingham, MA) by Connie Bonham. Liquid chromatography-mass spectrometry (LC-MS) was performed using an Accela HPLC system (Thermo) connected to a Finnigan LTQ mass spectrometer (Thermo) operated in positive ion mode by Tzu-Yi Yang.

Standard Conditions for Q5 PCR. Standard PCRs (50 μL final volume) contained Q5 DNA polymerase (1 unit), two ODNs (50 nmol each, Table 3.3), template DNA (14 ng), dNTPs (25 nmol each), $MgCl_2$ (2 mM), and Q5 buffer (1x, proprietary components). PCR products were amplified with standard conditions: annealing temperature of 52 °C with a 30 s hot start followed by melting, annealing, and extension times of 10 s, 30 s, and 30s for 25 cycles with a final extension time of 5 min.

Standard Conditions for Quikchange PCR. Standard PCRs (50 μL final volume) contained PfuUltra polymerase (1 unit), two ODNs (50 nmol each, Table 3.3), template DNA (70 ng), dNTP mix (1 μL of proprietary stock concentration), and reaction buffer (1x, proprietary components). PCR products were amplified with standard conditions: annealing temperature of 52 °C with a 30 s hot start followed by melting, annealing, and extension times of 60 s, 60 s, and 8 min for 16 cycles with a final extension time of 7 min.

Construction of AaPurE1 Plasmids for Protein Expression. Plasmid pJK175 which encodes the wild-type AaPurE1 with an extra methionine and plasmid pJK283 which encodes the catalytically inactive AaPurE1-H59N were used as templates for the generation of mutants.[26] Catalytically active mutants were generated using Quikchange II mutagenesis kits with plasmid pJK175 (70 ng) as template and an appropriate ODN pair (Table 3.3) to create plasmids pJK505 (AaPurE1-W34F), pJK506 (AaPurE1-W165F), pJK507 (AaPurE1-W34F, W165F), pJK525 (AaPurE1-W34F,W97Y), pJK526 (AaPurE1-W97Y,W165F), pJK559 (AaPurE1-W34F,Y154F,W165F), pJK562 (AaPurE1- W34F,Y154L,W165F), pJK563 (AaPurE1-W34F,Y154I,W165F), pJK601 (AaPurE1-Y154F), pJK603 (AaPurE1-W34F,Y154F), and pJK663 (AaPurE1-Y154F,W165F). Catalytically inactive mutants were generated using Quikchange II mutagenesis kits with plasmid pJK283 (70 ng) as template and an appropriate ODN pair (Table 3.3) to create plasmids pJK508 (AaPurE1-W34F,H59N,W165F), pJK509 (AaPurE1-W34F,H59N), pJK510 (AaPurE1-H59N,W165F), pJK600 (AaPurE1-W34F,H59N,Y154F, W165F), pJK602 (AaPurE1-H59N,Y154F), pJK604 (AaPurE1-W34F,H59N,Y154F), pJK664 (AaPurE1-H59N,Y154F,W165F), pJK665 (AaPurE1-W34F,H59N,W97Y), and pJK666 (AaPurE1-H59N,W97Y,W165F).

Construction of AaPurE1$_{fwf}$ Plasmid for Expression with T5 Promoter. A 0.2 kb product containing the T5 promoter[32] was amplified using standard Q5 PCR conditions from template plasmid acs1 (25 ng), using ODNs 2410 and 2411. The PCR product was purified using a Qiagen PCR purification kit, digested with *BglII* and *NdeI*, and ligated into the same sites of the destination vector pJK507 to yield AaPurE1-W34F,W165F expression plasmid pJK698.

Construction of TdPurE2–F79W Plasmid pJK648. A 0.32 kb primary PCR product containing *purE2* was amplified using standard Q5 PCR conditions from template pJK376 (14 ng), using ODNs 2124 and 2329. The crude product was digested with *DpnI* and purified using a Qiagen PCR purification kit. A 0.421 kb primary PCR product containing *purE2* was amplified using standard Q5 PCR conditions from template pJK376 (14 ng), using ODNs 2125 and 2330. The crude product was digested with *DpnI* and purified using a Qiagen PCR purification kit. Cross-over PCR product was obtained using standard Q5 PCR conditions, with a single exception: the annealing time was increased to 1 min, from a mixture containing primary PCR products (25 ng each) and ODNs 2124 and 2125. The 0.79 kb cross-over product was digested with *NdeI* and *XhoI*, and ligated into the same sites of the destination vector pET23a to yield TdPurE2-F79W expression plasmid pJK648.

AaPurE1 Overexpression and Isolation. AaPurE1 was overexpressed and isolated according to a previously published protocol.[26] BL21(DE3) cells transformed with the appropriate plasmid (Table 3.4 and Table 3.5) were grown to saturation at 37 °C in LB containing 100 μg mL^{-1} ampicillin (Amp). After a 1:50 dilution into fresh medium, cells were grown at 37 °C to $OD_{600} = 0.6$. IPTG (0.4 mM) was added and growth was continued for an additional 4 h. All subsequent steps were performed at 4 °C. Cells (4 g L^{-1} of culture) were harvested by centrifugation (5000 g, 15 min), resuspended in 50 mM Tris-HCl, 100 mM KCl, pH 8 (6 mL g^{-1} of cells), and disrupted by sonication. The lysate was cleared by centrifugation (30000 g, 30 min) and the supernatant adjusted to 1% streptomycin from a 10% (w/v) stock. Solids were removed by centrifugation (30000 g, 30 min) and the supernatant adjusted to 35% saturation (208 g L^{-1}) by the addition of solid ammonium sulfate over 30 min, with continuous stirring. After stirring overnight, solids were collected by centrifugation (30000g, 10 min). The pellet was redissolved in a minimal volume of 10 mM potassium phosphate, pH 8 (Buffer A) and applied in 2.5 mL portions to a PD10 column (1.5 × 5 cm) equilibrated in Buffer A. Desalted protein fractions were applied to a hydroxyapatite column (2.5 × 1.5 cm) equilibrated in Buffer A and AaPurE1 was eluted with 10 column volumes (CV) of Buffer A. Fractions containing AaPurE1, which does not adsorb to hydroxyapatite, were pooled and concentrated to > 3 mg mL^{-1} with an Amicon ultrafiltration device containing a YM30 membrane. The protein solution was frozen by drop-wise addition to liquid N_2 and stored at -80 °C.

Mutant AaPurE1 Overexpression and Isolation. All AaPurE1 forms were overexpressed and isolated as detailed above for wild-type AaPurE1.[26] Fresh column media were used for each mutant to avoid any possibility of cross-contamination. AaPurE1 mutants were concentrated to >3 mg mL^{-1} with an Amicon ultrafiltration device containing a YM30 membrane. Protein solutions were frozen by drop-wise addition to liquid N_2 and stored at -80 °C.

Biosynthetic Incorporation of the 5FW Analog in AaPurE1$_{fwf}$. AaPurE1$_{\text{fwf}}$ was overexpressed by adapting previously published protocols.[18,33] DL41 cells transformed with plasmid pJK698 and pCDFDuet (to incorporate the *lacI* gene)[34] were grown on LB + 1% glucose medium containing 100 μg mL^{-1} ampicillin and 100 μg mL^{-1} streptomycin (LB-Amp/Stm). A single colony was used to inoculate a LB-Amp/Stm + 1% glucose culture (5 mL) that was grown to OD$_{600}$ = 0.8 at 37 °C. Cells were harvested by centrifugation (2500 g, 10 min), resuspended in sterile glycerol (1 mL; 50% v/v) and stored at -80 °C. A LB-Amp/Stm + 1% glucose culture (50 mL) was inoculated from the frozen stock, grown to an OD$_{600}$ = 0.8, and harvested by centrifugation (2500 g, 10 min). Cells were resuspended in sterile glycerol (5 mL 50% v/v) and stored at -80 °C. The larger frozen starter culture was used to inoculate a M9 minimal media-Amp/Stm + 0.5% glucose culture (1L) supplemented with amino acids (40 mg L^{-1} of each amino acid in water; prepared by weighing out each amino acid separately and adjusting to pH to 7 with sodium hydroxide) and thiamine (0.01 mM) and grown at 37 °C until OD$_{600}$ = 0.5. Cells were washed twice with 0.9% NaCl (250 mL) and resuspended into fresh M9 minimal media-Amp/Stm (1L) supplemented with amino acids (40 mg L^{-1} of each amino acid *except* tryptophan; prepared as above), DL-5-fluorotryptophan (100 mg L^{-1}), and thiamine (0.01 mM). The resuspended culture was incubated for 10 min before IPTG addition (1 mM) and grown at 37 °C for an additional three hours before harvesting the cells by centrifugation (5000 g, 15 min). AaPurE1$_{\text{fwf}}$-5FW was isolated as wild-type AaPurE1.[26]

Mutant TdPurE2 Overexpression and Isolation. TdPurE2-F79W was overexpressed and isolated like wild-type TdPurE2.[29] CC1215 cells transformed with plasmid pJK648 and were grown to saturation at 37 °C in MGD media[35] containing 100 μg mL^{-1} ampicillin (Amp). After a 1:100 dilution into fresh ZYM 5052-Amp[35] medium, cells were grown at 37 °C for 4.5 h and shifted to 15 °C for an additional 16 h. All subsequent steps were performed at 4 °C. Cells (4 g L^{-1} of culture) were harvested by centrifugation (5000 g, 15 min), resuspended in 50 mM Tris-HCl, 100 mM KCl, pH 8 (5 mL g^{-1} of cells), and disrupted by sonication. The lysate was cleared by centrifugation (30000 g, 30 min), and the supernatant adjusted to 1% streptomycin from a 10% (w/v) stock. Solids were removed by centrifugation (30000 g, 30 min), and the supernatant adjusted to 70% saturation (472 g L^{-1}) by the addition of solid ammonium sulfate over 30 min with continuous stirring. After stirring overnight, solids were pelleted by centrifugation (30000g, 10 min). The supernatant was applied in to a Phenyl Sepharose column (2.5 × 8 cm) equilibrated in 20 mM Tris-HCl, 1.5 M ammonium sulfate, pH 8 (Buffer B). The column was washed with 5 CV of Buffer B and then developed with a linear gradient of Buffer B to 20 mM Tris-HCl, pH 8 (Buffer C) (10 CV x 10 CV). Fractions containing TdPurE2 were pooled and buffer exchanged into Buffer C with an Amicon ultrafiltration device containing a YM30 membrane. The desalted TdPurE2 solution was then applied to a hydroxyapatite column (2.5 × 3 cm) equilibrated in 10 mM phosphate, pH 8 (Buffer A). The column was washed with 5 CV of Buffer A and developed with a linear gradient of Buffer A to 500 mM phosphate, pH 8 (10 CV x 10 CV). Fractions containing TdPurE2 were pooled, buffer-exchanged into Buffer A, and concentrated to > 3 mg mL^{-1} with an Amicon ultrafiltration device containing a YM30 membrane. The protein solution was frozen by drop-wise addition to liquid N_2 and stored at -80 °C.

PurE1 and PurE2-mediated Decarboxylation Assays. Continuous assays of PurE1- or PurE2-mediated CAIR decarboxylation were performed according to a published method.[26] A final volume of 0.6 mL in a masked, 1 cm pathlength cuvette containing 50 mM Tris-HCl, pH 8 and 100 μM CAIR was incubated at 30 °C for at least 3 min. Reactions were initiated by addition of either an AaPurE1 or TdPurE2 mutant (12-80 ng, 1.4-8.4 nM [subunits]). The initial velocity of CAIR decarboxylation to AIR ($\Delta\varepsilon_{260}$ =8930 M^{-1} cm^{-1}) was recorded at 260 nm, with a small background decarboxylation rate subtracted. CAIR was quantitated by endpoint assay using the same method, except that 50 μg mL^{-1} TdPurE2 was the enzyme. A unit is defined as the amount of enzyme that forms 1 μmol of product per minute.

Quantum Yield Determinations. Quantum yields of AaPurE1$_{fwf}$ and AaPurE1$_{fwf}$-5FW were determined according to a previously published protocol.[4] Fluorescence emission spectra were recorded at 25 °C using an excitation wavelength of 295 nm and slit widths of 1.5 nm (excitation) and 5 nm (emission). A buffer only-spectrum was subtracted from as the background from all spectra. To calculate the quantum yield, the unobservable portions of the spectra were estimated by obtaining a spectrum using a lower excitation wavelength (280 nm) and normalizing the maxima to spectra obtained with an excitation of 295 nm. These normalized 280nm spectra were then used to estimate the unobservable area. The normalized spectra were superimposable with the spectra obtained from excitation at 295 nm. The integrated fluorescence intensity was determined using the peak analyzer module in Origin (OriginLab, Northampton, MA). Quantum yields were determined using equation 3.1, where Φ and is the quantum yield, OD is the absorbance at 295 nm, and η is the refractive index of the solution, with the subscript R denoting the reference sample.[3,36]

$$\Phi = \Phi_{\mathrm{R}} \frac{I}{I_{\mathrm{R}}} \frac{\mathrm{OD}_{\mathrm{R}}}{\mathrm{OD}} \frac{\eta^2}{\eta_{\mathrm{R}}^2} \qquad \text{Equation 3.1}$$

Quantum Yield Determinations with Ligands. Quantum yields of AaPurE1$_{\mathrm{fwf}}$ and AaPurE1$_{\mathrm{fwf}}$-5FW with citrate or AIR (present at 5 times K_d 0.014-1 mM citrate and 2.5-7 µM AIR) were determined according to above protocol for AaPurE1$_{\mathrm{fwf}}$-5FW with one exception: citrate bound spectra were obtained in 50 mM potassium acetate, 100 mM KCl, pH 4.6 at 25 °C. NATA emission spectra were recorded with each ligand and the integrated fluorescence was corrected for any inner filter effect.

EcPurE1 Single-Trp Fluorescence Emission Spectra. Fluorescence emission spectra were recorded using an excitation wavelength of 295 nm and slit widths of 2 nm (excitation) and 5 nm (emission). Spectra were recorded in a 1 cm pathlength fluorometer cell that contained 30 µM EcPurE1-W20F or EcPurE1-W151F (isolated by S. Tranchimand) in 50 mM Tris, pH 8 in a total volume of 2 mL.

Fluorescence Titrations. Spectra were obtained using a 1 cm pathlength fluorometer cell that contained 2.0 mL prior to the titration. The excitation wavelength was 295 nm (2 nm slit width) and emission spectra were collected from 305 to 450 nm (5 nm slit width). A buffer only-spectrum was subtracted from as the background from all spectra. The intensity of the fluorescence emission *F* for each titration point was measured at 320 nm and then corrected for dilution.

Citrate Titrations (0-25 mM final concentration, added from a 200 mM stock, pH 4.6) were performed in 50 mM potassium acetate, 100 mM KCl, pH 4.6, with varying amounts of AaPurE1 or TdPurE2 at 25 °C. Emission intensities at 320 nm (F) were divided by the intensity at zero ligand (L) concentration (F_0) to obtain fractional saturation values. The AaPurE1 titration data were fit using gnuplot 4.4 and TdPurE2 were fit using Origin to a binding isotherm (equation 2.2) by allowing K_d and ΔF (the value of F/F_0 as $[L] \rightarrow \infty$) to vary.

$$\frac{\mathrm{F}}{\mathrm{F}_0} = 1 - \Delta\mathrm{F}\left(\frac{[L]}{[L]+K_\mathrm{d}}\right) \qquad \text{Equation 3.2}$$

AIR titrations (0-25 μM final concentration, added from a 600 μM stock in 50 mM Tris-HCl, pH 8) were performed in 50 mM Tris-HCl, pH 8 with varying amounts of AaPurE1 or TdPurE2 at 30 °C. Emission intensities at 320 nm (F) were divided by the intensity at zero ligand (L) concentration (F_0) to obtain fractional saturation values. The TdPurE2 data were fit using Origin to a binding isotherm (equation 3.2) by allowing K_d and ΔF (the value of F/F_0 as $[L] \rightarrow \infty$) to vary. AaPurE1 titration data were, with the exception of AaPurE1$_{\mathrm{fyw}}$-H59N, fit using gnuplot 4.4 to a binding isotherm that accounts for ligand depletion (equation 3.3) assuming that AIR binds to a maximum of half the enzyme subunits (E =0.5[subunit]). The half-sites assumption is based upon the observation that only four AIR molecules bind to a single face of the AaPurE1 octamer (PDB id 2fwj). [26]

$$\frac{\mathrm{F}}{\mathrm{F}_0} = 1 + \frac{\Delta\mathrm{F}}{E}\left[\left(K_\mathrm{d} + L + \frac{E}{2}\right) - \sqrt{\left(K_\mathrm{d} + L + \frac{E}{2}\right)^2 - 2EL}\right] \qquad \text{Equation 3.3}$$

CAIR titrations (0-25 μM final concentration, added from a 600 μM stock in 50 mM Tris-HCl, pH 8) were performed in 50 mM Tris-HCl, pH 8 with varying amounts of AaPurE1 at 30 °C. Emission intensities at 320 nm (F) were divided by the intensity at zero ligand (L) concentration (F_0) to obtain fractional saturation values. The titration data were, with the exception of AaPurE1$_{\mathrm{fyw}}$-H59N, fit using gnuplot 4.4 to a binding isotherm that accounts for ligand depletion (equation 3.3).

Solution Studies of AaPurE1s. Solution aggregation state was determined on an AKTA FPLC system (Amersham) using a Pharmacia G200-16/60 high-load column. The mobile phase was 50 mM Tris-HCl, 100 mM KCl, pH 8 that was applied at 1 mL min^{-1}. Injections (100 μL) contained 0.5 mg of protein adjusted to 5% (v/v) glycerol. Protein solution sizes and aggregation states were determined by comparison with protein size standards (29-669 kDa; Sigma MW-GF-1000), blue dextran (2 MDa; V_o), and acetone (60 Da, V_i) using the K_{av} partition coefficient method [37].

Crystallization of AaPurE1s. AaPurE1 forms intended for crystal production were buffer exchanged into 5 mM Tris-HCl, 15 mM NaCl, pH 8 and concentrated to 10 mg mL^{-1} using Millipore Ultra spin columns (MWCO 30000). Crystals were grown by the hanging drop vapor diffusion method using reservoir solutions containing 25-35% PEG 4000, 200 mM $LiSO_4$, 100 mM Tris-HCl, pH 8.3.

X-ray Data Collection and Processing. Prior to data collection, crystals were placed briefly into a cryoprotectant solution that consisted of artificial mother liquor with an additional 2% PEG 4000 and 15% (v/v) ethylene glycol. Crystals were immediately flash-cooled in liquid N_2. X-Ray diffraction data were collected on either a MAR-225 or MAR-300 CCD detector at the LS-CAT beamline (Advanced Photon Source - Argonne National Laboratory). Diffraction data were indexed, integrated, and scaled with HKL-2000.

Crystals used for subsequent mass spectrometric analysis were subjected to irradiation at the LS-CAT beamline, by collecting 360 frames with a delta of 1 degree.

Structure Determination and Refinement. All crystals had the same space group with similar unit cell parameters, previously observed in structures of AaPurE1.[26,27] Molecular replacement was performed using AutoMR/Phaser[38] with the AaPurE1 monomer (PDB code 2fw1 chain A) as the search model. Structures for AaPurE1-Y154F, AaPurE1$_{\text{fwf}}$-Y154F, and AaPurE1$_{\text{fwf}}$-Y154L were determined by using the AaPurE1$_{\text{fwf}}$ monomer (PDB code 4ycb) as the search model. First, 15 rounds of TLS with all B-factors set to 30 were performed followed by subsequent rounds using rigid body, TLS, Cartesian coordinate optimization, individual isotropic temperature factor refinement, and automatic water picking in PHENIX.[39] Later rounds of refinement were performed using Cartesian coordinate optimization, individual isotropic temperature factor refinement, TLS, and occupancy refinement. Model building, manual inspection, and rebuilding were performed using Coot.[40] Coordinates and structure factors have been deposited in the RCSB Protein Data Bank (PDB) with accession numbers 4ycb (AaPurE1$_{\text{fwf}}$), 4ycc (AaPurE1$_{\text{fwf}}$-Y154L), 4ycd (AaPurE1$_{\text{fwf}}$-Y154F), and 4ycj (AaPurE1-Y154F). Figures were prepared using PyMOL.[41]

Previously deposited models of AaPurE1s lack a hydrogen bond between the Asn78 carboxamide oxygen and the Tyr154 phenol.[26,27] For comparison with the newly obtained structures, structure factors were obtained from EDS, the Asn78 side chain was flipped, and a single round of one round of refinement performed using Cartesian coordinate optimization, individual isotropic temperature factor refinement, and occupancy refinement.

Mass Spectrometry of AaPurE1$_{fwf}$. Each AaPurE1 form (0.8 mg) was dried and resuspended in 50 µL of 70% (v/v) formic acid containing 0.5 M cyanogen bromide. After 24 h at room temperature, the solvent was removed in a rotary evaporator. Solids were dissolved in 80 µL of 50 mM ammonium bicarbonate and a portion (20 µL) was mixed with trypsin (2 µg, Sigma proteomics grade from pig pancreas T6567) in a final volume of 120 µL. After 18 h at 37 °C, 100 µL of 0.1% formic acid was added and the reaction mixture was lyophilized, and stored at -80 °C. Dried peptide samples (~2 µg) were resuspended in 25 µL of water:acetonitrile:trifluoroacetic acid (50:50:0.1 ratio) and a portion was analyzed by LC-MS. Peptides were separated at 50 °C on a C18 column

(Kinetex 1.7 μ, 50 x 2.10 mm; Phenomenex) that was developed at 0.5 mL min^{-1} in a linear gradient of acetonitrile (5-65%) in 0.1% formic acid.

Mass Spectrometry of Dissolved AaPurE1$_{fwf}$ Crystals. Crystals of AaPurE1s were prepared for mass spectrometric analysis by adapting a published method.[42] Cryo-cooled AaPurE1 and AaPurE1$_{\mathrm{fwf}}$ crystals were washed twice with acetonitrile and dissolved in 10 mM potassium phosphate, pH 8. The dried protein was then digested and analyzed as described above.

3.3 Results

Creation and Isolation of EcPurE1 Mutants. EcPurE1 single-Trp mutants were generated by Yi Li and isolated by Sylvain Tranchimand to investigate the fluorescence response of each individual Trp fluorophore upon ligand binding

Fluorescence Emission Spectra of EcPurE1 Single-Trp Mutants. EcPurE1 was previously used to elucidate mechanistic details of the reaction catalyzed by PurE1.[25] EcPurE1 contains two Trp residues per monomer and like AaPurE1 it would be advantageous to use a single-Trp form.

Fluorescence emission spectra were obtained for single-Trp mutants of EcPurE1. The single-Trp EcPurE1 forms have a 7 nm difference in λ_{max} (EcPurE1-W20F λ_{max} = 330 nm and EcPurE1-W151F λ_{max} = 337 nm) indicating the Trps occupy different local environments (Figure 3.5). This does not occur with the corresponding AaPurE1 single-Trp mutants, which do not display significant shifts in λ_{max} (Appendix Figures A1-A22).

Another caveat unique to the EcPurE1 single-Trp forms is the large amount of enzyme necessary to produce adequate signal (30 μM subunit concentration). This concentration is 40 times higher than used for wild-type EcPurE1 titrations.[25] Therefore, we could not perform fluorescence titrations to determine the fluorescence response of each Trp to ligand addition.

Creation of AaPurE1 Mutants. AaPurE1 Trp mutants were generated to investigate the fluorescence response of each individual Trp fluorophore upon ligand binding. AaPurE1 Tyr mutants were generated in an effort to resolve the structural ambiguity observed in the AaPurE1$_{fwf}$ structure. Quikchange site directed mutagenesis was successful in generating a suite of combinatorial Trp and Tyr mutants (Table 3.3).

Purification of Recombinant AaPurE1s. The previously published isolation protocol[26] was successfully used to isolate all AaPurE1 forms with varying specific activites and high purity (Table 3.6, Figure 3.4 and Figure 3.5).

Identities of each AaPurE1 form were also established by MALDI analysis (Table 3.4). Five full-length forms of AaPurE deviated from the excepted mass by more than 3 Da. AaPurE$_{wwf}$-H59N was 5 Da higher, AaPurE$_{wwf}$-H59N,Y154F was 8 Da lower, AaPurE$_{yfw}$-H59N was 7 Da higher, AaPurE$_{fyw}$ was 8 Da lower, and AaPurE$_{fyw}$-H59N was 4 Da higher than expected.

Physical Characterization of AaPurE1s. Analytical size exclusion chromatography was used to determine the biological unit and relative stabilities of the AaPurE1 mutant forms. Gel-filtration analyses confirmed the presence of the PurE1 octamer for all forms, but also high molecular weight aggregate. The amount of aggregation roughly correlates to the number of mutations in each form (Figures 3.8, 3.9, and 3.10). AaPurE1s lacking Trp34 and Trp165 appear to be associated with increased aggregate, whether in a single or multiple Trp form. Forms lacking Trp165 also appear to dissociate into tetramers as evidenced by a peak at ~76 Da (Figure 3.9 and 3.10). Despite having an increased portion of aggregate, it was possible to crystallize all forms with two exceptions: any proteins lacking Trp97 and the quadruple mutant AaPurE1$_{fwf}$-H59N, Y154F.

Kinetic Parameters of AaPurE1s. All proteins containing the critical active site His retain at least 50% of wild-type activity. The AaPurE1 forms that have lower relative specific activites tend to dissociate in solution studies (Table 3.7 and Figures 3.8-3.10). The W79Y AaPurE forms had the lowest activity, indicating this form is especially unstable.
Structure of AaPurE1$_{fwf}$. The crystal structure of AaPurE1$_{\mathrm{fwf}}$ was obtained to aid in interpretation of single-Trp fluorescence data. This single AaPurE1$_{\mathrm{fwf}}$ crystal resulted in the highest resolution data set of any available PurE1 (PDB code 4ycb) (Table 2.8 and 2.9). At 1.35 Å, there is a great level of detail; the dimer in the asymmetric unit contains 25 residues with alternative conformations (including Trp97), a PEG molecule coordinated to potassium, several ethylene glycols, and acetate.

The previously deposited AaPurE1 structure (PDB code 1ull) was aligned with AaPurE1$_{\mathrm{fwf}}$ and root-mean squared differences (RMSDs) calculated for all residues within 10 Å of the all three Trp residues. No significant difference in the environment is observed when the Trps are replaced by Phes: residue 34, 0.24 Å; residue 97, 0.22 Å; and residue 165, 0.22 Å. Trp97 is present in both structures and has an RMSD between structures that is equal or similar to the Phe34 and Phe165 replacements. The Phe/Trp replacements do not appear to alter the surrounding structure (Figure 3.11). This is beneficial for interpretation of single-Trp fluorescence data, because the environment surrounding the Trp replacements has not been notably changed.

Another observation unique to the high resolution AaPurE1$_{\mathrm{fwf}}$ structure is that the orientation Asn78 side chains in previously deposited structures, [26,27] should be flipped. This new orientation allows the Asn78 carboxamide to form a hydrogen bond with the Gly76 backbone carbonyl oxygen. The Asn78 is likely a hydrogen bond acceptor for Tyr154 from the same subunit, thus creating a “chain” of hydrogen bonds.

Tyr154s at the Dimer Interface. The most puzzling residues within AaPurE1$_{\mathrm{fwf}}$ are two Tyr154s, from adjacent subunits, that sit at the dimer interface. An iterative-build simulated annealing composite omit map[43] appears to contain continuous electron density across the dimer interface and incomplete density for some Tyr154 atoms. $F_o - F_c$

difference maps show positive density peaks between the CE2 atoms at the interface, and negative peaks for CD1, CE1, and OH of the phenol (Figure 3.12 panel C). Residue 68 is the only other Tyr in AaPurE1, which has excellent electron density in both subunits consistent with an unmodified residue (Figure 3.13). Any molecule that could be derived from Tyrs at the dimer interface, which fits to the density, had unrealistic bond lengths and angles (data not shown).

To study the ambiguous density at the dimer interface, mutations were introduced at position 154. Structures were obtained for AaPurE1-Y154F (PDB code 4ycj), AaPurE1-Y154L (PDB code 4ycc), and AaPurE1$_{\mathrm{fwf}}$-Y154F (PDB code 4ycd) (Table 2.8 and 2.9). In stark contrast to Tyr154 structures, those containing a Phe at position 154 had clear unambiguous density for the benzene ring with real space correlation coefficients (RSCCs) near unity (Table 3.10 and Figure 3.12). The structure containing Leu154 was less ordered and is populated by multiple rotamers (Figure 3.12 panel F).

A single deposited AaPurE1-H59F structure (PDB code 2fw9) contains Tyr154s that superimpose on the Phe154s (PDB codes 4ycd and 4ycj) and make hydrogen bond contacts with the Asn78s (Figure 3.12, panels B, D, and E). This structure and the Phe154 position provided the prototypal Tyr poses. In this prototypal pose, the Tyr phenols are almost perpendicular in almost parallel planes with a dihedral of 87° between the Cβ-OH axes. The phenol oxygen makes a hydrogen bond contact to the Asn78 carboxyamide as discussed prior. In addition to the prototypal pose, each Tyr154 has an alternative conformation. Tyr154 from subunit A reaches across the dimer interface and occupies the density previously assigned to the cross-link. Tyr154 from subunit B is pointed out into solvent (Figure 3.12, panel C).

The first assumption about the Tyr154 chemical identity was it might be a tyrosine derived cross-link spanning the dimer interface. Dityrosine and isodityrosine crosslinks are common structural features and oxidative stress markers in proteins[44–48] and formation of radiation-induced Tyr dimerization in solution has been observed.[49] The chemical structure consistent with the observed electron density in AaPurE1$_{\mathrm{fwf}}$ is not dityrosine or isodityrosine. The crosslink is not evident in solution; the protein always runs as a monomer on SDS-denaturing page gels (Figure 3.5), and LC-ESI-MS analyses show the expected mass for non-cross-linked peptides of AaPurE1, AaPurE1-Y154F, AaPurE1$_{fwf}$, and AaPurE1$_{fwf}$-Y154F (Figures 3.14-3.17).

Inspection of the AaPurE1 structures deposited in the PDB revealed that all contain some extent of disorder at Tyr154 (Figure 3.23). Tyr154 RSCCs average 0.91 in all AaPurE1 models (Table 3.10). The source of radiation and crystallization conditions had no clear effect on Tyr154 RSCC.

Fortunately, for direct comparison, two data sets were collected on a single AaPurE1$_{fwf}$ crystal. The first data set was collected on home source and a second at the synchronotron. Electron density was similar at the Tyr154 for both home source and synchronotron data sets. In addition, comparison of early to late frames of synchrotron data showed no difference in electron density (data not shown). Therefore, the “damage” or density that spans across the subunit interface is always present regardless of the type of energy the crystal is exposed to.

Crystals of AaPurE1 and AaPurE1$_{fwf}$ (radiated and un-radiated) were dissolved, run on SDS-denaturing page, and visualized with silver staining. These ran exclusively as monomers (Figure 3.18). LC-ESI-MS analysis of radiated crystals did not produce useable signal (data not shown). LC-ESI-MS analysis of dissolved and digested un-radiated crystals of AaPurE1 show no evidence of a cross-link, only peptides corresponding to Tyr154 were observed (Figure 3.19).

Citrate Titrations of AaPurE1s. Citrate is a non-substrate active site ligand that binds AaPurE1 weakly, under acidic conditions, leading to protein fluorescence quenching.[26] While it has little resemblance to CAIR, citrate interacts with the protonated form of the key His59 and all nucleotide-binding residues, except for the phosphate contact Ser32 and the exocyclic amine contacts in the 70s loop backbone. Therefore, titrations were carried out in 50 mM potassium acetate, 100 mM KCl, pH 4.6 with all AaPurE1 forms to determine the fluorescence response of each mutant upon citrate addition. It is possible that the acidic conditions destabilize the multiple-mutant variants more than others.

The fluorescence of all forms of AaPurE1s, with the exception of AaPurE1$_{fyw}$-H59N, was quenched by the addition of citrate (Table 3.7, Figure 3.20, and Appendix Figures A.1-A.21). A comparison the single-Trp AaPurE1 mutants shows Trp34 and Trp165 have opposing effects on fluorescence, and that most of the quenching is due to Trp97. Interestingly, we do not observe the enhancement of Trp165 fluorescence unless an inactive mutant is used.

The inactive AaPurE-H59N mutants show similar trends, but have lower citrate affinity and a smaller quenching magnitude (Figure 3.20). The effect of H59N on fluorescence quenching depends on the Trps present: H59N is associated with less quenching of Trp fluorescence upon citrate binding, unless Trp97 and Trp165 are both present.

Surprisingly, AaPurE1 forms containing the Y154F mutation had diminished quenching intensity, suggesting that it enhances the quenching of Trp97 fluorescence (Figure 3.12).

AIR Titrations of AaPurE1s. AIR is not a substrate for PurE1, it instead acts as a non-competitive inhibitor.[50] The addition of AIR to EcPurE1 does not result in an observable fluorescence change,[25] and it is small for AaPurE1 (C. Z. Constantine, unpublished observations). This small increase in fluorescence proved to be the result of a fluorescent species present in AIR (Chapter 2), which was derived from CAIR that had been synthesized using LiOH mediated saponification procedure.[28] To minimize the contribution of the fluorescent species to saturation plots, titrations were performed using an emission wavelength of 320 nm, which has less contribution from the fluorescent species than at the AaPurE1 λ_{max} of 338 nm.

AIR titrations were carried out in 50 mM Tris-HCl, pH 8.0 to determine the fluorescence response of proteins containing only one Trp to determine which Trp fluorophore is the most responsive to AIR addition.

The addition of AIR to AaPurE1 or single-Trp AaPurE1 mutants had little or no effect on fluorescence emission intensity (Table 3.7, Figure 3.21, and Appendix Figures A.1-A.21).

A much larger change was observed for the addition of AIR to inactive forms containing H59N (Figure 3.21). The H59N forms are impaired at binding AIR relative to active AaPurE1s. Single-Trp AaPurE1-H59N mutants showed approximately equal contributions from Trp34 and Trp97 to fluorescence enhancement, with Trp165 having a smaller quenching response.

The obvious difference between the inactive and active forms is presence of His59. This critical active site residue influences the overall fluorescence change and likely camouflages the fluorescence enhancement seen in the inactive forms.

The AaPurE1 forms containing the Y154F mutation had no effect on AIR titrations (Figure 3.21). Tyr154 has a slight effect with citrate and a marked effect with CAIR. The electrostatic properties of the ligand may determine if Tyr154 has an effect on Trp97.

CAIR Titrations of Inactive AaPurE1s. CAIR is a substrate for the decarboxylation reaction catalyzed by PurE1, and its addition results in an enhancement of AaPurE1-H59N fluorescence.[25] Conversely, CAIR addition to EcPurE1-H59N quenches fluorescence. Therefore, CAIR titrations were carried out in 50 mM Tris-HCl, pH 8.0 to determine the response of each AaPurE1 Trp fluorophore to CAIR addition.

The addition of CAIR to AaPurE1-H59N and single-Trp variants showed a similar trend as the AIR titrations, with positive contributions from Trp34 and Trp97 and a quenching contribution from Trp165 (Table 3.7, Figure 3.22, and Appendix Figures A.1, A.4-6, A.9-10, A.13, A.15, A.18-20).

Mutant AaPurE1 K_ds were slightly higher than AaPurE1-H59N with the exception of AaPurE1$_{fyw}$-H59N. The increased K_ds are likely associated with a decrease in stability.

The Y154F mutation had a complicated effect, with enhancement relative to AaPurE-H59N, suppression for two-Trp mutants, and elimination of the fluorescence enhancement of $\text{AaPurE}_{\text{fwf}}$-H59N (Table 3.7, Figure 3.22, and A.1, A.4-6, A.9-10, A.13, A.15, A.18-20).

Identification of the Primary Emitter. A primary emitter is defined as the fluorophore that is the most sensitive to ligand binding. There are three Trps within AaPurE1; however, results indicate that Trp97 which, is not conserved in EcPurE1, is the primary fluorophore. Therefore, further studies reported here will focus on Trp97 (or its equivalent in TdPurE2).

Generation of $AaPurE1_{fwf}$ Containing 5FW. Incorporation on 5FW can be used to determine the quenching mechanism associated with the primary emitter Trp97. The addition of an electron-withdrawing fluorine to the indole ring of Trp raises the ionization potential which should suppress quenching due to electron transfer.[16] A diminution in fluorescence quenching upon incorporation of 5FW, would indicate if electron transfer from the Trp indole is responsible.

Creation of $AaPurE1_{fwf}$ Plasmid with a T5 Promoter. AaPurE1 is normally produced using a T7 system in BL21(DE3) cells, however this system does not tightly control protein expression prior to induction. The successful incorporation of a 5FW analog into $\text{AaPurE1}_{\text{fwf}}$ with a high yield requires tight expression control. Therefore, we created an $\text{AaPurE1}_{\text{fwf}}$ plasmid with a T5 promoter to for protein expression in a DL41 Trp auxotrophic strain. Standard molecular biology techniques were used to successfully generate the $\text{AaPurE1}_{\text{fwf}}$ plasmid under the control of a T5 promoter (Table 3.3).

Expression and Isolation of $AaPurE1_{fwf}$ with 5FW. Control of induction is critical for successful 5FW analog incorporation. The plasmid pCDFDuet, which contains the *lacI* gene, was co-transformed with plasmid pJK698 to ensure $\text{AaPurE1}_{\text{fwf}}$ expression was tightly controlled. Adding *lacI* cultures, which in addition were supplemented with excess glucose (to suppress plasmid expression) and kept in log phase was necessary to control AaPurE$_{fwf}$ expression. These combined strategies allowed for the expression of AaPurE$_{fwf}$-5FW in DL41 cells without detectable protein expression until IPTG induction (Figure 3.23).

AaPurE1$_{fwf}$-5FW was successfully isolated using the previously published isolation protocol[26] with relatively high specific activity and purity (Figure 3.5-lane 21). To confirm incorporation of 5FW, full-length proteins were analyzed by MALDI mass spectrometry (Table 3.6). Only peaks corresponding to AaPurE1$_{fwf}$-5FW were observed and no signal corresponding to unlabeled AaPurE1$_{fwf}$ was identified (data not shown).

Absorbance and Fluorescence Emission Spectra of AaPurE1$_{fwf}$. The incorporation of 5FW into AaPurE1$_{fwf}$ should have an effect on the absorbance and fluorescence emission spectra. Absorbance spectra were obtained in 50 mM Tris-HCl, pH 8.0 containing either AaPurE1$_{fwf}$ (168 μg mL^{-1}) or AaPurE1$_{fwf}$ -5FW (123 μg mL^{-1}) present and the same solution was used to obtain fluorescence emission spectra with excitation at 295 nm. AaPurE1$_{fwf}$-5FW has shifted λ_{max} values for both absorbance and fluorescence emission spectra relative to AaPurE1$_{fwf,}$ with a large difference in the Stokes shift (AaPurE1$_{fwf}$ λ_{max} = 277 nm and 366 nm, and AaPurE1$_{fwf}$ -5FW λ_{max} = 264 nm and 341 nm; for absorbance and fluorescence respectively) (Figure 3.8). This indicates that 5FW was successfully incorporated and suggests a difference in local environment for the residue at position 97, or a small structural change in AaPurE1$_{fwf}$-5FW. All attempts to obtain a crystal structure of AaPurE1$_{fwf}$ -5FW resulted in poor diffraction.

Replacement of Trp with of 5FW analog typically results in a red shift of the fluorescence emission spreturm.[16,21,51] However, the AaPurE1$_{fwf}$-5FW emission spectrum is blue shifted by 5 nm. This change could be due to rearrangement of residues in close proximity to the Trp or a conformational change somewhere else in AaPurE1$_{fwf}$-5FW.

Quantum Yields of AaPurE1s. We obtained the λ_{max} for absorbance and fluorescence emission of AaPurE1$_{fwf}$ -5FW, next we wanted to obtain the other variable fluorescence property, quantum yield. The AaPurE1$_{fwf}$ -5FW quantum yield was about twice that of

AaPurE1$_{\mathrm{fwf}}$ (Figure 3.9, Table 3.6). This was surprising, as the quantum yield of 5FW is the same as the Trp in solution (Table 3.1).[36] The environment surrounding 5FW in AaPurE$_{\mathrm{fwf}}$ may significantly enhance the quantum yield. Two possibilities exist to enhance a quantum yield, either a positive charge is relocated near the benzene ring of Trp97 or some intramolecular quenching group such as an amide is removed. However, we do not have a crystal structure to examine either of these possibilities.

Quantum yields of AaPurE1s with Ligand Bound. If quenching of Trp97 fluorescence occurs by electron transfer, then quantum yields with 5FW incorporated should be diminished. Quantum yields for AaPurE1$_{\mathrm{fwf}}$ and AaPurE1$_{\mathrm{fwf}}$ -5FW were recorded in the presence of either AIR or citrate (5 times the K_{d}). Citrate and AIR had no or very little inner filter effect (0-4%) on the integrated fluorescence intensity of NATA (data not shown). Quantum yields for AaPurE1$_{\mathrm{fwf}}$ were determined using equation 3.1, after correcting the integrated fluorescence values for any inner filter effect.

If ligand dependent quenching of Trp97 fluorescence is due to electron transfer, we expect to see a lower quantum yield in AaPurE1$_{\mathrm{fwf}}$-5FW with citrate present. However, the overall change in fluorescence observed in the presence of citrate is higher for AaPurE1$_{\mathrm{fwf}}$-5FW (Table 3.11), indicating that fluorescence quenching does not occur by electron transfer from the Trp indole.

We see the same effect when AIR is present (AaPurE1$_{\mathrm{fwf}}$-5FW quantum yield is not diminished).

Citrate Titrations of AaPurE1$_{fwf}$-5FW. AaPurE1$_{\mathrm{fwf}}$-5FW was quenched to about the same extent as AaPurE1$_{\mathrm{fwf}}$. Incorporation of the 5FW analog produced very different binding parameters, the citrate K_{d} for AaPurE1$_{\mathrm{fwf}}$-5FW is 88 times lower than AaPurE1$_{\mathrm{fwf}}$ (Table 3.7 and Figure 3.26). Incorporation of 5FW may alter the environment of the active site, which could lead to increased affinity.

AIR Titrations of AaPurE1$_{fwf}$-5FW. Little increase in fluorescence occurred in AaPurE1$_{\mathrm{fwf}}$-5FW upon AIR addition, which is consistent with data for other active PurE1 forms (Figure 3.27). Incorporation of 5FW reduced the AaPurE1$_{\mathrm{fwf}}$-5FW K_d 2.8 times lower than AaPurE1$_{\mathrm{fwf}}$ (Table 3.7). Incorporation of 5FW alters the affinity of AaPurE1$_{\mathrm{fwf}}$ for both AIR and citrate. Again, indicating 5FW may alter the environment of the active site, which may lead to increased affinity.

Mechanism of Ligand-Dependent Trp97 Fluorescence Quenching. The replacement of Trp97 with 5FW was used to probe the mechanism of ligand-dependent fluorescence quenching. No diminution in fluorescence upon ligand binding was observed in either quantum yield determinations or titrations with AIR or citrate. The results indicate that quenching occurs by non-radiative processes and not electron transfer.

Creation of TdPurE2-F79W Mutant. TdPurE2 does not contain any Trp residues. Therefore, a TdPurE2 Trp introduction mutant (analogous to Trp97) was generated to investigate the fluorescence response of the Trp fluorophore upon ligand binding. Quikchange site directed mutagenesis repeatedly failed and instead cross-over PCR was employed to generate the TdPurE2-F79W mutant. Sequencing confirmed that only the intended mutations were obtained.

Purification of Recombinant TdPurE2 Tryptophan Introduction Mutant. The published isolation protocol[29] was successfully used to isolate TdPurE2-F79W with relatively high specific activity and purity (Table 3.6. and Figure 3.28).

Citrate Titrations of TdPurE2-F79W. Citrate titrations have never been done before with any TdPurE2. Therefore, titrations were carried out to determine if citrate binds to TdPurE-F79W and has any effect on Trp79 fluorescence. The TdPurE2-F79W mutant was quenched by the addition of citrate (Table 3.7 and Figure 3.29). The addition of Trp79 to TdPurE2 produces fluorescence changes similar to AaPurE1$_{\mathrm{fwf}}$. However, there is an obvious red shift in λ_{max} that does not occur with AIR titrations of TdPurE2-F79W (Figure 3.30). Citrate titrations are performed at pH 4.6, which may be destabilizing to TdPurE2-F79W.

AIR Titrations of TdPurE2-F79W. Unlike AaPurE1, AIR is a substrate for TdPurE2. AIR titrations were carried out in 50 mM Tris-HCl, pH 8.0. TdPurE2-F79W showed little change in fluorescence (8% $\Delta F/F_0$) upon addition of AIR, consistent with earlier studies of active PurE1s (Table 3.7 and Figure 3.16).[26,25] It was however, enough of a signal change to obtain a K_d.

TdPurE2-F79W has an AIR affinity similar to AaPurE1 wild-type (Table 3.7). This is slightly surprising because AIR is a substrate for TdPurE2, but is not a substrate for AaPurE1. AIR inhibits AaPurE1 and PurK may serve to not only supply NCAIR, but to also lower the concentration of AIR.

The single TdPurE2-F79W mutant is stable and is suitable for fluorescence titrations. However, the addition of any additional mutations appears to destabilize the enzyme to an extent that fluorescence titrations become impractical (Chapter 4).Therefore, TdPurE2 may prove to be unsuitable for fluorescence experiments. PurE2 from extremophilic bacteria (that already contain a Trp residue) offer a potential alternative that may be worth exploring.

3.4 Discussion

Initially this study had a single goal: to dissect the molecular basis of AaPurE1 and TdPurE2 fluorescence responses to ligand binding using single-Trp forms. These forms could then be used to monitor PurE1- and PurE2-medaited C—C bond forming, in real time. However, a single high-resolution AaPurE1$_{\mathrm{fwf}}$ crystal structure revealed two unexpected but relevant features: the primary emitter Trp97 adopts multiple rotamers and a residue at the dimer interface (Tyr154), adopts multiple conformations and may be chemically modified. This high-resolution structure led to the work discussed here: 1) Investigation of changes in fluorescence induced by the binding of ligands to defined single- and double-Trp forms of AaPurE1 and TdPurE2. 2) Characterization of the mutants of AaPurE1 position 154 to determine whether this disordered Tyr pair contributes to net protein fluorescence and ligand-dependent fluorescence changes.

(1) Investigation of fluorescence changes in single-Trp AaPurE1s and TdPurE2.

Trp97 is Responsible for the Differing Effects of CAIR on EcPurE1 and AaPurE1 Fluorescence. We determined that Trp97 is the primary fluorophore in AaPurE1. Our initial hypothesis, based on simple sequence alignments, was that Trp97 would be responsible for CAIR-dependent changes in the fluorescence of inactive H→N mutants of EcPurE1 (fluorescence quenching) and AaPurE1 (fluorescence enhancement). No evidence inconsistent with this hypothesis was found; Trp97 is therefore the best candidate to explain the observed difference between highly homologous PurE1 forms.

Citrate Titrations Report on the Introduction of an Electron-Deficient Carbonyl Carbon into the Carboxylate/CO_2 Binding Pocket. Both PurE classes are proposed to generate a C—C bond using similar chemistry. We can monitor the C—C bond forming reaction in real-time using changes in intrinsic fluorescence that report upon electrostatic changes within the active site. In order to follow these changes, and the reaction in real time, we must first understand how AaPurE1 fluorescence is affected by the introduction of electrostatics (electron-deficient carbonyl carbon of citrate or CO_2 from CAIR and the electron-rich aminoimidazole ring of AIR) into the active site.

Citrate is not a substrate for AaPurE1, but it binds to a region of the active site that overlaps the nucleotide-binding site, leading to progressive quenching of protein fluorescence.[26]

Citrate interacts with the critical active site His59 and several other residues that contact the nucleotide portion of AIR or CAIR. In the wild-type AaPurE1 crystal structure with citrate bound (PDB code 1u11), the *pro-R* arm of citrate interacts with Asp33 (the residue that contacts the AIR 2’ and 3’ hydroxyls) and the central carboxylate forms a hydrogen bond with the protonated δ^1-nitrogen of the His59 imidazole.[26,27] The inactive AaPurE1-H59N mutant binds citrate in a different position, with the *pro-R* arm occupying the carboxylate/CO_2 binding pocket and the *pro-S* arm interacting with Asp33. The central carboxylate instead forms a hydrogen bond with the δ^2-nitrogen of the Asn59. Differences in citrate binding modes may account for some of the observed differences in citrate K_ds for active and inactive AaPurE1 mutants.

The addition of citrate (carrying an electron-deficient carbonyl carbon)[52] appears to quench the intrinsic fluorescence of TdPurE2-F79W and all AaPurE1 forms with one exception, AaPurE1$_{fyw}$-H59N. In the crystal structure of AaPurE1-H59N (PDB entry 2fwp) the indole ring of Trp165 is positioned near the central carboxylate of citrate (Figure 3.1). The proximity of an electron-deficient carbonyl carbon to Trp165 may slightly enhance its fluorescence unless His59 is also present. Since protonated His and imidazole derivatives are known to quench indole fluorescence[5,53,54] it seems possible that a protonated His59 present in the active AaPurE1 forms might "mask" the fluorescence-enhancing effect of Trp165. This apparent electrostatic effect may resemble the effect of introducing an electron-deficient carbonyl carbon into the carboxylate/CO_2 pocket during catalysis.

AIR Enhances Fluorescence in Inactive AaPurE1. Fluorescence enhancement is observed upon the addition of AIR to inactive AaPurE1 forms but not to active AaPurE1 forms or TdPurE-F79W.[26] The only difference between these active and inactive AaPurE1 is the active site His. Replacement of the positively charged His by the neutral Asn abrogates catalytic activity, but may also alleviate intramolecular fluorescence quenching. This is again consistent with the possibility that Trp97 fluorescence is sensitive to the electrostatic environment within the active site pocket, with an effect proportional to the net charge (i.e. more negative = more quenching).

Intramolecular quenching by a protonated His59 could explain the large fluorescence enhancement upon AIR binding observed in inactive forms of AaPurE1. Protonated His contains an imidazolium ion capable of accepting an electron.[14] Therefore, the His may be an endogenous quencher of Trp97 fluorescence enhancement in the AIR bound complex. There is some precedence for such an effect: the active site His in the well-studied barnase has a similar intramolecular quenching effect. [55,56]

Two rotamers of Trp97 were detected in the crystal structure of AaPurE1$_{\text{fwf}}$, which are present at about equivalent occupancies. The Trp97 A rotamer has a χ_1 = -83° while the Trp97 B rotamer has a χ_1 = -97°. Both the rotamers have closer values for the χ_2 = -59 to -65°. In the AaPurE1 structure bound to AIR (PDB code 2fwj), Trp97 adopts only the A rotamer. Our working hypothesis is that the enhancement of AaPurE1 fluorescence upon addition of AIR or CAIR is caused by increasing the contribution of the Trp97 A rotamer. That is, a mixed population of Trp97 A and B rotamers may have lower fluorescence, but the more florescent A rotamer predominates as AIR or CAIR binds.

CAIR Enhances AaPurE1 Fluorescence to a Lesser Extent than AIR. CAIR is a substrate for AaPurE1 so binding equilibrium studies could only be performed using inactive enzymes. Even in the "inactive" mutants, CAIR decarboxylates to the stable ternary AIR•CO_2 complex, directly detected in crystals of AaPurE1-H59N (PDB code 2fwp).[26] Therefore, the fluorescence enhancement seen upon CAIR binding likely results from the AIR•CO_2 complex and not CAIR. To the extent that AIR binds to AaPurE1-H59N in the presence or absence of CO_2 - a somewhat controversial notion given that AIR is neither a PurE1 substrate nor a particularly powerful competitive inhibitor – a comparison with AIR titrations should give information on the net effect of CO_2 in the active site.

The presence of CO_2 could account for the differences in fluorescence enhancement observed in titrations with AIR or CAIR. The results indicate that the additional presence of CO_2 leads to a smaller enhancement of protein fluorescence when AIR binds to a given AaPurE-H59N form. Just as an electron-deficient carbonyl carbon (citrate) quenches AaPurE1 fluorescence, the presence of CO_2 in the CO_2/carboxylate pocket may suppress fluorescence enhancement due to AIR binding.

AaPurE1$_{fwf}$ Fluorescence Quenching Does Not Occur by Electron Transfer. AaPurE1$_{\mathrm{fwf}}$-5FW was used to determine if fluorescence quenching is the result of excited state electron transfer from the Trp indole to a quenching moiety (Q = quenching moiety in Figure 2.31). Indoles and indole derivatives such as Trp are good electron donors.[14,15] However, the addition of a fluorine atom to the indole raises the ionization potential, which should suppress ligand-dependent quenching caused by photoinitiated electron transfer from the indole to an acceptor (quencher).[16] If electron transfer is the mechanism of quenching, one expects a smaller fluorescence change in a protein containing 5FW instead of Trp.

The incorporation of 5FW did not affect the fluorescence changes linked to the binding of either AIR or citrate, indicating that electron transfer from the Trp indole is not primarily responsible in the observed fluorescence changes. Instead, the observed quenching of fluorescence is likely due to some other form of radiationless energy transfer. However, we cannot rule out that 5FW favors rotamer A since we have no structure.

TdPurE2-F79W is Not Suitable for Fluorescence Experiments. The long-term goal of this project was to generate isostructural single-Trp forms of AaPurE1 and TdPurE2 to monitor their C—C bond forming reaction in real time, using stopped-flow spectroscopy. This would provide a head-to-head comparison of the C—C bond forming steps involved in PurE1 and PurE2. Unfortunately, TdPurE2-F79W does not appear to be resilient enough to mutations to permit a suitable comparison with AaPurE1.

While TdPurE-F79W appears to be stable enough for AIR fluorescence titrations, we it eventually shows signs consistent with destabilization. A more significant problem is that any additional mutation appears to create significantly less stable enzyme (Chapter 4). Several *purE2* genes have been recently annotated from thermophilic bacteria (Chapter 1), one or more of which may prove to be suitable for fluorescence studies comparing PurE1 and PurE2.

(2) Characterize the Tyr at the dimer interface of AaPurE1 and investigate its contribution to fluorescence.

No Evidence for Formation of an Intersubunit Cross-Link in AaPurE1$_{fwf}$. Collectively, the results obtained from mass spectrometric and SDS-PAGE analyses indicate that no more then ~10% of Tyr154 is modified, which places an upper limit on the fraction of protein subunits that may be covalently linked. Since a cross-link has not been detected by any means other than macromolecular crystallography, motional disorder and conformational heterogeneity at this dimer interface is most probable cause for the crystallographic findings. Refined crystal structures show that Tyr154 from each subunit adopts two alternative conformations. One Tyr154 conformer in the AaPurE$_{\mathrm{fwf}}$ structure (PDB code 4ycb) closely resembles with the Phe154 conformer observed in both crystal structures of Y154F mutants (PDB codes 4ycd and 4ycj).

Tyr154 has an Unexplained Contribution to Protein Fluorescence. Relative to Trp, Tyr is not expected to have a large contribution to protein fluorescence. The excitation wavelength used (295 nm) has little overlap with Phe and Tyr absorption spectra at 258nm and 275 nm, respectively. Tyr154 appears to relay information on ligand binding to Trp97. The proximity of the phenol ring in each subunit could allow excited state interactions between Tyr154 residues to red shift its excitation envelope.

AaPurE1 forms in which Trp97 is the sole fluorophore showed substantial difference between AIR and CAIR titrations (Figures 3.20 and 3.21). The difference is particularly pronounced for AaPurE1$_{\mathrm{fwf}}$-H59N,Y154F fluorescence, which was unchanged by the addition of CAIR. The corresponding AaPurE1$_{\mathrm{fwf}}$-H59N still maintains moderate fluorescence change in response to the addition of CAIR, indicting that the deletion of a fluorophore (Tyr 154), which relays information on CAIR binding to Trp97 may be responsible for the loss of AaPurE1$_{\mathrm{fwf}}$-H59N,Y154F fluorescence change. Alternatively, the quadruple mutant AaPurE1$_{\mathrm{fwf}}$-H59N,Y154F may not stabilize the fluorescent Trp97

A rotamer as well as other AaPurE1 forms. Therefore, we do not observe any fluorescence enhancement upon CAIR addition.

The presence of CO_2 within the PurE1•AIR•CO_2 ternary complex and to a much lower extent, the carboxylate of citrate in the CO_2/carboxylate binding site appears to determine if Tyr154 has any role in fluorescence response to ligand binding. If a protein is engineered to contain Trp97 as the sole and primary fluorophore the presence of Tyr154 is required to elicit a fluorescence change in response to the electron deficient carbon in the PurE1•AIR•CO_2 complex.

Summary of Fluorescence Response in AaPurE1. Fluorescence changes that can be used to monitor AaPurE1 kinetic parameters would be beneficial in investigating C—C bond breakage and formation using real-time, using pre-steady state kinetics methods like stopped-flow fluorescence spectroscopy.

Fluorescence quenching occurs from the addition of an electron-deficient carbonyl carbon in citrate, and to a lesser extent of CO_2 in the stable ternary AIR•CO_2 complex. Upon excitation, the electron density of the Trp is shifted from the pyrrole ring to the benzene ring, increasing the permanent dipole moment of the indole (Figure 3.32). This interaction of the electron-deficient carbonyl carbon (CO_2 or citrate) in the CO_2/carboxylate pocket with the Trp indole may result in quenching of fluorescence.

Fluorescence enhancement results from the addition of AIR, unless His59 is present. Our working hypothesis is that enhancement of fluorescence may result from a shift in a mixed population of the fluorescent A and less-fluorescent B Trp97 rotamers to a population predominated by the of the Trp97 A rotamer. Alternatively, enhancement of fluorescence could result from the interaction of the electron-rich AIR aminoimidazole with an endogenous quencher of the Trp indole such as a backbone amide.

Quenching and enhancement of fluorescence is not due to electron transfer from the Trp indole. It does appear that some form of resonance energy transfer is occurring between the distant Tyr154 and the predominant fluorophore, Trp97.

The combined results indicate AaPurE1 and in some cases, AaPurE1$_{fwf}$ are the best forms of PurE1 to use in future fluorescence studies. While AaPurE1$_{fwf}$ did not provide any clear advantage over AaPurE1 in steady state fluorescence analysis, the single-Trp form may be a cleaner reporter for pre-steady state analysis. A more stable PurE2 is needed for future fluorescence studies

3.5 Future Directions

Acquisition of pre-steady state kinetic parameters with both active and inactive forms should be done using stopped-flow with AaPurE1$_{fwf}$ and AaPurE1$_{fwf}$-H59N.

A thermophilic PurE2 (preferably containing a Trp) should be characterized for future experiments with the ultimate goal to compare C—C bond formation mechanisms in each class of PurE.

3.6 References

1. Royer, C. A. Probing Protein Folding and Conformational Transitions with Fluorescence. *Chem. Rev.* **106,** 1769–1784 (2006).

2. Eftink, M., Jia, J., Hu, D. and Ghiron, C. Fluorescence Studies with Tryptophan Analogs: Excited State Interactions Involving the Side Chain Amino Group. *J. Phys.* 5713–5723 (1995).

3. Lackowicz, J. R. *Topics in Fluorescence Spectroscopy*. **6,** (Kluwer Academic Publishers, 2002).

4. Kurz, L. C., Fite, B., Jean, J., Park, J., Erpelding, T. and Callis, P. Photophysics of Tryptophan Fluorescence: Link with the Catalytic Strategy of the Citrate Synthase from *Thermoplasma acidophilum*. *Biochemistry* **44,** 1394–1413 (2005).

5. Steiner, R. F. and Kirby, E. P. The Interaction of the Ground and Excited States of Indole Derivatives with Electron Scavengers. *J. Phys. Chem.* **73,** 4130–4135 (1969).

6. Cai, K. and Schirch, V. Structural Studies on Folding Intermediates of Serine Hydroxymethyltransferase Using Single Tryptophan Mutants. *J. Biol. Chem.* **271,** 2987–2994 (1996).

7. Hansen, D., Altschmied, L. and Hillen, W. Engineered Tet Repressor Mutants with Single Tryptophan Residues as Fluorescent Probes. Solvent Accessibilities of DNA and Inducer Binding Sites and Interaction with Tetracycline. *J. Biol. Chem.* **262,** 14030–14035 (1987).

8. Watanabe, F., Jameson, D. M. and Uyeda, K. Enzymatic and Fluorescence Studies of Four Single-Tryptophan Mutants of Rat Testis Fructose 6-Phosphate,2-Kinase:Fructose 2,6-Bisphosphatase. *Protein Sci.* **5,** 904–913 (1996).

9. Vos, R., Engelborghs, Y., Izard, J. and Baty, D. Fluorescence Study of the Three Tryptophan Residues of the Pore-Forming Domain of Colicin A Using Multifrequency Phase Fluorometry. *Biochemistry* **34,** 1734–1743 (1995).

10. Li, J., Szittner, R. and Meighen, E. A. Tryptophan Fluorescence of the Lux-Specific *Vibrio harveyi* Acyl-ACP Thioesterase and its Tryptophan Mutants: Structural Properties and Ligand-Induced Conformational Change. *Biochemistry* **37,** 16130–16138 (1998).

11. Kovács, M., Málnási-Csizmadia, A., Woolley, R. J. and Bagshaw, C. R. Analysis of Nucleotide Binding to Dictyostelium Myosin II Motor Domains Containing a Single Tryptophan Near the Active Site. *J. Biol. Chem.* **277,** 28459–28467 (2002).

12. Málnási-Csizmadia, A., Woolley, R. J. and Bagshaw, C. R. Resolution of Conformational States of Dictyostelium Myosin II Motor Domain Using Tryptophan (W501) Mutants: Implications for the Open-Closed Transition Identified by Crystallography. *Biochemistry* **39,** 16135–16146 (2000).

13. Eftink, M. R. Fluorescence Techniques for Studying Protein Structure. *Methods of Biochemical Analysis* **35,** (1991).

14. Shintzky, Meir and Katchalski, E. Complexes between Indole and Imidazole Deravaties of the Charge-Transfer Type. *Molecular Associations in Biology* (Elsevier, 1967).

15. Pullman, B and Pullman, A. *Quantum Biochemistry*. (John Wiley and Sons, Ltd., 1963).

16. Broos, J., Maddalena, F. and Hesp, B. H. *In vivo* Synthesized Proteins with Monoexponential Fluorescence Decay Kinetics. *J. Am. Chem. Soc.* **126,** 22–23 (2004).

17. Alexander Ross, J. B., Szabo, A. G. and Hogue, C. W. V. Fluorescence Spectroscopy. *Methods in Enzymology* **278,** (Elsevier, 1997).

18. Chadegani, F., Lovell, S., Mullangi, V., Miyagi, M., Battaile, K. P. and Bann, J. G. ^{19}F Nuclear Magnetic Resonance and Crystallographic Studies of 5-Fluorotryptophan-Labeled Anthrax Protective Antigen and Effects of the Receptor on Stability. *Biochemistry* **53,** 690–701 (2014).

19. Danielson, M. A. and Falke, J. J. Use of ^{19}F NMR to Probe Protein Structure and Conformational Changes. *Annu. Rev. Biophys. Biomol. Struct.* **25,** 163–195 (1996).

20. Pfefferkorn, C. M. and Lee, J. C. 5-Fluoro-D,L-Tryptophan as a Dual NMR and Fluorescent Probe of α-Synuclein. *Methods Mol. Biol.* **895,** 197–209 (2012).

21. Winkler, G. R., Harkins, S. B., Lee, J. C. and Gray, H. B. α-Synuclein Structures Probed by 5-Fluorotryptophan Fluorescence and ^{19}F NMR Spectroscopy. *J. Phys. Chem. B* **110,** 7058–7061 (2006).

22. Li, E., Quian, S. J., Nader, L., Yang, N. C., D'Avignon, A., Sacchettini, J. C. and Gordon, J. I. Nuclear Magnetic Resonance Studies of 6-Fluorotryptophan-Substituted Rat Cellular Retinol-binding Protein II Produced in *Escherichia coli.* Analysis of the Apoprotein and the Holoprotein Containing Bound All-trans-Retinol and All-trans-retinal. *J. Biol. Chem.* **264,** 17041–17048 (1989).

23. Hott, J. L. and Borkman, R. F. The Non-Fluorescence of 4-Fluorotryptophan. *Biochem. J.* **264,** 297–299 (1989).

24. Bronskill, P. M. and Wong, J. T. Suppression of Fluorescence of Tryptophan Residues in Proteins by Replacement with 4-Fluorotryptophan. *Biochem. J.* **249,** 305–308 (1988).

25. Hoskins, A. A., Morar, M., Kappock, T. J., Mathews, I. I., Zaugg, J. B., Barder, T. E., Peng, P., Okamoto, A., Ealick, S. E. and Stubbe, J. N^5-CAIR mutase: Role of a CO_2 Binding Site and Substrate Movement in Catalysis Danielson. *Biochemistry* **46,** 2842–2855 (2007).

26. Constantine, C. Z., Starks, C. M., Mill, C.P., Ransome, A. E., Karpowicz, S.J., Francois, J.A., Goodman, R.A. and Kappock, T. J. Biochemical and Structural Studies of N^5-Carboxyaminoimidazole Ribonucleotide Mutase from the Acidophilic Bacterium *Acetobacter aceti. Biochemistry* **45,** 8193–8208 (2006).

27. Settembre, E. C., Chittuluru, J. R., Mill, C. P., Kappock, T. J. and Ealick, S. E. Acidophilic Adaptations in the Structure of *Acetobacter aceti* N^5-Carboxyaminoimidazole Ribonucleotide Mutase (PurE). *Acta Crystallogr. Sect. D Biol. Crystallogr.* **60,** 1753–1760 (2004).

28. Sullivan, K. L., Huma, L. C., Mullins, E. a, Johnson, M. E. and Kappock, T. J. Metal Stopping Reagents Facilitate Discontinuous Activity Assays of the *de novo* Purine Biosynthesis Enzyme PurE. *Anal. Biochem.* **452,** 43–45 (2014).

29. Tranchimand, S., Starks, C. M., Mathews, I. I., Hockings, S. C. and Kappock, T. J. *Treponema denticola* PurE is a bacterial AIR Carboxylase. *Biochemistry* **50,** 4623–4637 (2011).

30. Bradford, M. M. A Rapid and Sensitive Method for the Quantitation of Microgram Quantities of Protein Utilizing the Principle of Protein-Dye Binding. *Anal. Biochem.* **72,** 248–254 (1976).

31. Scopes, R. K. K. Measurement of Protein by Spectrophotometry at 205 nm. *Anal. Biochem.* **59,** 277–282 (1974).

32. Bujard, H., Gentz, R., Lanzer, M., Stueber, D., Mueller, M., Ibrahimi, I. and Dobberstein, B. A T5 Promoter-Based Transcription-Translation System for the Analysis of Proteins *in vitro* and *in vivo*. *Methods in Enzymology* **155**, 416–433 (1987).

33. Broos, J. Biosynthetic Incorporation of Tryptophan Analogs in Proteins. *Methods Mol. Biol.* **1076,** 359–370 (2014).

34. Miller, J. H. The *lacI* Gene: Its Role in Lac Operon Control and Its Use as a Genetic System. *Cold Spring Harbor Monograph Archive* **07,** 31–88 (1980).

35. Studier, F. W. Protein Production by Auto-Induction in High Density Shaking Cultures. *Protein Expr. Purif.* **41,** 207–234 (2005).

36. Chen, R. F. Fluorescence Quantum Yields of Tryptophan and Tyrosine. *Anal. Lett.* **1,** 35–42 (1967).

37. Laurent, T. C. and Killander, J. A Theory of Gel Filtration and its Exeperimental Verification. *J. Chromatogr. A* **14,** 317–330 (1964).

38. McCoy, A. J. Grosse-Kunstleve, R. W., Adams, P. D., Winn, M. D., Storoni, L. C. and Read, R. J. Phaser Crystallographic Software. *J. Appl. Crystallogr.* **40,** 658–674 (2007).

39. Adams, P. D., Afonine, P. V., Bunkóczi, G., Chen, V. B., Davis, I. W., Echols, N., Headd, J. J., Hung, L. W., Kapral, G. J., Grosse-Kunstleve, R. W., McCoy, A. J., Moriarty, N.W., Oeffner, R., Read, R. J., Richardson, D. C., Richardson, J. S., Terwilliger, T. C. and Zwart, P. H. Phenix: A Comprehensive Python-based System for Macromolecular Structure Solution. *Acta Crystallogr. Sect. D Biol. Crystallogr.* **66,** 213–221 (2010).

40. Emsley, P., Lohkamp, B., Scott, W. G. and Cowtan, K. Features and Development of Coot. *Acta Crystallogr. Sect. D Biol. Crystallogr.* **66,** 486–501 (2010).

41. DeLano, W. L. The PyMOL Molecular Graphics System. (2002). http://www.pymol.org

42. Nettleship, J. E., Walter, T. S., Aplin, R., Stammers, D. K. and Owens, R. J. Sample Preparation and Mass-Spectrometric Characterization of Crystal-Derived Protein Samples. *Acta Crystallogr. D. Biol. Crystallogr.* **61,** 643–645 (2005).

43. Terwilliger, T. C. Grosse-Kunstleve, R. W., Afonine, P. V., Moriarty, N.W., Adams, P. D., Read, R. J., Zwart, P. H. and Hung, L. W. Iterative-Build Omit Maps: Map Improvement by Iterative Model Building and Refinement without Model Bias. *Acta Crystallogr. D. Biol. Crystallogr.* **64,** 515–524 (2008).

44. Tilley, K. A. Benjamin, R. E., Bagorogoza, K. E., Okot-Kotber, B. M., Prakash, O. and Kwen, H. Tyrosine Cross-Links: Molecular Basis of Gluten Structure and Function. *J. Agric. Food Chem.* **49,** 2627–2632 (2001).

45. Aeschbach, R., Amadoò, R. and Neukom, H. Formation of Dityrosine Cross-Links in Proteins by Oxidation of Tyrosine Residues. *Biochim. Biophys. Acta-Protein Struct.* **439,** 292–301 (1976).

46. Andersen, S. O. The Cross-Links in Resilin Identified as Dityrosine and Trityrosine. *Biochim. Biophys. Acta - Gen. Subj.* **93,** 213–215 (1964).

47. Eickhoff, H., Jung, G. and Rieker, A. Oxidative Phenol Coupling-Tyrosine Dimers and Libraries Containing Tyrosyl Peptide Dimers. *Tetrahedron* **57,** 353–364 (2001).

48. Giulivi, C. and Davies, K. J. Dityrosine: a Marker for Oxidatively Modified Proteins and Selective Proteolysis. *Methods Enzymol.* **233,** 363–71 (1994).

49. Boguta, G. and Dancewicz, A. M. Radiation-Induced Dimerization of Tyrosine and Glycyltyrosine in Aqueous Solutions. *Int. J. Radiat. Biol. Relat. Stud. Phys. Chem. Med.* **39,** 163–74 (1981).

50. Meyer, E. Two New Activities and a New Intermediate in the Purine Pathway. (1996). Ph.D. Thesis, Massachusetts Institute of Technology, Cambridge, MA.

51. Wong, C. Y. and Eftink, M. R. Incorporation of Tryptophan Analogues into Staphylococcal Nuclease, its V66W Mutant, and Delta 137-149 Fragment: Spectroscopic Studies. *Biochemistry* **37,** 8938–46 (1998).

52. Martell, A. E. and Smith, R. M. *Critical Stability Constants*. (Springer US, 1982).

53. Shinttzky, M. and Goldman, R. Fluorometric Detection of Histidine-Tryptophan Complexes in Peptides and Proteins. *Eur. J. Biochem.* **3,** 139–144 (1967).

54. Shinitzky, M., Katchalski, E., Grisaro, V. and Sharon, N. Inhibition of Lysozyme by Imidazole and Indole Derivatives. *Arch. Biochem. Biophys.* **116,** 332–343 (1966).).

55. Loewenthal, R., Sancho, J. and Fersht, A. R. Fluorescence spectrum of Barnase: Contributions of Three Tryptophan Residues and a Histidine-Related pH Dependence. *Biochemistry* **30,** 6775–6779 (1991).

56. Loewenthal, R., Sancho, J. and Fersht, A. R. Histidine-Aromatic Interactions in Barnase. Elevation of Histidine pK_a and Contribution to Protein Stability. *J. Mol. Biol.* **224,** 759–70 (1992).

3.7 Figures and Tables

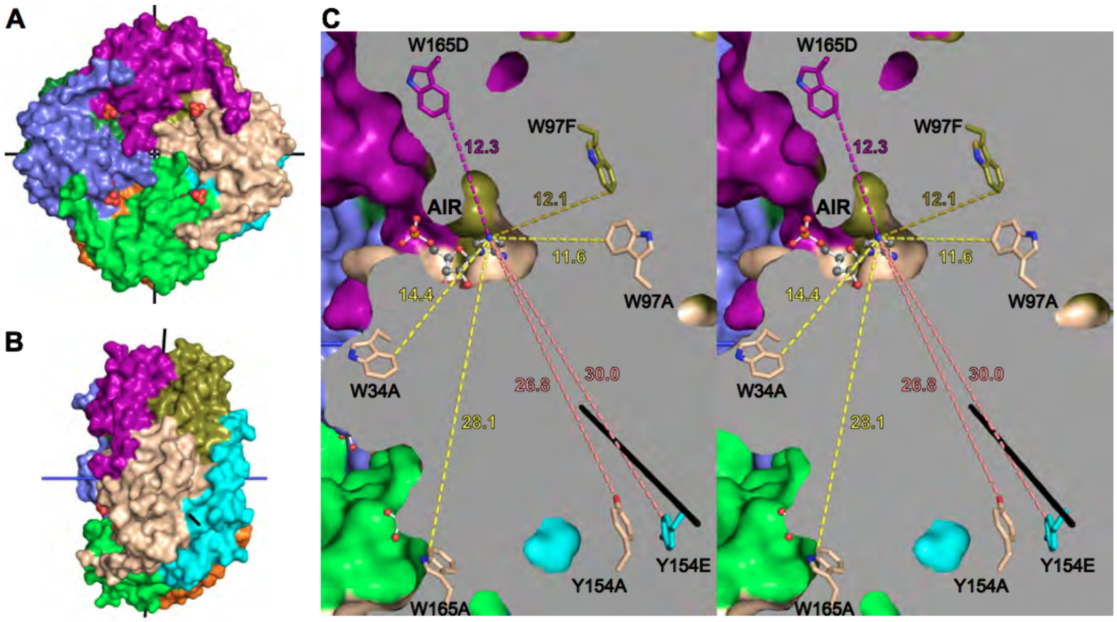

Figure 3.1 AaPurE1 octamer with Trps and Tyr154 shown. (A) AaPurE1 (PDB code 2fwj) octamer shown along its four-fold symmetry axis (AIR depicted as spheres) and each subunit shown in a different color. (B) Orientation of the AaPurE1 octamer shown in cutaway in panel C. (C) AaPurE1 octamer presented in cutaway view to show Trp and Tyr154 positions relative to AIR. Colors of subunits are the same as panels A and B. The gray plane is the interior of the protein; all residues shown are between the plane and the viewer. All distances (in Å) between AIR N3 and the nearest indole or phenol are indicated.

Table 3.1 Fluorescence emission properties of Trp analogs.

Analog	λ_{max}, nm[a]	Φ[b]
N-Acetyl-L-tryptophanamide	356	0.14
5-hydroxytryptophan	341	0.22
7-azatryptophan	415	0.01
5-fluorotryptophan	358	0.14
4-fluorotryptophan	na	≤0.0014

[a] λ_{max} values from literature [3,23]

[b] Φ; quantum yield values from literature measured in pH 7 water at 20 ºC.[3,23]

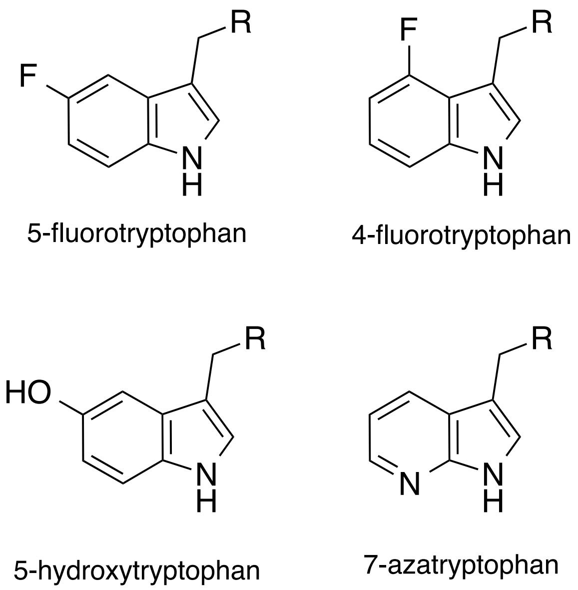

5-fluorotryptophan 4-fluorotryptophan

5-hydroxytryptophan 7-azatryptophan

Figure 3.2 Commonly used tryptophan analogs.

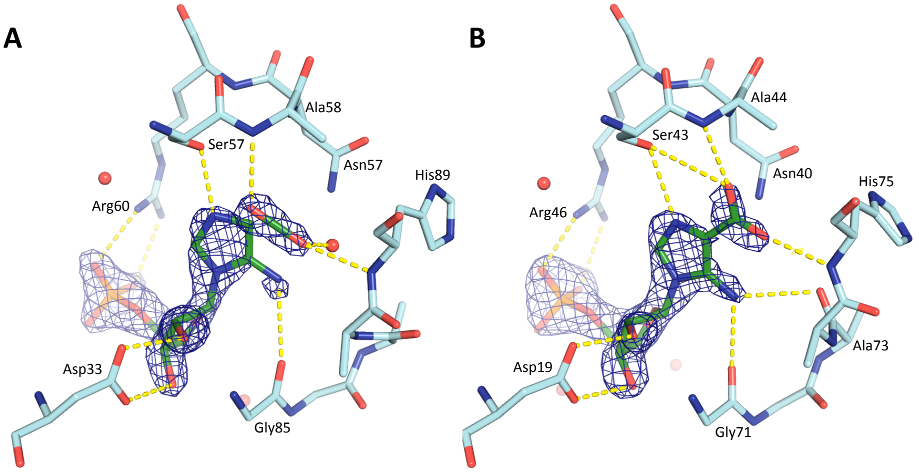

Figure 3.3 Structures of AaPurE1-H59N and EcPurE1-H45N with AIR•CO_2 and CAIR bound. Left: AaPurE1-H59N (PDB code 2fwp). and Right: EcPurE1-H45N (PDB code 2nsl) active sites are shown with active site contacts to AIR•CO_2 and CAIR shown. CAIR has different chemical outcomes between the PurE1s and might lead to different fluorescence responses. The AIR and CO_2 are not co-planar in AaPurE1, but are co-planar in EcPurE1. Electron density maps for $2F_o$-F_c (blue mesh) are contoured at 1.0 σ and have a carve radius of 2.0 Å.

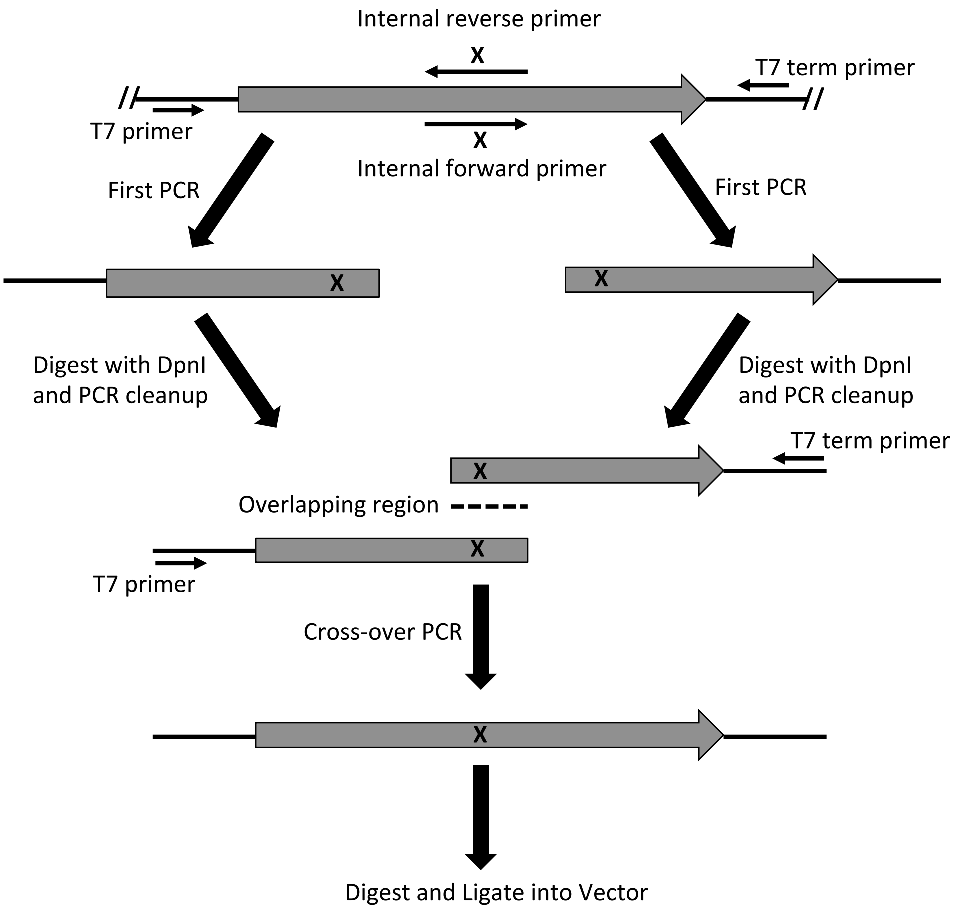

Figure 3.4 Illustration of cross-over PCR used to generate the TdPurE2-F79W mutant.

Table 3.2 *E.coli* strains used in this chapter.

Strain	Description	Source
DH5α	F′ φ80lacZΔM15 Δ(lacZYA-argF)U169 *deoR recA1 endA1 hsdR17(*r_K^- m_K^+) *phoA supE44 thi-1 gyrA96 relA1*	Lab stock
BL21(DE3)	F$^-$ *ompT gal dcm lon hsd*S$_B$(r_B^- m_B^-) λ(DE3 [*lacI lacUV5*-T7 *gene 1 ind1 sam7 nin5*])	Lab stock
CC1215	F$^-$ *ompT gal dcm lon hsd*S$_B$(r_B^- m_B^-) *ΔpurE*736::kan λ(DE3 [*lacI lacUV5*-T7 *gene 1 ind1 sam7 nin5*])	Lab stock
DL41	F$^-$, *λ*$^-$, *metA28, trp*	*E. coli* Genetic Stock Center

Table 3.3 Oligodeoxynucleotides (ODNs) used in this chapter.

ODN	Sequence (5'→3') [a]	
2042	CCAGTCAGACTtcGAAACCATGCGCCA	AaPurE1-W34F
2043	TGGCGCATGGTTTCgaAGTCTGACTGG	AaPurE1-W34F
2044	CCTTGAAACATttCGCGCATTGCAG	AaPurE1-W165F
2045	CTGCAATGCGCGaaATGTTTCAAGG	AaPurE1-W165F
2048	GTTTCAGCAaATCGTACGCCAGACCGGTTGGC	AaPurE1-H59N
2049	CGTACGATtTGCTGAAACAATGAGGGTTTCATGCG	AaPurE1-H59N
2109	GTATGTGTGCGGCATatACACGCCTGCCCGTG	AaPurE1-W97Y
2110	CACGGGCAGGCGTGTATatGCCGCACACATAC	AaPurE1-W97Y
2170	GGGCCGGGTTAaACAGTGCAAGAATGG	AaPurE1-Y154F
2171	CCATTCTTGCACTGTtTAACCCGGCCC	AaPurE1-Y154F
2172	GCAAGGGCCGGGTTtaACAGTGCAAGAATGG	AaPurE1-Y154L
2173	CCATTCTTGCACTGTtaAACCCGGCCCTTGC	AaPurE1-Y154L
2174	GGCAAGGGCCGGGTTgatCAGTGCAAGAATGG	AaPurE1-Y154I
2175	CCATTCTTGCACTGatcAACCCGGCCCTTGCC	AaPurE1-Y154I
2329	GGTTGCACCTTTGACccAGCCATCAACAAAG	AaPurE1-F79W
2330	CTTTGTTGATGGCTggGTCAAAGGTGCAACC	AaPurE1-F79W
2410	CCGAGATCTCCCCGAAAAGTGCCACCTG	T5 promoter region
2411	GCTCATCATATGTTAATTTCTCCTCTTTAATGAATTC	T5 promoter region

[a] Changes in the coding region that deviate from the genomic sequence are in lower case.

Table 3.4 Previously published plasmids used in this chapter.

Plasmid	Description	Source	Protein encoded
pET23a	Expression vector	Novagen	na
pCDFDuet	Expression vector	Novagen	na
acs1	*acs1* in pQE80	Addgene	na
pJK175	*purE1*$_{Aa}$ in pET23a	[26]	AaPurE
pJK283	*purE1*$_{Aa}$*-H59N* in pET23a	[26]	AaPurE-H59N

[a] na- not applicable

Table 3.5 Newly generated plasmids used in this chapter.

Plasmid	Description	Protein encoded
Three Trp		
pJK601	*purE1*$_{Aa}$*-Y154F* in pET23a	AaPurE-Y154F
pJK602	*purE1*$_{Aa}$*-H59N,Y154F* in pET23a	AaPurE-H59N,Y154F
Two Trp		
pJK506	*purE1*$_{Aa}$*-W165F* in pET23a	AaPurE$_{\text{wwf}}$
pJK663	*purE1*$_{Aa}$*-Y154F,W165F* in pET23a	AaPurE$_{\text{wwf}}$-Y154F
pJK510	*purE1*$_{Aa}$*-H59N,W165F* in pET23a	AaPurE$_{\text{wwf}}$-H59N
pJK664	*purE1*$_{Aa}$*-H59N,Y154F,W165F* in pET23a	AaPurE$_{\text{wwf}}$-H59N
pJK505	*purE1*$_{Aa}$*-W34F* in pET23a	AaPurE$_{\text{fww}}$
pJK603	*purE1*$_{Aa}$*-W34F, Y154F* in pET23a	AaPurE$_{\text{fww}}$-Y154F
pJK509	*purE1*$_{Aa}$*-W34F, H59N* in pET23a	AaPurE$_{\text{fww}}$-H59N
pJK604	*purE1*$_{Aa}$*-W34F,H59N,Y154F* in pET23a	AaPurE$_{\text{fww}}$H59N-Y154F
One Trp		
pJK526	*purE1*$_{Aa}$*-W97Y,W165F* in pET23a	AaPurE$_{\text{wyf}}$
pJK666	*purE1*$_{Aa}$*-H59N,W97Y,W165F* in pET23a	AaPurE$_{\text{wyf}}$-H59N
pJK507	*purE1*$_{Aa}$*-W34F, W165F* in pET23a	AaPurE$_{\text{fwf}}$
pJK508	*purE1*$_{Aa}$*-W34F, H59N, W165F* in pET23a	AaPurE$_{\text{fwf}}$-H59N
pJK600	*purE1*$_{Aa}$*-W34F,H59N,Y154F,W165F* in pET23a	AaPurE$_{\text{fwf}}$-H59N,Y154F
pJK559	*purE1*$_{Aa}$*-W34F,Y154F,W165F* in pET23a	AaPurE$_{\text{fwf}}$-Y154F
pJK562	*purE1*$_{Aa}$*-W34F,Y154L,W165F* in pET23a	AaPurE$_{\text{fwf}}$-Y154L
pJK525	*purE1*$_{Aa}$*-W34F,W97Y* in pET23a	AaPurE$_{\text{fyw}}$
pJK665	*purE1*$_{Aa}$*-W34F,H59N,W97Y* in pET23a	AaPurE$_{\text{fyw}}$-H59N
pJK698	*purE1*$_{Aa}$*-W34F, W165F* in pET23a with T5 promoter	AaPurE$_{\text{fwf}}$
pJK500	*purE1*$_{Ec}$*-W20F* in pET23a	EcPurE1-W20F
pJK501	*purE1*$_{Ec}$*-W20F* in pET23a	EcPurE-W151F
pJK648	*purE2*$_{Td}$*-F79W* in pET23a	TdPurE-F79W

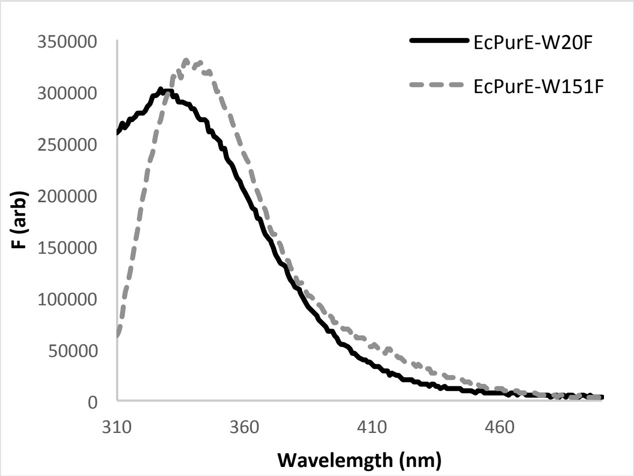

Figure 3.5 Fluorescence emission spectra of EcPurE1-W20F and EcPurE1-W151F. EcPurE1s were present at 30 μM [subunit]. The excitation wavelength was 295 nm. The λ_{max} EcPurE1-W20F is 330 nm and the λ_{max} for EcPurE1-W151F is 337 nm.

Table 3.6 Mass spectrometric analysis of AaPurE1 forms.

AaPurE1form	Observed Mass (Da)	Expected Mass (Da)[a]	Difference
Three Trp			
AaPurE1 (wild-type)	18867[b]	18867	0
AaPurE1-H59N	18845[c]	18844	-1
AaPurE1-H59N, Y154F	18827	18828	+1
AaPurE1-Y154F	18850	18852	+2
Two Trp			
AaPurE1$_{wwf}$	18829	18828	-1
AaPurE1$_{wwf}$-Y154F	18812	18812	0
AaPurE1$_{wwf}$-H59N	18810	18805	-5
AaPurE1$_{wwf}$-H59N,Y154F	18790	18798	+8
AaPurE1$_{fww}$	18830	18828	-2
AaPurE1$_{fww}$-Y154F	18813	18812	-1
AaPurE1$_{fww}$-H59N	18805	18805	0
AaPurE1$_{fww}$-H59N, Y154F	18791	18789	-2
One Trp			
AaPurE1$_{wyf}$	18802	18805	+3
AaPurE1$_{wyf}$-H59N	18789	18782	-7
AaPurE1$_{fwf}$	18790	18789	-1
AaPurE1$_{fwf}$-H59N	18766	18766	0
AaPurE1$_{fwf}$-H59N, Y154F	18752	18750	-2
AaPurE1$_{fwf}$-Y154F	18774	18773	-1
AaPurE1$_{fwf}$-Y154L	18739	18739	0
AaPurE1$_{fyw}$	18797	18805	-8
AaPurE1$_{fyw}$-H59N	18786	18782	-4
AaPurE1$_{fwf}$-5-FW	18804	18806	+2

[a] Molecular masses ([M+H+]+) were determined by MALDI. Expected masses were calculated using ExPaSy ProtParam. All AaPurE1s have an additional N-terminal Met[26].

[b] ESI-MS observed 18865 (expected 18865.7).[26]

[c] ESI-MS observed 18842 (expected 18842.7).[26]

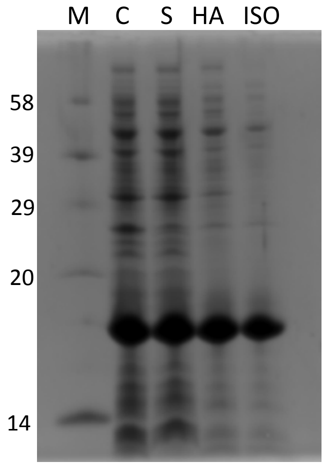

Figure 3.6 SDS-PAGE analysis of a representative AaPurE1 Trp mutant (AaPurE1$_{fwf}$) isolation. A 12% polyacrylamide gel was loaded with 5 ug protein per lane: M, Sigma biotinylated marker; S, soluble lysate; CL, cleared lysate; HA, hydroxyapatite input; and ISO, isolated AaPurE1-S57V. Molecular weights (kDa) are denoted along the left side of the gel.

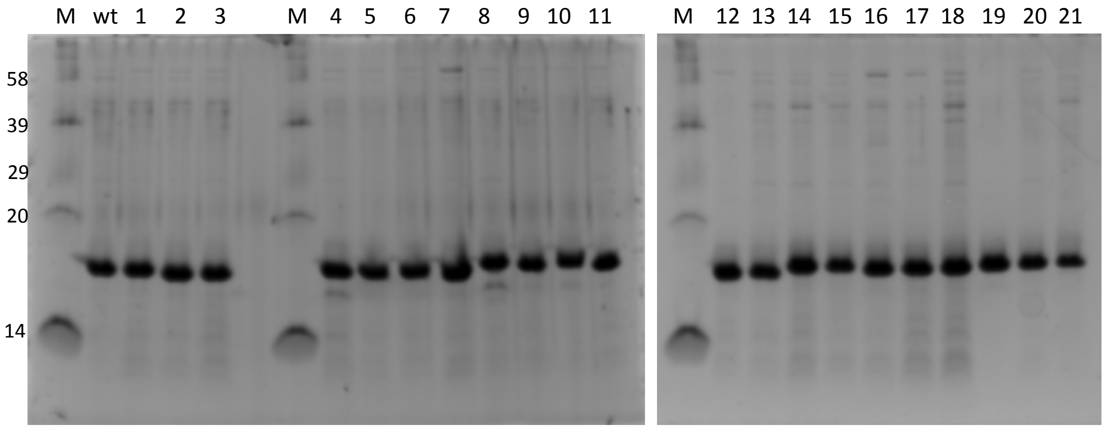

Figure 3.7 SDS-PAGE analysis of isolated AaPurE1 forms. A 12% polyacrylamide gel was loaded with 5 ug protein per lane: M, Sigma biotinylated marker; AaPurE1 is denoted by wt; 1, AaPurE1-H59N; 2, AaPurE1-H59N,Y154F; 3, AaPurE1-Y154F; 4, AaPurE1$_{wwf}$; 5, AaPurE1$_{wwf}$-Y154F; 6, AaPurE1$_{wwf}$-H59N; 7, AaPurE1$_{wwf}$-H59N,Y154F; 8, AaPurE1$_{fww}$; 9, AaPurE1$_{fww}$-Y154F; 10, AaPurE1$_{fww}$-H59N; 11, AaPurE1$_{fww}$-H59N,Y154F; 12, AaPurE1$_{wyf}$; 13, AaPurE1$_{wyf}$-H59N; 14, AaPurE1$_{fwf}$; 15, AaPurE1$_{fwf}$-H59N; 16, AaPurE1$_{fwf}$-H59N,Y154F; 17, AaPurE1$_{fwf}$-Y154F; 18, AaPurE1$_{fwf}$-Y154L; 19, AaPurE1$_{fyw}$; 20, AaPurE1$_{fyw}$-H59N; and 21, AaPurE1$_{fwf}$-5FW. Molecular weights (kDa) are denoted along the left side of the gel.

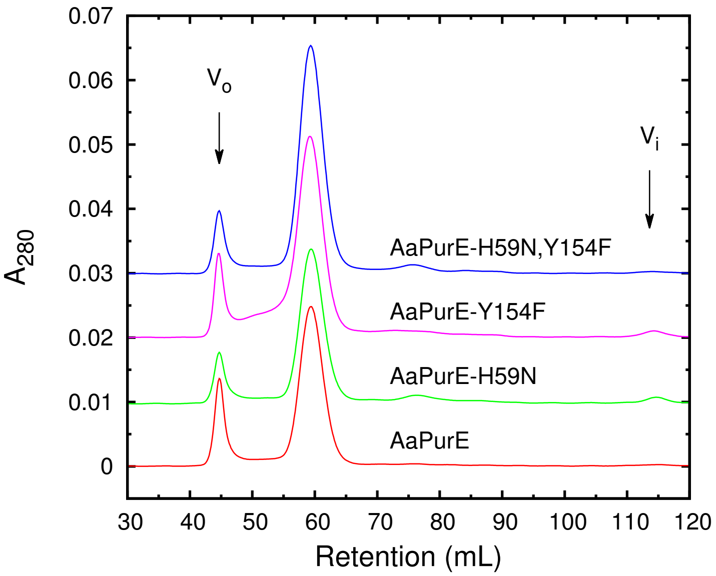

Figure 3.8 Gel-filtration analysis of AaPurE1 forms containing all three Trps. The traces are shifted 0.01 A_{280}. The PurE1 octamer elutes at ~57 mL and aggregate elutes within the excluded volume. The completely excluded (V_o, 44.7 mL) and included (V_i, 113.6 mL) volumes are indicated with arrows above.

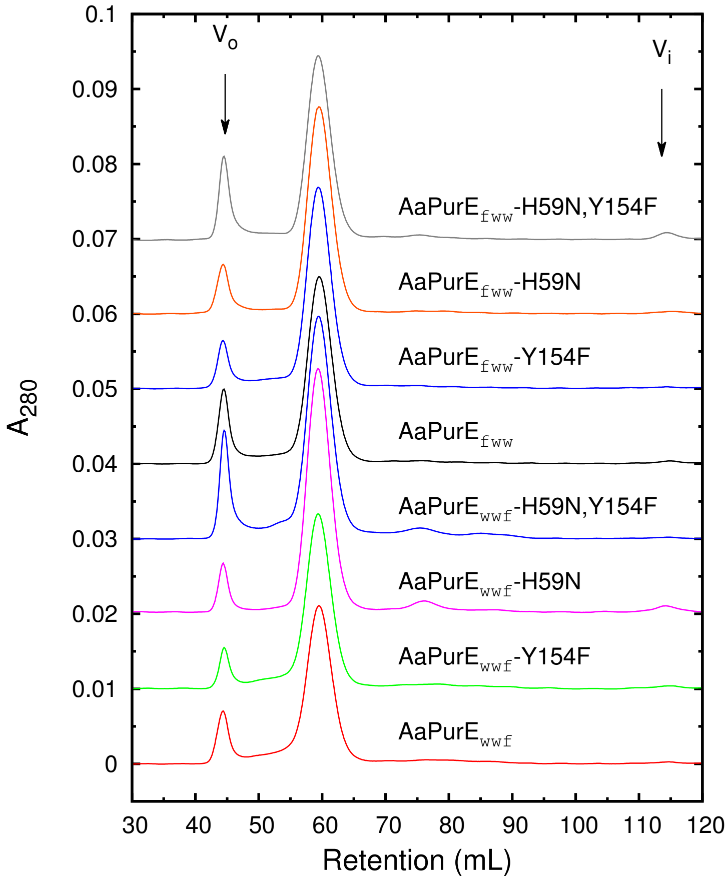

Figure 3.9 Gel-filtration analysis of AaPurE1 forms containing two Trps. The traces are shifted 0.01 A_{280}. The PurE1 octamer elutes at ~57 mL and aggregate elutes within the excluded volume. The completely excluded (V_o, 44.7 mL) and included (V_i, 113.6 mL) volumes are indicated with arrows above. A small peak (~76 mL) is observed in some forms lacking Trp165, this may be dissociation of the octamer into tetramer.

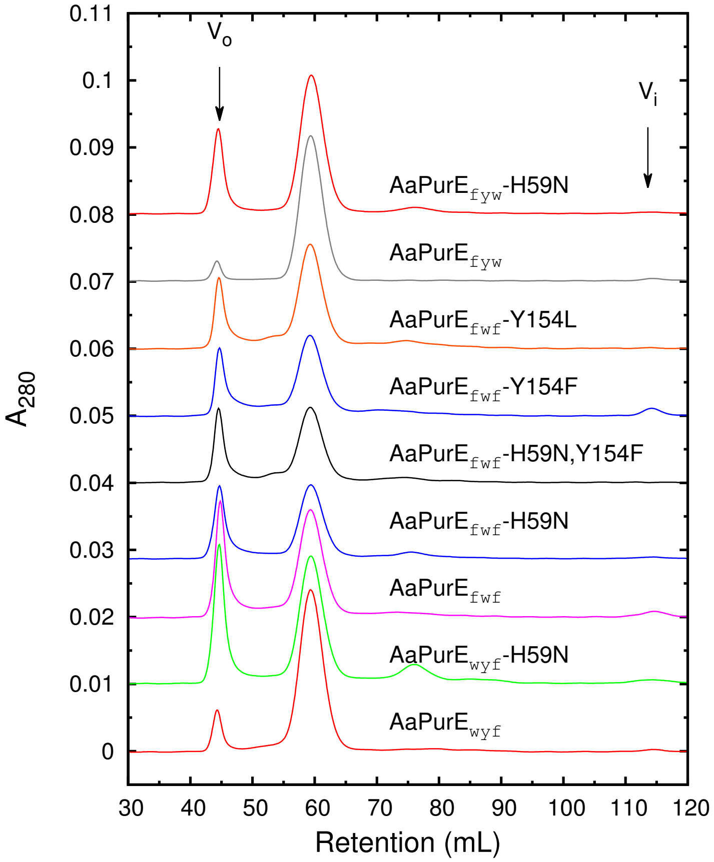

Figure 3.10 Gel-filtration analysis of AaPurE1 forms containing a single-Trp. The traces are shifted 0.01 A_{280}. The PurE1 octamer elutes at ~57 mL and aggregate elutes within the excluded volume. The completely excluded (V_o, 44.7 mL) and included (V_i, 113.6 mL) volumes are indicated with arrows above. A small peak (~76 mL) is observed in some forms lacking Trp165, this may be dissociation of the octamer into tetramer.

Table 3.7 Specific activities and dissociation constants for selected proteins.

		ΔF			K_d (μM)		
PurE1 or PurE2 form	rSA[a]	Citrate[b]	AIR[c]	CAIR[c]	Citrate[b]	AIR[c]	CAIR[c]
AaPurE1 (wild-type)	1.0[d]	-0.214	0.040	na[e]	275[f]	2.2	na
AaPurE1-H59N	~0[d]	-0.198	0.309	0.140	560[g]	0.61	0.96[h]
AaPurE1-H59N, Y154F	~0	-0.154	0.310	0.314	870	1.3	1.4
AaPurE1-Y154F	0.8	-0.214	-0.024	0.312	275	0.6	na
AaPurE1$_{\text{wwf}}$	1.0	-0.319	~0	na	247	is[i]	na
AaPurE1$_{\text{wwf}}$-Y154F	0.87	-0.366	~0	na	390	is	na
AaPurE1$_{\text{wwf}}$-H59N	~0	-0.199	0.382	0.21	700	1.45	3.5
AaPurE1$_{\text{wwf}}$-H59N,Y154F	~0	-0.294	0.302	0.078	530	1.36	1.4
AaPurE1$_{\text{fww}}$	0.8	-0.326	-0.050	na	820	1.1	na
AaPurE1$_{\text{fww}}$-Y154F	0.6	-0.234	-0.051	na	285	1.2	na
AaPurE1$_{\text{fww}}$-H59N	~0	-0.326	0.337	0.33	820	1.57	2.8
AaPurE1$_{\text{fww}}$-H59N, Y154F	~0	-0.177	0.290	0.24	780	1.57	4.8
AaPurE1$_{\text{wyf}}$	0.54	-0.233	~0	na	220	Is	na
AaPurE1$_{\text{wyf}}$-H59N	~0	-0.117	0.235	0.208	420	1.60	3.8
AaPurE1$_{\text{fwf}}$	0.90	-0.368	-0.050	na	210	1.4	na
AaPurE1$_{\text{fwf}}$-H59N	~0	-0.285	0.268	0.107	520	4.3	5.7
AaPurE1$_{\text{fwf}}$-H59N, Y154F	~0	-0.221	0.236	~0	500	3.5	is
AaPurE1$_{\text{fwf}}$-Y154F	0.7	-0.228	-0.062	na	283	1.3	na
AaPurE1$_{\text{fwf}}$-Y154L	0.7	-0.213	-0.090	na	259	1.8	na
AaPurE1$_{\text{fyw}}$	0.59	-0.170	~0	na	180	is	na
AaPurE1$_{\text{fyw}}$-H59N	~0	0.088	-0.069[j]	-0.051[j]	900	2.7	0.31[j]
AaPurE1$_{\text{fwf}}$-5-FW	0.78	-0.393	-0.078	na	2.4	0.47	na
TdPurE2-F79W	93	-0.240	-0.110	na	43	3	na

[a] rSA, specific activity relative to wild-type AaPurE1(39 units per mg protein, determined at 0.1 mM CAIR, pH 8, and °C).

[b] Determined at pH 4.6 and 25 Representative spectra and fits to equation 3.1 are given in the Appendix as panels A and B of Figures A.1-A.22.

[c] Determined at pH 8 and 30 °C Representative spectra and fits to equation 3.2 (except as noted) are given in the Appendix as panels C and D of Figures A.1-A.22(AIR) and panels E and F of Appendix Figures A.1, A.4-6, A.9-10, A.13, A.15, A.18-20 (CAIR).

[d] rSA, % specific activity in the CAIR decarboxylation reaction relative to wild-type AaPurE1 (39 U mg^{-1}) and TdPurE2 (185 U mg^{-1}) at 100 μM CAIR, pH 8.0, 30 °C.

[e] na, not applicable

[f] 0.4 mM reported previously.[26]

[g] 2 mM reported previously.[26]

[h] 0.78 μM reported previously.[26]

[i] is, insufficient signal change.

[j] Fit to equation 3.2.

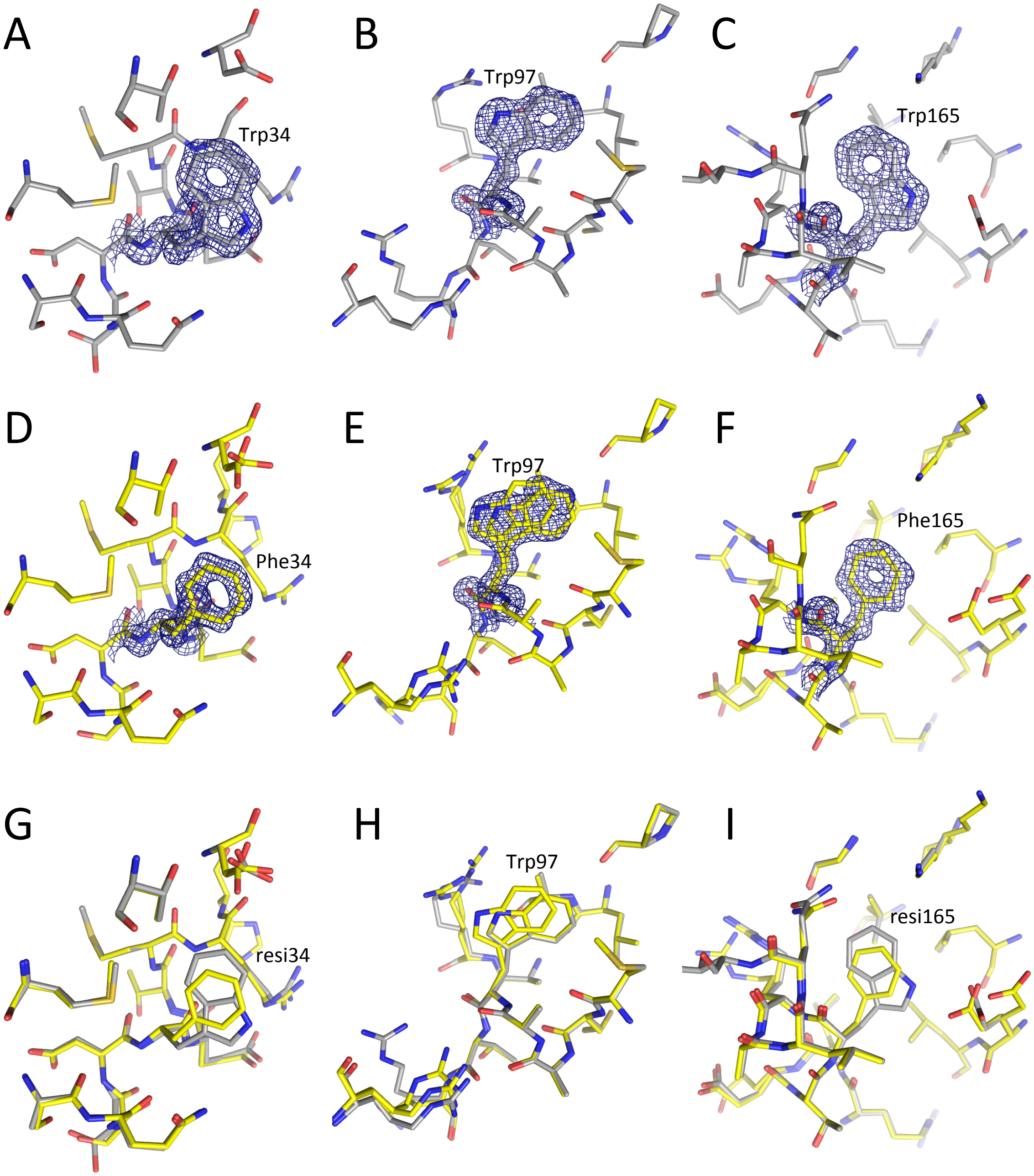

Figure 3.11 Electron density maps for the residues 34, 97, and 165 in AaPurE1. Individual Phes and Trps and the residues within 10 Å are shown for AaPurE1 (PDB code 1u11) in dark gray and AaPurE1$_{\mathrm{fwf}}$ (PDB code 4ycb) in yellow. (A) Trp34 of AaPurE1 shown. (B) Trp97 of AaPurE1 shown. (C) Trp165 of AaPurE1 shown. (D) Phe34 of AaPurE1$_{\mathrm{fwf}}$ shown. (E) Trp97 alt conformations of AaPurE1$_{\mathrm{fwf}}$ shown. (F) Phe165 of AaPurE1$_{\mathrm{fwf}}$ shown. (G-I) The alignment of residue 34, Trp97, and residue 165 of AaPurE and AaPurE1$_{\mathrm{fwf}}$ are shown. Electron density maps $2F_o$-F_c (blue mesh) are contoured at 1.8 σ and all maps have a carve radius of 2.0 Å.

Table 3.8 X-ray data collection statistics.

	AaPurE1$_{fwf}$			AaPurE1
	-	Y154L	Y154F	Y154F
PDB entry	4ycb	4ycc	4ycd	4ycj
Beamline	21-ID-G	21-ID-F	21-ID-F	21-ID-G
Wavelength (Å)	0.97856	0.97872	0.97872	0.97856
Space group [b]	I422	I422	I422	I422
Unit cell param. (Å)	a=b= 99.803, c= 164.409	a=b=99.458, c=165.567	a=b=100.336, c=165.712	a=b= 99.761, c= 165.008
Resolution (Å)	50-1.35 (1.37–1.35)[a]	50-2.25 (2.29-2.25)	50–1.65 (1.68–1.65)	50-1.84 (1.88-1.84)
No. meas. refl.	1,319,978	158,696	419,831	429,790
No. unique refl.	90,070 (3925)	19,660 (950)	51,530 (2538)	35,774 (1748)
Completeness (%)	99.2 (87.5)	98.9 (99.6)	100 (100)	100 (100)
Multiplicity	14.7 (22.9)	8.1 (20.7)	8.1 (20.3)	12.0 (11.7)
R_{merge} (%) [c]	7.1 (52.3)	10.2 (22.8)	8.7 (53.8)	7.8 (55.1)
Mean I/σ (I)	48.1 (2.0)	37.2 (10.6)	26.8 (3.6)	44.1 (5.4)
V_M (Å^3 Da^{-1}) [d]	2.49	2.49	2.53	2.48
Est. solvent (%)	50.5	50.6	51.5	50.4

[a] Values in parenthesis are for the highest resolution shell.

[b] All have α=β=γ=90°.

[c] $R_{\text{merge}} = \frac{\Sigma_{hkl} \Sigma \,|\, I_i\,(hkl) - \langle I(hkl)\rangle |}{\Sigma_{hkl}\, \Sigma_i\, I_i(hkl)}$, where $I_i\,(hkl)$ is the ith measurement of the intensity of reflection hkl and $\langle I(hkl)\rangle$ is its mean value.

[d] Matthews coefficient.

Table 3.9 Summary or refinement statistics.

	AaPurE1$_{\mathrm{fwf}}$			AaPurE1
	-	Y154L	Y154F	Y154F
PDB entry	4ycb	4ycc	4ycd	4ycj
Resolution(Å)	31.6-1.35 (1.37-1.35) [a]	49.7-2.24 (2.36-2.34)	47.9-1.63 (1.67-1.63)	35.5-1.84 (1.90-1.84)
No. reflections used				
working	89999	19350	49684	34671
test set	3547	933	1966	1481
Completeness (%)	99.2	96.2	96.0	95.8
Rcryst[b]*(%)*	14.0 (23.43)	13.5 (14.3)	15.6 (17.6)	13.5 (15.1)
Rfree[c]*(%)*	14.9 (25.8)	17.2 (20.2)	17.4 (22.6)	15.4 (68.8)
No. of atoms				
all atoms	2963	2554	2752	2841
protein atoms	2519	2328	2341	2446
solvent atoms	397	215	396	355
R.m.s. deviations from ideality				
Bondlengths (Å)	0.011	0.008	0.006	0.007
Bond angles (°)	1.110	1.089	1.091	0.985
Average isotropic B factors (Å^2)				
protein atoms	13.8	26.7	14.1	20.6
ligand atoms	40.7	54.3	45.9	49.6
solvent atoms	35.7	27.9	31.2	38.8
Ramachandran plot statistics (%)				
Residues in favored regions	99.1	98.8	98.8	98.8
Residues in allowed regions	0.7	1.3	1.2	0.7
Outliers	0.4	0.4	0.4	0
MolProbity score [percentile]	1.27 (94)	1.13 (100)	1.03 (100)	1.07 (98)
MolProbity clashscore [percentile]	5.12(89)	3.35 (99)	5.50 (99)	2.79 (99)

[a] Values in parenthesis are for the highest resolution shell.

[b] $R_{\mathrm{cryst}} = = \frac{\Sigma_{hkl} \,||F_{\mathrm{obs}}| - |F_{\mathrm{calc}}||}{\Sigma_{hkl} \,|F_{\mathrm{obs}}|}$

[c] R_{free} is R_{cryst} with a test set of 5% of the reflections excluded from refinement.

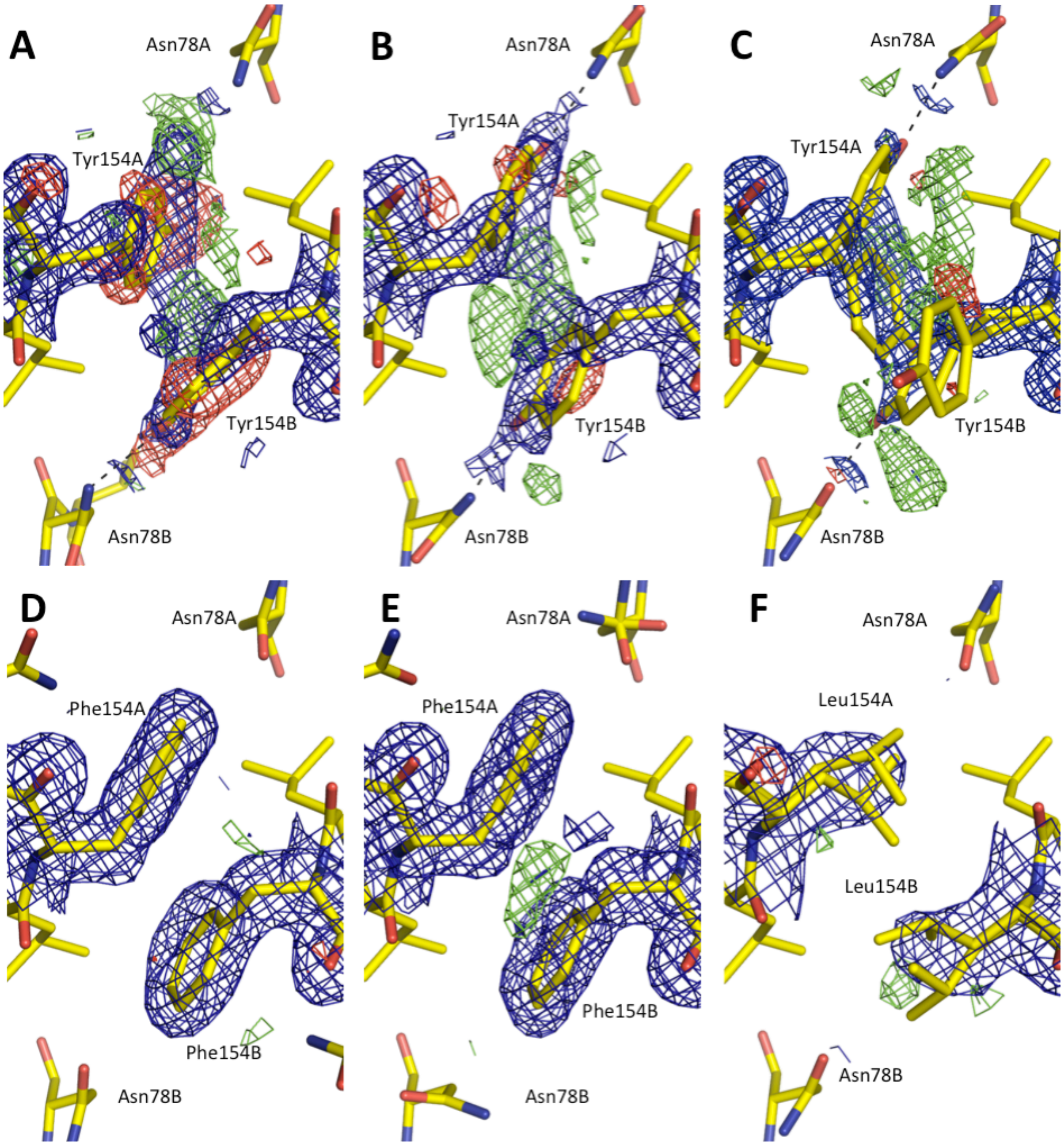

Figure 3.12 Electron density at residue 154 in multiple AaPurE1 forms. Each panel represents the pseudo two-fold NCS symmetry axis at the dimer interface; the axis runs through each figure from the bottom right corner to the upper left corner between residues 154A and 154B. Electron density maps (shown for residues 78 and 154) for $2F_o$-F_c (blue mesh) are contoured at 1.0 σ, F_o-F_c positive differences (green mesh) are contoured at +3.0 σ, F_o-F_c negative differences (red mesh) are contoured at -3.0 σ, and all maps have a carve radius of 2.0 Å. (A) AaPurE1 (PDB code 1u11). (B) AaPurE1-H59N (PDB code 2fw9). (C) AaPurE1$_{fwf}$ (PDB code 4ycb). (D) AaPurE1$_{fwf}$-Y154F (PDB code 4ycd). (E) AaPurE1-Y154F (PDB code 4ycj). (F) AaPurE1-Y154L (PDB code 4ycc).

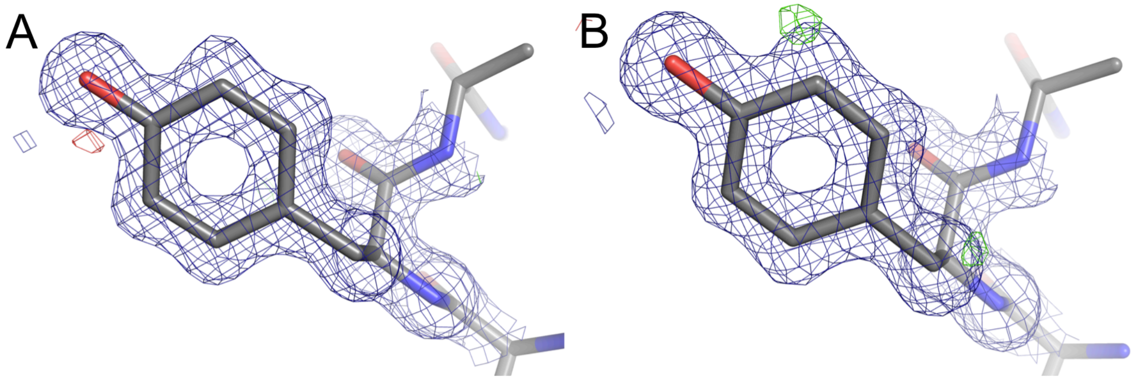

Figure 3.13 Electron density at Tyr68 in both AaPurE1$_{fwf}$ subunits. (PDB code 4ycb) Electron density maps for 2F$_o$-F$_c$ (blue mesh) are contoured at 1.0 σ, F$_o$-F$_c$ positive differences (green mesh) are contoured at +3.0 σ, F$_o$-F$_c$ negative differences (red mesh) are contoured at -3.0 σ, and all maps have a carve radius of 2.0 Å around residue 68. (A) Tyr68 from subunit A. (B) Tyr68 from subunit B.

Table 3.10 R-Factors and RSCC$_{154}$ values for AaPurE1 structures.

PDB entry	AaPurE1	$d_{\min}$ (Å)	R_{work} (%)	R_{free} (%)	RSCC$_{154}$^{b}	Ref.
1u11^{a}	WT	1.55	16.2	17.7	0.785/0.785	[27]
2fw1^{a}	WT	2.00	17.3	18.1	0.869/0.875	[26]
2fw6^{a}	H59N	1.85	16.3	17.9	0.856/0.813	[26]
2fw7^{a}	H59N	1.75	16.1	17.5	0.856/0.860	[26]
2fw8^{a}	H89G	1.75	16.7	18.8	0.904/0.820	[26]
2fw9^{a}	H59F	1.75	16.4	18.6	0.890/0.856	[26]
2fwa^{a}	H89N	1.90	17.4	19.3	0.799/0.821	[26]
2fwb^{a}	H89F	2.00	17.3	19.0	0.885/0.866	[26]
2fwi^{a}	H59D	1.94	16.6	18.1	0.872/0.843	[26]
2fwj^{a}	WT	1.95	16.1	18.7	0.815/0.869	[26]
2fwp^{a}	H59N	1.85	17.3	20.1	0.827/0.858	[26]
4ycb	fwf	1.35	16.2	17.3	0.877/0.816	This study
4ycd	fwf-Y154F	1.65	14.8	18.2	0.981/0.976	This study
4ycc	fwf-Y154F	2.25	15.6	17.4	0.948/0.954	This study
4ycj	Y154F	1.84	15.7	16.9	0.979/0.969	This study

[a] Previously deposited-RSCC values are computed after the Asn78 flip was completed.

[b] Values are for subunit A and B, respectively.

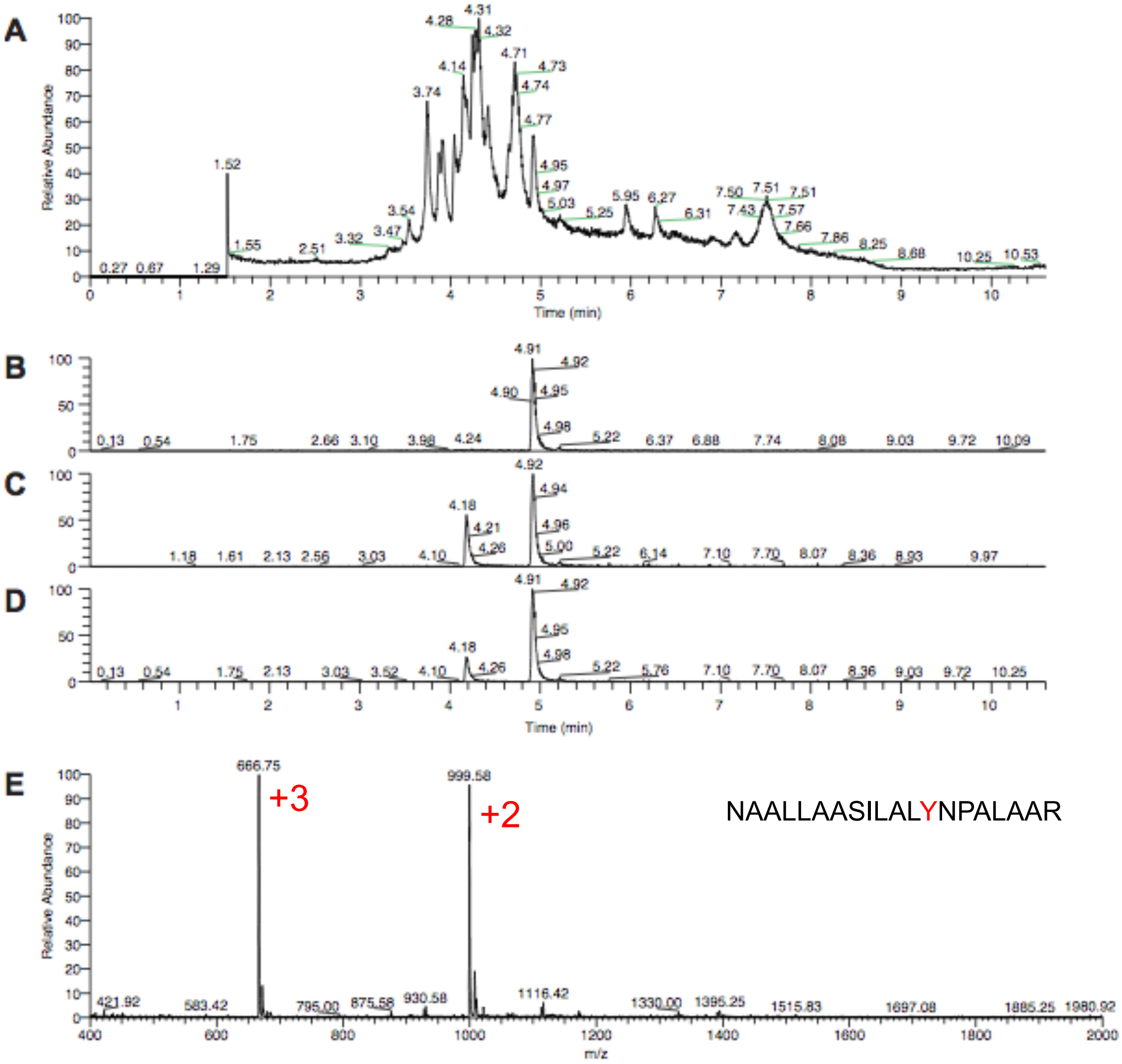

Figure 3.14 LC-MS analysis of AaPurE1 peptide from solution. (A) Total ion count chromatogram (TIC) of peptide injected into the MS. (B-D) Elution profiles from LC that contain masses corresponding to the peptide of interest (666 and 999 m/z). (E) Mass spectrum from elutions (4.88-4.99 min) that contains the expected masses for the +2 (999 Da) and +3 (666 Da) peptide of interest.

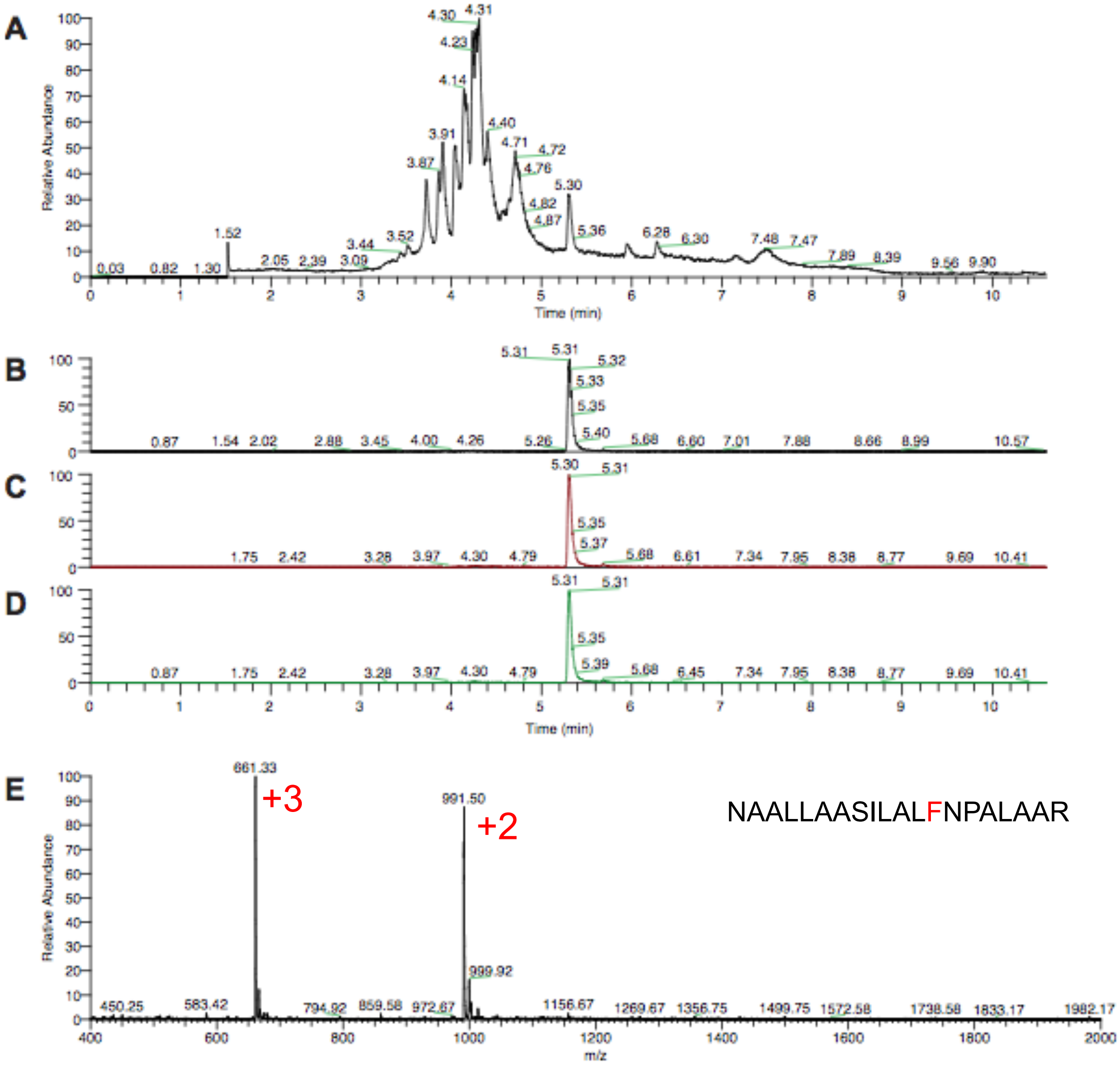

Figure 3.15 LC-MS analysis of AaPurE1-Y154F peptide from solution. (A) Total ion count chromatogram (TIC) of peptide injected into the MS. (B-D) Elution profiles from LC that contain masses corresponding to the peptide of interest (661 and 991 m/z). (E) Mass spectrum from elutions (5.28-5.36 min) that contains the expected masses for the +2 (991 Da) and +3 (661 Da) peptide of interest.

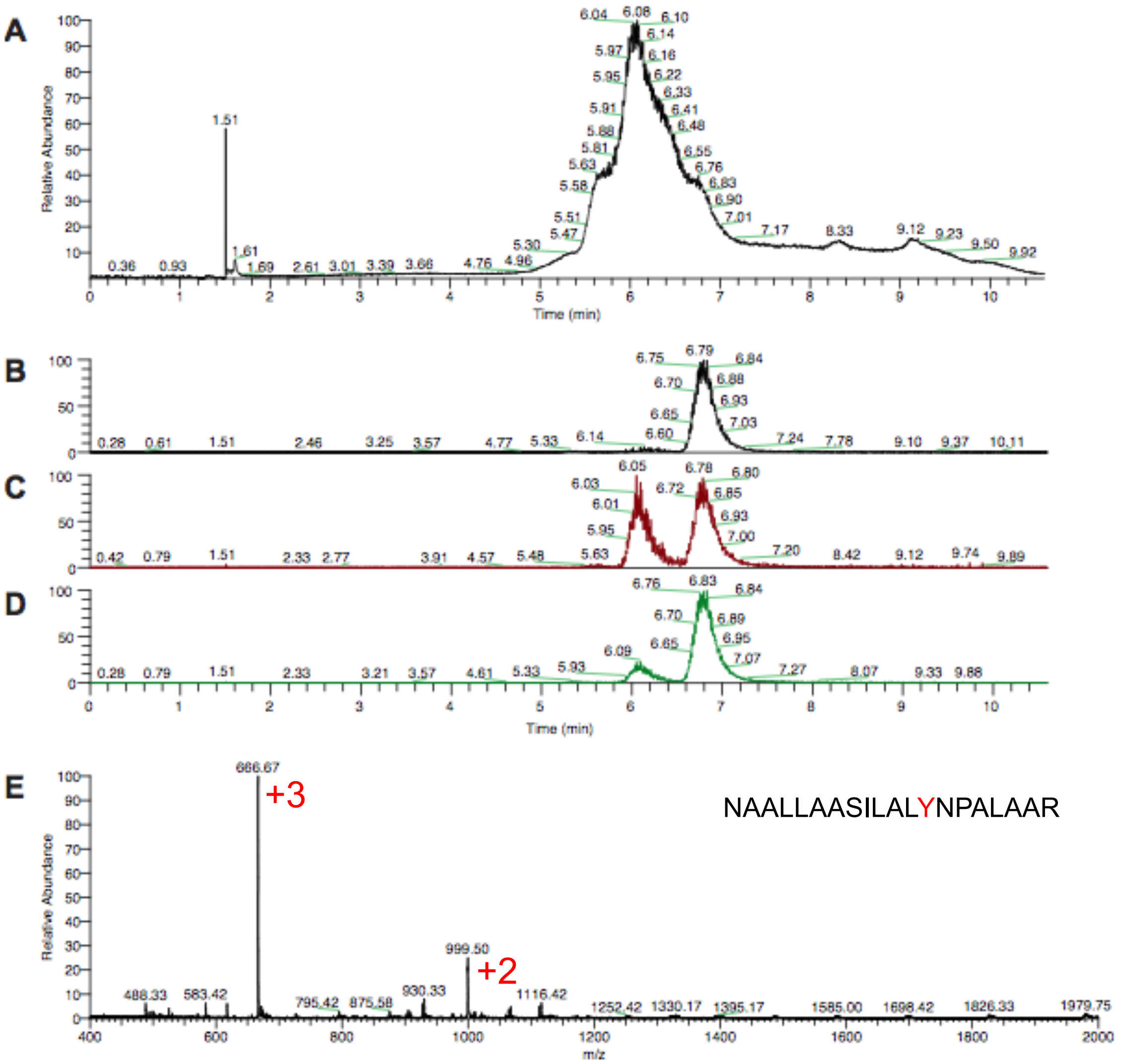

Figure 3.16 LC-MS analysis of AaPurE1$_{fwf}$ peptide from solution. (A) Total ion count chromatogram (TIC) of peptide injected into the MS. (B-D) Elution profiles from LC that contain masses corresponding to the peptide of interest (666 and 999 m/z). (E) Mass spectrum from elutions (6.73-6.93 min) that contains the expected masses for the +2 (999 Da) and +3 (666 Da) peptide of interest.

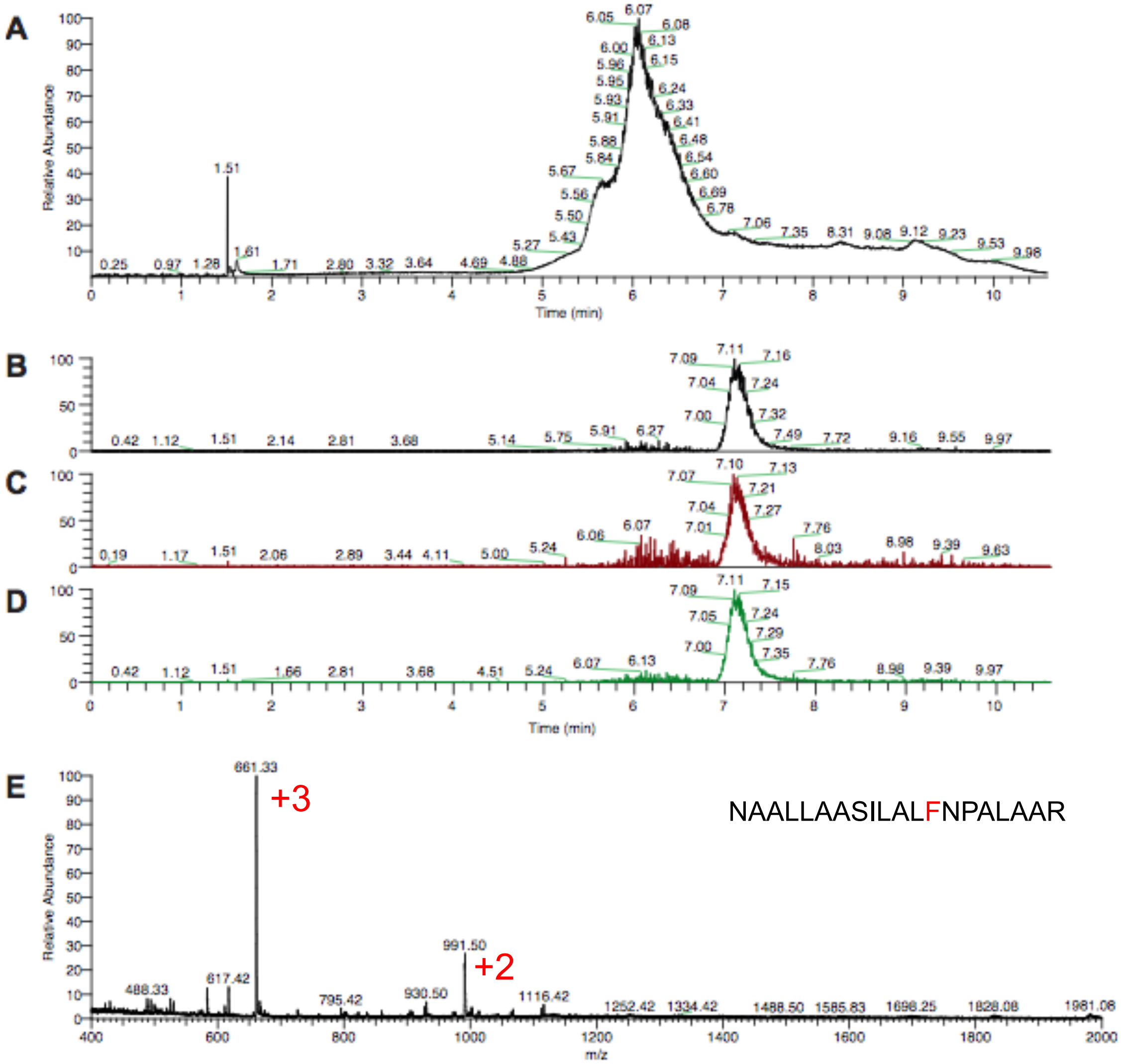

Figure 3.17 LC-MS analysis of AaPurE1$_{fwf}$-Y154F peptide from solution. (A) Total ion count chromatogram (TIC) of peptide injected into the MS. (B-D) Elution profiles from LC that contain masses corresponding to the peptide of interest (661 and 991 m/z). (E) Mass spectrum from elutions (7.04-7.29 min) that contains the expected masses for the +2 (991 Da) and +3 (661 Da) peptide of interest.

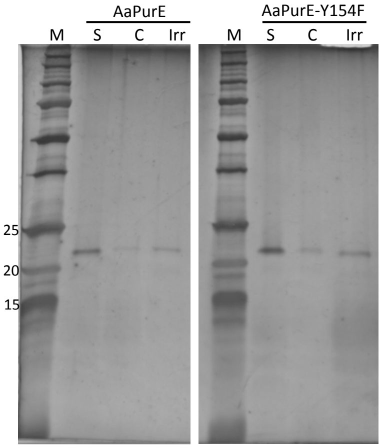

Figure 3.18 SDS-PAGE analysis of irradiated and dissolved AaPurE1 crystals. A 12% polyacrylamide gel was loaded with 25 ng protein per lane and visualized with silver staining. AaPurE1 is labeled on the left gel and AaPurE1-Y154F is on the right gel. Key to symbols: M, Sigma wide molecular weight marker; S, protein from solution; C, dissolved crystals; and IR, irradiated and dissolved crystals. Molecular weights (kDa) are denoted along the left side of the gel.

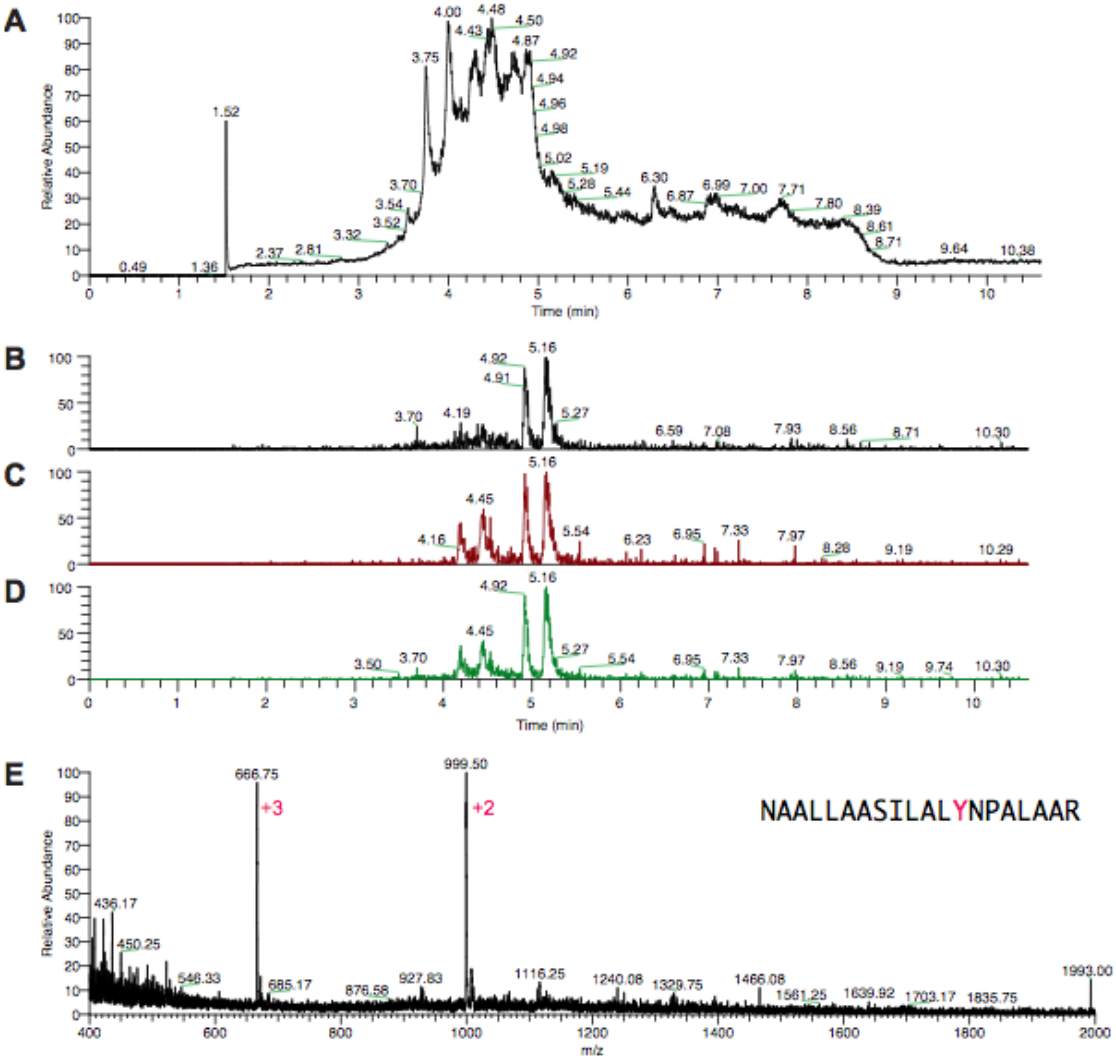

Figure 3.19 LC-MS analysis of dissolved AaPurE1 crystals. (A) Total ion count chromatogram (TIC) of peptide injected into the MS. (B-D) Elution profiles from LC that contain masses corresponding to the peptide of interest (666 and 999 m/z). (E) Mass spectrum from elutions (5.15-5.23 min) that contains the expected masses for the +2 (999 Da) and +3 (666 Da) peptide of interest.

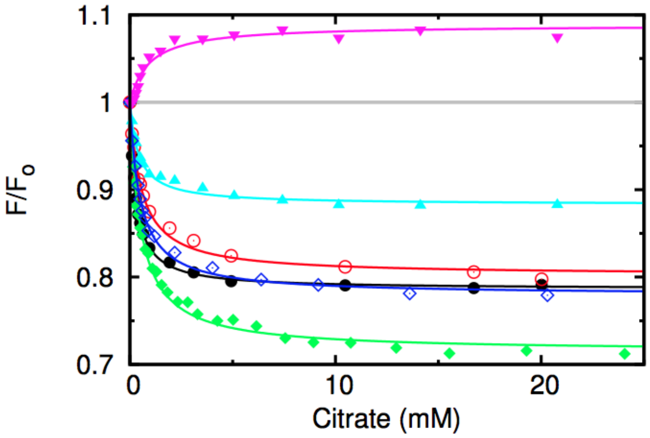

Figure 3.20 Fluorescence titrations of wild-type and inactive AaPurE1 forms with citrate. Observed fluorescence emission intensity at 320 nm, as a function of AIR is represented by the symbols: AaPurE1 (black filled circles), AaPurE1-H59N (red open circles), AaPurE1$_{wyf}$-H59N (cyan filled triangles), AaPurE1$_{fwf}$-H59N (green filled diamonds), AaPurE1$_{fwf}$-H59N, Y154F (blue open diamonds), and AaPurE1$_{fyw}$-H59N (purple filled inverted triangles). Solid lines are the observed data fit using gnu plot with equation 3.2

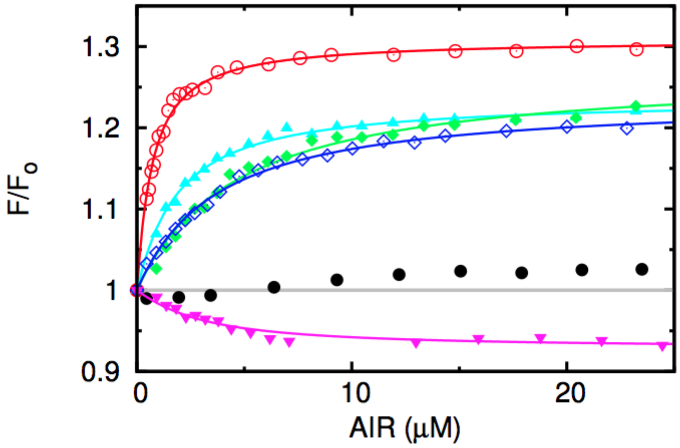

Figure 3.21 Fluorescence titrations of wild-type and inactive AaPurE1 forms with AIR. Observed fluorescence emission intensity at 320 nm, as a function of AIR is represented by the symbols: AaPurE1 (black filled circles), AaPurE1-H59N (red open circles), AaPurE1$_{wyf}$-H59N (cyan filled triangles), AaPurE1$_{fwf}$-H59N (green filled diamonds), AaPurE1$_{fwf}$-H59N, Y154F (blue open diamonds), and AaPurE1$_{fyw}$-H59N (purple filled inverted triangles). Solid lines are the observed data fit using gnu plot with equation 3.3, with the exception of AaPurE1.

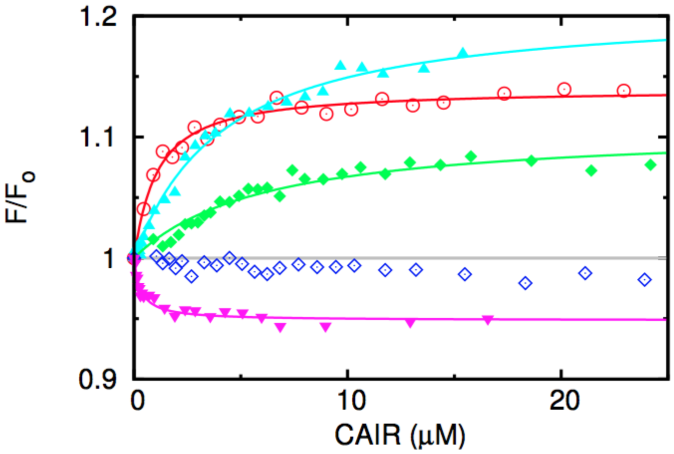

Figure 3.22 Fluorescence titrations of inactive AaPurE1 forms with CAIR. Observed fluorescence emission intensity at 320 nm, as a function of CAIR is represented by the symbols: AaPurE1-H59N (red open circles), AaPurE1$_{wyf}$-H59N (cyan filled triangles), AaPurE1$_{fwf}$-H59N (green filled diamonds), AaPurE1$_{fwf}$-H59N, Y154F (blue open diamonds), and AaPurE1$_{fyw}$-H59N (purple filled inverted triangles). Solid lines are the observed data fit with equation 3.3.

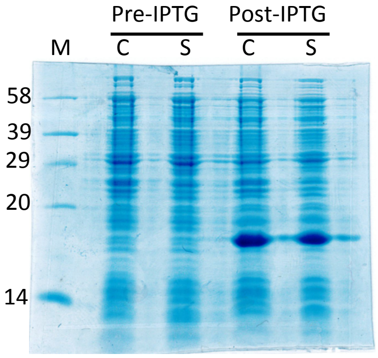

Figure 3.23 SDS-PAGE analysis of AaPurE1$_{fwf}$-5FW and pCDFDuet expression in DL41. A 12% polyacrylamide gel was loaded with 5 μg protein per lane: M, Sigma biotinylated marker; C, crude lysate; and S, soluble lysate. The Pre-IPTG samples were taken before washing steps and the post-IPTG samples were taken after final harvest of cells. Molecular weights (kDa) are denoted along the left side of the gel.

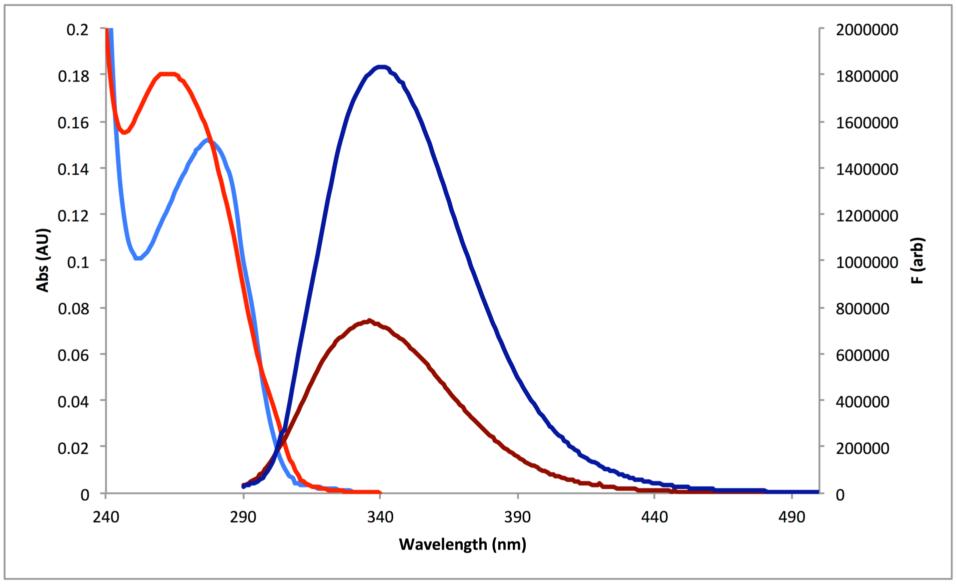

Figure 3.24 Absorbance spectra and fluorescence emission spectra for AaPurE1$_{\text{fwf}}$ and AaPurE1$_{\text{fwf}}$-5FW. AaPurE1$_{\text{fwf}}$ absorbance spectra are shown in red and fluorescence emission spectra (Excitation at 295 nm) are shown in dark red. AaPurE1$_{\text{fwf}}$ -5FW absorbance spectra are shown in light blue and fluorescence emission spectra are shown in dark blue. The λ_{max} for absorbance and fluorescence spectra of AaPurE1$_{\text{fwf}}$ and AaPurE1$_{\text{fwf}}$-5FW are Abs = 277 nm, F = 366 nm and Abs = 264 nm, F = 341 nm; respectively.

Table 3.11 Quantum yields for AaPurE1$_{\text{fwf}}$ and AaPurE1$_{\text{fwf}}$-5FW.

Sample	Unliganded Quantum yield	Quantum yield with AIR	Quantum yield with citrate	Conc. Protein (μg mL^{-1})
NATA	nd[a]	nd	nd	9.0
L-Trp	0.14[b]	0.14	0.14	8.4
AaPurE1$_{\text{fwf}}$	0.039 ± 0.004	0.042	0.039	168
AaPurE1$_{\text{fwf}}$ -5FW	0.088 ± 0.002	0.096	0.083	123

[a] not determined.

[b] value from literature[36]

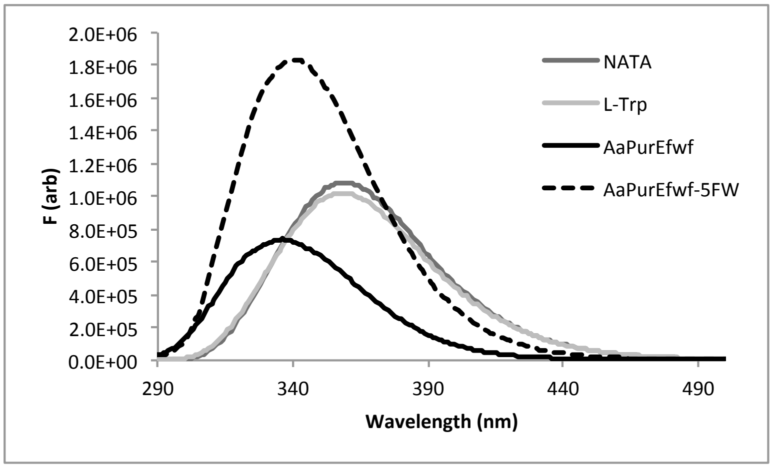

Figure 3.25 Fluorescence emission spectra used to determine quantum yields for AaPurE1$_{fwf}$ and AaPurE1$_{fwf}$-5FW. Emission spectra of NATA, L-Trp, AaPurE1$_{fwf}$ and AaPurE1$_{fwf}$-5FW with excitation at 295 nm. All solutions had an absorbance of 0.06 AU and quantum yield values are listed in Table 2.5.

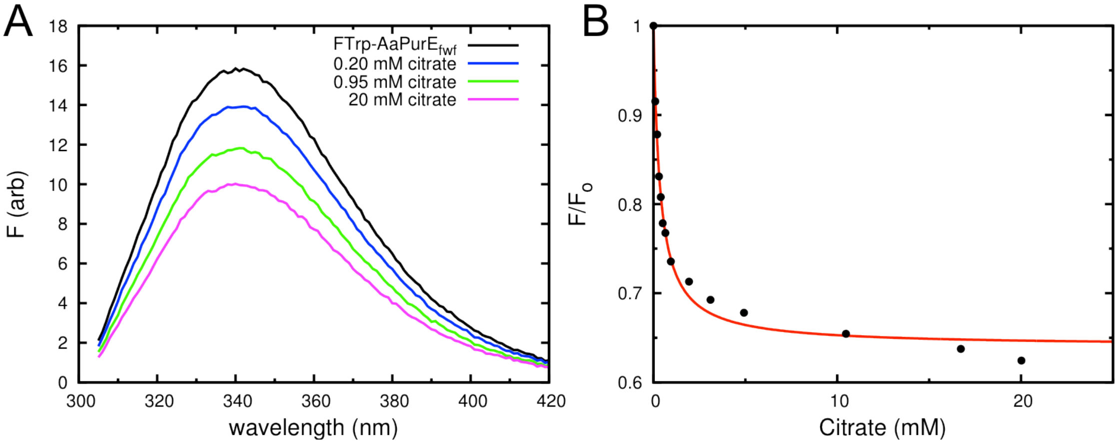

Figure 3.26 Fluorescence titrations with AaPurE1$_{fwf}$-5FW with citrate. Excitation wavelength was 295 nm. Citrate titrations were performed with 0.2 μM [subunit] in 50 mM acetate, 100 mM KCl, pH 4.6 at 25 °C and data were fit to equation 3.2. K_d values are given in Table 3.7. (A) Fluorescence emission spectra with increasing amounts of citrate. (B) Recorded emission at 320 nm upon citrate addition was plotted as a function of [citrate] and data were fit using equation 3.5 using gnu plot. The K_d values are listed in Table 3.7.

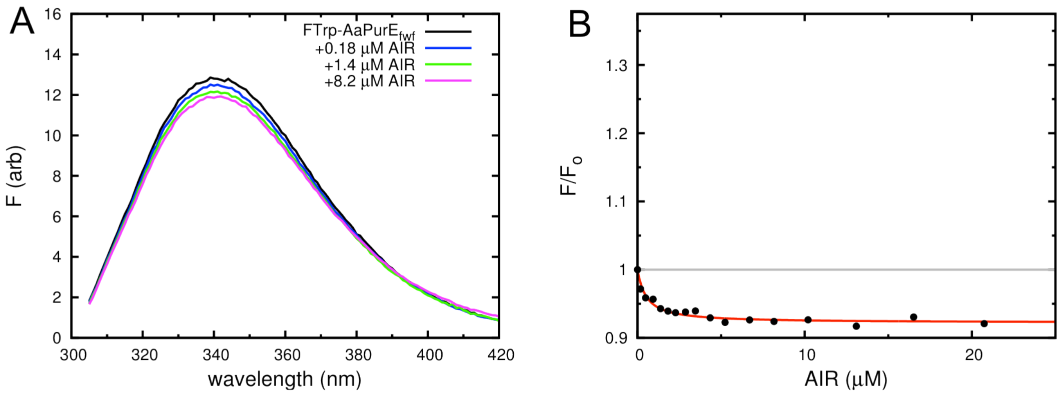

Figure 3.27 AIR Fluorescence titrations with AaPurE1$_{\mathrm{fwf}}$-5FW. Excitation wavelength was 295 nm. AIR titrations were performed with 0.18 µM [subunit] in 50 mM Tris-HCl, pH 8 at 30 °C and data were fit to equation 3.2. K_d values are given in Table 3.7. (A) Fluorescence emission spectra with increasing amounts of AIR. (B) Recorded emission at 320 nm upon AIR addition was plotted as a function of [AIR] and data were fit using equation 3.6 using gnu plot. The K_d values are listed in Table 3.7.

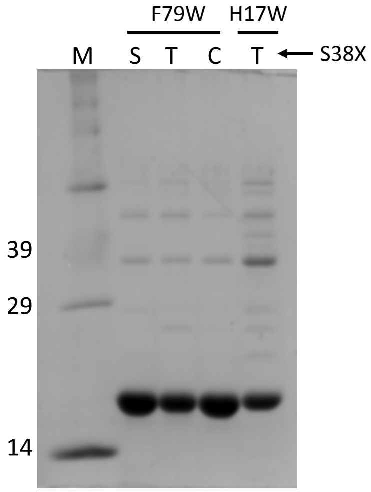

Figure 3.28 SDS-PAGE analysis of isolated TdPurE2 Trp introduction forms. A 12% polyacrylamide gel with 5 ug protein loaded per lane: 12% polyacrylamide gel was loaded with 5 ug protein per lane: M, Sigma biotinylated marker. Each mutation in Ser 38 is indicated by the one letter code directly above each lane. Each mutation to introduce a Trp into TdPurE2 is indicated above the solid line. Molecular weights (kDa) are denoted along the left side of the gel.

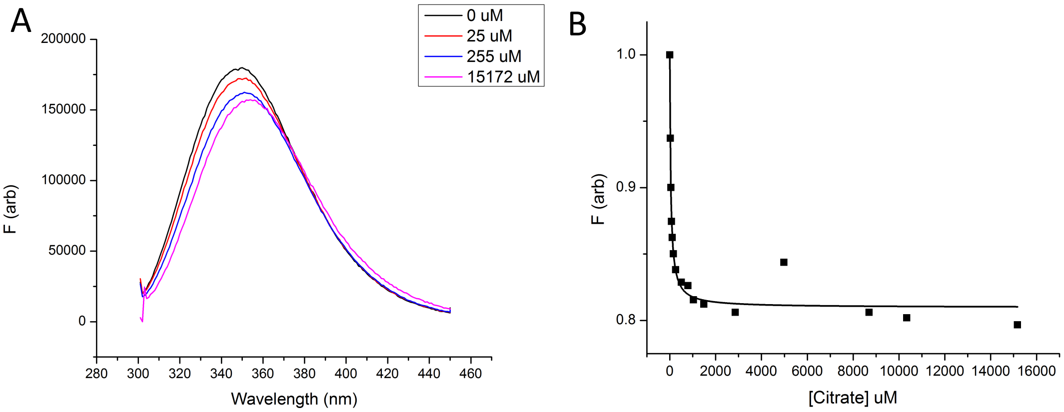

Figure 3.29 Citrate fluorescence titrations of TdPurE2-F79W. Excitation wavelength was 295. Citrate titrations were performed with 0.4 µM [subunit] in 50 mM potassium acetate, 100 mM KCl, pH 4.6 at 25 °C and data were fit to equation 3.5. K_d values are given in Table 3.7. (A) Fluorescence emission spectra of TdPurE2-F79W recorded in 50 mM potassium acetate, 100 mM KCl, pH 4.6 at 25 °C with an excitation of 295 nm. (B) Fluorescence emission intensity at 320 nm was plotted as a function of [citrate] and data were fit using equation 3.5 using Origin software. The K_d values are listed in Table 3.7.

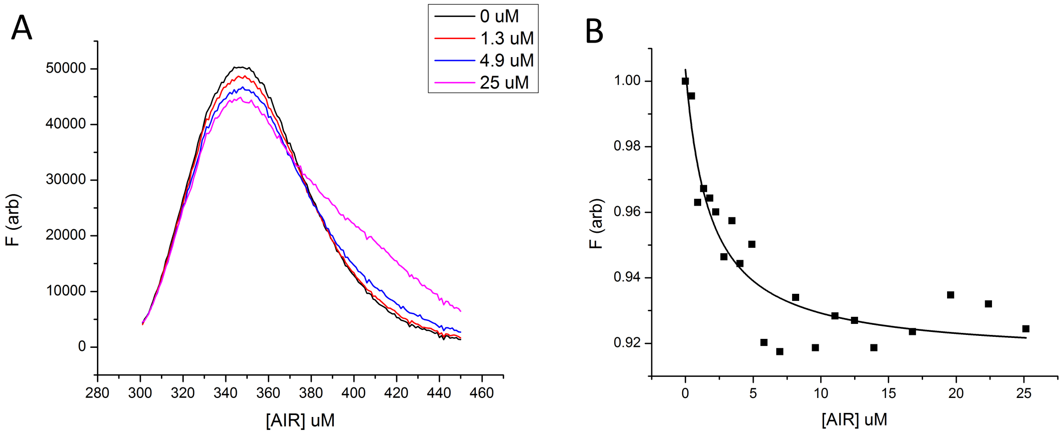

Figure 3.30 AIR fluorescence titrations of TdPurE2-F79W. Excitation wavelength was 295 AIR titrations were performed with 0.56 µM [subunit] in 50 mM Tris-HCl, pH 8 at 30 °C. (A) Fluorescence emission spectra with increasing amounts of AIR. (B) Recorded emission at 320 nm upon AIR addition. Titrations were performed with [subunit] of 0.4 µM. Fluorescence emission intensity at 320 nm was plotted as a function of [AIR] and data were fit using equation 3.5 using Origin software. The K_d values are listed in Table 3.7.

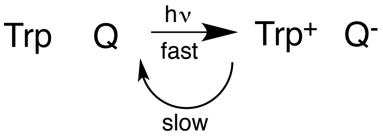

Figure 3.31 Scheme for excited state electron transfer from the Trp indole to a quenching moiety (Q). Q could be the ligand or some other intramolecular quenching group in the protein (e.g. a backbone amide).

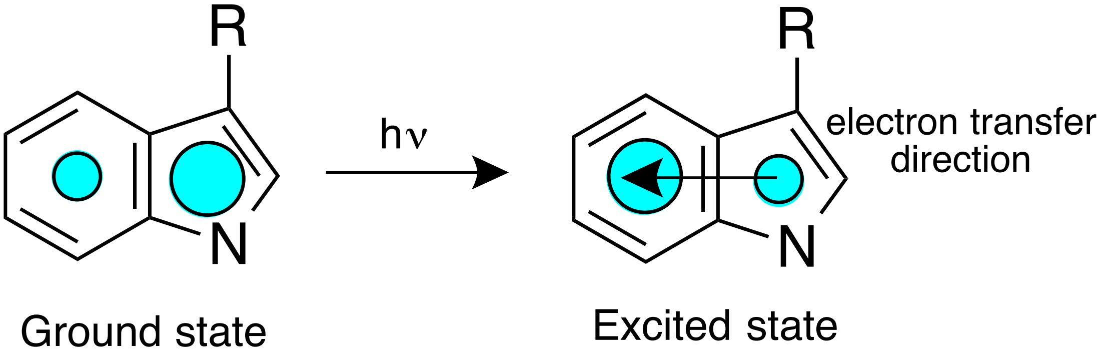

Figure 3.32 Electron density of the Trp indole in the excited state. The teal circles represent the relative electron density in Trp at the ground state or excited state. When excited, the electron density shifts from the pyrrole ring to the benzene ring and creates a temporary dipole.

CHAPTER 4 ROLE OF THE CONSERVED ACTIVE SITE SERINE RESIDUE IN PURE1 AND PURE2

4.1 Introduction

PurE1 and PurE2 have similar structures and similar active sites. Crystal structures of PurE1 and PurE2 with AIR bound (PDB codes 2fwj and 3rgg)[1,2] reveal that the universally conserved Ser is the sole polar contact between the substrate aminoimidazole ring and any PurE side chain. Due to its strict conservation in both PurE classes, Ser was thought to have a similar role in both enzymes.

PurE1 and PurE2 Carbon-Carbon Bond-Forming Chemistry is Conserved. PurE1 and PurE2 appear to form a new C−C bond, the conversion of PurE•AIR•CO2 to PurE•CAIR, the same way (Figure 4.1).[3] An absolute difference is the source of CO_2: PurE1 acquires it by decarboxylation of bound NCAIR (or CAIR), while PurE2 binds it directly.

PurE1 converts either NCAIR or CAIR to a PurE•AIR•CO_2 ternary complex from which CO_2 does not escape (brackets in Figure 4.1). Confining CO_2 in PurE1 preserves the investment made by PurK, which uses ATP to activate bicarbonate (Chapter 1). A strong electrostatic interaction between the polarized C4 of AIR and CO_2 may help PurE1 to achieve quantitative retention of the transiently formed CO_2 within the active site.

Hydrogen bonds involving AIR N3 with the conserved 40s loop Ser and the 70s loop backbone carbonyls with the exocyclic amine N6 may further polarize AIR and promote the reaction between AIR C4 and CO_2.

The 40s Loop Ser May Have Different Roles in Each PurE Class. The PurE1 and PurE2 active sites differ most in two active site loops (Figure 4.2).[4,5] The 40s loop contains a class-specific motif, SAH[R/K] in PurE1 and PurE2, respectively. The conserved active site His serves as the general acid/general base catalyst and is essential for activity.[1,2,6] The 40s loop Ser is proposed to serve as a hydrogen bond donor to AIR N3 and is the sole polar contact between the substrate aminoimidazole ring and any side chain of PurE1 and PurE2 (Figure 4.2).[1,2]

Decarboxylation of CAIR gives a ternary PurE•AIR•CO_2 complex, which only dissociates from PurE2. In contrast, the PurE1 reaction continues with an aminoimidazole ring flip and NCAIR formation. Ser may provide a hydrogen bond to AIR N3 and, in PurE1 only; function as a pivot-point for the aminoimidazole ring to rotate and position either AIR C4 or N6 of the exocyclic amine for attack on the bound CO_2 to form either NCAIR or CAIR, respectively (Figure 4.1).[6]

The pH rate profiles for PurE1 are bell-shaped and the basic arm (pK_2) is unambiguously assigned to the active site His.[1,6] The acidic pK_1 likely corresponds to the protonation of CAIR N3, which is mutually exclusive with protonation at C4 (Figure 4.2). Ser may function as a hydrogen bond donor to (C)AIR N3, favoring protonation by the conserved His at C4 instead of N3. This would be an example of “negative catalysis” in that the hydrogen bonding interaction prevents an *unproductive* event but is not itself required. This contrasts with a conclusion based on non-enzymatic model studies, where the N3 protonation occurs first and the proton is transferred to the C4 position for decarboxylation to occur.[7,8] While, N3 protonation is inhibitory for PurE1, it may allow PurE2 to do different chemistry at low pH.

In PurE2, an *increase* in velocity at acidic pH (pK_1) has been proposed to correspond to a change in polarity in the hydrogen bond formed between Ser and the aminoimidazole N3.[2] At low pH, Ser could *accept* a hydrogen bond from the *protonated* N3. Furthermore, the order of CAIR protonation and decarboxylation events may be reversed by this interaction, as C4 protonation would pose serious electrostatic barriers (two positive charges on the aminoimidazole ring). Instead, decarboxylation may lead to formation of a nitrogen ylide of AIR (yAIR), which is a proposed intermediate for decarboxylation of CAIR ribonucleoside.[8] Similar intermediates have been proposed for both 3-aminopicolinic acid decarboxylation and orotidine 5'-monophosphate decarboxylase.[9,10]

Characteristics of PurE1 and PurE2 Examined in this Chapter. This chapter details the kinetic and structural analysis of Ser mutants from *Acetobacter aceti* (AaPurE1) and *Treponema denticola* (TdPurE2). Several functional mutants have pH-dependent activity that indicates a class-divergent role for this residue. The requirement a hydrogen bond donor at the Ser position is more important for PurE2 function. Our working hypothesis is that the hydrogen bond provided by Ser is important to ensure efficient C4 protonation and without it decarboxylation may occur through a different mechanism beginning with N3 protonation.

4.2 Materials and Methods

Materials. Chemicals were obtained from Sigma or Fisher in the highest purity available unless otherwise noted. CAIR was prepared from 5-aminoimidazole-4-carboxamide ribonucleotide (Toronto Research Chemicals, catalogue number: A611705) as described previously.[11] AIR was generated enzymatically from CAIR using *Treponema denticola* PurE2 (TdPurE2) and quantitated by Bratton-Marshall assay as described previously.[2] Oligodeoxynucleotides (ODNs) were obtained from Integrated DNA Technologies and used without further purification. Restriction endonucleases, Vent polymerase, Q5 DNA polymerase, CIP, T4 PNK, and T4 DNA ligase were obtained from New England Biolabs. Mutagenesis was accomplished using Quikchange Mutagenesis using kits (Agilent). Phenyl sepharose CL-6B was obtained from Sigma. Hydroxyapatite (Bio-Gel ® HT) and Bradford reagent were obtained from Bio-Rad. PD-10 desalting columns were obtained from GE Health Care. Protein concentrations were determined by the method of Bradford with bovine serum albumin as the standard.[12] Solution makeup was determined on an AKTA FLPC system (Amersham). Small-scale centrifugation steps were performed using an Eppendorf 5424 centrifuge. All other centrifugation steps were performed using a Beckman Avanti J-E centrifuge with a JLA-10.5 or JA-20 rotor. Cell disruption was performed by sonication using a Fisher Scientific Dismembrator 550 at 25% output for 3 cycles (1 min each with 1 min cooling periods in-between) at 4 °C. Spectroscopic measurements were recorded on a Varian CARY-100 UV/Vis spectrophotometer thermostated by a Cary Dual Peltier Accessory temperature controller. Steady state fluorescence measurements were recorded on a Horiba Fluoromax-3 fluorometer thermostated with a Peltier Accessory and a Wavelength Electronics temperature controller. . Data were analyzed using Origin (OriginLab, Northampton, MA) or using gnuplot 4.4 by T. J. Kappock. Plasmid DNA was sequenced by the staff of the Purdue University Genomics Core Facility. Full-length protein masses were determined by Matrix-assisted laser desorption/ionization mass spectrometry (MALDI-MS) on a Voyager-DE PRO mass spectrometer (Applied Biosystems, Framingham, MA) by Connie Bonham.

Standard Conditions for Vent PCR. Standard PCRs (50 µL final volume) contained Vent DNA polymerase (1 unit), two ODNs (50 nmol each, Table 4.2), template DNA (14 ng), dNTPs (25 nmol each), $MgCl_2$ (2 mM), and 1x thermopol buffer (20 mM Tris-HCl, 10 mM $(NH_4)_2SO_4$, 10 mM KCl, 0.1% Trition® X-100, pH 8.8). PCR products were amplified with standard conditions: annealing temperature of 52 °C with a 30 s hot start followed by melting, annealing, and extension times of 30 s, 60 s, and 30s for 25 cycles with a final extension time of 5 min.

Generation of Protein Production Strain CC1215. Strain CC1215 was created using a previously published protocol.[13] P1 lysates [W3110] were a gift of Dr. Ronald Somerville. The Keio strain JW0512 served as the donor and BL21(DE3) served as the recipient strain.

P1 Lysate Preparation: JW0512 cells were grown overnight on LB-Kan plates and a single colony was used to inoculate a 5 mL overnight LB-Kan culture. A portion of the saturated overnight culture (50 μL) was mixed with 2.5 mL of molten top agar and plated onto LB soft agar plates supplemented with $CaCl_2$ (2.5 mM). P1 [W3110] lysate (50 μL) was spotted onto the solidified top agar and grown overnight. Lytic plaques were excised from the top agar with a nickel spatula and transferred to 0.5 mL of LB in a sterile 15 mL falcon tube. Tubes were then vortexed and incubated at room temperature for 30 min. A portion of saturated overnight JW0512 culture (100 μL) was added to each tube and incubated at room temperature for an additional 30 min. A control incubation was carried out lacking any P1 lysate. Molten top agar (2.5 mL) was added to each tube, mixed gently, and then poured on top of LB soft agar plates supplemented with $CaCl_2$ (2.5 mM). Plates were grown at 37 °C for 8 h until they had a "lacey" appearance. After 8 h, the plates were flooded with 3-5 mL of LB and placed at 4 °C overnight. Lysate was pipetted off, transferred into sterile glass screw-cap vials, and chloroform (~100 μL) was added. The tubes were shaken forcefully and then centrifuged (2000 g, 10 min) at 4 °C to pellet bacteria. Lysates (P1 [JW0512]) were then decanted into sterile glass screw-cap vials for storage at 4 °C. Portions of the lysates were streaked onto LB plates to ensure the lysate had no bacterial contamination.

P1 Transduction: BL21(DE3) cells were grown overnight on LB plates and a single colony chosen to inoculate a 5 mL overnight LB culture. A 10 mL LB culture was inoculated at 1:100 and grown at 37 °C, shaking for 2-3 h to reach log phase (OD_{600}=0.3-0.7). The cells were centrifuged (5000 g, 15 min) at 4 °C, the resulting supernatant discarded, and cells resuspended in 1 mL of LB. Donor strain lysate, P1 [JW0512], was mixed with an equal volume of sterile 0.85% (w/v) saline (1 mL) in a 60 x15 mm petri dish. The dish was placed ~30 cm under a UV-lamp (254 nm), with the lid removed, and incubated for 5 min. Transductions were carried out in duplicates: 1 mL irradiated lysate, 0.05 mL $CaCl_2$ (0.5 M stock), and 0.1 mL of concentrated log phase BL21(DE3) cells. Control transductions contained 0.1 mL of LB in place of irradiated lysate. The transductions were incubated at 37 °C for 20 min and then a portion (0.1 mL) was plated undiluted, 1:3, and 1:15 on LB Kan plates. The resulting colonies were streaked onto M9 minimal media plates lacking exogenous purines and grown overnight at 37 °C to test for purine autotrophy. Kan cassette insertion from the donor strain JW0512 into BL21(DE3) was confirmed by PCR with ODNs 1161 and 1164.

Construction of AaPurE1 Plasmids for Protein Expression. Plasmid pJK175, which encodes the wild-type AaPurE1, was used as a template for the generation of serine mutants.[1] Mutants were generated using Quikchange II mutagenesis kits (with standard PCR conditions outlined in in Chapter 3) with plasmid pJK175 (25 ng) as template, and the appropriate ODNs (Table 4.2) to create plasmids pJK582 (AaPurE1-S57A), pJK583 (AaPurE1-S57C), pJK584 (AaPurE1-S57T), pJK608 (AaPurE1-S57D), pJK677 (AaPurE1-S57V), and pJK686 (AaPurE1-S57N).

Construction of TdPurE2 Plasmids for Protein Expression. Plasmid pJK376, which encodes the wild-type TdPurE2, was used as a template for the generation of serine mutants.[2] Mutants were generated using Quikchange II mutagenesis kits (with standard PCR conditions outlined in in Chapter 3) with plasmid pJK376 (25 ng) as template, and the appropriate ODNs (Table 4.2) to create plasmids pJK607 (TdPurE2-S38C), pJK617 (TdPurE2-S38A), pJK684 (TdPurE2-S38V), and pJK685 (TdPurE2-S38N).

Construction of TdPurE2–S38T Construct Plasmid pJK643. The general cloning strategy is illustrated in Chapter 3 (Figure 3.4). A 0.21 kb primary PCR product containing *purE2* was amplified using standard Vent PCR conditions from template pJK376 (14 ng), using ODNs 2124 and 2316. The crude product was digested with *DpnI* and purified using a Qiagen PCR purification kit. A 0.55 kb product containing *purE2* was amplified using standard Vent PCR conditions from template pJK376 (14 ng), using ODNs 2125 and 2317. The crude product was digested with *DpnI* and purified using a Qiagen PCR purification kit. Cross-over PCR product was obtained using standard Vent PCR conditions, with a single exception: the annealing time was increased to 1 min, from a mixture containing primary PCR products (25 ng each) and ODNs 2124 and 2125. The 0.79 kb cross-over was digested with *NdeI* and *XhoI*, and ligated into the same sites of the destination vector pET23a to yield TdPurE2-S38T expression plasmid pJK643.

Construction of TdPurE2–S38D Construct Plasmid pJK644. A 0.21 kb primary PCR product containing *purE2* was amplified using standard Vent PCR conditions from template pJK376 (14 ng), using ODNs 2124 and 2320. The crude product was digested with *DpnI* and purified using a Qiagen PCR purification kit. A 0.55 kb product containing *purE2* was amplified using standard Vent PCR conditions from template pJK376 (14 ng), using ODNs 2125 and 2321. The crude product was digested with *DpnI* and purified using a Qiagen PCR purification kit. Cross-over PCR product was obtained using standard Vent PCR conditions, with a single exception: the annealing time was increased to 1 min, from a mixture containing primary PCR products (25 ng each) and ODNs 2124 and 2125. The 0.79 kb cross-over product was digested with *NdeI and XhoI*, and ligated into the same sites of the destination vector pET23a to yield TdPurE2-S38D expression plasmid pJK644.

Construction of TdPurE2–S38T,F79W Construct Plasmid pJK653. A 0.21 kb primary PCR product containing *purE2* was amplified using standard Vent PCR conditions from template pJK648 (14 ng), using ODNs 2124 and 2316. The crude product was digested with *DpnI* and purified using a Qiagen PCR purification kit. A 0.55 kb product containing *purE2* was amplified using standard Vent PCR conditions from template pJK648 (14 ng), using ODNs 2125 and 2317. The crude product was digested with *DpnI* and purified using a Qiagen PCR purification kit. Cross-over PCR product was obtained using standard Vent PCR conditions, with a single exception: the annealing time was increased to 1 min, from a mixture containing primary PCR products (25 ng each) and ODNs 2124 and 2125. The 0.79 kb cross-over product was digested with *NdeI and XhoI*, and ligated into the same sites of the destination vector pET23a to yield TdPurE2-S38T,F79W expression plasmid pJK653.

Construction of TdPurE2–S38C,F79W Construct Plasmid pJK659. A 0.21 kb primary PCR product containing *purE2* was amplified using standard Vent PCR conditions from template pJK648 (14 ng), using ODNs 2124 and 2366. The crude product was digested with *DpnI* and purified using a Qiagen PCR purification kit. A 0.55 kb product containing *purE2* was amplified using standard Vent PCR conditions from template pJK648 (14 ng), using ODNs 2125 and 2367. The crude product was digested with *DpnI* and purified using a Qiagen PCR purification kit. Cross-over PCR product was obtained using standard Vent PCR conditions, with a single exception: the annealing time was increased to 1 min, from a mixture containing primary PCR products (25 ng each) and ODNs 2124 and 2125 The 0.79 kb cross-over product was digested with *NdeI and XhoI*, and ligated into the same sites of the destination vector pET23a to yield TdPurE2-S38C,F79W expression plasmid pJK659.

Construction of T. denticola purE2–H17W,S38T Construct Plasmid pJK692. A 0.651 kb product containing *pur2E* was amplified using standard Q5 PCR conditions from template pJK643 (14 ng), using ODNs 2125 and 2393 with a extension time of 1 min. The PCR product was digested with *NdeI and XhoI*, and ligated into the same sites of the destination vector pJK643 to yield TdPurE2-H17W,S38T expression plasmid pJK692.

Construction of TdPurE2–M15W,S38T Construct Plasmid pJK697. The general cloning strategy is illustrated in Figure 3.6. ODNs 2398 and 2399 (100 nmol each) were phosphorylated, annealed, and ligated at a 1:20 molar ratio of vector: linker into the *NheI* and *BamHI* sites of destination vector pJK692 to yield TdPurE2-M15W,S38T expression plasmid pJK697.

Cell Growth Media. M9 minimal media plates (1 L) contained: 750 mL H_2O autoclaved with 20 g of agar, was mixed with 200 mL sterile 5x M9 salts, 20 mL sterile 20% glucose, 10 mM thiamine, 100 ug mL^{-1} Amp and 70 ug mL^{-1} Kan (30 mL media per plate). A control set of plates was supplemented with hypoxanthine (0.1 mM) as an exogenous source of purines. Autoinduction media (ZYM-5052) used for expression of TdPurEs was prepared as previously published.[14]

Functional Complementation of JW0512. Plasmids containing AaPurE1-S57X and TdPurE2-S38X mutants and pET23a (negative control) were transformed into Keio strain JW0512 (*ΔpurE*) and assessed for their ability to restore purine prototrophy on solid M9 minimal media. Cells were grown for 16 h on LB-Amp/Kan plates and a single colony was used to inoculate a 5 mL LB-Amp/Kan culture that was then grown to log phase (OD_{600}=0.3-0.7) at 37 °C. Cultures were back-diluted to OD_{600}=0.0005 and 10 μL was applied to solid M9 minimal media. A duplicate set of plates was grown in a high CO_2 environment. This high CO_2 environment was achieved by placing the plates along with a lit candle into a desiccator. The desiccator was sealed and the candle was allowed to extinguish. The desiccator was then placed into a large 37 °C incubator.

Mutant AaPurE1 Overexpression and Isolation. AaPurE1-S57X mutants were overexpressed and isolated like wild-type AaPurE1[1] (Chapter 3), with a single exception: the buffers used to isolate AaPurE1-S57C contained 20 mM 2-mercaptoethanol. Fresh column media were used for each mutant to avoid any possibility of cross-contamination. AaPurE1 mutants were concentrated to >3 mg mL^{-1} with an Amicon ultrafiltration device containing a YM30 membrane. The protein solutions were frozen by drop-wise addition to liquid N_2 and stored at -80 °C.

Mutant TdPurE2 Overexpression and Isolation. TdPurE2-S38X,F79W was overexpressed and isolated like wild-type TdPurE2 (Chapter 3),[2] with two exceptions: the lysis buffer contained PMSF (1 mM) and the buffers used to isolate TdPurE2-S38C contained 20 mM 2-mercaptoethanol. Fresh column media were used for each mutant to avoid any possibility cross-contamination. TdPurE2 mutants were concentrated to >3 mg mL^{-1} with an Amicon ultrafiltration device containing a YM30 membrane. The protein solution was frozen by drop-wise addition to liquid N_2 and stored at -80 °C.

Quantitation of Free Sulfhydryl Groups in AaPurE1-S57C. AaPurE1-S57C was incubated with 5,5'-dithiobis-(2-nitrobenzoic acid) (DTNB, Ellman's reagent) to determine the oxidation state of two Cys, one Cys (Cys97) near the surface and the active site Cys mutant. DTNB reactions were performed according to a previous protocol.[15] A 1 cm path length cuvette contained (final volume of 0.5 mL) 100 mM Tris-HCl, pH 8 with DTNB (10 mM) added immediately prior to the start of the experiment. Reactions were initiated by the addition of AaPurE1 or AaPurE1-S57C (10 nmoles, 20 μM) and the absorbance at 412 nm was monitored. The number of unmodified Cys (free thiols) was determined by using the observed absorbance at 412 nm (ε_{412} = 14,150 M^{-1} cm^{-1}). Proteins were quantified by the method of Bradford[12] with bovine serum albumin as the standard.

PurE1 and PurE2-Mediated Decarboxylation Assays. Continuous assays of PurE1 and PurE2-mediated CAIR decarboxylation were performed according to a published method.[1] A final volume of 0.6 mL in a masked, 1 cm pathlength cuvette containing 50 mM Tris-HCl, pH 8 and 100 μM CAIR was incubated at 30 °C for at least 3 min. High concentrations of CAIR (>100 μM) required the use of a 0.5 cm cuvette. Reactions were initiated by addition of either an AaPurE1 or TdPurE2 mutant (12-80 ng, 1.4-8.4 nM [subunits]). The initial velocity of CAIR decarboxylation to AIR ($\Delta\varepsilon_{260}$ =8930 M^{-1} cm^{-1}) was recorded at 260 nm, with a small background decarboxylation rate subtracted. CAIR was quantitated by endpoint assay using the same method, except that 50 μg mL^{-1} TdPurE2 was the enzyme. A unit is defined as the amount of enzyme that forms 1 μmol of product per minute.

PurE1 and PurE2 CAIR Decarboxylation pH-Rate Profiles. The initial rates of reaction for AaPurE1-S57C, AaPurE1-S57A, TdPurE2-S38C and TdPurE2-S38D were determined as above, except that a triple buffer system (100 mM Tris-HCl, 50 mM MES, 50 mM acetic acid) was used across different pHs, and various $\Delta\varepsilon_{260}$ values for CAIR→NCAIR were used.[1] Reactions contained variable amounts of CAIR (2-200 μM) and variable amounts of AaPurE1 and TdPurE2 (12-80 ng, 1.4-8.4 nM [subunits]). Velocity (units mg^{-1}) at each pH was plotted as a function of [CAIR] and the data fit to an alternative Michaelis-Menten equation (equation 4.1) where $j = (V_{max}/K_m)$. Values of k_{cat} and k_{cat}/K_m were plotted as a function of pH and fit to equation 4.2 (or equation 4.3 for AaPurE1-S57C k_{cat}, which accounts for two ionizations). AaPurE1-S57A k_{cat} and k_{cat}/K_m were fit to equation 4.4, which accounts for two ionizations.

$$v = \frac{j}{1+[S\}/K_m} \qquad \text{Equation 4.1}$$

$$\log j = B - a \times pH \qquad \text{Equation 4.2}$$

$$\log V_{max} = \log\left[\frac{\bar{V}_{max}}{1+K_{ES}^{A}[H^{+}]}\right] \qquad \text{Equation 4.3}$$

$$\log y = \log\left[\frac{C}{1+\frac{H}{K_1}+\frac{K_2}{H}}\right] \qquad \text{Equation 4.4}$$

Determination of Extinction Coefficients for SAICAR at Varying pH. The extinction coefficient is known for SAICAR at pH 7.5, which allows for the computation of $\Delta\varepsilon_{282}$ for CAIR→SAICAR at various pHs. SAICAR solutions (350-500 μM) were obtained from AIR carboxylation assays in which the reaction was allowed to go to completion. SAICAR solutions were diluted into varying buffers at different pHs (triple buffer at pH 6, 6.5, 7, 7.5, 8, and 9) and recorded in at least triplicate and corrected for background ATP contribution at 282 nm. The recorded A_{282} was used to calculate a $\Delta\varepsilon_{282}$ for each pH (with the known SAICAR $\Delta\varepsilon_{282}$ = 8607 M^{-1} cm^{-1} at pH 7.5). Calculated $\Delta\varepsilon_{282}$ values were plotted against pH and fit to a linear equation.

AaPurE1 NCAIR→CAIR pH-Rate Profiles. Continuous assays of PurE1-mediated CAIR carboxylation were performed according to a published method.[16] Assays were carried out at 23 °C in in a final volume of 0.7 mL, 1x triple buffer (100 mM Tris-HCl, 50 mM MES, 50 mM acetic acid) of varying pH, 10 mM $MgCl_2$, 2 mM PEP, 0.5 mM ATP, 10 mM L-aspartate, 1 mM $KHCO_3$, 1.2 units of pyruvate kinase (477 units mg^{-1}, Sigma P9136), 5 units of H6PurK (isolated by Jesse Murphy), 4 units of H6PurC (isolated by Jesse Murphy), and varying amounts of AaPurE1s. After pre-incubation for 3 min the reaction was initiated by the addition of AIR (12.5-500 μM) and SAICAR formation monitored directly ($\Delta\varepsilon_{282}$ = 128.04 x pH + 7684.4, units of M^{-1} cm^{-1}). Velocity (units mg^{-1}) at each pH was plotted as a function of [CAIR] and the data were fit to equation 4.1. Values of k_{cat} and k_{cat}/K_m were plotted as a function of pH and fit to equation 4.4.

Fluorescence Titrations. Spectra were obtained using a 1 cm pathlength fluorometer cell that contained 2.0 mL prior to the titration. The excitation wavelength was 295 nm (2 nm slit width) and emission spectra were collected from 305 to 450 nm (5 nm slit width). A buffer only-spectrum was subtracted from as the background from all spectra. The intensity of the fluorescence emission *F* for each titration point was measured at 320 nm and then corrected for dilution.

Citrate Titrations (0-25 mM final concentration, added from a 200 mM stock, pH 4.6) were performed in 50 mM potassium acetate, 100 mM KCl, pH 4.6, with varying amounts of AaPurE1 or TdPurE2 at 25 °C. Emission intensities at 320 nm (F) were divided by the intensity at zero ligand (L) concentration (F_0) to obtain fractional saturation values. The AaPurE1 titration data were fit using gnuplot 4.4 to a binding isotherm (equation 4.2) by allowing K_d and ΔF (the value of F/F_0 as $[L] \rightarrow \infty$) to vary.

$$\frac{F}{F_0} = 1 - \Delta F \left(\frac{[L]}{[L]+K_d}\right) \qquad \text{Equation 4.5}$$

AIR titrations (0-25 μM final concentration, added from a 600 μM stock in 50 mM Tris-HCl, pH 8) were performed in 50 mM Tris-HCl, pH 8 with varying amounts of AaPurE1 at 30 °C. Emission intensities at 320 nm (F) were divided by the intensity at zero ligand (L) concentration (F_0) to obtain fractional saturation values. The data were fit using Origin to a binding isotherm (equation 4.5) by allowing K_d and ΔF (the value of F/F_0 as $[L] \rightarrow \infty$) to vary.

Solution Studies of AaPurE1s. Solution aggregation state was determined on an AKTA FPLC system (Amersham) using a Pharmacia G200-16/60 high-load column. The mobile phase was 50 mM Tris-HCl, 100 mM KCl, pH 8 applied at 1 mL min^{-1}. Injections (100 μL) contained 0.5 mg of protein adjusted to 5% (v/v) glycerol. Protein solution sizes and aggregation states were determined by comparison with protein size standards (29-669 kDa; Sigma MW-GF-1000), blue dextran (2 MDa; V_o), and acetone (60 Da, V_i) using the K_{av} partition coefficient method [17].

Crystallization and Soaking of AaPurE1s. AaPurE1 forms intended for crystal production were buffer-exchanged into 5 mM Tris-HCl, 15 mM NaCl, pH 8 and concentrated to 10 mg mL^{-1} using Millipore Ultra spin columns (MWCO 30000). Crystals were grown by the hanging drop vapor diffusion method using reservoir solutions containing 25-35% PEG 4000, 200 mM $LiSO_4$, 100 mM Tris-HCl, pH 8.3. To generate nucleotide bound complexes, AaPurE1 crystals were soaked for 1-3 h in artificial mother liquor containing 5 mM CAIR.

Crystallization of TdPurE2s. TdPurE2 forms intended for crystal production were buffer exchanged into 5 mM Tris-HCl, 20 mM KCl, pH 8 and concentrated to 10 mg mL^{-1} using Millipore Ultra spin columns (MWCO 30000). Crystals were grown by the hanging drop vapor diffusion method using reservoir solutions containing 14-16% PEG 1000, 100mM $MgCl_2$, 100 mM imidazole, pH 8.

X-ray Data Collection and Processing. Prior to data collection, AaPurE1 crystals were placed briefly into a cryoprotectant solution that consisted of artificial mother liquor with an additional 2% PEG 4000 and 15% (v/v) ethylene glycol. TdPurE2 crystals were placed briefly into a cryoprotectant solution that consisted of artificial mother liquor and 20% (v/v) ethylene glycol. Crystals were immediately flash-cooled in liquid N_2. X-Ray diffraction data were collected on either a MAR-225 or MAR-300 CCD detector at the LS-CAT beamline (Advanced Photon Source - Argonne National Laboratory). Diffraction data were indexed, integrated, and scaled with HKL-2000..

Structure Determination and Refinement. All crystals had the same space group with similar unit cell parameters, previously observed in structures of AaPurE1.[1,18] Molecular replacement was performed using AutoMR/Phaser[19] with AaPurE1 monomer (PDB code 2fw1 chain A) as the search model. Structures for AaPurE1-S57A, AaPurE1-S57C, AaPurE1-S57T, AaPurE1-S57D, AaPurE1-S57N, and AaPurE1-S57V were determined by using the AaPurE1$_{fwf}$ monomer (PDB code 4YCB chain A) as the search model. The TdPurE2-S38D crystal had the same space group with similar unit cell parameters, t to a previous TdPurE2 structure.[2] Early rounds of refinement were performed using rigid body, simulated annealing, Cartesian coordinate optimization, individual isotropic temperature factor refinement, and automatic water picking in PHENIX [20]. Later rounds of refinement were performed using Cartesian coordinate optimization, individual isotropic temperature factor refinement, automatic water picking, automatic outlier correction, and occupancy refinement. Model building, manual inspection, and rebuilding were performed using Coot [21]. Coordinates and structure factors have been deposited in the RCSB Protein Data Bank (PDB) with accession numbers TBD (AaPurE1-S57A), TBD (AaPurE1- S57C), TBD (AaPurE1-S57T), TBD (AaPurE1-S57V), TBD (AaPurE1-S57N), TBD (AaPurE1-S57D), and TBD (TdPurE1- S38D). Figures were prepared using PyMOL.[22]

4.3 Results

Construction of CC1215 Strain. Recombinant PurE expression was carried out in BL21(DE3) cells that contain an endogenous copy of EcPurE1. The generation of the CC1215 strain ensures there is no contamination of endogenous EcPurE1 in recombinant PurE1 and PurE2 isolations.

The Keio strain JW0152 contains an in-frame replacement of the *purE1* gene with a kanamycin resistance cassette.[23] The use of P1 phage transduction to transfer the kanamycin cassette to the BL21(DE3) strain was straightforward and successful on the first attempt.

Creation of AaPurE1 and TdPurE2 Mutants. AaPurE1-S57X and TdPurE2-S38X mutants were generated to investigate the role of the absolutely conserved active site serine.

The most stable AaPurE1 mutant, Ser→Thr was chosen as the background to test the stability of Trp introduction mutants. TdPurE2-M15W,S38T; TdPurE2-H17W,S38T;

TdPurE2-F79W; TdPurE2-F79W,S38T; and TdPurE2-F79W,S38C mutants were generated to determine if an intrinsic fluorophore (Trp) could be introduced into TdPurE2 for obtaining kinetic parameters by fluorescence methods.

Quikchange site directed mutagenesis was successful in generating the AaPurE1-S57X mutants and some TdPurE2-S38X mutants (Table 4.4). TdPurE2 mutants proved to be very difficult to generate by standard Quikchange mutagenesis. Therefore, cross-over PCR was employed to generate most TdPurE2 mutants. Cross-over PCR was performed using standard techniques with a single addition to the protocol, a *DpnI* digestion step was introduced after the primary PCR to ensure the parental plasmid did not contaminate the secondary PCR. This extra step significantly decreased the amount of false-positive colonies (data not shown). Finally, a cassette carrying the M15W mutation was generated from synthetic oligonucleotides and ligated into a plasmid encoding TdPurE2-H17W,S38T to replace the H17W mutation. Multiple molecular cloning techniques were used to generate TdPurE2 plasmids because Quikchange repeatedly failed. Sequencing confirmed all the intended mutations were obtained.

Functional Complementation of JW0512. Ser mutants were assessed for the ability to restore prototrophy to the Keio strain JW012 (*ΔpurE1*). Only wild-type PurE1 and PurE2 complement a *ΔpurE1* strain under normal atmospheric conditions. This is consistent with the low specific activites obtained for all S57X and S38X mutants (Tables 4.4 and 4.6).

Of the AaPurE1-S57X mutants, only AaPurE1-S57T complemented under high CO_2 conditions. Under high CO_2 levels, TdPurE2-S38T complemented almost as well as wild-type TdPurE2. While this mutant has the highest residual activity *in vitro*, it did not produce crystals and its combination with any additional mutation (M15W, H15W, or F97W) was highly destabilizing. There may be enough activity in TdPurE2-S38T to support growth on minimal media, or some component *in vivo* such as a chaperone may help to stabilize TdPurE2-S38T. Cells producing either TdPurE2-S38A or TdPurE2-S38C grow after 120 h (Table 4.4).

Purification of Recombinant AaPurE1-S57X Mutants. The previously published isolation protocol[1] was successfully used to isolate all AaPurE1 forms with varying specific activites and high purity (Table 4.9, Figure 4.5, and Figure 4.7).

Purification of Recombinant TdPurE2-S38X Mutants. The previously published isolation protocol[2] was successfully used to isolate all TdPurE2 forms with varying specific activites and high purity (Table 4.9, Figure 4.6, and Figure 4.7).

Purification of Recombinant TdPurE Tryptophan Introduction Mutants. The previously published isolation protocol[2] was successfully used to isolate all TdPurE2 forms with varying specific activites and high purity (Table 4.9 and Figure 4.8).

Forms not suitable for further analyses were: TdPurE2-S38T,F79W (activity is lost when diluted and cannot be stored), TdPurE2-H17W,S38T (retains only 4% of TdPurE-S38T activity), and TdPurE2-M15W,S38T (precipitates out of solution during isolation). It appears the addition of multiple mutations to TdPurE2 creates an unstable protein.

Solution Studies of AaPurE1 Forms. Analytical size exclusion chromatography was used to determine the biological unit and relative stability of each AaPurE1-S57X mutant. Gel-filtration analyses confirmed the presence of the PurE octamer for all AaPurE1 forms, but also showed formation of some high molecular weight aggregates (Figure 4.9). AaPurE1-S57V has a peak at ~76 mL that corresponds to dissociation into tetramers.

Citrate Titrations of AaPurE1-S57X Mutants. Citrate is a non-substrate active site ligand that binds AaPurE1 weakly, under acidic conditions, leading to protein fluorescence quenching.[1] While it has little resemblance to CAIR, citrate interacts with the protonated form of the key His59 and all nucleotide-binding residues, except for the phosphate contact Ser32 and the exocyclic amine contacts in the 70s loop backbone. Therefore, titrations were carried out in 50 mM potassium acetate, 100 mM KCl, pH 4.6 with all AaPurE1-S57X forms to determine the fluorescence response of each mutant upon citrate addition.

The fluorescence of all AaPurE1-S57X mutants was quenched by the addition of citrate. Mutation of Ser decreases the affinity for citrate (Table 4.9 and Figure 4.10), indicating that the hydrogen bond provided by Ser is likely involved in binding citrate. The inactive mutant AaPurE1-S57D does bind citrate and, along with crystal structures, indicates that the active site is intact (Figure 4.17).

AIR Titrations of AaPurE1-S57X Mutants. AIR is not a substrate for PurE1, it instead acts as a inhibitor.[24] The addition of AIR to active AaPurE1 forms results in small increase as result of a fluorescent species present in AIR (Chapter 2). AIR titrations were carried out in 50 mM Tris-HCl, pH 8.0.

The addition of AIR to AaPurE1-S57X mutants had little or no effect on fluorescence emission intensity, consistent with earlier studies of active PurE1s (Table 4.9 and Figure 4.11).[1,6] AaPurE1-S57A did have enough signal to obtain a K_d which was similar to wild-type, indicating that Ser may not be involved in substrate binding. Alternatively, the replacement of Ser57 with a smaller side chain, could allow an adventitious water to provide a hydrogen bond to the AIR N3.

Crystallization of AaPurE1-S57X Mutants. Structures were obtained for all six Ser mutants (Tables 4.7- 4.8 and Figure 4.12). The structures of AaPurE1-S57X mutants confirm that the active sites are intact, with the exception of AaPurE-S57C (Figure 4.13). The electron density surrounding the Cys57 residues clearly indicates the oxidized species are cysteine sulfenic and cysteine sulfinic acid, even before the acids are introduced into the model (Figure 4.13). The oxidation could be due to radiation damage or components (PEG 4000) in the crystallization solution.

The existence of oxidized cysteines in the AaPurE1-S57C active site was examined using DTNB. AaPurE1-S57C isolated without 2-mercaptoethanol present was used to determine the oxidation state of the active site cysteine. AaPurE1 was used to determine the background formation of TNB (Cys94 is buried, but may still react with DTNB).

Five independent replicates were performed with each form of AaPurE1 and the average amount of TNB formation was calculated. The amount of TNB formation for AaPurE1 is 0.1 ± 0.01 thiol/subunit and the amount of TNB formation for AaPurE-S57C is 1.12 ± 0.04 thiol/subunit. These results indicate Cys94 is largely inaccessible to DTNB and that a 1:1 molar relationship of TNB to the active site Cys57 exists. Therefore, the AaPurE-S57C mutant is not oxidized in solution.

Mass Spectrometric Analysis of AaPurE1-S57C. MALDI Mass Spectrometric analysis was performed with AaPurE-S57C to determine if Cys57 is oxidized in solution. The mass for AaPurE1-S57C is consistent with the presence of cysteines and not the oxidized form(s) (Table 4.6).

Crystallization of TdPurE2-S38X mutants. Crystals of TdPurE2-S38X mutants were harder to obtain and most resulted in modest diffraction at ~6-8 Å. However, a 1.69 Å structure was obtained for TdPurE2-S38D (Tables 4.7-4.8 and Figure 4.14). A model of the Asp38 mutant, with AIR transferred from the TdPurE2•AIR structure (PDB code 3rgg)[2], reveals a steric clash between the Asp carboxylate and AIR N3. In addition, the active site His appears to be displaced by 2.0 Å in the S38D structure (Figure 4.14). The S38D mutant is active therefore; it is likely that a conformational change occurs in S38D that allows CAIR to bind and decarboxylation to occur.

Kinetic Characterization of AaPurE1-S57X Mutants at pH 8. Kinetic constants (K_m and k_{cat}) for CAIR decarboxylation were obtained for all active forms of AaPurE1-S57X mutants. Of the mutants tested, only Thr, Ala, Val, and Cys mutants had detectable catalytic activity. Asn and Asp mutants had no detectable activity.

We then wondered if AaPurE1-S57D might be active at low pH, which could allow protonation of this more acidic residue. AaPurE1-S57D did not have activity at pH 6, indicating that protonation of the Asp may not be sufficient to allow catalysis. Both Asp and Asn are may be too bulky (and negatively charged in the case of the Asp) to permit CAIR binding. All active mutants, with the exception of AaPurE1-S57V, could be saturated with substrate under assay conditions (Table 4.9 and Figure 4.15). The higher K_m of AaPurE1-S57V may indicate that Val inhibits CAIR binding.

The K_ms of AaPurE1-S57X mutants (with the exception of S57V) are relatively unchanged relative to wild-type. This observation suggests that Ser57 is not essential for substrate binding, but that loss of the hydrogen bond provided by Ser does negatively affect catalysis.

Kinetic Characterization of TdPurE2-S38X Mutants at pH 8. All Ser mutants retained a low level of activity, lower than the corresponding AaPurE1-S57X mutants, with the exception of TdPurE2-S38V. Of the mutants tested, only Thr, Ala, Val, Cys, and Asn had detectable activity. Asp mutants had no detectable activity at pH 8. However, TdPurE2-S38D had detectable activity at pH 6 (Figure 4.16).

Kinetic constants (K_m and k_{cat}) for CAIR decarboxylation were only obtained for the TdPurE2-S38C mutant at pH 8 (Table 4.8 and Figure 4.16, panel A). Comparison of the TdPurE2 and TdPurE2-S38C kinetic parameters suggests that both binding and catalysis are affected by the loss of a hydrogen bond normally provided by Ser57.

At low substrate concentration, both TdPurE2-S38T and TdPurE2-S38A mutants had slightly sigmoidal saturation curves (Figure 4.16, panels B and C). These mutations appear to destabilize TdPurE2; crystals of either mutant were not obtained. Both TdPurE2-S38T and TdPurE2-S38V mutants show substrate inhibition above 100 μM

CAIR, indicating that CAIR may act as an inhibitor at high concentrations (Figure 4.16, panels B and D).

While mutation of the universal Ser appears to destabilize both AaPurE1 and TdPurE2, the mutation of Ser38 impacts TdPurE2 activity more profoundly. AaPurE1 demonstrates heat and acid stability beyond a protein from a mesophilic bacterium.[1] We have uncovered that TdPurE2 cannot tolerate mutations as well as AaPurE1.

pH Rate Profiles. By determining the velocity of a reaction at varying pH we can obtain the pK_a(s) of ionizable groups on the enzyme and substrate necessary for binding and catalysis to occur. We can also determine the proton stoichiometry of the ionizable groups involved. However, assigning the pK_a values to a specific residue or a chemical moiety of the substrate is difficult. We generated pH rate profiles of AaPurE1-S57X and TdPurE2-S38X mutants to gain insight into the ionizations that occur when Ser57 is replaced by an ionizable residue. A triple buffer system was used to ensure constant ionic strength for each pH tested.

The log k_{cat}/K_m versus pH rate profile reports on ionizations within the free enzyme and free substrate. Changes in the k_{cat}/K_m across pHs are suggestive of ionizations required for productive binding of substrate. The log k_{cat} versus pH rate profile reports on ionizations within the Michaelis complex (ES). Changes in the k_{cat} across pHs are suggestive of ionizations required in the ES complex for catalysis.

CAIR Decarboxylation pH Rate Profiles for AaPurE1-S57X Mutants. To further investigate the effect of protonation at the Ser position in PurE1, pH rate profiles were constructed using the AaPurE1-S57C ionizable mutant. pH rate profiles were constructed with AaPurE1-S57A to examine the effect of pH without an ionizable residue at the Ser position. We expected the effect of pH on AaPurE1-S57A activity to match that of wild-type but with lower activity.

AaPurE1-S57A initial velocity data from each pH were fit using equation 4.4. Both the log k_{cat}/K_m versus pH and log k_{cat} versus pH data produced bell shaped profiles consistent with two pK_as. The likely origin of pK_1 is the N3 of CAIR and pK_2 is His59.[1,6] AaPurE1-S57C initial velocity data from each pH were fit to equations 4.2 and 4.3. The log k_{cat}/K_m versus pH data produced a log-linear fit with a slope near negative unity and the log k_{cat} versus pH produced a fit consistent with two indistinguishable pK_as.

k_{cat}/K_m pH Rate Profiles. The log k_{cat}/K_m versus pH profiles for both wild-type and AaPurE1-S57A are similar bell-shaped curves with comparable pK_as (pK_1 = 6.0 ± 0.1 and 5.9 ± 0.1, respectively; pK_2 = 7.2 ± 0.1 and 8.3 ± 0.2, respectively) (Figure 4.17, panel A), indicating similar ionizations are required for CAIR binding in both AaPurE1 and AaPurE1-S57A.[1]

The log k_{cat}/K_m versus pH profile for AaPurE1-S57C demonstrates log-linear dependence on pH, fit to equation 4.2 yielded a slope of -0.86 ± 0.03, indicating that a single ionizable proton is required for the free enzyme or free substrate to bind CAIR (Figure 4.17, panel A). The proton required may be located on the active site His or on the ribose 5'-phosphate (pK_a = 6.3),[24] but could be located on any ionizable group involved in CAIR binding.

k_{cat} pH Rate Profiles. The log k_{cat} versus pH profiles for both wild-type and AaPurE1-S57A are similar bell-shaped curves with comparable pK_as (pK_1 = 5.1 ± 0.2 and, = 5.8 ± 0.1 respectively; pK_2 = 8.4 ± 0.1 and 8.6 ± 0.1, respectively)[1] (Figure 4.17, panel B).

The log k_{cat} versus pH profile for AaPurE1-S57C fit to a model in which two protons with indistinguishable pK_as (averaging ~6.7) are required for activity. One of the pK_as is likely associated with the active site His. The other pK_a may be associated with the active site Cys, however, this would require the pK_a be lowered to around 7.

CAIR Decarboxylation pH Rate Profiles of TdPurE2-S38X Mutants. To further investigate the effect of protonation at the Ser position in PurE2, pH rate profiles were constructed using the TdPurE2-S38C and TdPurE2-S38D ionizable mutants. TdPurE2-S38C and TdPurE2-S38D initial velocity data from each pH were fit to equation 4.2. All the log k_{cat}/K_m versus pH and log k_{cat} versus pH data produced log-linear fits.

k_{cat}/K_m pH Rate Profiles. The log k_{cat}/K_m versus pH profiles for wild-type TdPurE2 is a bell-shaped curve with pK_1 = 5.7 ± 0.2 and pK_2 = 7.3 ± 0.1 (Figure 4.18, panel A).[2]

The log k_{cat}/K_m versus pH profiles for TdPurE2-S38C and TdPurE2-S38D did demonstrate log-linear dependence on pH, fits to equation 4.2 yielded a slopes of -0.21 ± 0.06 and -0.90 ± 0.04, respectively (Figure 4.18, panel A). The Asp pK_a is much lower than that of the Cys, indicating that Asp protonation is likely required for CAIR binding.

k_{cat} pH Rate Profiles. The log k_{cat} versus pH profile for wild-type TdPurE2 is a bell-shaped curve with pK_1 = 5.9 ± 0.5 and pK_2 = 8.4 ± 0.1 (Figure 4.18 panel B).^{2}

The log k_{cat} versus pH profiles for TdPurE2-S38C and TdPurE2-S38D demonstrate log-linear dependence on pH, fits to equation 4.2 yielded slopes of -0.52 ± 0.09 and -1.5 ± 0.08, respectively. This difference in slopes (exactly -1) of the two S38X mutants is likely due to the protonation of the Asp.

NCAIR→CAIR pH Rate Profiles of AaPurE1 and AaPurE1-S57C. . To further investigate the effect of protonation at the Ser position in PurE1, pH rate profiles were constructed in the biosynthetic direction (NCAIR→CAIR) with AaPurE1 and AaPurE1-S57C.

AaPurE1 and AaPurE1-S57C initial velocity data from each pH were fit to equation 4.4. The AaPurE1 log k_{cat}/K_m versus pH data produced a bell shaped profile consistent with two pK_as, while the AaPurE1-S57C log k_{cat}/K_m versus pH data produced a log-linear fit. The log k_{cat} versus pH data for AaPurE1 and AaPurE-S57C produced log-linear fits.

k_{cat}/K_m pH Rate Profiles. The binding of CAIR to AaPurE1 requires His57 to be protonated and AIR to de deprotonated. However, due to the microequilibria, a small mole fraction will be present in the reverse protonation state. If this reverse protonation state is the “correct” protonation state for AaPurE1 to bind NCAIR, then the pK_as obtained by fitting the log k_{cat}/K_m versus pH will be opposite relative to the pH rate profile constructed from CAIR decarboxylation assays.

The log k_{cat}/K_m versus pH profile for AaPurE1 fit to equation 4.4 results in is a bell-shaped curve with pK_1 = 8.8 and pK_2 = 5.45, indicating a reverse protonation mechanism in the forward direction (Figure 4.19, panel A).

The log k_{cat}/K_m versus pH profile for AaPurE1-S57C did not demonstrate log-linear dependence on pH, fit to equation 4.2 yielded slopes -0.094 ± 0.079, indicating that protonation is not required for the free enzyme or free substrate to bind NCAIR.

k_{cat} pH Rate Profiles. The log k_{cat} versus pH profiles for wild-type and AaPurE1-S57C did not demonstrate log-linear dependence on pH, fits to equation 4.4 yielded slopes of -0.12 ± 0.09 and -0.05 ± 0.12, respectively (Figure 4.19, panel B). The lack of dependence on pH indicates that protonation is not important for catalysis in the NCAIR→CAIR direction for either wild-type AaPurE1 or AaPurE1-S57C.

4.4 Discussion

Our initial hypothesis was that Ser assists in catalysis, but would not be as important as the absolutely conserved His acid-base catalyst.[3] Our results show, however, that Ser→X mutants have substantially diminished activity in both PurE1 and PurE2, indicating that a hydrogen bond formed between Ser and N3 is very important for catalysis.

Ser could support PurE1 and PurE2 function in one or more ways:

1) In PurE1 and PurE2 (at high pH), Ser has been proposed to provide a hydrogen bond to (C)AIR N3 thereby directing protonation to C4.[1,6] This would be an example of “negative catalysis”, whereby the Ser itself does not participate in catalysis but deters protonation of the N3.

2) In PurE1, Ser57 has been proposed to provide a pivot-point that allows AIR in the AIR•CO_2 ternary complex to “ring flip” to position either AIR C4 or N6

for attack on the retained CO_2 to produce CAIR or NCAIR, respectively. No similar behavior is suspected for PurE2, which cannot accommodate NCAIR (Figure 4.1).

3) In PurE2, Ser38 may switch hydrogen bond polarity at low pH to become a hydrogen bond acceptor for a protonated N3.[2] This role is not suspected for PurE1, since the active site is closed and N3 protonation is associated with inhibition of activity.

Not one of these functions is mutually exclusive, so Ser could play any or all of these roles. To differentiate between these possibilities, ionizable mutants were used to construct pH rate profiles.

A simple conclusion from site-directed mutagenesis is that Ser is indeed involved in hydrogen bonding, as the mutants with the highest detectable activity are able to supply a hydrogen bond. The Ser→Ala mutants may allow an adventitious water to perform this function. The pH rate profiles indicate that protonation at the Ser position is important for catalysis.

pH Rate Profiles of PurE1 and PurE2 are Consistent with Different Mechanisms of CAIR Decarboxylation . pH rate profiles indicate that replacement of the Ser with an ionizable residue changes the shape of the pH profile, except for the AaPurE1-S57A mutant. AaPurE1-S57A does not posses an ionizable residue at the Ser57 position, but nevertheless has p*K* values similar to wild-type, indicating that both enzyme forms use the classic C4 protonation mechanism proposed for CAIR decarboxylation[3] (Figure 4.3, panel A).

A log-linear pH dependence was observed in AaPurE1-S57C log k_{cat}/K_m, TdPurE2-S38C (log k_{cat}/K_m and log k_{cat}), and TdPurE2-S38D (log k_{cat}/K_m and log k_{cat}) pH rate profiles. The different shape of Ser mutant pH rate profiles versus wild-type suggests a change in mechanism of CAIR decarboxylation. Loss of the hydrogen bond provided by the Ser hydroxyl may "break" the classic C4 protonation mechanism. A weaker hydrogen-bonding partner provided by the Cys may actually *facilitate* protonation at AIR N3, allowing decarboxylation by the ylide (N3 protonation) mechanism (Figure 4.3, panel B). While this reaction may be slower, the Ser→X mutants are still able to catalyze CAIR decarboxylation.

If decarboxylation occurs through the ylide mechanism, it may explain why we do not observe a pK_a in the Ser→X mutant pH rate profiles. We know the pK_a of N3 for CAIR and AIR in solution (~5.9 and ~6.05, respectively), but the pK_a of the ylide intermediate N3 could be much higher.

An observation unique to the AaPurE1-S57C mutant is that the log k_{cat} pH profile shows loss of the inhibitory pK_I, the one associated with N3 protonation of CAIR in wild-type AaPurE1. The shape of the S57C profile resembles the TdPurE2 log k_{cat} versus pH profile, which could indicate that AaPurE1-S57C uses a PurE2-like mechanism. The Cys mutant cannot form a strong hydrogen bond with AIR N3, which may facilitate (or at least allow) N3 protonation and decarboxylation through the ylide reaction manifold.

The Replacement of Ser with Asp or Cys May Have Electrostatic Effects on CAIR C4. In addition to diminishing the polarity of the Ser-N3 hydrogen bond, the effect of Cys and Asp may be to diminish the negative character of C4 (Figure 4.20). Our working hypothesis is that N3 protonation is favored over C4 protonation unless something decreases the likelihood of the former. If N3 is protonated, decarboxylation could occur by the proposed ylide mechanism.

Mutagenesis and kinetic analysis versus pH both indicate that the polarized hydrogen bond provided by the Ser hydroxyl is important for C4 protonation. Therefore, this suggests the primary role for Ser is to direct protonation to C4 in both PurE1 and PurE2 by thwarting N3 protonation.

The Asp in TdPurE2-S38D May Directly Participate in Catalysis. The pH rate profile for TdPurE2-S38D suggests that Asp38 may participate in catalysis (S38D retains 96% of wild-type activity at pH 5.8). Asp38 could share a proton with N3 and decarboxylation could proceed by the ylide mechanism. The AaPurE1 active site His mutant, AaPurE1-H59D, is also a surprisingly efficient enzyme at low pH.[2] This non-conservative mutation appears to support catlysis at either the Ser or His position.

AaPurE1 NCAIR→CAIR Conversion Uses a Reverse Protonation Mechanism. The mechanism of CAIR decarboxylation requires a protonated His59 (its acid form) and a deprotonated AIR N3 (its basic form).[26] At the optimal pH for CAIR decarboxylation, a small mole fraction of AaPurE1 is present in the reverse protonation state. Enzymes, which use a reverse protonation mechanism, are commonly associated with one direction of a reversible enzyme reaction.[25,] PurE1 catalyzes the fully reversible interconversion of NCAIR⇌CAIR and the reverse protonation state appears to be the "correct" protonation state for activity in the NCAIR→CAIR direction.

The AaPurE1 log k_{cat}/K_m versus pH profile is a bell-shaped curve with two distinct pK_as. The pK_as obtained for the forward direction are opposite relative to the CAIR decarboxylation pK_as (Figure 4.17 and Figure 4.19). The basic pK_1 is likely associated with a deprotonated His and the acidic pK_2 may be associated with the N3 position or the carbamate of NCAIR. These protonation states are required for NCAIR binding.

However, the AaPurE1 log k_{cat} pH profile is not dependent upon pH, indicating protonation is not required for catalysis.

The replacement of the conserved Ser with Cys abrogates any detectable ionization within the pH range tested. The AaPurE1-S57C log k_{cat}/K_m and log k_{cat} pH profiles are not dependent upon pH, indicating the presence of a proton is not required for NCAIR to bind to the Cys mutant or for catalysis (Figure 4.19).

4.5 Future Directions

Acquisition of pH rate profiles in the forward direction with both S57X and S38X mutants should be done to determine if the loss of a hydrogen bond at the Ser position causes a switch to the irreversible ylide (N3 protonation) mechanism.

4.6 References

1. Constantine, C. Z., Starks, C. M., Mill, C.P., Ransome, A. E., Karpowicz, S.J., Francois, J.A., Goodman, R.A. and Kappock, T. J. Biochemical and Structural Studies of N^5-Carboxyaminoimidazole Ribonucleotide Mutase from the Acidophilic Bacterium *Acetobacter aceti. Biochemistry* **45,** 8193–8208 (2006).

2. Tranchimand, S., Starks, C. M., Mathews, I. I., Hockings, S. C. and Kappock, T. J. *Treponema denticola* PurE is a Bacterial AIR Carboxylase. *Biochemistry* **50,** 4623–4637 (2011).

3. Meyer, E., Kappock, T. J., Osuji, C. and Stubbe, J. Evidence for the Direct Transfer of the Carboxylate of N^5-Carboxyaminoimidazole Ribonucleotide (N^5-CAIR) to Generate 4-Carboxy-5-Aminoimidazole Ribonucleotide Catalyzed by *Escherichia Coli* PurE, an N^5-CAIR Mutase. *Biochemistry* **38,** 3012–3018 (1999).

4. Mathews, I. I., Kappock, T. J., Stubbe, J. and Ealick, S. E. Crystal structure of *Escherichia coli* PurE, an Unusual Mutase in the Purine Biosynthetic Pathway. *Structure* **7,** 1395–1406 (1999).

5. Li, S., Tong, Y., Xie, X., Wang, Q., Zhou, H., Han, Y., Zhang, Z., Gao, W., Li, S., Zhang, X. and Bi, R. Octameric Structure of the Human Bifunctional Enzyme PAICS in Purine Biosynthesis. *J. Mol. Biol.* **366,** 1603–1614 (2007).

6. Hoskins, A. A., Morar, M., Kappock, T. J., Mathews, I. I., Zaugg, J. B., Barder, T. E., Peng, P., Okamoto, A., Ealick, S. E. and Stubbe, J. N^5-CAIR mutase: Role of a CO_2 Binding Site and Substrate Movement in Catalysis. *Biochemistry* **46,** 2842–2855 (2007).

7. Litchfield, G. J. and Shaw, G. The Mechanism of Decarboxylation of Some 5-Aminoimidazole-4-Carboxylic Acids and the Influence Of Transition Metals. *Chem. Commun.* 563-565 (1965).

8. Litchfield, G. J. and Shaw, G. Purines, Pyrimidines, and Imidazoles. Part XXXVIII. A Kinetics Study of the Decarboxylation of 5-Amino-1-β-D-Ribofuranosylimidazole-4-Carboxylic acid 5'-Phosphate and Related Compounds. *J. Chem. Soc. B Phys. Org.* 1474-1484 (1971).

9. Dunn, G. E., Thimm, H. F. and Mohanty, R. K. Kinetics and Mechanism of Decarboxylation of Some Pyridinecarboxylic Acids in Aqueous Solution. III. 3-Hydroxy and 3-Aminopyridine-2-Carboxylic Acids. *Can. J. Chem.* 1098-1104 (2011).

10. Amyes, T. L., Wood, B. M., Chan, K., Gerlt, J. A. and Richard, J. P. Formation and Stability of a Vinyl Carbanion at the Active Site of Orotidine 5'-Monophosphate Decarboxylase: pK_a of the C-6 Proton of Enzyme-Bound UMP. *J. Am. Chem. Soc.* **130,** 1574–1575 (2008).

11. Sullivan, K. L., Huma, L. C., Mullins, E. a, Johnson, M. E. and Kappock, T. J. Metal Stopping Reagents Facilitate Discontinuous Activity Assays of the *de novo* Purine Biosynthesis Enzyme PurE. *Anal. Biochem.* **452,** 43–45 (2014).

12. Bradford, M. M. A Rapid and Sensitive Method for the Quantitation of Microgram Quantities of Protein Utilizing the Principle of Protein-Dye Binding. *Anal. Biochem.* **72,** 248–254 (1976).

13. Lennox, E. S. Transduction of Linked Genetic Characters of the Host by Bacteriophage P1. *Virology* **1,** 190–206 (1955).

14. Studier, F. W. Protein Production by Auto-Induction in High Density Shaking Cultures. *Protein Expr. Purif.* **41,** 207–234 (2005).

15. Collier, H. B. Letter: A Note on the Molar Absorptivity of Reduced Ellman's Reagent, 3-Carboxylato-4-Nitrothiophenolate. *Anal. Biochem.* **56,** 310–311 (1973).

16. Firestine, S. M., Misialek, S., Toffaletti, D.L., Klem, T. J., Perfect, J. R. and Davisson, V. J. Biochemical Role of the *Cryptococcus neoformans* ADE2 Protein in Fungal *de novo* Purine Biosynthesis. *Arch. Biochem.* **351,** 123–134 (1998).

17. Laurent, T. C. and Killander, J. A Theory of Gel Filtration and its Experimental Verification. *J. Chromatogr. A* **14,** 317–330 (1964).

18. Settembre, E. C., Chittuluru, J. R., Mill, C. P., Kappock, T. J. and Ealick, S. E. Acidophilic Adaptations in the Structure of *Acetobacter aceti* N^5-Carboxyaminoimidazole Ribonucleotide Mutase (PurE). *Acta Crystallogr. Sect. D Biol. Crystallogr.* **60,** 1753–1760 (2004).

19. McCoy, A. J. Grosse-Kunstleve, R. W., Adams, P. D., Winn, M. D., Storoni, L. C. and Read, R. J. Phaser Crystallographic Software. *J. Appl. Crystallogr.* **40,** 658–674 (2007).

20. Adams, P. D., Afonine, P. V., Bunkóczi, G., Chen, V. B., Davis, I.W., Echols, N., Headd, J.J., Hung, L. W., Kapral, G. J., Grosse-Kunstleve, R. W., McCoy, A. J., Moriarty, N.W., Oeffner, R., Read, R. J., Richardson, D. C., Richardson, J. S., Terwilliger, T. C. and Zwart, P. H. Phenix: A Comprehensive Python-Based System for Macromolecular Structure Solution. *Acta Crystallogr. Sect. D Biol. Crystallogr.* **66,** 213–221 (2010).

21. Emsley, P., Lohkamp, B., Scott, W. G. and Cowtan, K. Features and Development of Coot. *Acta Crystallogr. Sect. D Biol. Crystallogr.* **66,** 486–501 (2010).

22. DeLano, W. L. The PyMOL Molecular Graphics System. (2002). http://www.pymol.org

23. Baba, T. Ara, T., Hasegawa, M., Takai, Y., Okumura, Y., Baba, M., Datsenko, K. A., Tomita, M., Wanner, B. L. and Mori, H. Construction of *Escherichia coli* K-12 In-Frame, Single-Gene Knockout Mutants: the Keio Collection. *Mol. Syst. Biol.* **2,** 2006.0008 (2006).

24. Meyer, E. Two New Activities and a New Intermediate in the Purine Pathway. (1996). Ph.D. Thesis, Massachusetts Institute of Technology, Cambridge, MA.

4.7 Figures and Tables

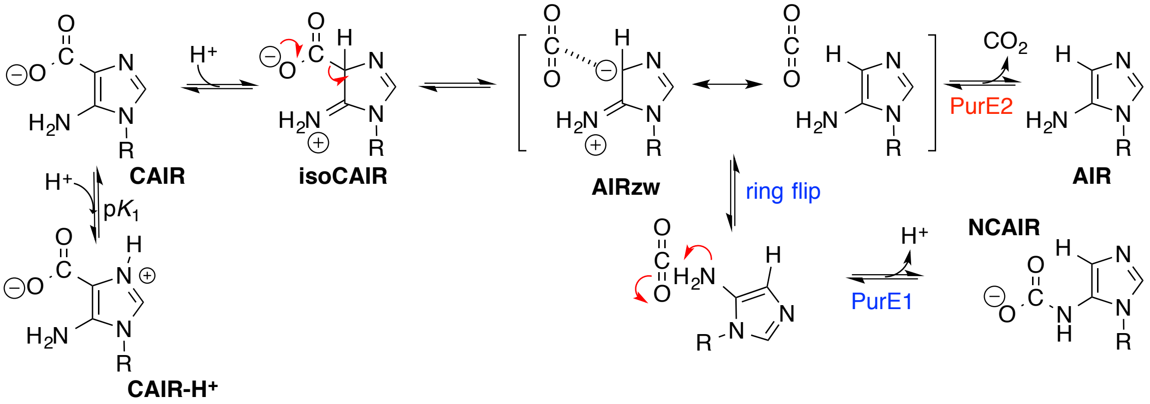

Figure 4.1 CAIR decarboxylation reaction catalyzed by PurE1 and PurE2. Reactions are shown in the nonphysiological CAIR decarboxylase direction because CAIR is a substrate for both PurE1 and PurE2. (A) CAIR decarboxylation (R = R5P) begins with protonation at C4 by an essential His residue.[1,2] Decarboxylation gives a ternary complex containing AIR and CO_2, which only dissociates from PurE2. The PurE1 reaction continues with an aminoimidazole ring flip and NCAIR formation.[6]

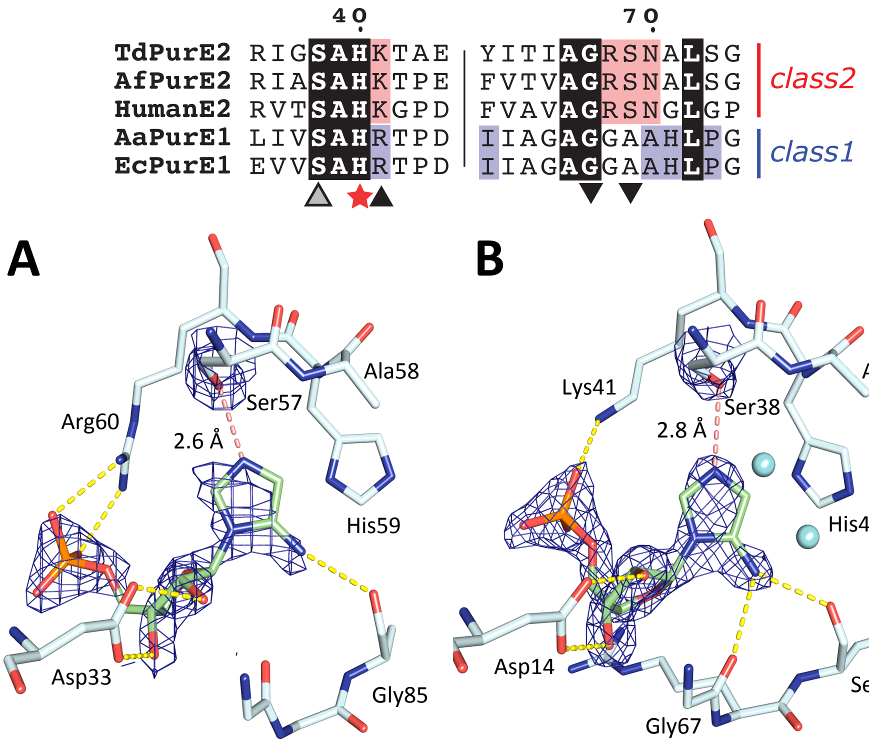

Figure 4.2 PurE1 and PurE2 sequence alignment and active site structures with AIR bound. (A) Sequence alignment of the conserved residues in the active site of PurE2 and PurE1 (*T. denticola* numbering). Bold residues are conserved across the different classes; the red boxes are conserved among PurE2s and the blue boxes are conserved among PurE1s. The critical active site acid/base catalyst His is denoted by a star. Residues that are hydrogen bond acceptors are indicated by, ▲ and hydrogen bond donors ▼. (B) AaPurE1 (PDB code 2FWJ) (C) TdPurE2 (PDB code 3RGG) active site is shown with contacts to the AIR nucleotide shown. The hydrogen bond between the N3 of AIR and Ser is colored in salmon. Electron density maps for $2F_o$-F_c (blue mesh) are contoured at 1.0 σ and have a carve radius of 2.0 Å around the AIR ligand. "Place holder" waters that bind in the carboxylate/CO_2 pocket are shown as cyan spheres.

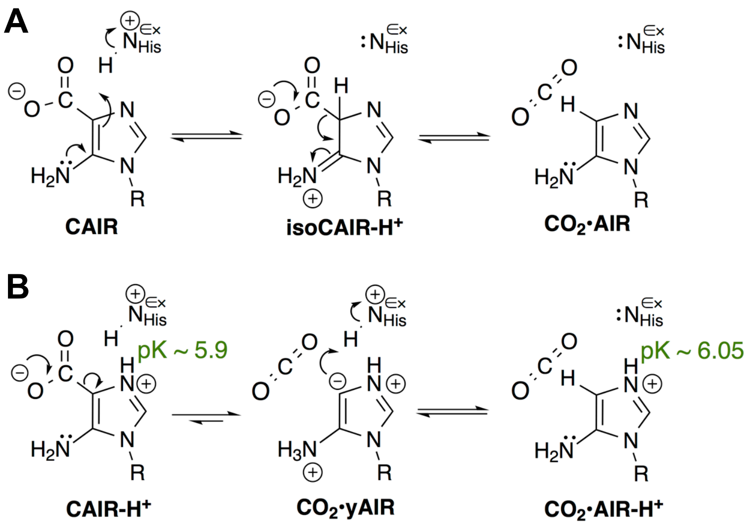

Figure 4.3 Proposed mechanisms for decarboxylation by PurE1 and PurE2. Reactions are shown in the reverse biosynthetic direction. (A) Classic C4 protonation mechanism proposed for PurE1 and PurE2 (at high pH).[1,2] (B) Ylide (N3 protonation) mechanism proposed for low pH decarboxylation in PurE2.[2]

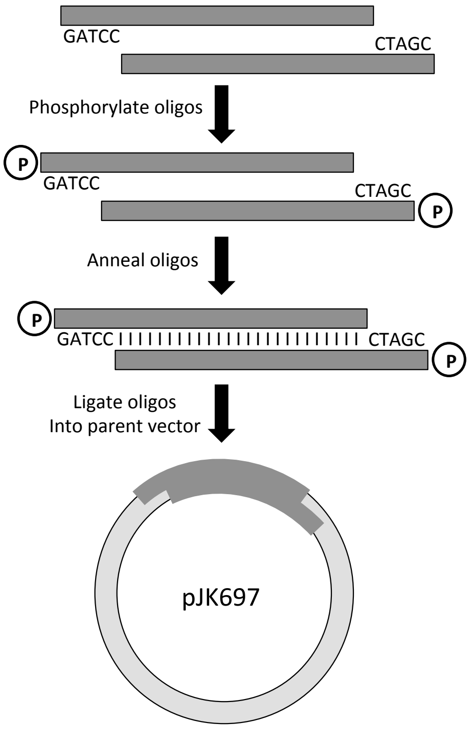

Figure 4.4 Illustration of the protocol using synthetic oligonucleotides to generate TdPurE2-M15,S38T.

Table 4.1 Description of bacterial strains used in this chapter.

Strain	Description	Source
DH5α	F′ φ80lacZΔM15 Δ(lacZYA-argF)U169 *deoR recA1 endA1 hsdR17(r*$_{K}^{-}$ m$_{K}^{+}$) *phoA supE44 thi-1 gyrA96 relA1*	Lab stock
BL21(DE3)	F^{-} *ompT gal dcm lon hsd*S$_{B}$*(*r$_{B}^{-}$ m$_{B}^{-}$*)* λ(DE3 [*lacI lacUV5*-T7 *gene 1 ind1 sam7 nin5*])	Lab stock
CC1215	F^{-} *ompT gal dcm lon hsd*S$_{B}$*(*r$_{B}^{-}$ m$_{B}^{-}$*) ΔpurE*736::kan λ(DE3 [*lacI lacUV5*-T7 *gene 1 ind1 sam7 nin5*])	This study
JW0512	F^{-} *Δ*(*araD-araB*)567 Δlac*Z*4787(::rrnB-3) *ΔpurE*736::kan, λ^{-}, *rph-1* Δ(*rhaD-rhaB*)568, *hsdR514*	CGSG
W3110	*LAM- ln*(*rrnD-rrnE*)1 *rph*-1	Lab stock

Table 4.2 Oligodeoxynucleotides (ODNs) used in this chapter.[a]

ODN	Sequence (5'→3')	
1161	CGGATGACGTTGAGCTGATTCATTTTCC	Sequencing
1164	CAGCTCACCTAAACGATCAAACAC	Sequencing
2124	TAATACGACTCACTATAGGG	T7 promoter
2125	GCTAGTTATTGCTCAGCGG	T7 terminator
2203	GCGTACGATGTGCTGcAACAATGAGGG	AaPurE1-S57A
2204	CCCTCATTGTTgCAGCACATCGTACGC	AaPurE1-S57A
2205	CTGGCGTACGATGTGCgcAAACAATGAGGG	AaPurE1-S57C
2206	CCCTCATTGTTTgcGCACATCGTACGCCAG	AaPurE1-S57C
2207	GGCGTACGATGTGCTGtAACAATGAGGG	AaPurE1-S57T
2208	CCCTCATTGTTaCAGCACATCGTACGCC	AaPurE1-S57T
2285	CATGAAACCCTCATTGTTgtAGCACATCGTACGCCAG	AaPurE1-S57V
2286	CTGGCGTACGATGTGCTacAACAATGAGGGTTTCATG	AaPurE1-S57V
2316	CCGCTGTTTTATGCGCGGtACCGATGCGAATGGCATAC	TdPurE2-S38T
2317	GTATGCCATTCGCATCGGTaCCGCGCATAAAACAGCGG	TdPurE2-S38T
2320	GCTCCGCTGTTTTATGCGCGtcGCCGATaCGtATGGCATACTC	TdPurE2-S38D
2321	GAGTATGCCATaCGtATCGGCgaCGCGCATAAAACAGCGGAGC	TdPurE2-S38D
2235	GCGTACGATGTGCgtcAACAATGAGGG	AaPurE1-S57D
2236	CCCTCATTGTTgacGCACATCGTACGC	AaPurE1-S57D
2345	CATTCGCATCGGCgTCGCGCATAAAACAG	TdPurE2-S38A
2346	CTGTTTTATGCGCGAcGCCGATGCGAATG	TdPurE2-S38A
2355	CATTCGCATCGGCGtnGCGCATAAAACAG	TdPurE2-S38V
2356	CTGTTTTATGCGCnaCGCCGATGCGAATG	TdPurE2-S38V
2366	CGCATCGGCTgCGCGCATAAAACAGCtGAGCATGTAGTGTC	TdPurE2-S38C
2367	CGTCTGAATTGAAAACTTTTGGTATTGAGTATGCCATTCGCATCGGCTgCG	TdPurE2-S38C
2374	CCGCTGTTTTATGCGCGtTACCGATGCGAATGGCATAC	TdPurE2-S38N
2375	GTATGCCATTCGCATCGGTAaCGCGCATAAAACAGCGG	TdPurE2-S38N
2376	GGCGTACGATGTGCGTtAACAATGAGGG	AaPurE1-S57N
2377	CCCTCATTGTTaACGCACATCGTACGCC	AaPurE1-S57N
2393	GATATACATATGCGTCCGCTGGTGATTATCCTTATGGGatcCAGTTCAGATATGGGTtggGCCGAGAAAATTGCtagcGAATTGAAAAC	TdPurE2-H17W
2398	GatcCAGTTCAGATtgGGGgCAtGCCGAGAAAATTG	TdPurE2-M15W
2399	ctaGCAATTTTCTCGGCaTGcCCCcaATCTGAACTG	TdPurE2-M15W

[a] Changes in the coding region that deviate from the genomic sequence are in lower case.

Table 4.3 Previously published plasmids used in this study**.**

Plasmid	Description	Source	Protein encoded
pJK175	*purE1*$_{Aa}$ in pET23a	[1]	AaPurE

Table 4.4 Plasmids used in this chapter.

Plasmid	Description	Protein encoded
pJK582	*purE1*$_{Aa}$*-S57A* in pET23a	AaPurE-S57A
pJK583	*purE1*$_{Aa}$*-S57C* in pET23a	AaPurE-S57C
pJK584	*purE1*$_{Aa}$*-S57T* in pET23a	AaPurE-S57T
pJK608	*purE1*$_{Aa}$*-S57D* in pET23a	AaPurE-S57D
pJK643	*purE2*$_{Td}$*-S38T* in pET23a	TdPurE-S38T
pJK644	*purE2*$_{Td}$*-S38D* in pET23a	TdPurE-S38D
pJK653	*purE2*$_{Td}$*-S38T*, *F79W* in pET23a	TdPurE-S38T,F79W
pJK659	*purE2*$_{Td}$*-S38C*, *F79W* in pET23a	TdPurE-S38C,F79W
pJK677	*purE1*$_{Aa}$*-S57V* in pET23a	AaPurE-S57V
pJK684	*purE2*$_{Td}$*-S38V* in pET23a	TdPurE-S38V
pJK685	*purE2*$_{Td}$*-S38N* in pET23a	TdPurE-S38N
pJK686	*purE1*$_{Aa}$*-S57N* in pET23a	AaPurE-S57N
pJK692	*purE2*$_{Td}$*-H17W, S38T* in pET23a	TdPurE-H17W,S38T
pJK697	*purE2*$_{Td}$*-M15W, S38T* in pET23a	TdPurE-M15W,S38T

Table 4.5 Results of functional complementation of JW0512 (*ΔpurE*) Keio strain.

Plasmid (PurE form)	MM^a + hypoxanthine	MM	MM+ CO$_2$ ^{b}+ hypoxanthine	MM + CO$_2$
pET23a	+++^{c}	-	++++	-
pJK175 (*purE1*$_{Aa}$)	+++	+++	++++	+++
pJK283 (*purE1*$_{Aa}$*-H59N*)	+++	-	++++	-
pJK582 (*purE1*$_{Aa}$*-S57A*)	+++	-	++++	-
pJK583 (*purE1*$_{Aa}$*-S57C*)	+++	-	++++	-
pJK584 (*purE1*$_{Aa}$*-S57T*)	+++	-	++++	+
pJK677 (*purE1*$_{Aa}$*-S57V*)	+++	-	++++	-
pJK686 (*purE1*$_{Aa}$*-S57N*)	+++	-	++++	-
pJK608 (*purE1*$_{Aa}$*-S57D*)	+++	-	++++	-
pJK376 (*purE2*$_{Td}$)	+++	++	++++	++++
pJK392 (*purE2*$_{Td}$*-H40N*)	+++	-	++++	-
pJK617 (*purE2*$_{Td}$*-S38A*)	+++	-	++++	+
pJK607 (*purE2*$_{Td}$*-S38C*)	+++	-	++++	+
pJK643 (*purE2*$_{Td}$*-S38T*)	+++	-	++++	+++
pJK684 (*purE2*$_{Td}$*-S38V*)	+++	-	++++	-
pJK685 (*purE2*$_{Td}$*-S38N*)	+++	-	++++	-
pJK644 (*purE2*$_{Td}$*-S38D*)	+++	-	++++	-

[a] minimal media described above in experimental details

[b] plates grown in a candle jar.

[c] symbols:++++, large colonies at 24 h +++, small colonies at 24 h;, ++, small colonies at 48 h; +, small colonies at 120 h; -, no growth observed at 144 h.

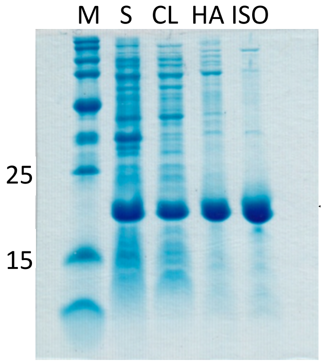

Figure 4.5 SDS-PAGE analysis of a representative AaPurE1-S57X (X = V) isolation. A 12% polyacrylamide gel was loaded with 5 ug protein per lane: M, Sigma biotinylated marker; S, soluble lysate; CL, cleared lysate; HA, hydroxyapatite input; and ISO, isolated AaPurE1-S57V. Molecular weights (kDa) are denoted along the left side of the gel.

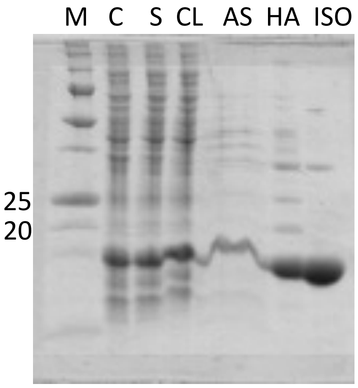

Figure 4.6 SDS-PAGE analysis of a representative TdPurE2-S38X (X = A) isolation. A 12% polyacrylamide gel was loaded with 5 ug protein per lane: M, Sigma biotinylated marker; S, soluble lysate; CL, cleared lysate; AS, ammonium sulfate supernatant; ; HA, hydroxyapatite input; and ISO, isolated TdPurE2-S38A. Molecular weights (kDa) are denoted along the left side of the gel.

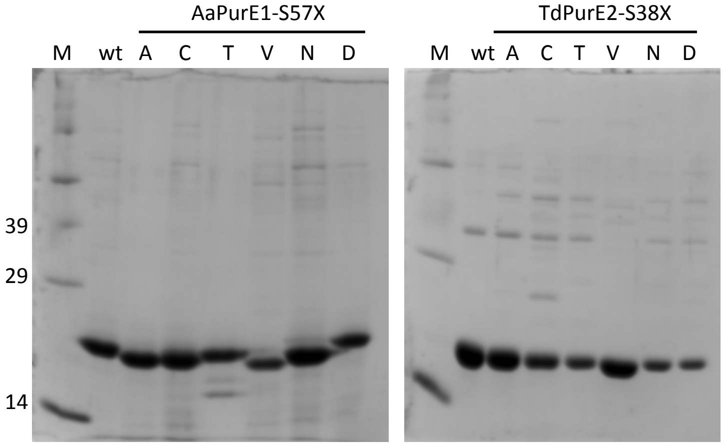

Figure 4.7 SDS-PAGE analysis of isolated AaPurE1-S57X and TdPurE2-S38X forms. A 12% polyacrylamide gel was loaded with 5 ug protein per lane: M, Sigma biotinylated marker; AaPurE1 is denoted by wt; and each mutation in Ser57 or Ser 38 is indicated by the one letter code. Note the slightly decreased mobility of S57D, which is presumably due to the addition of a negatively charged residue. Molecular weights (kDa) are denoted along the left side of the gel.

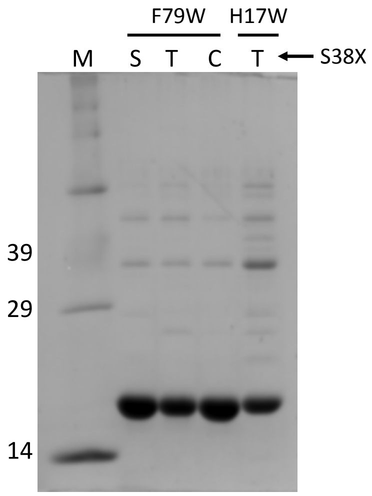

Figure 4.8 SDS-PAGE analysis of isolated TdPurE2 Trp introduction forms. A 12% polyacrylamide gel with 5 ug protein loaded per lane: 12% polyacrylamide gel was loaded with 5 ug protein per lane: M, Sigma biotinylated marker. Each mutation in Ser 38 is indicated by the one letter code directly above each lane. Each mutation to introduce a Trp into TdPurE2 is indicated above the solid line. Molecular weights (kDa) are denoted along the left side of the gel.

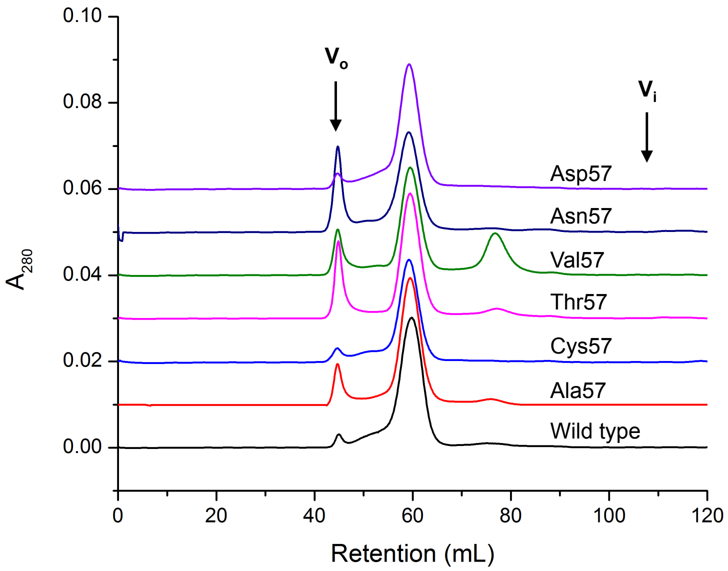

Figure 4.9 Gel-filtration analysis of AaPurE1-S57X mutants. The traces are shifted 0.1 A_{280}. The AaPurE1 octamer elutes at ~57 mL and aggregate elutes at the excluded volume (V_o). The completely excluded volume (V_o, 44.7 mL) and included volume (V_i, 113.6 mL) volumes are indicated with arrows. A small peak at (~76 mL) observed in AaPurE1-S57V is likely due to the formation of tetramers.

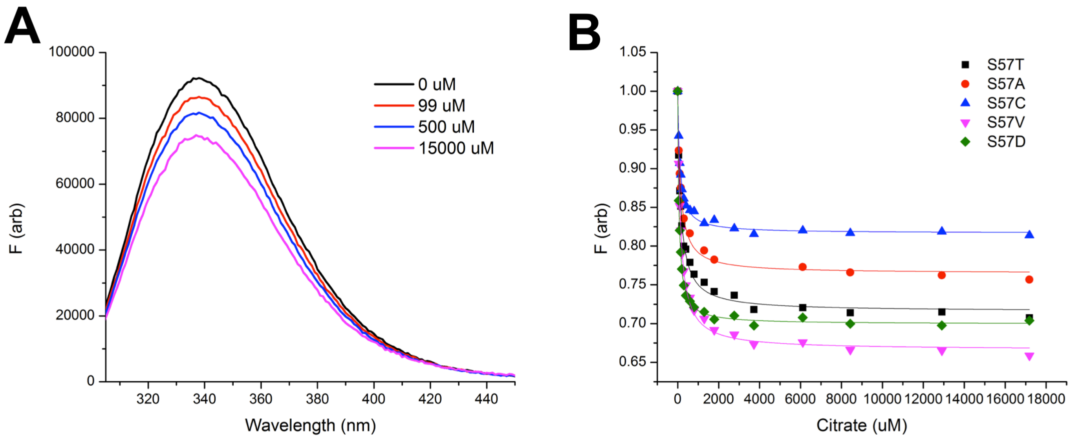

Figure 4.10 Fluorescence titrations of AaPurE1-S57X mutants with citrate. (A) Fluorescence emission spectra of AaPurE1-S57C were recorded in 50 mM potassium acetate, 100 mM KCl, pH 4.6 at 25 °C with an excitation at 295 nm. (B) Fluorescence emission intensity at 320 nm plotted as a function of [citrate] for AaPurE1-S57T (black filled squares), AaPurE1-S57A (red filled circles), AaPurE-S57C (blue filled triangles), AaPurE1-S57V (pink filled inverted triangles), and AaPurE1-S57D (green filled diamonds). Titrations were performed with [subunit] of 0.4 µM, 1.29 µM, 0.4 µM, 0.4 µM and 0.4 µM, respectively. Data were fit to equation 4.5 in Origin to obtain K_d values (Table 4.9).

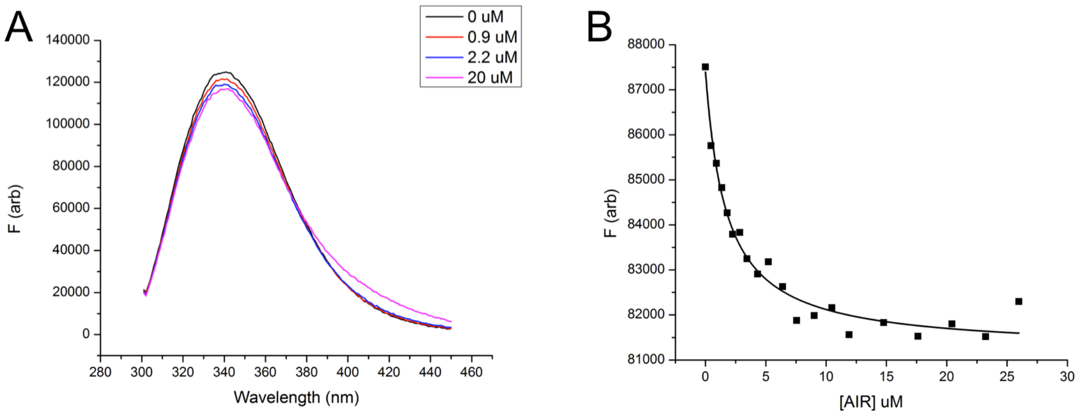

Figure 4.11 Fluorescence titrations of AaPurE1-S57A with AIR. (A) Fluorescence emission spectra of AaPurE1-S57A were recorded in 50 mM potassium acetate, 100 mM KCl, pH 4.6 at 25 °C with excitation at 295 nm. (B) Fluorescence emission intensity at 320 nm, plotted as a function of [AIR]. Titrations were performed with [subunit] of 0.4 µM. Data were fit to equation 4.6 using Origin to obtain K_d values (Table 4.9).

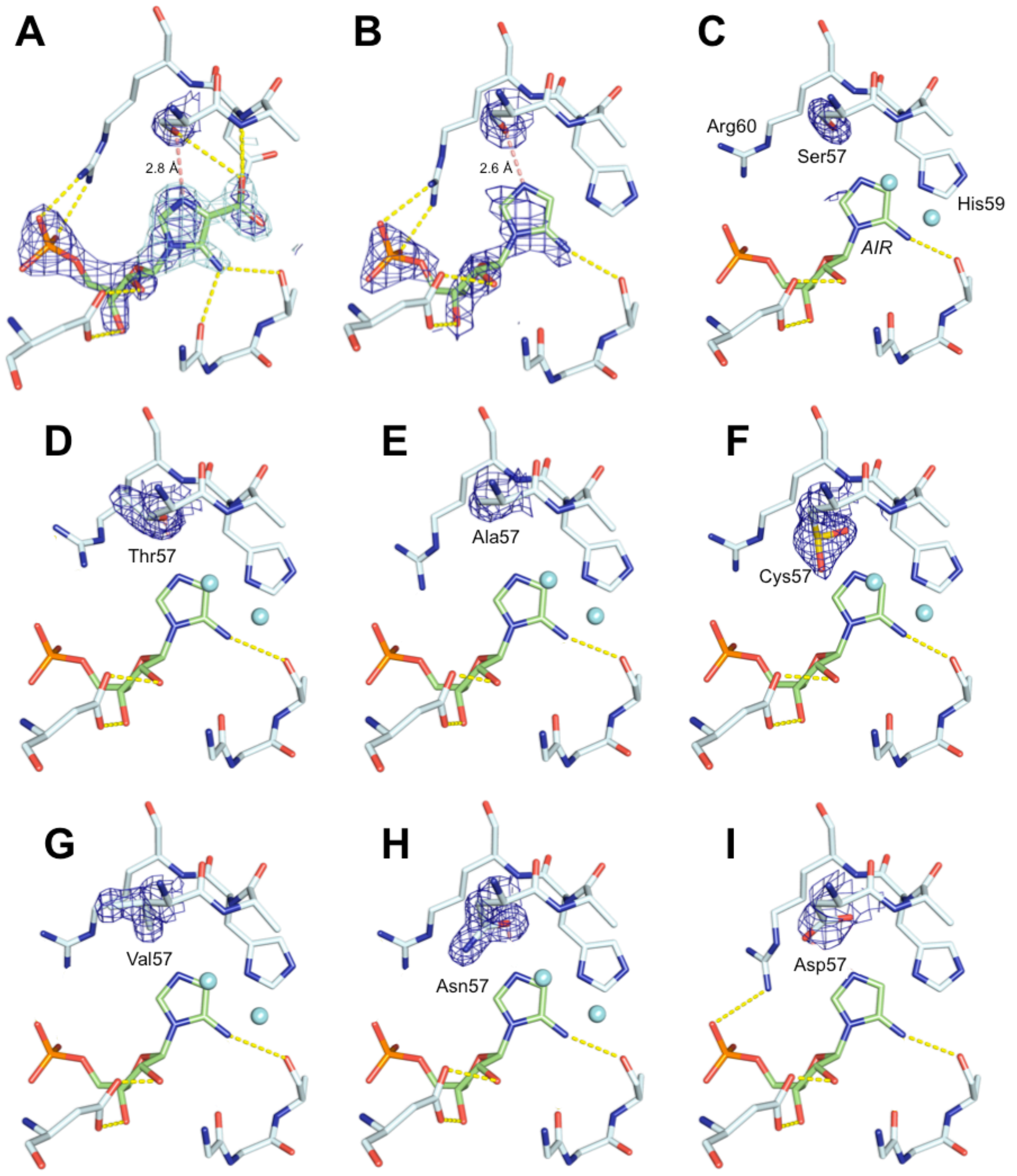

Figure 4.12 Active sites AaPurE1-S57X mutants with AIR modeled in from the 2fwj structure. (A) EcPurE1•CAIR complex (PDB code 2NSL). (B) AaPurE1•AIR complex (PDB code 2FWJ). (C) AaPurE1 (PDB code 1U11). (D) AaPurE-S57T (PDB code TBD). (E) AaPurE1-S57A (PDB code TBD). (F) AaPurE1-S57C (PDB code TBD). (G) AaPurE1-S57V (PDB code TBD). (H) AaPurE1-S57N (PDB code TBD). (I) AaPurE1-S57D (PDB code TBD). An electron density map (final $2F_o{-}F_c$, blue mesh) is shown for AIR atoms and residue 57 with a 1.0 σ contour and 2.0 Å carve. The $F_o{-}F_c$ map is contoured at +3 σ (green mesh) and –3 σ (red mesh). Note the two "placeholder waters" shown as cyan spheres. These oxygen atoms occupy the same location as those in CO_2 or CAIR carboxylate in PurE1 structures.

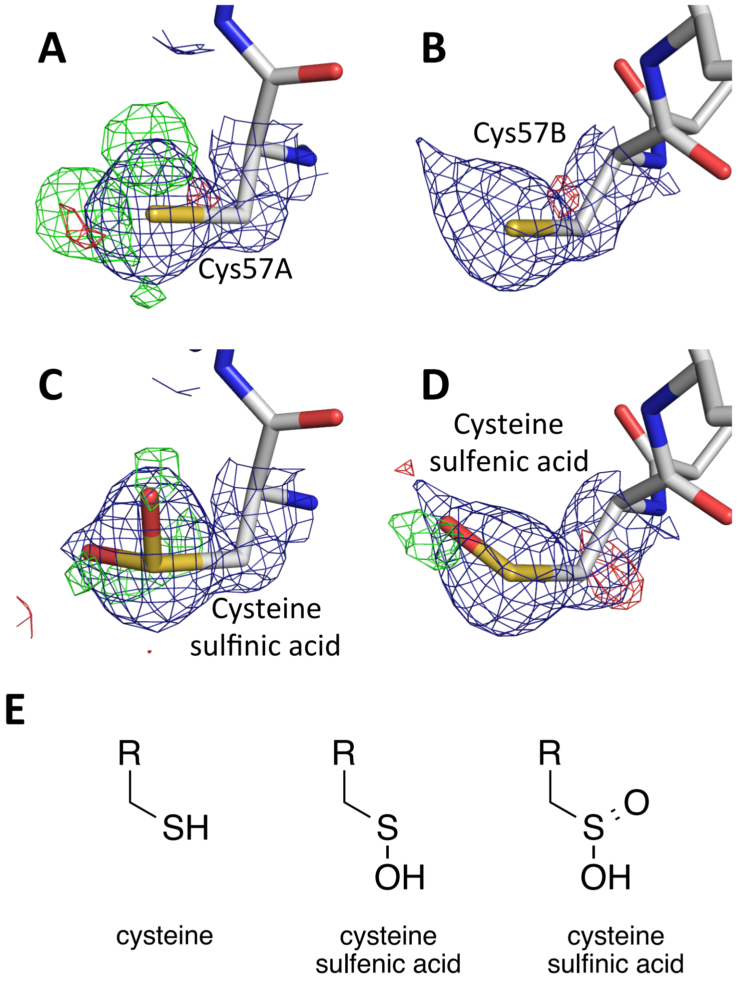

Figure 4.13 Oxidized cysteines in the AaPurE1-S57C structure. (A) The density in subunit A is not consistent with Cys57. (B) The density in subunit B not consistent with Cys57. (C) The density in subunit A is consistent with the oxidized cysteine sulfinic acid. (D) The density in subunit B is consistent with the oxidized cysteine sulfenic acid. (E) Possible chemical structures for Cys57. An electron density map (final $2F_o{-}F_c$, blue mesh) is shown for residue 57 with a 1.8 σ contour and 2.0 Å carve. The $F_o{-}F_c$ map is contoured at +3 σ (green mesh) and –3 σ (red mesh).

Table 4.6 Mass spectrometric analysis of AaPurE1 forms.

PurE1	Observed Mass (Da)	Expected Mass (Da)[a]
AaPurE1 (wild-type)	18869[c]	18867
AaPurE1-S57C	18880	18882

[a] Molecular masses ($[M+H^+]^+$) were determined by MALDI., Expected masses were calculated using ExPaSy ProtParam. All AaPurE1s have an additional N-terminal Met[2]

[b] Difference in mass between expected and observed.

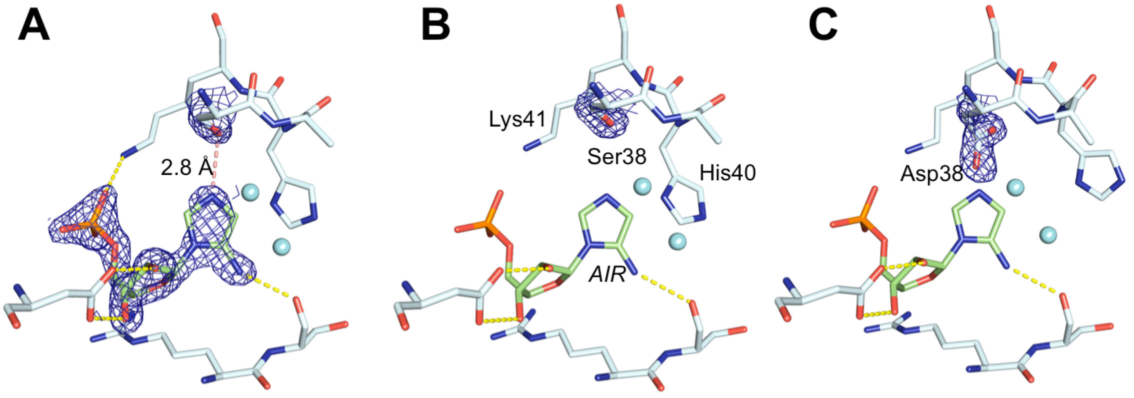

Figure 4.14 Active sites of TdPurE2 and the TdPurE2-S38D mutant. (A) TdPurE2 with AIR bound (PDB code 3rgg). (B) TdPurE2 (PDB code 3rg8) with AIR modeled in from alignment with the 3rgg structure. (C) TdPurE2-S38D (PDB code TBD) with AIR modeled in from alignment with the 3rgg structure. An electron density map (final $2F_o{-}F_c$, blue mesh) is shown for AIR atoms and residue 57 with a 1.0 σ contour and 2.0 Å carve. The $F_o{-}F_c$ map is contoured at +3 σ (green mesh) and –3 σ (red mesh). Note the two "placeholder waters" shown as cyan spheres.

Table 4.7 X-ray data collection statistics.

	AaPurE1						TdPurE2
	S57T_6	S57A_4	209_S57C	S57V2	206_S57N	S57D_102	207_S38D
PDB entry	TBD	TBD	TBD	TBD	TBD	TBD	TBD
Beamline	21-ID-D	21-ID-D	21-ID-F	21-ID-F	21-ID-F	21-ID-F	21-ID-F
Wavelength (Å)	0.97856	0.97872	0.97856	0.97872	0.97872	0.97856	0.97872
Space group [b]	I422	I422	I422	I422	I422	I422	$C222_1$
Unit cell param. (Å)	a=b= 99.775, c= 165.021	a=b=99.430, c=164.168	a=b=99.803, c=164.409	a =b= 99.803, c= 164.409	a =b= 99.981 c= 164.716	a =b= 99.703 c= 165.606	a= 84.084 b= 154.958 c= 89.130
Resolution (Å)	50-1.75 (1.78–1.75) [a]	50-1.98 (2.01-1.98)	50–2.00 (2.03–2.00)	50-1.80 (1.83-1.80)	50-1.79 (1.82-1.79)	50-2.75 (2.80-2.75)	50-1.70 (1.73-1.70)
No. meas. refl.	611,211	275154	360568	751400	1130009	124466	950714
No. unique refl.	41,986 (2080)	29106 (1430)	28501 (1390)	37948 (1871)	39536 (1958)	11217 (535)	64883 (3188)
Completeness (%)	100 (100)	99.3 (99.9)	100 (100)	100 (100)	100 (100)	99.8 (99.4)	99.9 (100)
Multiplicity	14.6 (14.7)	9.5 (8.7)	12.7 (12.4)	19.8 (18.7)	28.6 (28.0)	11.1 (10.9)	14.7 (14.3)
R_{merge} (%) [c]	8.7 (86.6)	10.3 (30.9)	12.2 (80.2)	9.3 (44.2)	9.3 (83.5)	8.9 (63.9)	7.0 (50.4)
Mean I/σ (I)	45.2 (2.9)	46.4 (9.8)	34.0 (3.9)	61.1 (10.7)	51.7 (6.3)	25.3 (3.4)	55.3 (5.3)
V_M (Å^3 Da^{-1}) [d]	2.49	2.48	2.48	2.47	2.50	2.50	2.71
Est. solvent (%)	50.7	50.4	50.4	50.3	50.8	50.7	54.6

[a] Values in parenthesis are for the highest resolution shell.

[b] All have α=β=γ=90°.

[c] $R_{\text{merge}} = \frac{\sum_{hkl}\sum|I_i(hkl)-\langle I(hkl)\rangle|}{\sum_{hkl}\sum_i I_i(hkl)}$, where $I_i(hkl)$ is the ith measurement of the intensity of reflection hkl and $\langle I(hkl)\rangle$ is its mean value.

[d] Matthews coefficient.

Table 4.8 Summary or refinement statistics.

	AaPurE1						TdPurE2
	S57T_6	S57A_4	209_S57C	S57V2	206_S57N	S57D_102	207_S38D
PDB entry	TBD	TBD	TBD	TBD	TBD	TBD	TBD
Resolution (Å)	35.6-1.75 (1.81-1.75) [a]	29.4-1.99 (2.06-1.99)	43.1-1.99 (2.06-1.99)	42.7-1.81 (1.86-1.81)	43.2-1.79 (1.85-1.79)	48.0-2.73 (3.00-2.73)	44.6-1.69 (1.72-1.69)
No. reflections used							
working	40297	27738	27435	37370	38493	10484	63737
test set	1608	1391	1369	1863	1531	505	3189
Completeness (%)	95.9	96.9	94.6	98.4	97.3	91.9	97.5
Rcryst[b]*(%)*	18.1 (19.8)	16.2 (15.9)	16.1 (18.1)	16.0 (17.4)	15.5 (17.0)	17.3 (21.2)	19.5 (25.9)
Rfree[c]*(%)*	18.8 (24.8)	18.6 (20.5)	18.2 (24.9)	17.6 (22.1)	17.4 (26.9)	21.3 (29.3)	22.3 (31.8)
No. of atoms							
all atoms	2460	2577	2549	2971	2637	2321	5198
protein atoms	2303	2347	2336	2351	2328	2312	4716
solvent atoms	337	221	203	293	309	9	482
R.m.s. deviations from ideality							
Bondlengths (Å)	0.007	0.007	0.007	0.006	0.007	0.008	0.006
Bond angles (°)	1.008	0.997	1.011	1.002	1.009	1.051	1.097
Average isotropic B factors (Å^2)							
protein atoms	26.5	22.5	24.6	17.1	17.9	47.7	27.3
ligand atoms	-	48.5	49.9	-	-	-	-
solvent atoms	37.1	35.7	38.1	31.9	32.0	45.1	33.9
Ramachandran plot statistics (%)							
Residues in favored regions	98.7	98.8	99.4	99.1	99.8	98.4	98.2
Residues in allowed regions	1.3	1.3	0.6	0.9	1.3	1.6	1.6
Outliers	0	0	0	0	0	0	0.2
MolProbity score [percentile]	1.02 (100)	0.92 (100)	0.71 (100)	1.08 (100)	1.9 (100)	1.49 (100)	2.84 (99)
MolProbity clashscore [percentile]	0.64 (100)	1.26 (100)	0.64 (99)	2.3 (99)	1.03 (100)	1.14 (100)	1.07 (100)

[a] Values in parenthesis are for the highest resolution shell.

[b] $R_{\text{cryst}} = = \frac{\sum_{hkl} || F_{\text{obs}} | - | F_{\text{calc}} ||}{\sum_{hkl} | F_{\text{obs}} |}$

[c] $R_{\text{free is}}$ R_{cryst} with a test set of 5% of the reflections excluded from refinement

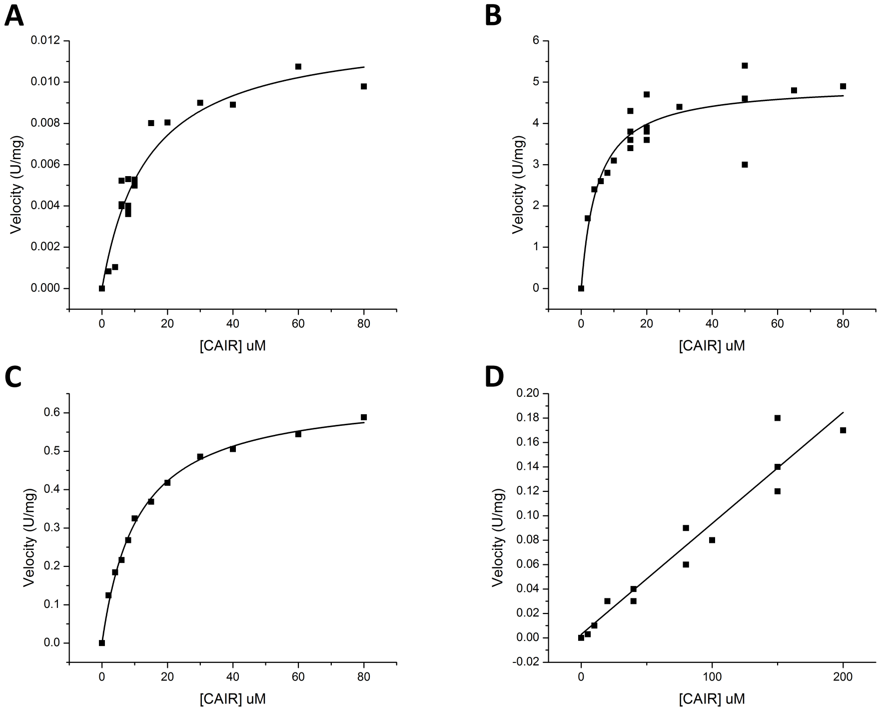

Figure 4.15 Saturation curves of active AaPurE1-S57X mutants. All data were collected in 50 mM Tris-HCl, pH 8 at 30 °C. The velocity (units mg^{-1}) for CAIR decarboxylation of active AaPurE-S57X mutants was plotted against [CAIR] and fit to the Michaelis-Menten equation in Origin, with the exception of AaPurE1-S57V, which was fit to a linear equation. Data for each active AaPurE-S57X mutant is shown above: A, AaPurE1-S57C; B, AaPurE1-S57T; C, AaPurE1-S57A; and D, AaPurE1-S57V.

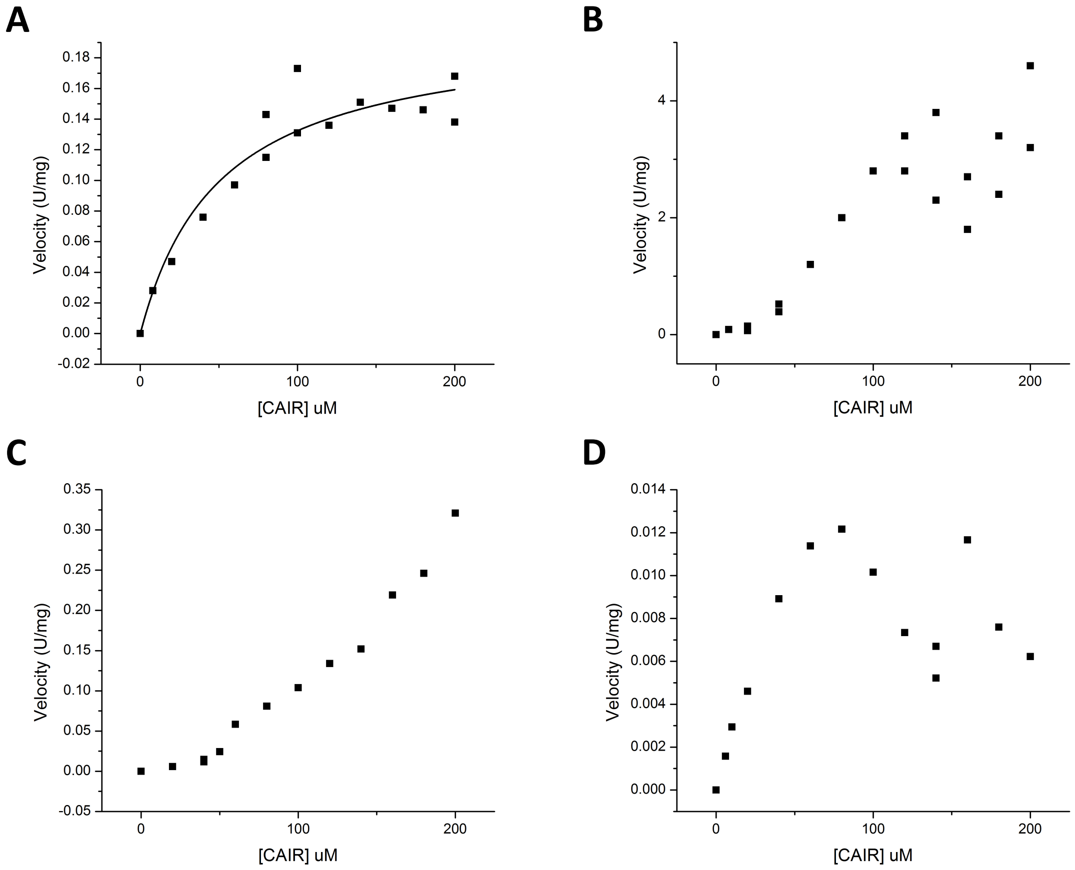

Figure 4.16 Saturation curves of active TdPurE1-S38X mutants. All data were collected in 50 mM Tris-HCl, pH 8 at 30 °C. The velocity (units mg^{-1}) for CAIR decarboxylation of active AaPurE-S57X mutants was plotted against [CAIR] and the TdPurE-S38C data fit to the Michaelis-Menten equation in Origin. Data for each active TdPurE-S38X mutant is shown above: A, TdPurE2-S38C; B, TdPurE2-S38T; C, TdPurE2-S38A; and D, TdPurE2-S38V.

Table 4.9 Kinetic parameters for PurE1 and PurE2 Ser→X mutants at pH 8.

PurE form	rSA[a]	rel. k_{cat}/K_m[b]	k_{cat}/K_m ($\mathrm{M^{-1}\,s^{-1}}$)	k_{cat} ($\mathrm{s^{-1}}$)	K_m (μM)	$K_\mathrm{d\ citrate}$ (μM)[c]	$K_\mathrm{d\ AIR}$ (μM)[d]
AaPurE1	100	100	1.5×10^{6}	12.6	11	275	2.2
AaPurE1-S57T	10	20	3.0×10^{5}	1.5	5	141	is[e]
AaPurE1-S57A	1.4	1.2	1.8×10^{4}	0.2	11	133	is
AaPurE1-S57C	0.03	0.02	2.8×10^{2}	3.9×10^{3}	14	102	is
AaPurE1-S57V	0.03	0.2	2.9×10^{3}	nd[f]	nd	132	is
AaPurE1-S57D	~0	na[g]	na	na	na	63	is
AaPurE1-S57N	~0	na	na	na	na	nd	is
TdPurE2	100	100	7.2×10^{6}	65	9	nd	na
TdPurE2-S38T[h]	9	nd	nd	nd	nd	nd	na
TdPurE2-S38T,F79W	9	nd	nd	nd	nd	nd	nd
TdPurE2-H17W,S38T	0.4	nd	nd	nd	nd	nd	nd
TdPurE2-S38A	0.05	nd	nd	nd	nd	nd	na
TdPurE2-S38C	0.05	0.00002	1.13	5.7×10^{2}	51	nd	na
TdPurE2-S38C,F79W	0.11	nd	nd	nd	nd	237	6
TdPurE2-S38V[h]	0.05	nd	nd	nd	nd	nd	na
TdPurE2-S38D	~0	na	na	na	na	na	na
TdPurE2-S38N	0.02	nd	nd	nd	nd	nd	na
TdPurE2-S38C,F79W	0.11	nd	nd	nd	nd	237	6

[a] rSA, % specific activity relative to wild-type AaPurE1 (39 units per mg protein) or TdPurE2 (185 units per mg protein), determined at 100 μM CAIR, pH 8, 30 °C.

[b] rel. k_{cat}/K_m, % k_{cat}/K_m relative to wild-type AaPurE1 or TdPurE2.

[c] Citrate titrations carried out in 50 mM potassium acetate, 100 mM KCl, pH 4.6 at 25 °C.

[d] AIR titrations carried out in 50 mM Tris-HCl, pH 8.0 at 30 °C.

[e] is, insufficient signal.

[f] nd, not determined.

[g] na, not applicable.

[h] Saturation curves show substrate inhibition above 100 μM CAIR.

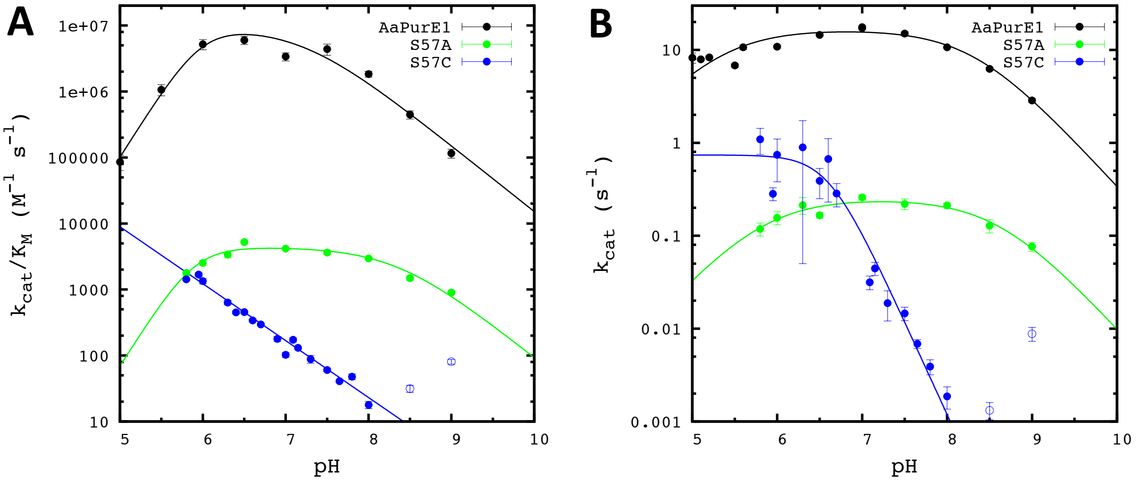

Figure 4.17 pH-rate profiles for AaPurE1 CAIR decarboxylation. The wild-type (black circles) [2], AaPurE1-S57A (green circles), and AaPurE1-S57C (blue circles) k_{cat}/K_m and k_{cat} data are shown above with fits to the data shown in the same color. (A) The log k_{cat}/K_m versus pH profiles are similar bell-shaped curves for both wild-type and S57A ($pK_1 = 6.0 \pm 0.1$ and 5.9 ± 0.1, respectively; $pK_2 = 7.2 \pm 0.1$ and 8.3 ± 0.2, respectively). The log k_{cat}/K_m versus pH profile for S57C has a log-linear dependence on pH with a slope of -0.86 ± 0.03. (B) The log k_{cat} versus pH profiles for wt[2] and S57A are similar bell-shaped curves ($pK_1 = 5.1 \pm 0.2$ and, $= 5.8 \pm 0.1$ respectively; $pK_2 = 8.4 \pm 0.1$ and 8.6 ± 0.1, respectively). The log k_{cat} versus pH profile for S57C has two pK_as averaging ~6.7. Data for pHs 8.5 and 9.0 were excluded from the fit.

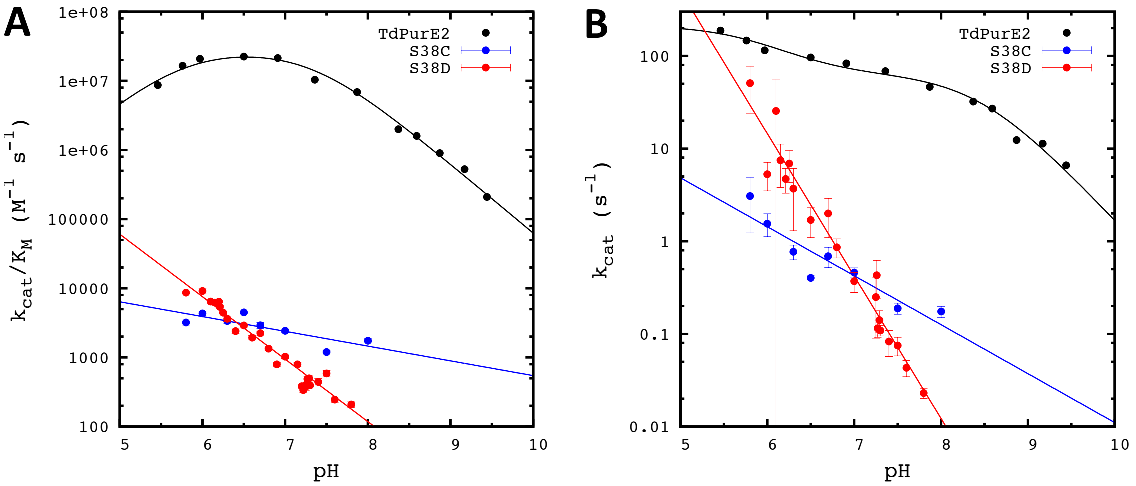

Figure 4.18 pH-rate profiles for TdPurE2 CAIR decarboxylation. The wild-type (black circles)[2], TdPurE2-S38D (red circles), and TdPurE2-S38C (blue circles) k_{cat}/K_m and k_{cat} data are shown above with fits to the data shown in the same color. (A) The log k_{cat}/K_m versus pH profile for wt is bell-shaped curve with $pK_1 = 5.7 \pm 0.2$ and $pK_2 = 7.3 \pm 0.1$. The log k_{cat}/K_m versus pH profile for both S38C and S38D has a log-linear dependence on pH with slopes of -0.21 ± 0.06 and -0.90 ± 0.04, respectively. (B) The log k_{cat} versus pH profile for wt is bell-shaped curve with $pK_1 = 5.9 \pm 0.5$ and $pK_2 = 8.4 \pm 0.1$. The log k_{cat} versus pH profile for both S38D and S38C has a log-linear dependence on pH with slopes of -1.5 ± 0.08 and -0.52 ± 0.09, respectively.

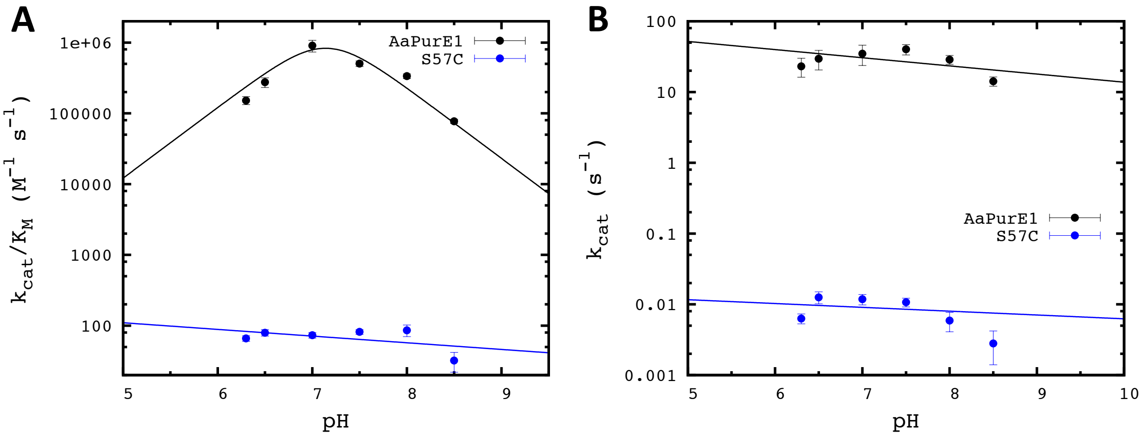

Figure 4.19 pH-rate profiles for AaPurE1 NCAIR→CAIR conversion. The wild-type (black circles) and AaPurE1-S57C (blue circles) k_{cat}/K_m and k_{cat} data are shown above with fits to the data shown in the same color. (A) The log k_{cat}/K_m versus pH profile for wt is a bell-shaped curve with $pK_1 = 8.8$ and $pK_2 = 5.45$. The log k_{cat}/K_m versus pH profile for AaPurE1-S57C has a log-linear dependence on pH with a slope of -0.09 ± 0.08. (B) The log k_{cat} versus pH profiles for wt or AaPurE1-S57C have log-linear dependence on pH with a slopes of -0.12 ± 0.09 and -0.05 ± 0.12, respectively.

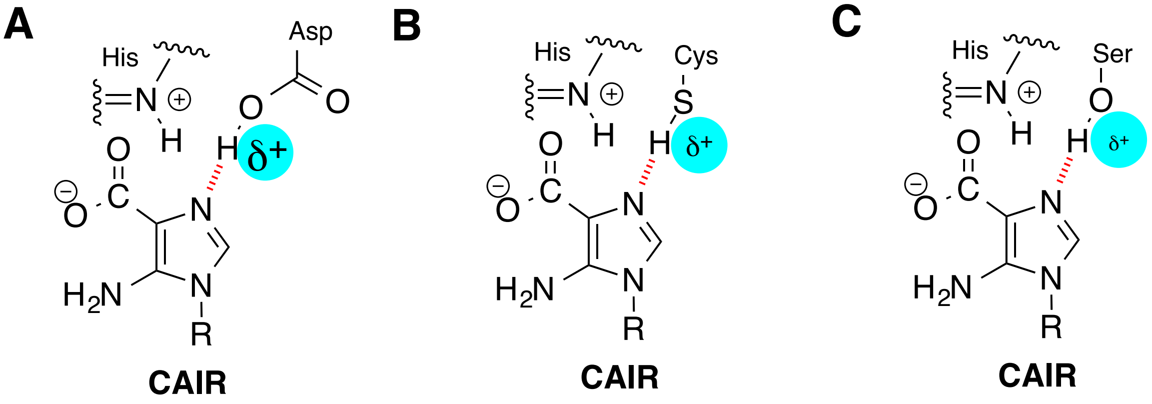

Figure 4.20 The replacement of Ser with Asp or Cys may have electrostatic effects. The strong hydrogen bond provided by Ser is important for C4 protonation. The electrostatic effects of Cys and Asp may diminish the negative character of C4, making C4 more difficult to protonate.

CHAPTER 5 ROLE OF THE CONSERVED ACTIVE SITE LYSINE RESIDUE IN PURE2 FROM *TREPONEMA DENTICOLA*

5.1 Introduction

In Chapter 4 we examined the role of the universally conserved active site Ser. Crystal structures of PurE1 and PurE2 with AIR bound (PDB id 2fwj and 3rgg) reveal that the Ser makes *similar* contacts with the substrate and would appear to have *similar* roles. Surprisingly, this conserved residue appears to have *different* roles between PurE1 and PurE2. In this chapter we examine the role of the class-specific active site Lys in PurE2 to determine if it has different roles in PurE1 and PurE2.

The 40s Loop Basic Residue is Differentially Conserved. The strictly conserved 40s loop sequence SAH[R/K] contains a single absolute, class-linked divergence. The *differentially* conserved basic residue, Arg in PurE1 and Lys in PurE2, contacts the phosphate moiety of the nucleotide and appears to be involved in high affinity substrate binding. [1–3] The *E. coli* PurE1-R46K mutant, which replaces the class-specific Arg, is active, as expected for a residue that is mainly involved in substrate bidning.[3] It is therefore, curious why there are no known exceptions to the class-linked divergence in the basic residue.

Lys May Play a Role Beyond Substrate Binding. An absolute difference between PurE1 and PurE2 is the source of CO_2: PurE1 acquires it by decarboxylation of bound NCAIR (or CAIR), while PurE2 binds it directly from solution. The challenging acquisition of CO_2 by PurE2 has been hypothesized to involve intermediate formation of an N-carboxylated carbamate species on the conserved Lys. This function would be unique to

PurE2 and not necessary in PurE1, as the carbamate moiety of NCAIR serves a similar role as a CO_2 carrier.

The ability to form a carbamate is limited to Lys or the N-terminus. Both urease and Rubisco reactions require the formation of a Lys-carbamate within the active site, and hemoglobin uses an N-terminal carbamate to carry CO_2.[4–6] PurE2 may instead use a Lys-carbamate as a source of substrate. Formation of a Lys-carbamate could also function as a CO_2 concentrating mechanism, which would be advantageous in environments with limited CO_2 availability (Figure 5.1A).

Alternatively, the AIR carbanion could directly attack the fixed carbonyl of the Lys-carbamate (Figure 5.1B). In this scenario, the Lys-carbamate would play a role analogous to N-carboxybiotin in the reaction catalyzed by acetyl-CoA carboxylase, in which the acetyl-CoA carbanion attacks carboxybiotin to form malonyl-CoA and biotin (Figure 5.1C).[7] While this “deactivates” CO_2 as an electrophile, it would confer an potentially compensatory entroptic advantage relative to collisional capture of a gaseous substarte.

This chapter tests the hypothesis that formation of a Lys-carbamate is an obligatory intermediate in TdPurE2 catalysis. We show that the TdPurE2-K41R mutant retains both AIR carboxylase and CAIR decarboxylase activities, indicating that a N-carboxylated Lys is not a required intermediate in the TdPurE2 reaction. We cannot however, rule out a role for Lys-carbamate in other PurE2s under low CO_2 conditions.

5.2 Materials and Methods

Materials. Chemicals were obtained from Sigma or Fisher in the highest purity available unless otherwise noted. CAIR was prepared as described in Chapter 2.[8] AIR was generated enzymatically from CAIR using TdPurE2 and quantitated by Bratton-Marshall assay as described previously.[2] Oligodeoxynucleotides (ODNs) were obtained from Integrated DNA Technologies and used without further purification. Restriction endonucleases, Q5 DNA polymerase, CIP, and T4 DNA ligase were obtained from New

England Biolabs. Phenyl Sepharose CL-6B was obtained from Sigma. Hydroxyapatite (Bio-Gel® HT) and Bradford reagent were obtained from Bio-Rad. PD-10 desalting columns were obtained from GE Health Care.

Methods. Protein concentrations were determined by the method of Bradford with bovine serum albumin as the standard.[9] Small-scale centrifugation steps were performed using an Eppendorf 5424 centrifuge. All other centrifugation steps were performed using a Beckman Avanti J-E centrifuge with a JLA-10.5 or JA-20 rotor. Cell disruption was performed by sonication using a Fisher Scientific Dismembrator 550 at 25% output for 3 cycles (1 min each separated by 1 min cooling intervals) at 4 °C. Spectroscopic measurements were recorded on a Varian CARY-100 UV/Vis spectrophotometer thermostated by a Cary Dual Peltier Accessory temperature controller. Data were analyzed using gnuplot 4.4 by T. J. Kappock. Plasmid DNA was sequenced by the staff of the Purdue University Genomics Core Facility.

Construction of TdPurE–K41M Construct Plasmid pJK687. The general cloning strategy is illustrated in Chapter 3 (Figure 3.4) A 0.21 kb primary PCR product containing *purE2* was amplified using standard Q5 PCR conditions from template pJK376 (14 ng), using ODNs 2124 and 2362. The crude product was digested with *DpnI* and purified using a Qiagen PCR purification kit. A 0.55 kb primary PCR product containing *purE2* was amplified using standard Q5 PCR conditions from template pJK376 (14 ng), using ODNs 2125 and 2363. The crude product was digested with *DpnI* and purified using a Qiagen PCR purification kit. Cross-over PCR product was obtained using standard Q5 PCR conditions, with a single exception: the annealing time was increased to 1 min, from a mixture containing primary PCR products (25 ng each) and ODNs 2124 and 2125. The 0.723 kb cross-over product was digested with *NdeI* and *XhoI*, and ligated into the same sites of the destination vector pET23a to yield TdPurE2-K41M expression plasmid pJK687.

Construction of TdPurE2–K41R Construct Plasmid pJK688. A 0.21 kb primary PCR product containing *purE2* was amplified using standard Q5 PCR conditions from template pJK376 (14 ng), using ODNs 2124 and 2364. The crude product was digested with *DpnI* and purified using a Qiagen PCR purification kit. A 0.55 kb primary PCR product containing *purE2* was amplified using standard Q5 PCR conditions from template pJK376 (14 ng), using ODNs 2125 and 2365. The crude product was digested with *DpnI* and purified using a Qiagen PCR purification Cross-over PCR product was obtained using standard Q5 PCR conditions, with a single exception: the annealing time was increased to 1 min, from a mixture containing primary PCR products (25 ng each) and ODNs 2124 and 2125.The product was digested with *NdeI* and *XhoI,* and ligated into the same sites of the destination vector pET23a to yield TdPurE2-K41R expression plasmid pJK688.

Mutant TdPurE2 Overexpression and Isolation. TdPurE2-K41M was overexpressed and isolated as detailed for wild-type TdPurE2 (Chapter 3).[2] TdPurE2-K41R was expressed using the same TdPurE2 protocol,[2] but isolated using the AaPurE1 isolation protocol (Chapter 3).[1] Fresh column media were used for each mutant to avoid any possibility of cross-contamination. TdPurE2 mutants were concentrated to >3 mg mL^{-1} with an Amicon ultrafiltration device containing a YM30 membrane. The protein solution was frozen by drop-wise addition to liquid N_2 and stored at -80 °C.

PurE2-mediated Decarboxylation Assays. Continuous assays of PurE2-mediated CAIR decarboxylation were performed according to a published method.[1] A final volume of 0.6 mL in a masked, 1 cm pathlength cuvette containing 50 mM Tris-HCl, pH 8 and 100 µM CAIR was incubated at 30 °C for at least 3 min. Reactions were initiated by addition of either TdPurE2-K41X (12-24 ng, 1.4-2.8 nM [subunits]). The initial velocity of CAIR decarboxylation to AIR ($\Delta\varepsilon_{260}$ =8930 M^{-1} cm^{-1}) was recorded at 260 nm, with a small background decarboxylation rate subtracted. CAIR was quantitated by endpoint assay using the same method, except that 50 µg mL^{-1} TdPurE2 was the enzyme. A unit is defined as the amount of enzyme that forms 1 µmol of product per minute. Kinetic constants were determined by fitting the plotted concentration versus velocity (units mg^{-1}) to the standard Michaelis-Menten equation.

PurE2-mediated AIR Carboxylation Assays. Continuous assays of PurE2-mediated AIR carboxylation were modified from published method for PurE1 NCAIR→CAIR carboxylation assays.[10] Assays were carried out at 23 °C in in a final volume of 0.7 mL, 1x triple buffer (100 mM Tris-HCl, 50 mM MES, 50 mM acetic acid) pH 7.5, 10 mM $MgCl_2$, 2 mM PEP, 0.5 mM ATP, 10 mM L-aspartate, 1 mM $KHCO_3$, 1.2 units of pyruvate kinase (477 units mg^{-1}, Sigma P9136), 4 units of H6PurC (isolated by Jesse Murphy), AIR (100 μM), and varying amounts of TdPurE2s at 10 °C. After pre-incubation for 3 min, the reaction was initiated by addition of CO_2 (variable amounts of a 53 mM solution in water, generated by constant bubbling of gas released from dry ice through nanopure water at 10 °C) and SAICAR formation monitored directly ($\Delta\varepsilon_{282}$ = 8607 M^{-1} cm^{-1}) with a correction for PurE2-independent SAICAR formation. Reactions containing all assay components except PurE2 were performed to determine a background velocity for PurE2-independent SAICAR formation.

5.3 Results

Creation of TdPurE2-K41X Mutants. TdPurE-K41R mutants were created to investigate the role of the class-specific Lys in the TdPurE2 reaction. TdPurE2 mutants could not be created by standard Quikchange mutagenesis. Therefore, cross-over PCR was employed to generate both TdPurE2-K41X mutants. Sequencing confirmed that only the intended mutations were obtained.

Purification of the Recombinant TdPurE2-K41M Mutant. The published isolation protocol[2] was successfully used to isolate TdPurE2-K41M with relatively high specific activity and purity (Table 5.4 and Figure 5.2).

Purification of the Recombinant TdPurE2-K41R2 Mutant. TdPurE2-K41R could not be isolated using the published TdPurE2 protocol.[2] Unexpectedly, the published AaPurE1 isolation protocol[1] was successfully used to isolate TdPurE2-K41R with relatively high activity and purity (Table 5.4 and Figure 5.2).

Kinetic Characterization of the TdPurE2-K41R Mutant at pH 8. Kinetic constants (K_m and k_{cat}) for CAIR decarboxylation were obtained for the TdPurE2-K41R mutant to determine if the diminished activity of K41R is due to binding, catalysis, or both. The substitution of Lys with either the positively charged Arg or uncharged Met residue does not abrogate activity in either K41X mutant (Table 5.4 and Figure 5.3). Formation of a Lys-carbamate is therefore not an *obligatory* catalytic intermediate in TdPurE2 catalysis. This does not exclude a role in CO_2 enhancement or off-pathway formation of Lys-carbamate in PurE2s.

The K_m of TdPurE2-K41R is ~3.6 times higher than TdPurE, indicating that the Lys→Arg mutation may impair CAIR binding.

The observed TdPurE2-K41R AIR carboxylase activity is very low compared to wild-type TdPurE2 (Table 5.4), but may be an underestimate, because the AIR carboxylase activity of TdPurE-K41R was likely recorded below its AIR K_m. We did not obtain kinetic parameters for AIR carboxylation by TdPurE2-K41R, but we assume the mutant should have a higher AIR K_m relative to wild-type.

5.4 Discussion

TdPurE2 Activity Does Not Require Formation of a Lys-Carbamate Intermediate. PurE2 acquires CO_2 directly from solution and this challenging acquisition was suggested to require the intermediate formation of an N-carboxylated species on the active site Lys. Therefore, we tested the hypothesis that formation of a Lys-carbamate is necessary for PurE2 function by replacing it with residues that are unable to form carbamates. We found that TdPurE2-K41R retains substantial activity and is capable of both CAIR decarboxylation and CAIR generation from AIR and CO_2, indicating the formation of a Lys-carbamate is not an obligatory intermediate in TdPurE2 catalysis.

The Differentially Conserved Residue Appears to Have the Same Role in Both PurE1 and PurE2. Logic would dictate that the single *differentially conserved* side chain contact to the substrate should have different roles in each class. However, the observation that both EcPurE1-R46K[3] and TdPurE2-K41R mutants retain activity suggests that this residue has a relatively simple role in substrate binding.

The Conserved Basic residue is Not Critical for Catalysis. Perhaps the most unanticipated result in this chapter is that the non-conservative TdPurE2-K41M mutant retains substantial activity. We and others have thought that the electrostatic interaction is important for catalysis, as neither PurE form reacts with the AIR and CAIR nucleosides. Evidently an interaction between the phosphate moiety of the substrate and a positively charged residue is not essential for PurE2 function.

Lys Could Have a Role Beyond Simple Substrate Binding. TdPurE2 is from the mesophilic bacterium *T. denticola*, which occupies an microaerophilic subgingival niche that may provide sufficient CO_2 for catalysis. While formation of a Lys-carbamate is not obligatory for TdPurE2 it could be required for PurE2s from other organisms that face larger challenges in acquiring CO_2.

Under limiting CO_2 conditions the formation of the Lys-carbamate could either 1) react directly with the AIR carbanion or 2) serve as a CO_2 concentrating mechanism. (Figure 5.1). We consider these possibilities separately, although they are not necessarily mutually exclusive.

The first case, is analogous to the reaction catalyzed by acetyl-CoA carboxylase, in which the Lys-carbamate would be attacked by the AIR carbanion to form CAIR. However, examination of the PurE2•AIR crystal structure (PDB id 3rgg) suggests that a large protein rearrangement would have to occur to allow the Lys-carbamate to position itself within range of AIR C4. There is no evidence for large-scale rearrangement of any PurE form.

In the second case, formation of a Lys-carbamate as a CO_2 concentrating mechanism could confer an advantage by increasing the local concentration of CO_2 under low CO_2 conditions. This possibility is directly addressed by the results reported here.

Environmental Constraints May Have Affected the Strict Conservation of Lys in PurE2. Environmental CO_2 availability is influenced by a number of factors including CO_2 partial pressure, pH and most important, temperature. CO_2 solubility is greatly diminished at high temperatures (Figure 5.4).

If we assume that PurE2 evolved under warm, anaerobic, conditions on early Earth,[11,12] then the presence of abundant CO_2 makes the ability to concentrate CO_2 superfluous. However, as primitive organisms left the immediate vicinity of geological CO_2 sources (e.g. deep ocean sediments)[14] and as O_2 appeared in the atmosphere, the ability to concentrate CO_2 from the environment might have become advantageous.

Under low CO_2 conditions, a Lys acquired by mutation might have conferred a selective advantage in organisms that inherited a *purE2* gene. Its strict conservation could be a consequence of its early evolutionary importance in these low CO_2 environments. Lys could still be required in hot, low CO_2 environments, which could explain the retention of *purE2* genes in a small number of mostly thermophilic organisms (Chapter 1).

Increasing the local CO_2 concentration would also increase the substrate specificity for CO_2 over the smaller, more reactive O_2. In particular, this would have helped PurE2 avoid the fate of Rubisco, which evolved a catalytic strategy under anaerobic conditions that has liabilities under the modern oxic conditions (Chapter 6).

Conserved Residues Have Different Roles and Differentially Conserved Residues Do Not. In PurE, the *differentially conserved* basic residue appears to have *similar* roles in ligand binding. In contrast, the *universally conserved* Ser residue appears to have *different* roles in PurE1 and PurE2 (Chapter 4). Crystal structures of PurE1 and PurE2 with AIR bound (PDB id 2fwj and 3rgg) reveal that the Ser makes *similar* contacts with the substrate and would appear to have *similar* roles. Ser is usually associated with donation of a hydrogen bond, but is also capable of accepting a hydrogen bond, which may occur at low pH in the PurE2 reaction.

Mutation of a single residue in either PurE class does not generate a PurE of the other class. We hypothesize that several amino acid changes occurred during the evolutionary divergence of one class of PurE from another. These are likely to occur in the other three loops surrounding the substrate: the P loop, the 70s loop, and the P loop from an neighboring subunit.

5.5 Future Directions

The presence of a *purE2* gene in a small number of thermophilic bacteria may require the intermediate formation of a Lys carbamate. This can be tested by the expression, isolation, and characterization of a monofunctional PurE2 from the thermophilic bacteria discussed in Chapter 1.

5.6 References

1. Constantine, C. Z., Starks, C. M., Mill, C.P., Ransome, A. E., Karpowicz, S.J., Francois, J.A., Goodman, R.A. and Kappock, T. J. Biochemical and Structural Studies of N^5-Carboxyaminoimidazole Ribonucleotide Mutase from the Acidophilic Bacterium *Acetobacter aceti. Biochemistry* **45,** 8193–8208 (2006).

2. Tranchimand, S., Starks, C. M., Mathews, I. I., Hockings, S. C. and Kappock, T. J. *Treponema denticola* PurE is a bacterial AIR carboxylase. *Biochemistry* **50,** 4623–4637 (2011).

3. Hoskins, A. A., Morar, M., Kappock, T. J., Mathews, I. I., Zaugg, J. B., Barder, T. E., Peng, P., Okamoto, A., Ealick, S. E. and Stubbe, J. N^5-CAIR mutase: Role of a CO_2 Binding Site and Substrate Movement in Catalysis. *Biochemistry* **46,** 2842–2855 (2007).

4. Cleland, W. W., Andrews, T. J., Gutteridge, S., Hartman, F. C. and Lorimer, G. H. Mechanism of Rubisco: The Carbamate as General Base. *Chem. Rev.* **98,** 549–562 (1998).

5. Jabri, E., Carr, M. B., Hausinger, R. P. and Karplus, P. A. The Crystal Structure of Urease from *Klebsiella aerogenes*. *Science* **268,** 998–1004 (1995).

6. Lorimer, G. H. Carbon Dioxide and Carbamate Formation: the Makings of a Biochemical Control System. *Trends Biochem. Sci.* **8,** 65–68 (1983).

7. Polyak, S. W., Abell, A. D., Wilce, M. C. J., Zhang, L. and Booker, G. W. Structure, Function and Selective Inhibition of Bacterial Acetyl-Coa Carboxylase. *Appl. Microbiol. Biotechnol.* **93,** 983–992 (2012).

8. Sullivan, K. L., Huma, L. C., Mullins, E. A, Johnson, M. E. and Kappock, T. J. Metal Stopping Reagents Facilitate Discontinuous Activity Assays of the *de novo* Purine Biosynthesis Enzyme PurE. *Anal. Biochem.* **452,** 43–45 (2014).

9. Bradford, M. M. A Rapid and Sensitive Method for the Quantitation of Microgram Quantities of Protein Utilizing the Principle of Protein-Dye Binding. *Anal. Biochem.* **72,** 248–254 (1976).

10. Firestine, S. M., Misialek, S., Toffaletti, D.L., Klem, T. J., Perfect, J. R. and Davisson, V. J. Biochemical Role of the *Cryptococcus neoformans* ADE2 Protein in Fungal *de novo* Purine Biosynthesis. *Arch. Biochem.* **351,** 123–134 (1998).

11. Sheldon, N. D. Precambrian Paleosols and Atmospheric CO_2 Levels. *Precambrian Res.* **147,** 148–155 (2006).

12. Holland, H. D., Lazar, B. and McCaffrey, M. Evolution of the Atmosphere and Oceans. *Nature* **320,** 27–33 (1986).

13. Dodds, W. S., Stutzman, L. F. and Sollami, B. J. Carbon Dioxide Solubility in Water. *Ind. Eng. Chem. Chem. Eng. Data Ser.* **1,** 92–95 (1956).

14. Yanagawa, K., Morono, Y., de Beer, D., Haeckel, M., Sunamura, M., Futagami, T., Hoshino, T., Terada, T., Nakamura, K., Urabe, T., Rehder, G., Boetius, A. and Inagaki, F. Metabolically Active Microbial Communities in Marine Sediment Under High-CO_2 and Low-pH Extremes. *ISME J.* **7,** 555–567 (2013).

5.7 Figures and Tables

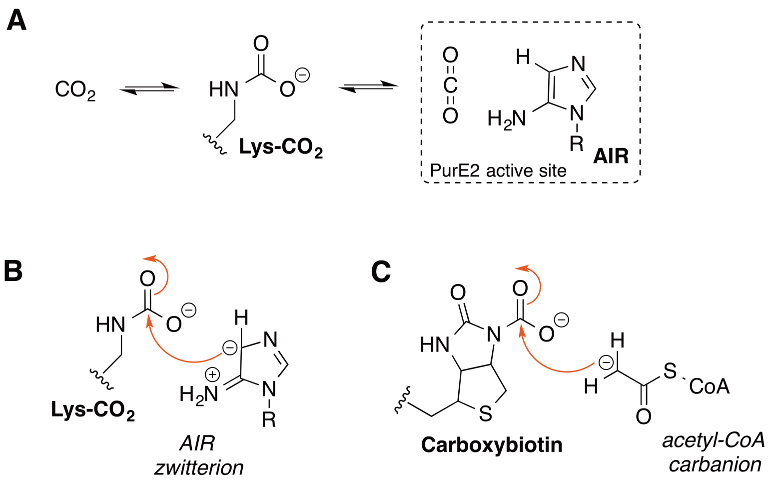

Figure 5.1 Potential roles for the Lys-carbamate in the PurE2 reaction. (A) The reversible formation of a Lys-carbamate would increase the local CO_2 concentration in the PurE2 reaction. (B) The AIR C4 carbanion may directly attack the carbonyl of the Lys-carbamate to form CAIR. (C) The acetyl-CoA carbanion directly attacks the carbonyl of enzyme-bound carboxybiotin to form malonyl-CoA.

Table 5.1 Description of bacterial strains used in this chapter.

Strain	Description	Source
DH5α	F′ φ80lacZΔM15 Δ(lacZYA-argF)U169 *deoR recA1 endA1 hsdR17(r*$_K^-$ m$_K^+$) *phoA supE44 thi-1 gyrA96 relA1*	Lab stock
CC1215	F$^-$ *ompT gal dcm lon hsd*S$_B$*(*r$_B^-$ m$_B^-$*) ΔpurE*736::kan λ(DE3 [*lacI lacUV5*-T7 *gene 1 ind1 sam7 nin5*])	This study

Table 5.2 Oligodeoxynucleotides (ODNs) used in this chapter.[a]

ODN	Sequence (5’→3’)	
2124	TAATACGACTCACTATAGGG	T7 promoter
2125	GCTAGTTATTGCTCAGCGG	T7 terminator
2362	GACACTACATGCTCaGCTGTcaTgTGCGCGGAGCCGATG	TdPurE2-K41M
2363	CATCGGCTCCGCGCAcAtgACAGCtGAGCATGTAGTGTC	TdPurE2-K41M
2364	GACACTACATGCTCaGCTGTTcTATGCGCGGAGCCGATG	TdPurE2-K41R
2365	CATCGGCTCCGCGCATAgAACAGCtGAGCATGTAGTGTC	TdPurE2-K41R

[a] Changes in the coding region that deviate from the genomic sequence are in lower case.

Table 5.3 Description of Plasmids used in this chapter.

Plasmid	Description	Source
pJK687	*purE2$_{Td}$-K41M* in pET23a	This study
pJK688	*purE2$_{Td}$-K41R* in pET23a	This study

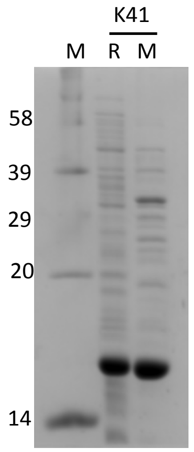

Figure 5.2 SDS-PAGE analysis of isolated TdPurE2-K41X forms. A 12% polyacrylamide gel was loaded with 3 μg protein per lane: M, Sigma biotinylated marker; R, TdPurE-K41R; and M, TdPurE-K41M. Note the slightly increased mobility of K41M, which is presumably due to the deletion of a positively charged residue. Molecular weights (kDa) are denoted along the left side of the gel.

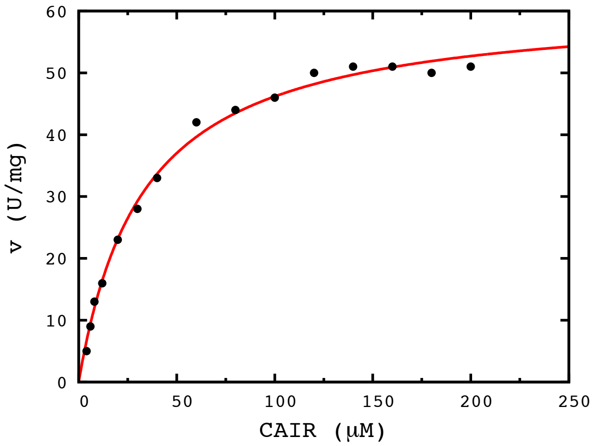

Figure 5.3 Saturation curve of TdPurE2-K41R. All data were collected in 50 mM Tris-HCl, pH 8 at 30 °C and fit to the Michaelis-Menten equation.

Table 5.4 Kinetic parameters for TdPurE2-K41X mutants at pH 8.

	rSA[a]	rel. k_{cat}/K_m [b]	k_{cat}/K_m (M^{-1} s^{-1})	k_{cat} (s^{-1})	K_m (µM)	rSA AIR→CAIR [c]
TdPurE2[d]	100	100	7.2×10^6	65	9	100
TdPurE2-K41R	25	74	5.3×10^5	17.5	33	1.2
TdPurE2-K41M	16	nd[e]	nd	nd	nd	nd

[a] rSA, % specific activity in the CAIR decarboxylation reaction relative to wild-type TdPurE2 (185 U mg^{-1}) at 100 µM CAIR, pH 8.0, 30 °C.

[b] rel. k_{cat}/K_m, % k_{cat}/K_m relative to wild-type TdPurE2 (7.2×10^6).

[c] rSA, % specific activity in the AIR carboxylase reaction relative to wild-type TdPurE2 (195 U mg^{-1}) at 100 µM CAIR, pH 7.5, 10 °C.

[d] Published values.[2]

[e] nd; not determined.

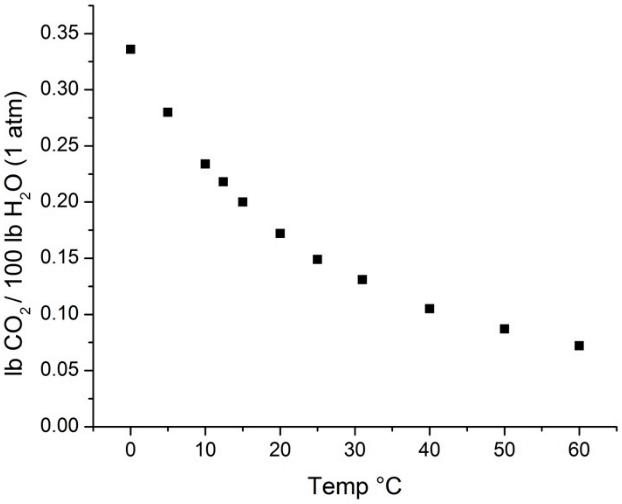

Figure 5.4 Dissolved CO_2 at various temperatures. CO_2 availability in water decreases as temperature increases. [13]

CHAPTER 6 OXYGENASE ACTIVITY IN AN “INACTIVE” MUTANT PURE FROM *TREPONEMA DENTICOLA*

6.1 Introduction

In both PurE1 and PurE2, the active site His provides the essential proton to CAIR C4 for C—C bond scission.[1–3] However, crystallography shows that the His is not required for CAIR cleavage. A CAIR-soaked crystal of the completely inactive *A. aceti* PurE1-H59N mutant (PDB code 2fwp) contained AIR and CO_2 in the active site (Figure 3.2, Chapter 3), mimicking the ternary PurE•AIR•CO_2 complex. This crystal structure was the first evidence that if the proton source is deleted, decarboxylation still occurs, indicating that PurE1, and possibly the PurE2 His mutants are not truly inactive. In this chapter we discuss an initial examination of oxygenase activity in the “inactive” TdPurE2-H40N mutant.

PurE2 and Rubisco are the most abundant CO_2-dependent carboxylases on the planet that do not require substrate activation by ATP or other energy inputs. Why these two enzymes have such different reactivities with O_2 or CO_2 is also considered in this chapter.

CO_2 Abundance Determines Rubisco Specificity. Most CO_2 removed from the atmosphere is converted to carbohydrates by Rubisco (ribulose-1,5-bisphosphate carboxylase/oxygenase) during photosynthesis.[4] Rubisco has a limited ability to promote reactions with CO_2 over O_2, a smaller, more abundant, and more reactive gas, leading to an “inevitable,” apparently wasteful oxygenase reaction.[5] Rubisco generates a reactive ribulose-1,5-bisphosphate enediol(ate) that attacks either CO_2 or O_2 (Figure 5.1). Rubisco

is therefore under pure kinetic control, with reaction outcomes determined by the relative gas concentrations and ratio of specificity constants (k_{cat}/K_m).[6]

Enzymes, including Rubisco that form a carbanionic intermediate often catalyze reactions with O_2. Oxygenase activity can be the primary[7,8] or a secondary (promiscuous) function.[9,10]

PurE1 and PurE2 Do Not React with O_2. PurE1 has no detectable oxygenase activity.[10] This is not surprising, as PurE1 supplies CO_2 stoichiometrically from either of its substrates and scrupulously prevents transiently produced CO_2 from escaping the active site. O_2 therefore has no opportunity to gain access to the AIR carbanion intermediate. In addition, the proximity of the electron-deficient carbon in CO_2 may be required to stabilize the AIR carbanion.

PurE2 encounters essentially the same situation as Rubisco. Unlike PurE1, it must expose a portion of its active site, including Lys 41 and AIR C4 to small molecules. The "CO_2 portal" (Chapter 1) is a consequence of the need for CO_2 to enter (or exit) *after* AIR, which comprises a large part of the gas-binding site and is probably required to ensure CO_2 binds to PurE2 at all.

Inspection of the proposed mechanisms for PurE2 and Rubisco shows they have a critical difference in the required sequence of deprotonation and C—C bond formation. Rubisco encounters CO_2 *after* carbon deprotonation. PurE2 flips the sequence of steps in C—C bond formation: its substrate reacts with CO_2 *before* carbon deprotonation (Figure 6.1). This apparently fundamental chemical difference in CO_2 fixation appears to have been overlooked. This seemingly small difference in chemical strategy would bypass both sluggish carbon deprotonation and greatly improve CO_2/O_2 selectivity

A Catalytically Inactive Form of PurE2 May React with O_2. The TdPurE2-H40N mutant, which lacks the key His, was generated with the expectation that it would be inactive.[3] Surprisingly, functional complementation experiments in Δ*purK* and Δ*purE1 E. coli* strains (a functional PurE2 should complement both deletions) revealed that TdPurE2-

H40N was not simply inactive but caused a growth defect: a Δ*purK* strain grew worse than a vector-only control on solid minimal medium. We wanted to know if the growth defect could be explained if TdPurE2-H40N were somehow capable of *destroying* AIR, CAIR, or both.

An X-ray crystal structure of the TdPurE2•AIR binary complex shows good electron density for all parts of AIR (Figure 6.2A).[3] In contrast, a *higher-resolution* crystal structure of TdPurE2-H40N co-crystallized with CAIR provides clear evidence that the aminoimidazole ring is disrupted by the "inactive" mutant TdPurE2-H40N (Figure 6.2B). The ligand contains an acyclic moiety of ≥3 non-H atoms that were tentatively modeled as 5-phosphoribofuranosylurea (PRU, Figure 6.2C).

PRU is not the only ligand consistent with the observed electron density, but it is anticipated to be more stable than alternatives that fit in the difference electron density maps. While the oxygen atom is not well modeled, it is necessary to avoid highly labile structures such as am iminoamine substituent (R5P-NHCH=NH_2^+). We can however, infer that the terminal atom is a hydrogen bond donor based on proximity to backbone carbonyls.

This chapter details the discovery of a very low level of oxygenase activity in the "inactive" PurE2 mutant, TdPurE2-H40N.

6.2 Materials and Methods

Materials. Chemicals were obtained from Sigma or Fisher in the highest purity available unless otherwise noted. CAIR was prepared as described in Chapter 2.[11] AIR was generated enzymatically from CAIR using TdPurE2 and quantitated by Bratton-Marshall assay as described previously.[3] Phenyl Sepharose CL-6B was obtained from Sigma. Hydroxyapatite (BioGel®-HT) and Bradford reagent were obtained from Bio-Rad. PD-10 desalting columns were obtained from GE Health Care.

Methods. Protein concentrations were determined by the method of Bradford with bovine serum albumin as the standard.[12] Small-scale centrifugation steps were performed using an Eppendorf 5424 centrifuge. All other centrifugation steps were performed using a Beckman Avanti J-E centrifuge with a JLA-10.5 or JA-20 rotor. Cell disruption was performed by sonication using a Fisher Scientific Dismembrator 550 at 25% output for 3 cycles (1 min each with 1 min cooling periods in-between) at 4 °C. Spectroscopic measurements were recorded on a Varian CARY-100 UV/Vis spectrophotometer thermostated by a Cary Dual Peltier Accessory temperature controller.

PurE1 and PurE2 Overexpression and Isolation. AaPurE1 and AaPurE1-H59N were overexpressed and isolated as detailed for wild-type AaPurE1 (Chapter 3).[1] TdPurE2 and TdPurE2-H40N were overexpressed and isolated as detailed for wild-type TdPurE2 (Chapter 3).[3]

Aerobic AIR Destruction Assays. A reaction mixture (0.55 mL total) contained 50 μM AIR in 50 mM Tris-HCl (pH 8.0). The reaction mixture was incubated at room temperature for 3 min prior the addition of AaPurE1 (60 μM, 620 μg), TdPurE2 (60 μM, 564 μg), AaPurE1-H59N (60 μM, 620 μg), or TdPurE2-H40N (60 μM, 564 μg). Controls lacking enzyme and containing BSA (1 mg mL^{-1}) were performed in parallel. Aliquots (0.1 mL) were removed at 0 min, 1 h, 3h, 5h, and 8 h and immediately quenched by addition to 0.2 mL of pre-mixed 665 mM potassium phosphate in 10% TCA (w/v) and $NaNO_2$ 0.05% (w/v). Reactions were then derivatized by the Bratton-Marshall Assay,[9] which is highly specific for diazotizable amines, and the absorbance spectra recorded.

Anaerobic AIR Destruction Assays. These experiments were performed in an anaerobic chamber (N_2 atmosphere, ≤5 ppm O_2) but were otherwise identical to above protocol for aerobic AIR destruction assay. After Bratton-Marshall derivatization samples were removed from the anaerobic chamber and absorbance spectra were recorded.

6.3 Results

TdPurE2-H40N has detectable oxygenase activity. In all of our experiments, no evidence was obtained for any Bratton-Marshall reactive species other than AIR. AIR concentrations decreased in the presence of TdPurE2-H40N, with a half-life of about 4 h. No decomposition was observed in reaction mixtures prepared without enzyme (not shown), in the presence of small amounts of either AaPurE1 (6.7 nM, 68 ng) or TdPurE2 (1.4 nM, 13 ng) (not shown), BSA, AaPurE1-H59N (±O_2), or TdPurE2-H40N maintained in an *anaerobic environment* (Figure 6.3). We concluded that TdPurE2-H40N has a function not previously described: it catalyzes the irreversible, O_2-dependent destruction of AIR to an unknown product. This low level of AIR oxygenase activity is the only known reaction performed by TdPurE2-H40N.

6.4 Discussion

PurE1 and PurE2 Do Not Have Detectable Oxygenase Activity. AIR is an inhibitor of PurE1,[13] but binds in the same orientation as in PurE2. PurE1 was previously shown to lack oxygenase activity[10] and our results confirm this. Neither AaPurE1 nor AaPurE1-H59N had detectable oxygenase activity when incubated with AIR. This is likely due to one of two things: either 1) PurE1 disallows access of O_2 to AIR or 2) an AIR carbanion is only formed when AIR•CO_2, delivered by NCAIR or CAIR, are confined together. In addition, a crystal structure of AaPurE1-H59N•AIR•CO_2 (PDB code 2fwp) contains no additional room for an O_2 to enter the vicinity of AIR.

The PurE2 reaction with CO_2 is *reversible*, but the proposed reaction with O_2 involves several *irreversible* steps. The first three steps are similar to the Rubisco oxygenation reaction, with the aminoimidazole ring opening being the first irreversible step. This is followed by a second hydrolysis step, which closely resembles 2′-deoxy-PRU formation in damaged DNA[8] to produce diformamide and PRU (Figure 6.4).

In its solvent-exposed active site, Rubisco generates a reactive carbanion that *irreversibly* reacts with either O_2 or CO_2. PurE2, like Rubisco, generates a reactive carbanion in a solvent-exposed active site but catalyzes a *reversible* reaction with CO_2. Although we cannot detect any reaction with O_2, it is possible that active PurE2 still allows O_2 to react with the AIR carbanion, but acts to prevent the subsequent irreversible steps including ring opening which would be required to detect products of the oxygenase reaction (boxed steps in Figure 6.4). Aminoimidazole ring opening would require a sterically demanding rearrangement within the rigid PurE2 active site, which cannot accommodate NCAIR or other analogs.[14]

The Critical Active Site His May Shield the AIR Carbanion. The "inactive" TdPurE2-H40N has oxygenase activity that has never been detected in wild-type TdPurE2 or any other PurE2 form. Wild-type PurE2 contains the general acid/general base His in the active site, which is located near the site of AIR carbanion formation at AIR C4. This residue could also serve to shield the reactive AIR carbanion from O_2, an effect lost when Asn replaces His. Asn is smaller and cannot donate a proton, although it could provide a hydrogen bond; this difference may be enough to allow a slow reaction with O_2.

Our working hypothesis for CO_2 selectivity, for both PurE1 and PurE2, is that the AIR carbanion does not form in the absence of CO_2. The AIR•CO_2 complex may be required to stabilize the AIR carbanion; therefore, without CO_2 present, AIR does not form the reactive intermediate and is unavailable to react with O_2 (Figure 6.1).

Did PurE1 and PurE2 Evolve in an Anaerobic Environment with Accidental and Inherent Selectivity for CO_2? PurE1, PurE2, and Rubisco developed in an anoxic environment. Modern Rubisco cannot suppress oxygenase activity without the support of carbon concentrating mechanisms within carboxysomes of CO_2 fixing bacteria[15] and CO_2 concentrating accessory systems in higher plants (C4 and crassulacean acid metabolism). All of these require specialized anatomy or extra catalysts that support CO_2 fixation. The complete lack of associated carbon concentration mechanisms suggests that PurE1 and PurE2 always had the ability to selectively react with CO_2 over O_2.

Chemical considerations and phylogenetic analyses do not indicate if PurE1 evolved from PurE2 or vice versa (Chapter 1). Results presented in this thesis deepen the mystery of which came first, as it is clear that a point mutant in the differentially conserved 40s loop has no functional significance. If an “ambidextrous” bifunctional PurE1/PurE2 is never discovered, it will be difficult to reconstruct the series of events that gave rise to the modern stark functional difference between PurE1 and PurE2.

PurE1 emerged either 1) in high-CO_2 conditions as a way to exploit abundant NCAIR forming spontaneously from AIR or 2) in low–CO_2 conditions, to exploit NCAIR produced by a serendipitous and likely promiscuous, activity of a PurK progenitor. In either case, PurE1 did not need to acquire selectivity for CO_2; its dependence on NCAIR ensured CO_2 would be available to shield the AIR carbanion. However, PurE2 may well have acquired increased CO_2 selectivity as the atmospheric O_2 levels on early Earth increased. The strict conservation of Lys in PurE2 (discussed in Chapter 5), suggests that it might have once served as a CO_2 concentrating mechanism, a useful feature under increasing O_2.

Is PurE Class “Choice” a Result of Positive Selection or is it an Accident? CO_2 is a membrane permeable gas produced by decarboxylations throughout cellular metabolism in both anaerobes and aerobes. Most early anaerobic environments probably contained abundant CO_2. However, under modern aerobic conditions, CO_2 produced from metabolism must be captured as bicarbonate or it will escape to the environment. This phenomenon explains why carbonic anhydrase is essential for aerobic bacteria and under low CO_2 conditions. Aerobic bacteria lacking carbonic anhydrase cannot efficiently recycle CO_2 so will starve for bicarbonate;[16,17] which is important to support essential subsequent anabolic processes such as fatty acid, amino acid, and nucleotide biosynthesis.[17] Carbonic anhydrase accelerates the spontaneous hydration of CO_2 to bicarbonate by ~10^5 fold. Carbonic anhydrase does not exist in most anaerobes including archea and microbes containing a PurE2.[3,18]

Like PurE2, systems containing PurE1-only simply require high CO_2 (Chapter 1). Selection of a PurE1+PurK system instead relies on bicarbonate as the source of CO_2 for purine biosynthesis. This system may place a burden on carbonic anhydrase to ensure sufficient CO_2 is recycled to support several high flux pathways. Selection of PurE2 under an anaerobic environment may confer a selective advantage. Because PurE2 can directly use CO_2, this would uncouple the demand for bicarbonate from the high flux purine pathway and lessen competition for available bicarbonate with other high flux pathways.

6.5 Future work

A TdPurE2-H40N crystal structure with authentic PRU nucleoside bound is a good first step to test the hypothesis that crystalline TdPurE2-H40N produces PRU.

Synthetic PRU could also be used as a standard to unambiguously identify the AIR oxygenase product in mutants with a higher oxygenase activity.

6.6 References

1. Constantine, C. Z., Starks, C. M., Mill, C.P., Ransome, A. E., Karpowicz, S.J., Francois, J.A., Goodman, R.A. and Kappock, T. J. Biochemical and Structural Studies of N^5 -Carboxyaminoimidazole Ribonucleotide Mutase from the Acidophilic Bacterium *Acetobacter aceti. Biochemistry* **45,** 8193–8208 (2006).

2. Hoskins, A. A., Morar, M., Kappock, T. J., Mathews, I. I., Zaugg, J. B., Barder, T. E., Peng, P., Okamoto, A., Ealick, S. E. and Stubbe, J. N^5-CAIR mutase: Role of a CO_2 Binding Site and Substrate Movement in Catalysis. *Biochemistry* **46,** 2842–2855 (2007).

3. Tranchimand, S., Starks, C. M., Mathews, I. I., Hockings, S. C. and Kappock, T. J. *Treponema denticola* PurE is a bacterial AIR Carboxylase. *Biochemistry* **50,** 4623–4637 (2011).

4. Ellis, R. J. The Most Abundant Protein in the World. *Trends Biochem. Sci.* **4,** 241–244 (1979).

5. Lorimer, G. H. and Andrews, T. J. Plant Photorespiration—An Inevitable Consequence of the Existence of Atmospheric Oxygen. *Nature* **243,** 359–360 (1973).

6. Laing, W. A., Ogren, W. L. and Hageman, R. H. Regulation of Soybean Net Photosynthetic CO_2 Fixation by the Interaction of CO_2, O_2, and Ribulose 1,5-Diphosphate Carboxylase. *Plant Physiol.* **54,** 678–685 (1974).

7. Kahn, K., Serfozo, P. and Tipton, P. A. Identification of the True Product of the Urate Oxidase Reaction. *J. Am. Chem. Soc.* **119,** 5435–5442 (1997).

8. Fetzner, S. and Steiner, R. A. Cofactor-Independent Oxidases and Oxygenases. *Appl. Microbiol. Biotechnol.* **86,** 791–804 (2010).

9. Hixon, M., Sinerius, G., Schneider, A., Walter, C., Fessner, W. and Schloss, J. V. Quo Vadis Photorespiration: A Tale of Two Aldolases. *FEBS Lett.* **392,** 281–284 (1996).

10. Abell, L. M. and Schloss, J. V. Oxygenase Side Reactions of Acetolactate Synthase and Other Carbanion-forming Enzymes. *Biochemistry* **30,** 7883–7887 (1991).

11. Sullivan, K. L., Huma, L. C., Mullins, E. a, Johnson, M. E. and Kappock, T. J. Metal Stopping Reagents Facilitate Discontinuous Activity Assays of the *de novo* Purine Biosynthesis Enzyme PurE. *Anal. Biochem.* **452,** 43–45 (2014).

12. Bradford, M. M. A Rapid and Sensitive Method for the Quantitation of Microgram Quantities of Protein Utilizing the Principle of Protein-Dye Binding. *Anal. Biochem.* **72,** 248–254 (1976).

13. Meyer, E. Two New Activities and a New Intermediate in the Purine Pathway. Ph.D. Thesis, Massachusetts Institute of Technology (1996).

14. Thoden, J. B., Holden, H. M., Paritala, H. and Firestine, S. M. Structural and Functional Studies of *Aspergillus clavatus* N^5-Carboxyaminoimidazole Ribonucleotide Synthetase . *Biochemistry* **49,** 752–760 (2010).

15. Shively, J. M., van Keulen, G. and Meijer, W. G. Something from Almost Nothing: Carbon Dioxide Fixation in Chemoautotrophs. *Annu. Rev. Microbiol.* **52,** 191–230 (1998).

16. Burghout, P., Cron, L. E., Gradstedt, H., Quintero, B., Simonetti, E., Bijlsma, J. J. E., Bootsma, H. J. and Hermans, P. W. M. Carbonic Anhydrase is Essential for *Streptococcus pneumoniae* Growth in Environmental Ambient Air. *J. Bacteriol.* **192,** 4054–4062 (2010).

17. Merlin, C., Masters, M., McAteer, S. and Coulson, A. Why is Carbonic Anhydrase Essential to *Escherichia coli*? *J. Bacteriol.* **185,** 6415–6424 (2003).

18. Smith, K. S., Jakubzick, C., Whittam, T. S. and Ferry, J. G. Carbonic anhydrase is an Ancient Enzyme Widespread in Prokaryotes. *Proc. Natl. Acad. Sci. U. S. A.* **96,** 15184–15189 (1999).

6.7 Figures and Tables

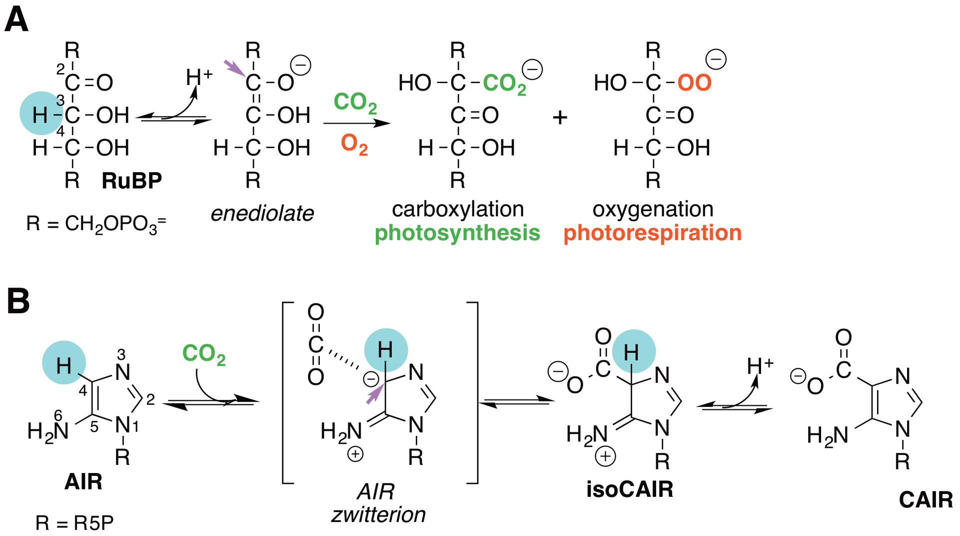

Figure 6.1 Rubisco and PurE2 reactions. (A) Rubisco carboxylase and oxygenase activities begin with the deprotonation of RuBP C3 to generate the reactive endiol(ate). This reactive intermediate can then react with either CO_2 or O_2. (B) PurE2 mediated AIR carboxylation begins with formation of the AIR•CO_2 ternary complex followed by deprotonation to form CAIR.

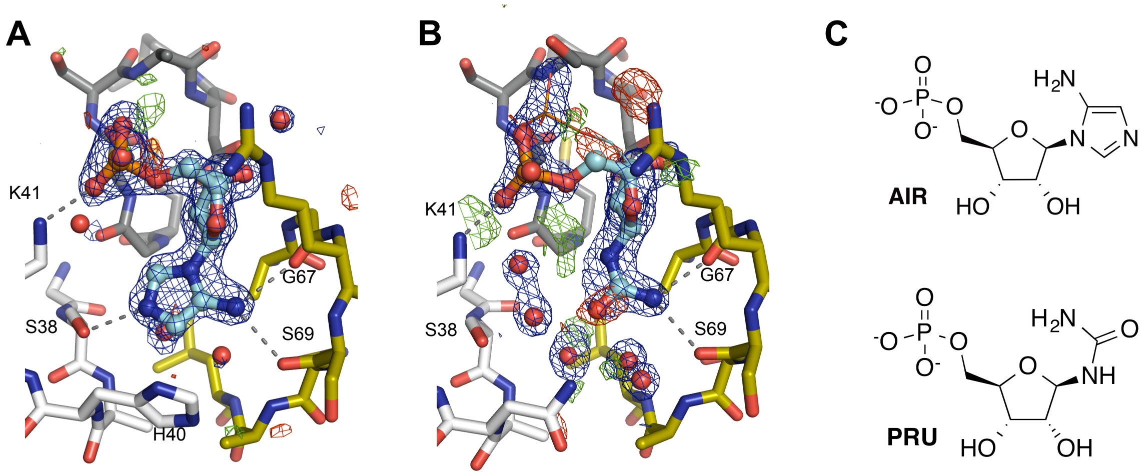

Figure 6.2 Destruction of AIR by the "inactive" mutant TdPurE2-H40N. (A) Crystal structure (1.82 Å resolution) of TdPurE2 bound to AIR (PDB code 3RGG).[3] An electron density map (final 2Fo − *Fc,* blue mesh) is shown for nonprotein atoms with a 1.2σ contour and 1.8 Å carve. The Fo−Fc map is contoured at +3σ (green mesh) and –3σ (red mesh). (B) Crystal structure (1.45 Å resolution) of TdPurE2-H40N bound to a CAIR-derived nucleotide modeled as PRU. Electron density maps are drawn as in panel A. (C) AIR and candidate PRU structures for the ligand in panel B. (T. J. Kappock and I. I. Mathews, unpublished observations).

Table 6.1 Description of bacterial strains used in this chapter.

Strain	Description	Source
DH5 α	F′ φ80lacZΔM15 Δ(lacZYA-argF)U169 *deoR recA1 endA1 hsdR17*(r_K^- m_K^+) *phoA supE44 thi-1 gyrA96 relA1*	Lab stock
CC1215	F^- *ompT gal dcm lon hsd*S_B(r_B^- m_B^-) *ΔpurE*736::kan λ(DE3 [*lacI lacUV5*-T7 *gene 1 ind1 sam7 nin5*])	Chapter 3

Table 6.2 Previously published plasmids used in this chapter.

Plasmid	Description	Source	Protein encoded
pJK175	*purE1*$_{Aa}$ in pET23a	[1]	AaPurE1
pJK283	*purE1*$_{Aa}$*-H59N* in pET23a	[1]	AaPurE1-H59N
pJK376	*purE2*$_{Td}$ in pET23a	[3]	TdPurE2
pJK392	*purE2*$_{Td}$*-H40N* in pET23a	[3]	TdPurE2-H40N

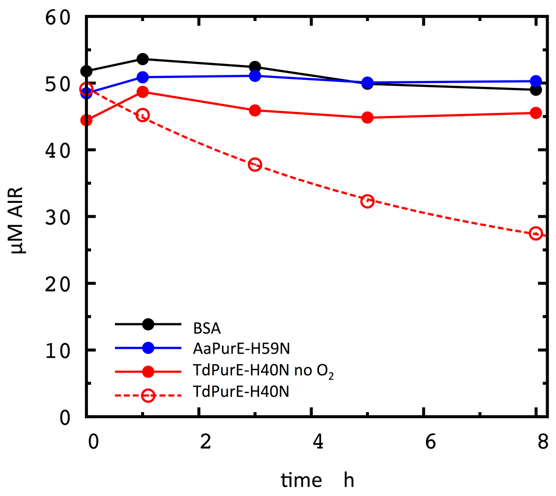

Figure 6.3 Decomposition of AIR (initially 50 µM) by 60 µM of the indicated enzyme form. The red dotted line is a fit of the aerobic TdPurE2-H40N data to a first-order decay function (half-life of 4 h), demonstrating that AIR is a substrate for a very slow oxygenase reaction.

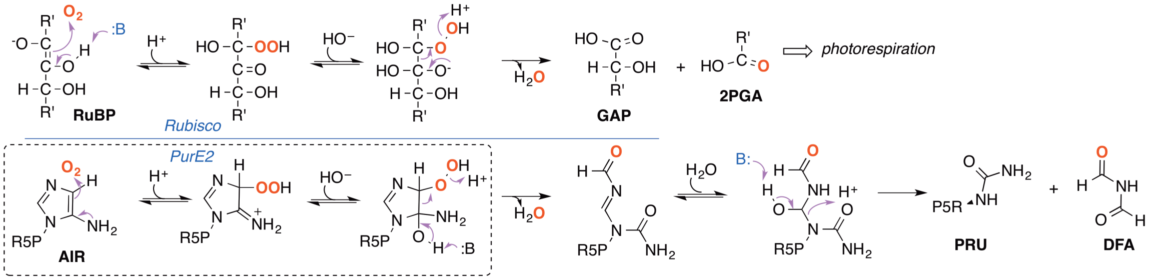

Figure 6.4 Oxygenase reactions of Rubisco and PurE2. Electron-pushing mechanism for the Rubisco ribulose-1,5-bisphosphate (RuBP) oxygenase reaction and electron-pushing mechanism for the PurE2 AIR oxygenase reaction. PurE2 is reversible and may react with O_2 until a steric hindrance is imposed by the PurE2 active site (boxed in the dotted line above).

APPENDIX

APPENDIX

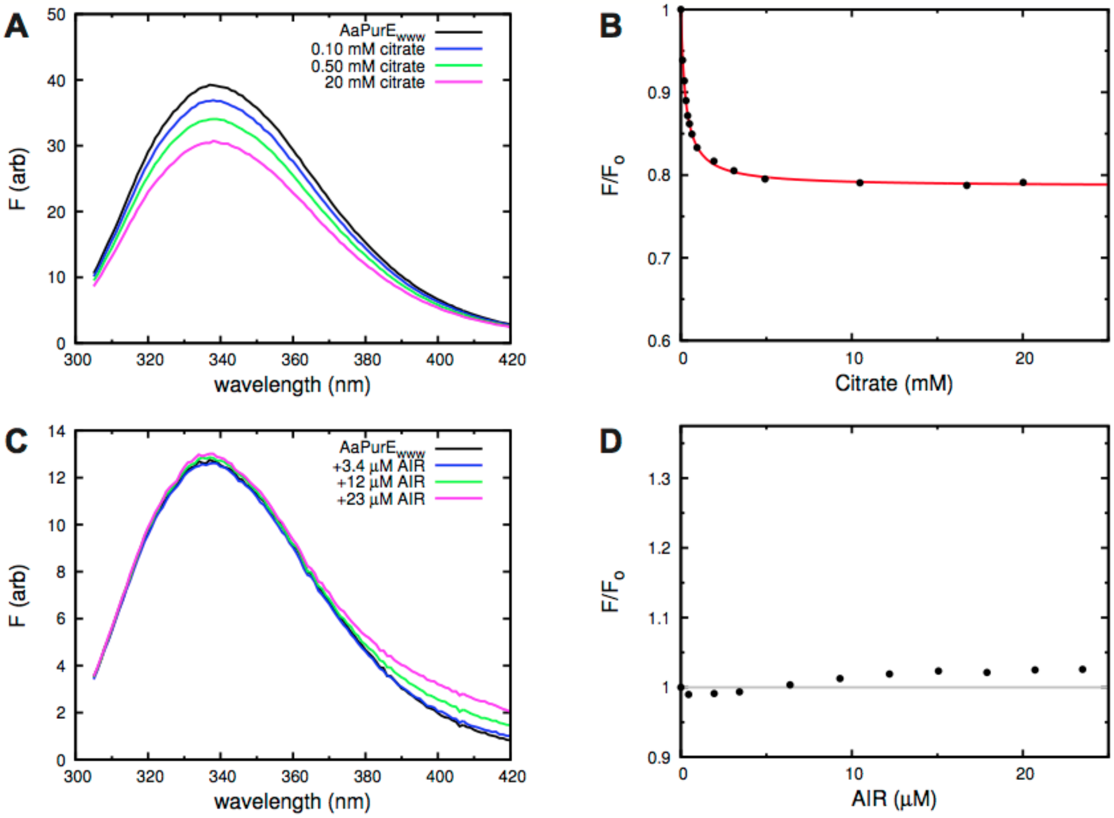

Figure A.1 Fluorescence titrations with wild-type AaPurE. Excitation wavelength was 295 nm. Citrate titrations were performed with 0.64 μM [subunit] in 50 mM Potassium acetate, 100 mM KCl, pH 4.6 at 25 °C and data were fit to equation 3.2. K_d values are given in Table 3.7. AIR titrations were performed with 0.31 μM [subunit] in 50 mM Tris-HCl, pH 8.0 at 30 °C. (A) Fluorescence emission spectra with increasing amounts of citrate. (B) Recorded emission at 320 nm upon citrate addition. (C) Fluorescence emission spectra with increasing amounts of AIR. (D) Recorded emission at 320 nm upon AIR addition.

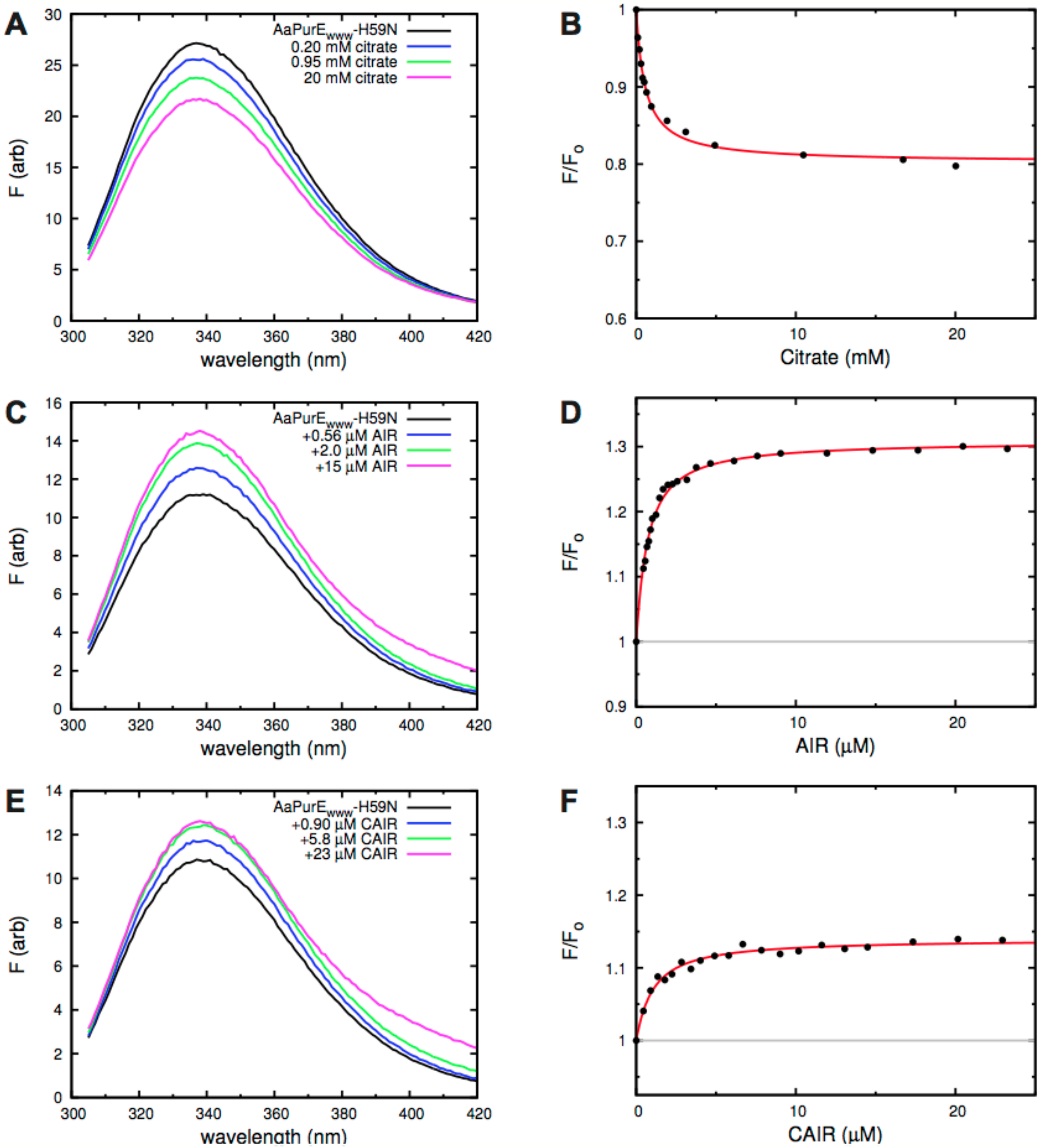

Figure A.2 Fluorescence titrations with AaPurE-H59N. Excitation wavelength was 295 nm. Citrate titrations were performed with 0.68 μM [subunit] in 50 mM Potassium acetate, 100 mM KCl, pH 4.6 at 25 °C and data were fit to equation 3.2. AIR and CAIR titrations were both performed with 0.38 μM [subunit] in 50 mM Tris-HCl, pH 8.0 at 30 °C and data were fit to equation 3.3. K_d values are given in Table 3.7. (A) Fluorescence emission spectra with increasing amounts of citrate. (B) Recorded emission at 320 nm upon citrate addition. (C) Fluorescence emission spectra with increasing amounts of AIR. (D) Recorded emission at 320 nm upon AIR addition. (E) Fluorescence emission spectra with increasing amounts of CAIR. (F) Recorded emission at 320 nm upon CAIR addition.

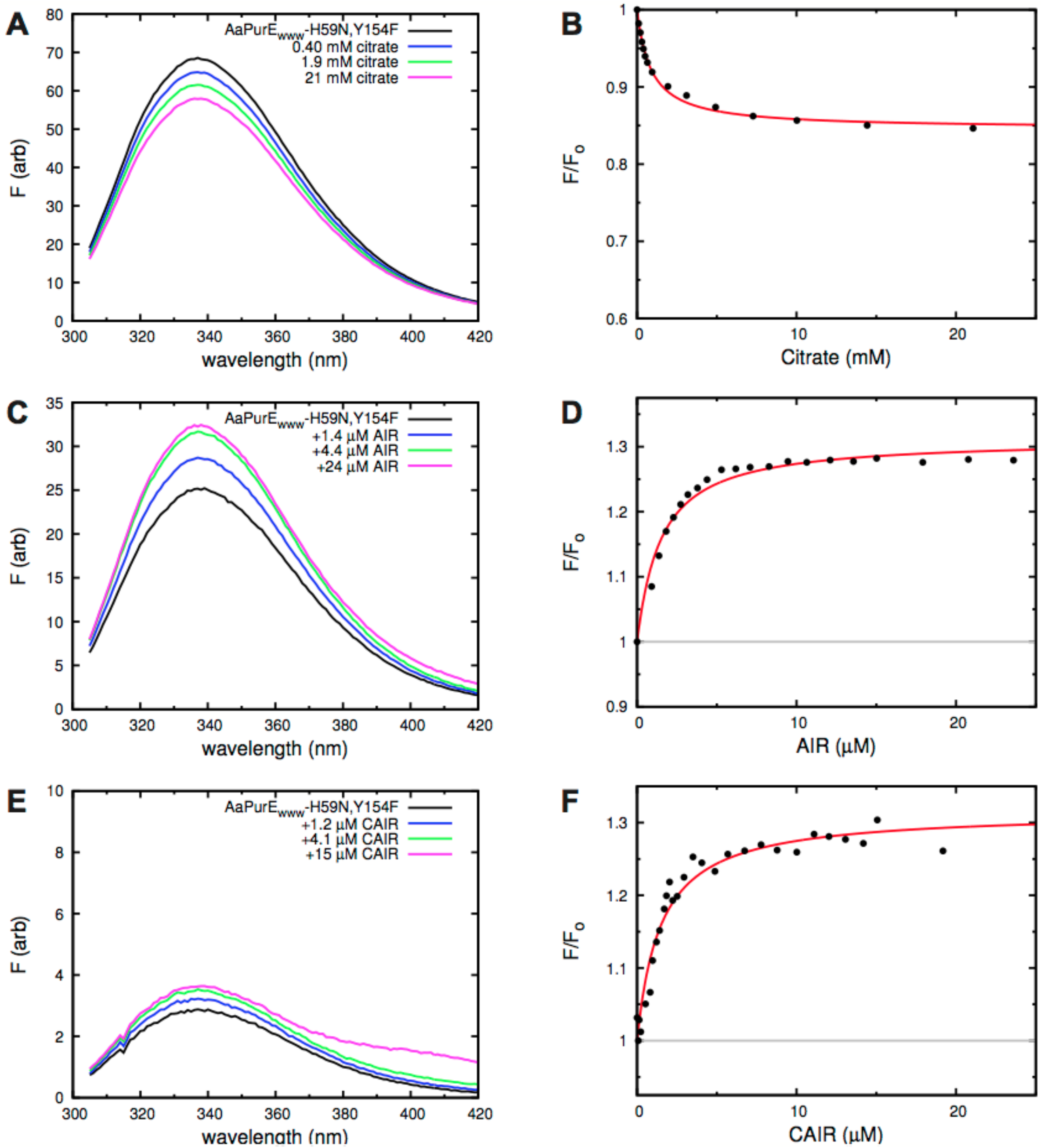

Figure A.3 Fluorescence titrations with AaPurE-H59N,Y154F. Excitation wavelength was 295 nm. Citrate titrations were performed with 1.91 µM [subunit] in 50 mM Potassium acetate, 100 mM KCl, pH 4.6 at 25 °C and data were fit to equation 3.2. AIR and CAIR titrations were performed with 0.80 µM [subunit] and 0.10 µM [subunit] in 50 mM Tris-HCl, pH 8.0 at 30 °C and data were fit to equation 3.3. K_d values are given in Table 3.7. (A) Fluorescence emission spectra for titration with increasing amounts of citrate. (B) Recorded emission at 320 nm upon citrate addition. (C) Fluorescence emission spectra with increasing amounts of AIR. (D) Recorded emission at 320 nm upon AIR addition. (E) Fluorescence emission spectra with increasing amounts of CAIR. (F) Recorded emission at 320 nm upon CAIR addition.

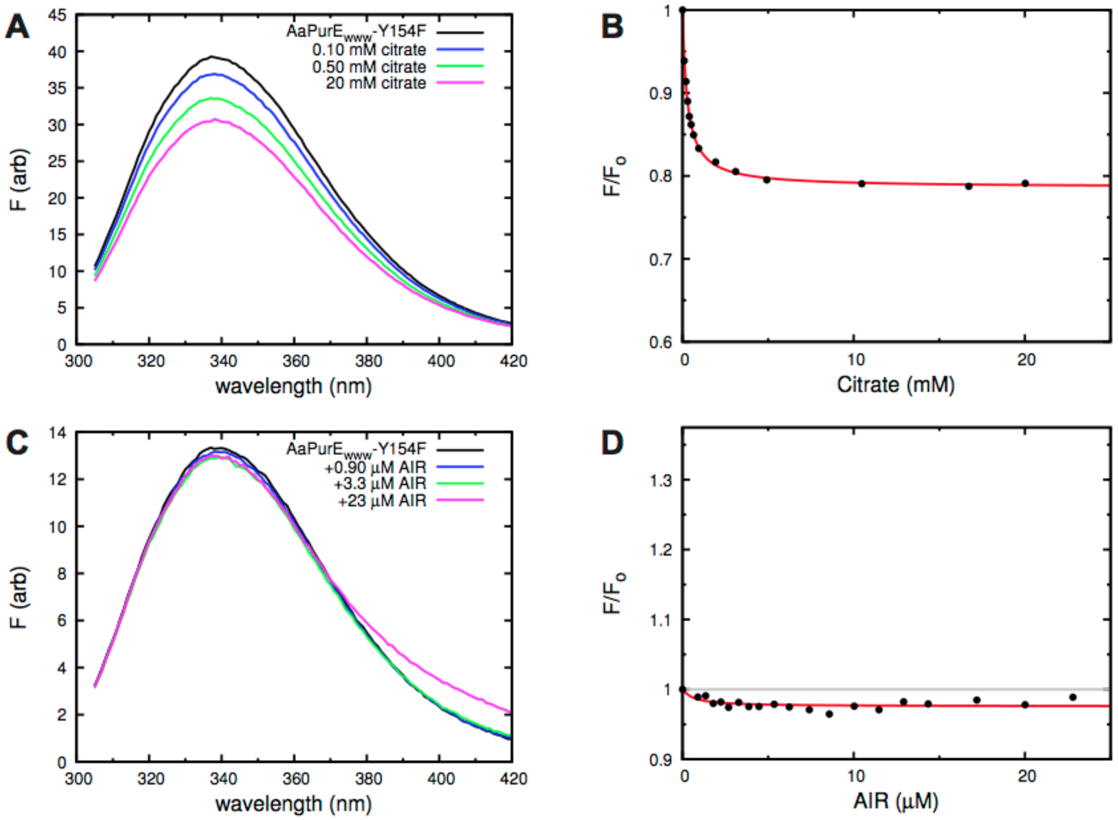

Figure A.4 Fluorescence titrations with AaPurE-Y154F. Excitation wavelength was 295 nm. Citrate titrations were performed with 1.24 μM [subunit] in 50 mM Potassium acetate, 100 mM KCl, pH 4.6 at 25 °C and data were fit to equation 3.2. AIR titrations were performed with 0.50 μM [subunit] in 50 mM Tris-HCl, pH 8.0 at 30 °C and data were fit to equation 3.3. K_d values are given in Table 3.7. (A) Fluorescence emission spectra with increasing amounts of citrate. (B) Recorded emission at 320 nm upon citrate addition. (C) Fluorescence emission spectra with increasing amounts of AIR. (D) Recorded emission at 320 nm upon AIR addition.

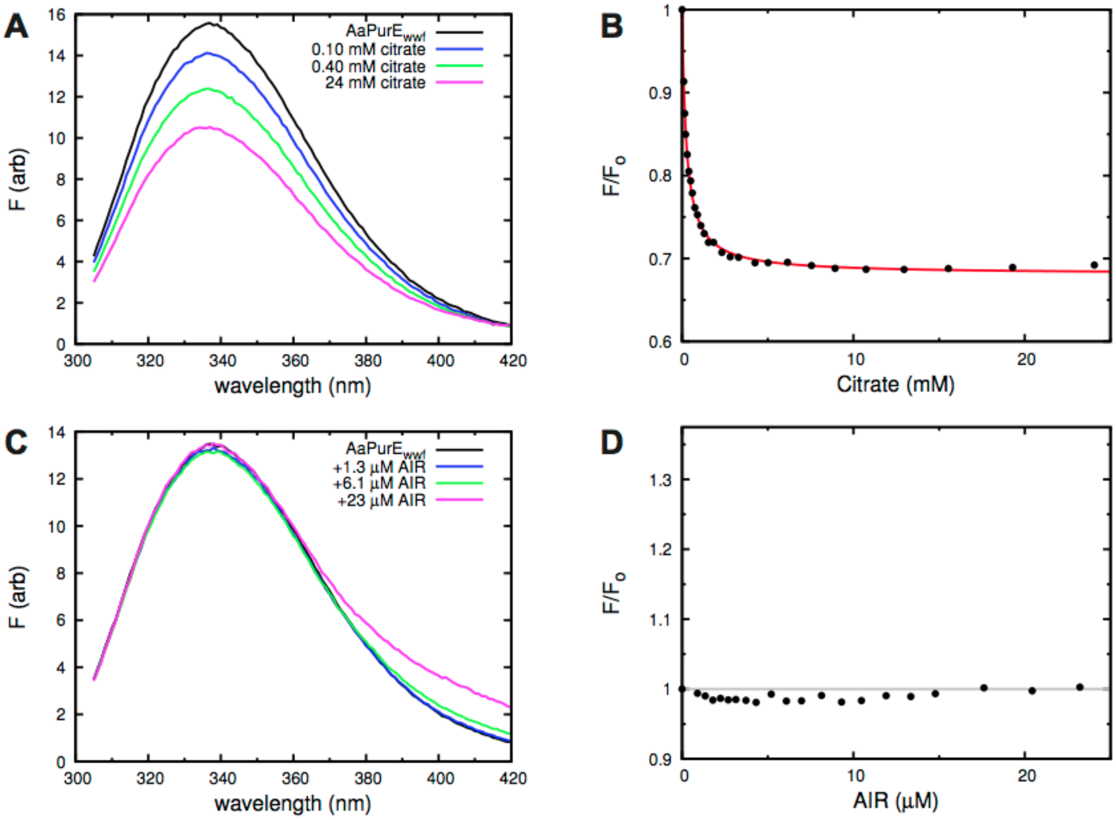

Figure A.5 Fluorescence titrations with AaPurE$_{\text{wwf}}$. Excitation wavelength was 295 nm. Citrate titrations were performed with 0.63 µM [subunit] in 50 mM Potassium acetate, 100 mM KCl, pH 4.6 at 25 °C and data were fit to equation 3.2. K_d values are given in Table 3.7. AIR titrations were performed with 0.63 µM [subunit] in 50 mM Tris-HCl, pH 8 at 30 °C. (A) Fluorescence emission spectra with increasing amounts of citrate. (B) Recorded emission at 320 nm upon citrate addition. (C) Fluorescence emission spectra with increasing amounts of AIR. (D) Recorded emission at 320 nm upon AIR addition.

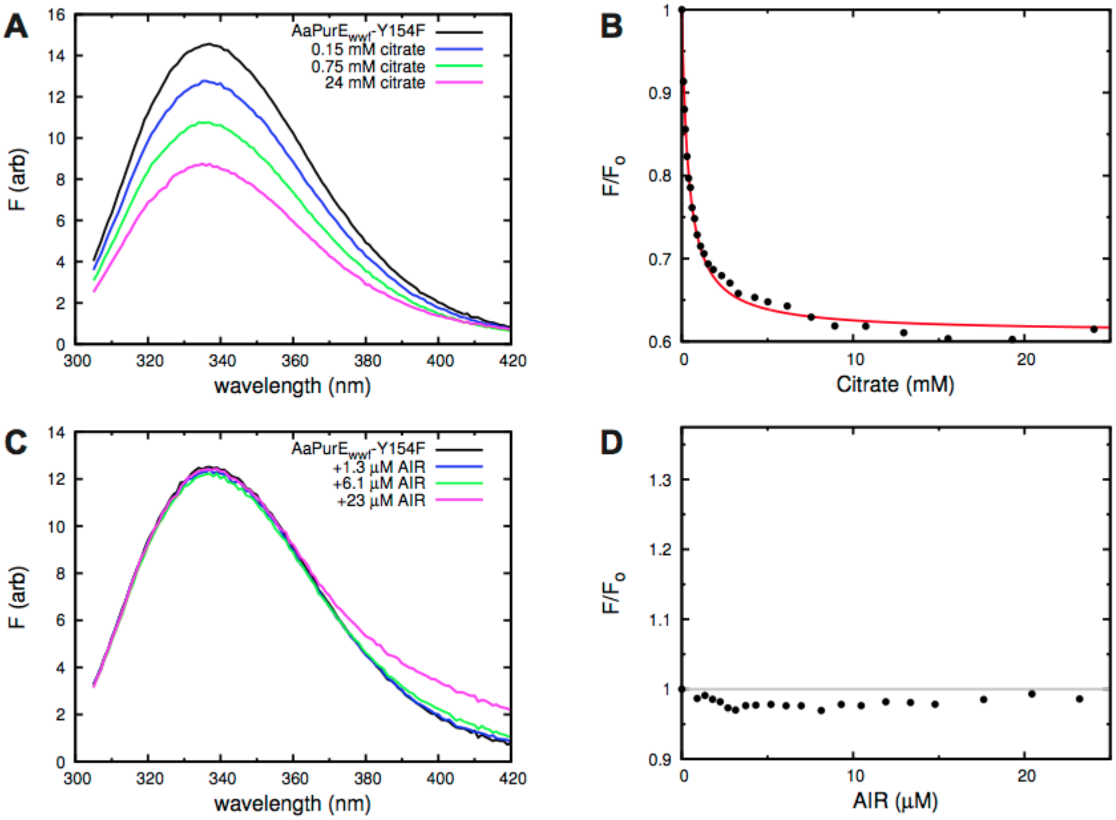

Figure A.6 Fluorescence titrations with AaPurE$_{wwf}$-Y154F. Excitation wavelength was 295 nm. Citrate titrations were performed with 0.59 μM [subunit] in 50 mM Potassium acetate, 100 mM KCl, pH 4.6 at 25 °C and data were fit to equation 3.2. K_d values are given in Table 3.7. AIR titrations were performed with 0.59 μM [subunit] in 50 mM Tris-HCl, pH 8 at 30 °C. (A) Fluorescence emission spectra with increasing amounts of citrate. (B) Recorded emission at 320 nm upon citrate addition. (C) Fluorescence emission spectra with increasing amounts of AIR. (D) Recorded emission at 320 nm upon AIR addition.

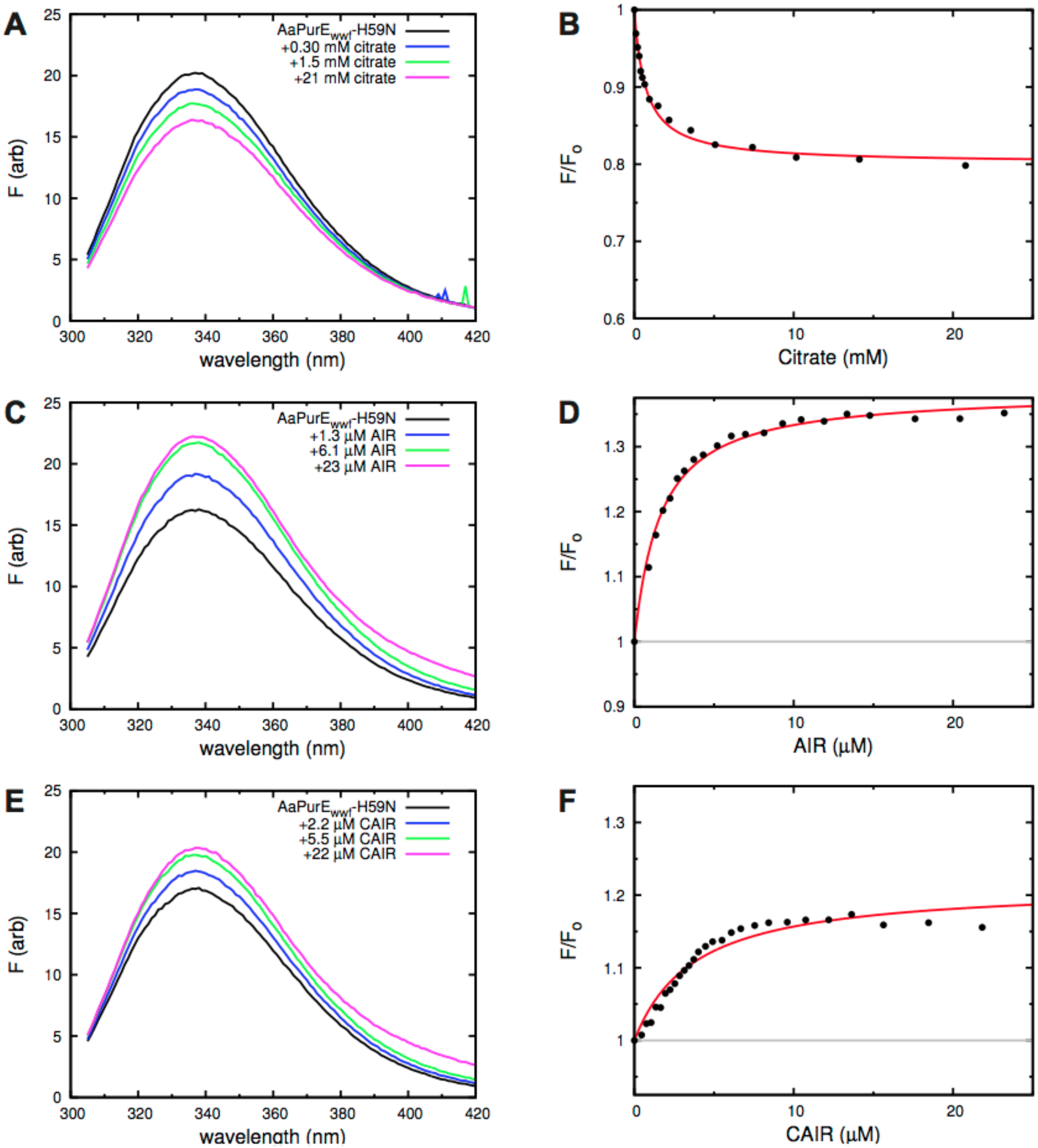

Figure A.7 Fluorescence titrations with AaPurE$_{wwf}$-H59N. Excitation wavelength was 295 nm. Citrate titrations were performed with 0.74 μM [subunit] in 50 mM Potassium acetate, 100 mM KCl, pH 4.6 at 25 °C and data were fit to equation 3.2. AIR and CAIR titrations were performed with 0.59 μM [subunit] and 0.59 μM [subunit] in 50 mM Tris-HCl, pH 8 at 30 °C and data were fit to equation 3.3. K_d values are given in Table 3.7. (A) Fluorescence emission spectra for titration with increasing amounts of citrate. (B) Recorded emission at 320 nm upon citrate addition. (C) Fluorescence emission spectra with increasing amounts of AIR. (D) Recorded emission at 320 nm upon AIR addition. (E) Fluorescence emission spectra with increasing amounts of CAIR. (F) Recorded emission at 320 nm upon CAIR addition.

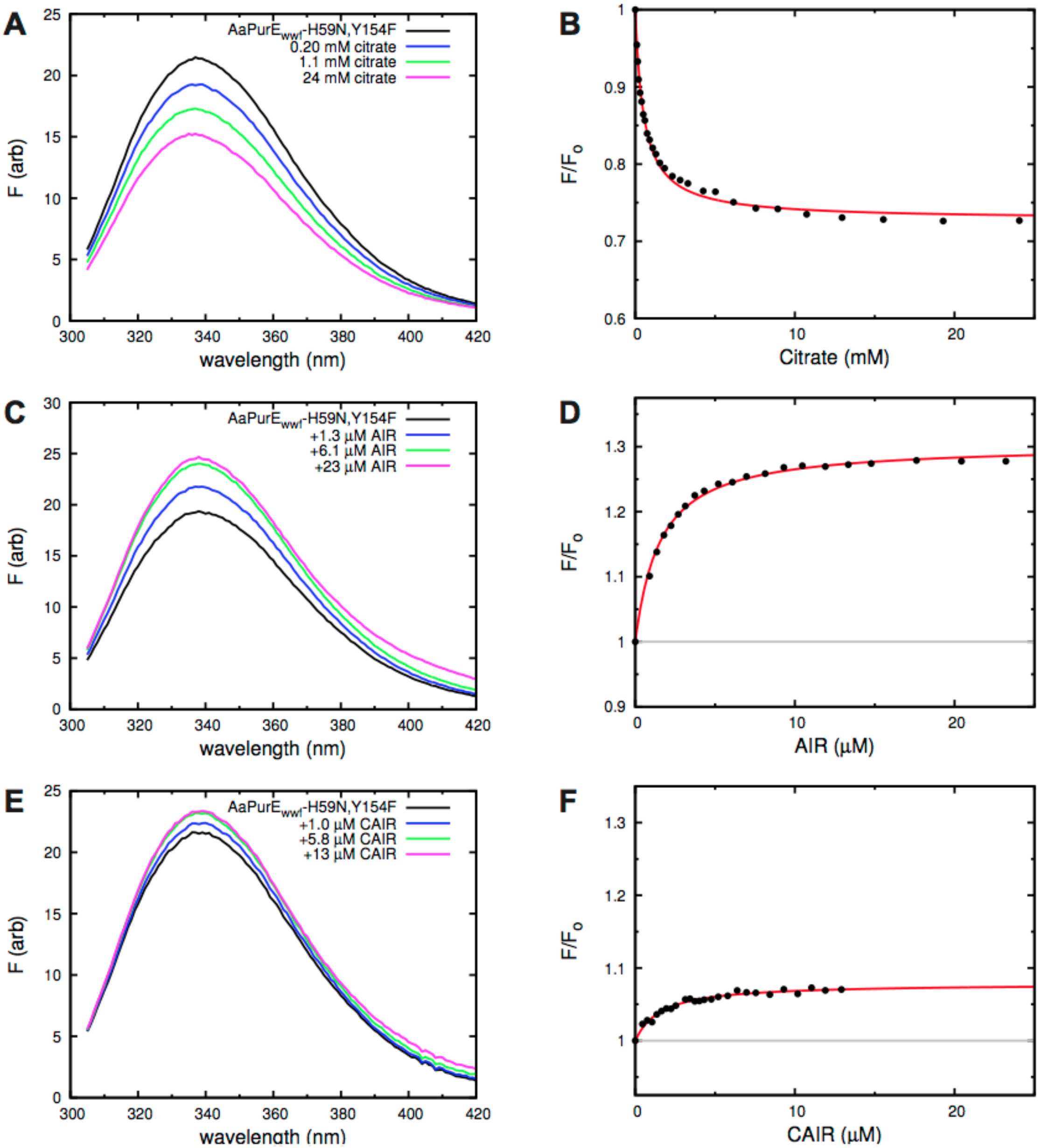

Figure A.8 Fluorescence titrations with AaPurE$_{wwf}$-H59N,Y154F. Excitation wavelength was 295 nm. Citrate titrations were performed with 0.89 µM [subunit] in 50 mM Potassium acetate, 100 mM KCl, pH 4.6 at 25 °C and data were fit to equation 3.2. AIR and CAIR titrations were performed with 0.59 µM [subunit] and 0.59 µM [subunit] in 50 mM Tris-HCl, pH 8 at 30 °C and data were fit to equation 3.3. K_d values are given in Table 3.7. (A) Fluorescence emission spectra for titration with increasing amounts of citrate. (B) Recorded emission at 320 nm upon citrate addition. (C) Fluorescence emission spectra with increasing amounts of AIR. (D) Recorded emission at 320 nm upon AIR addition. (E) Fluorescence emission spectra with increasing amounts of CAIR. (F) Recorded emission at 320 nm upon CAIR addition.

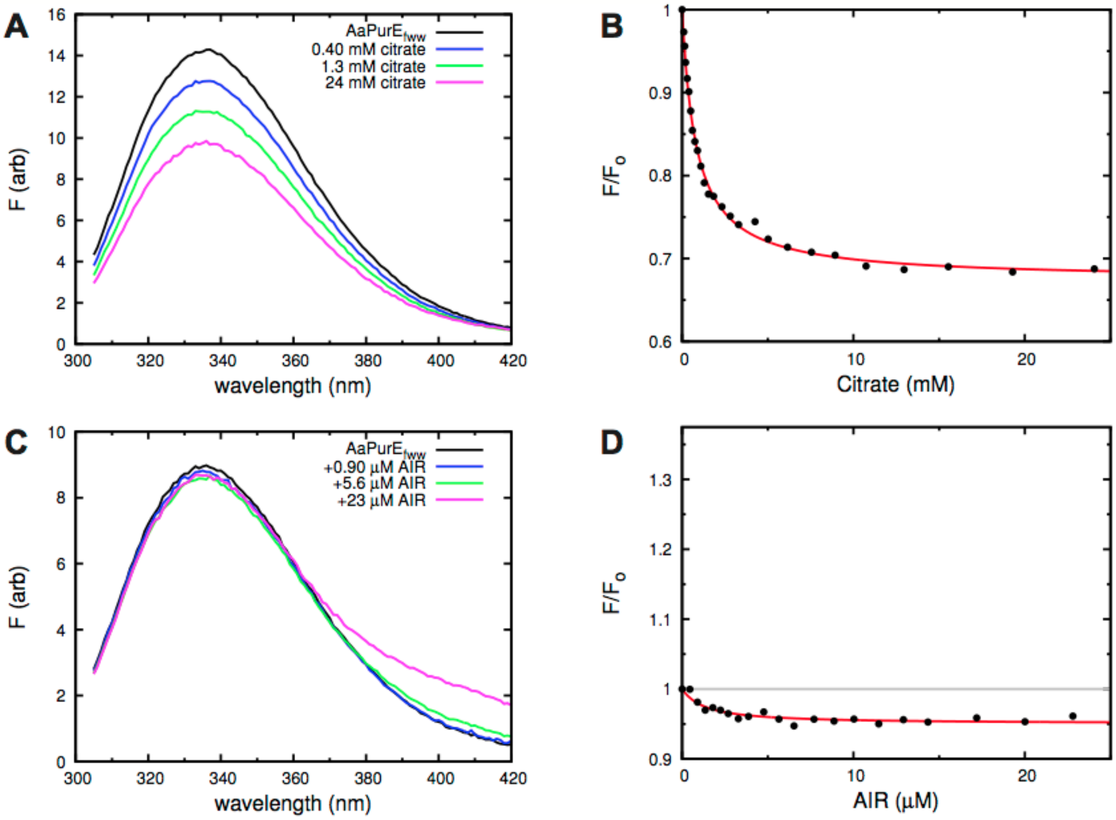

Figure A.9 Fluorescence titrations with AaPurE$_{\mathrm{fww}}$. Excitation wavelength was 295 nm. Citrate titrations were performed with 1.49 µM [subunit] in 50 mM Potassium acetate, 100 mM KCl, pH 4.6 at 25 °C and data were fit to equation 3.2. AIR titrations were performed with 0.56 µM [subunit] in 50 mM Tris-HCl, pH 8 at 30 °C and data were fit to equation 3.3. K_d values are given in Table 3.7. (A) Fluorescence emission spectra with increasing amounts of citrate. (B) Recorded emission at 320 nm upon citrate addition. (C) Fluorescence emission spectra with increasing amounts of AIR. (D) Recorded emission at 320 nm upon AIR addition.

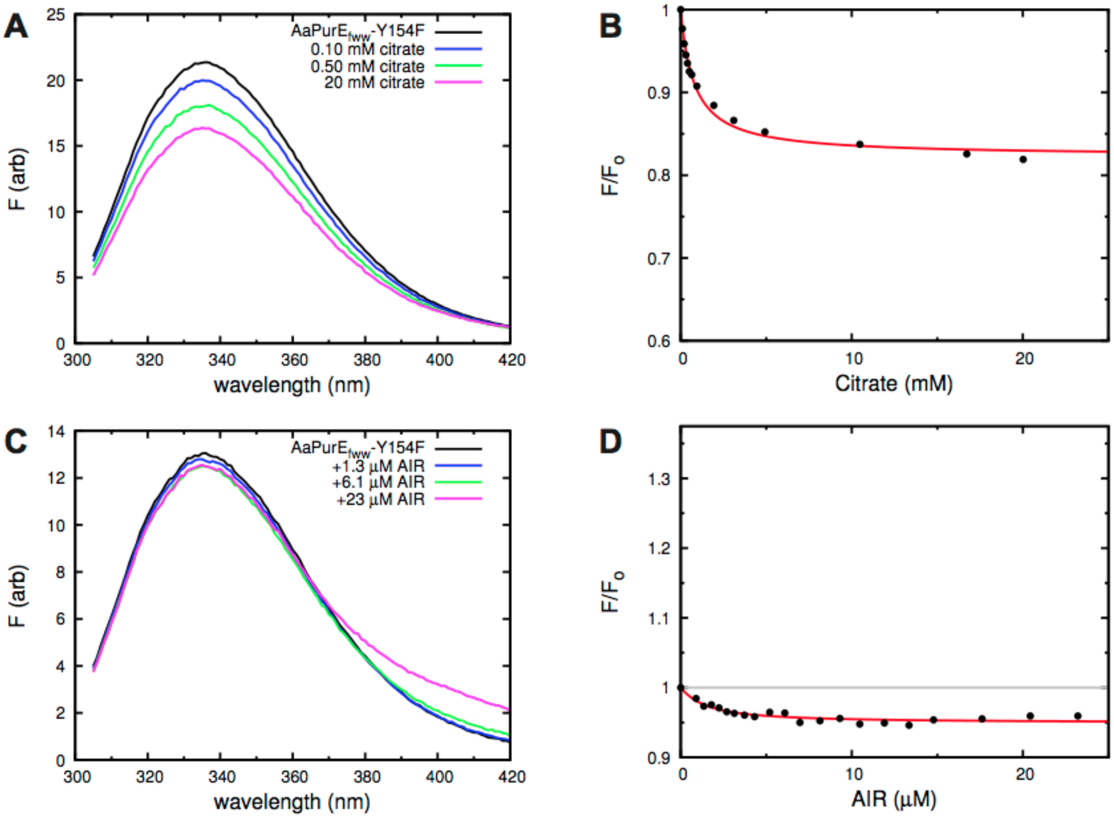

Figure A.10 Fluorescence titrations with AaPurE$_{fww}$-Y154F. Excitation wavelength was 295 nm. Citrate titrations were performed with 1.13 µM [subunit] in 50 mM Potassium acetate, 100 mM KCl, pH 4.6 at 25 °C and data were fit to equation 3.2. AIR titrations were performed with 0.87 µM [subunit] in 50 mM Tris-HCl, pH 8 at 30 °C and data were fit to equation 3.3. K_d values are given in Table 3.7. (A) Fluorescence emission spectra with increasing amounts of citrate. (B) Recorded emission at 320 nm upon citrate addition. (C) Fluorescence emission spectra with increasing amounts of AIR. (D) Recorded emission at 320 nm upon AIR addition.

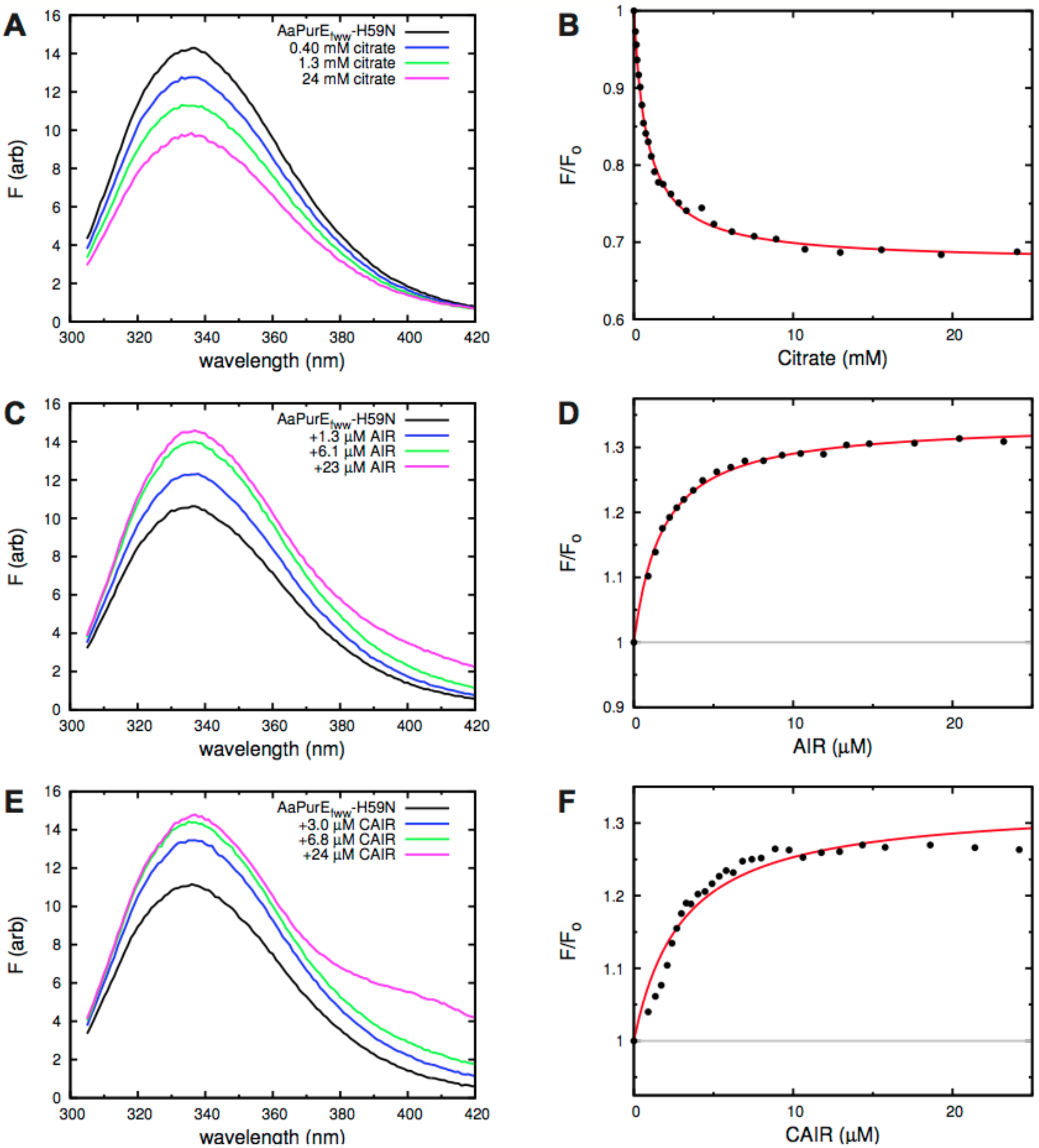

Figure A.11 Fluorescence titrations with AaPurE$_{\mathrm{fww}}$-H59N. Excitation wavelength was 295 nm. Citrate titrations were performed with 0.65 μM [subunit] in 50 mM Potassium acetate, 100 mM KCl, pH 4.6 at 25 °C and data were fit to equation 3.2. AIR and CAIR titrations were performed with 0.65 μM [subunit] and0.65 μM [subunit] in 50 mM Tris-HCl, pH 8 at 30 °C and data were fit to equation 3.3. K_{d} values are given in Table 3.7. (A) Fluorescence emission spectra for titration with increasing amounts of citrate. (B) Recorded emission at 320 nm upon citrate addition. (C) Fluorescence emission spectra with increasing amounts of AIR. (D) Recorded emission at 320 nm upon AIR addition. (E) Fluorescence emission spectra with increasing amounts of CAIR. (F) Recorded emission at 320 nm upon CAIR addition.

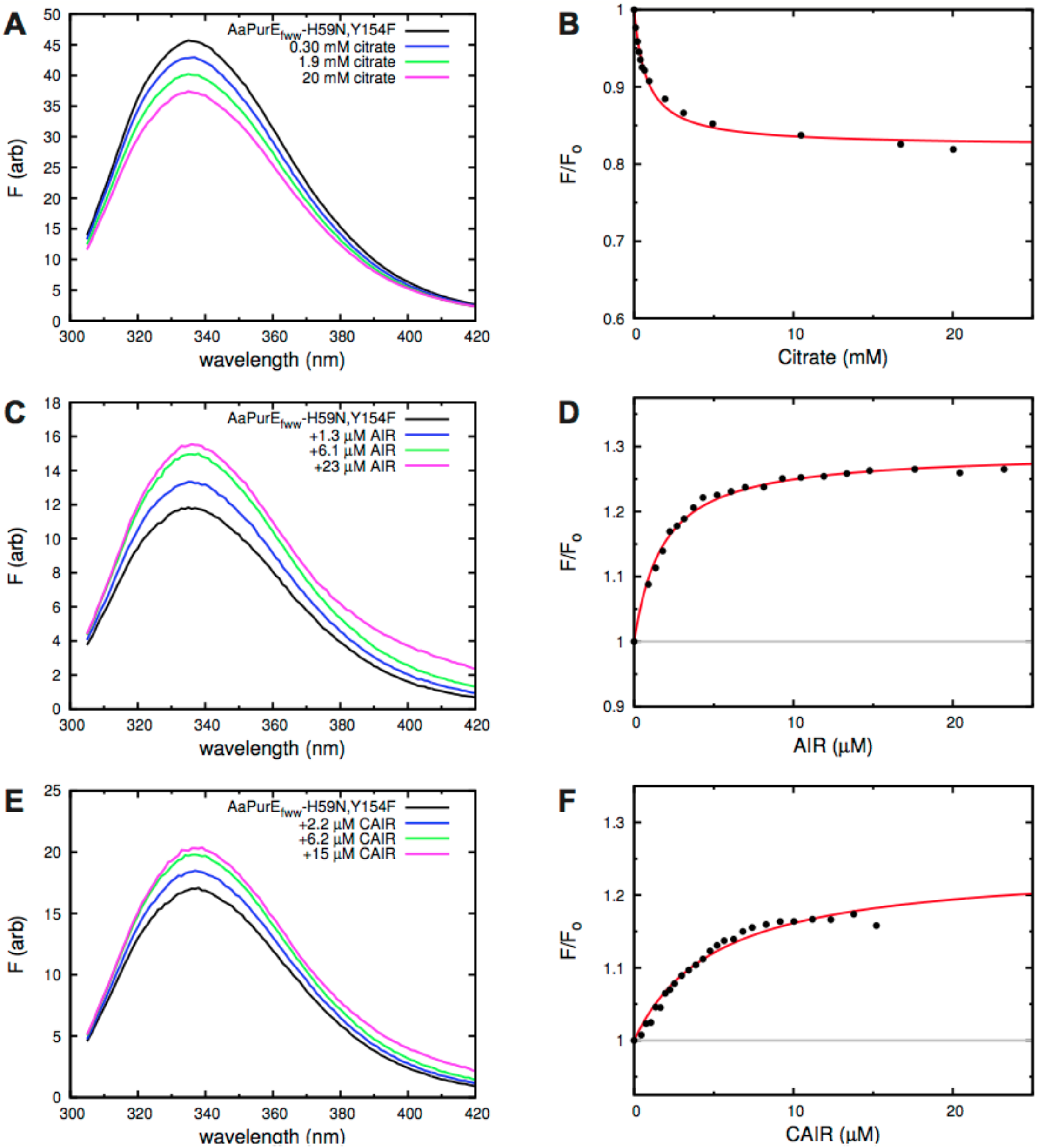

Figure A.12 Fluorescence titrations with AaPurE$_{fww}$-H59N,Y154F. Excitation wavelength was 295 nm. Citrate titrations were performed with 2.11 μM [subunit] in 50 mM Potassium acetate, 100 mM KCl, pH 4.6 at 25 °C and data were fit to equation 3.2. AIR and CAIR titrations were performed with 0.71 μM [subunit] and 0.71 μM [subunit] in 50 mM Tris-HCl, pH 8 at 30 °C and data were fit to equation 3.3. K_d values are given in Table 3.7. (A) Fluorescence emission spectra for titration with increasing amounts of citrate. (B) Recorded emission at 320 nm upon citrate addition. (C) Fluorescence emission spectra with increasing amounts of AIR. (D) Recorded emission at 320 nm upon AIR addition. (E) Fluorescence emission spectra with increasing amounts of CAIR. (F) Recorded emission at 320 nm upon CAIR addition.

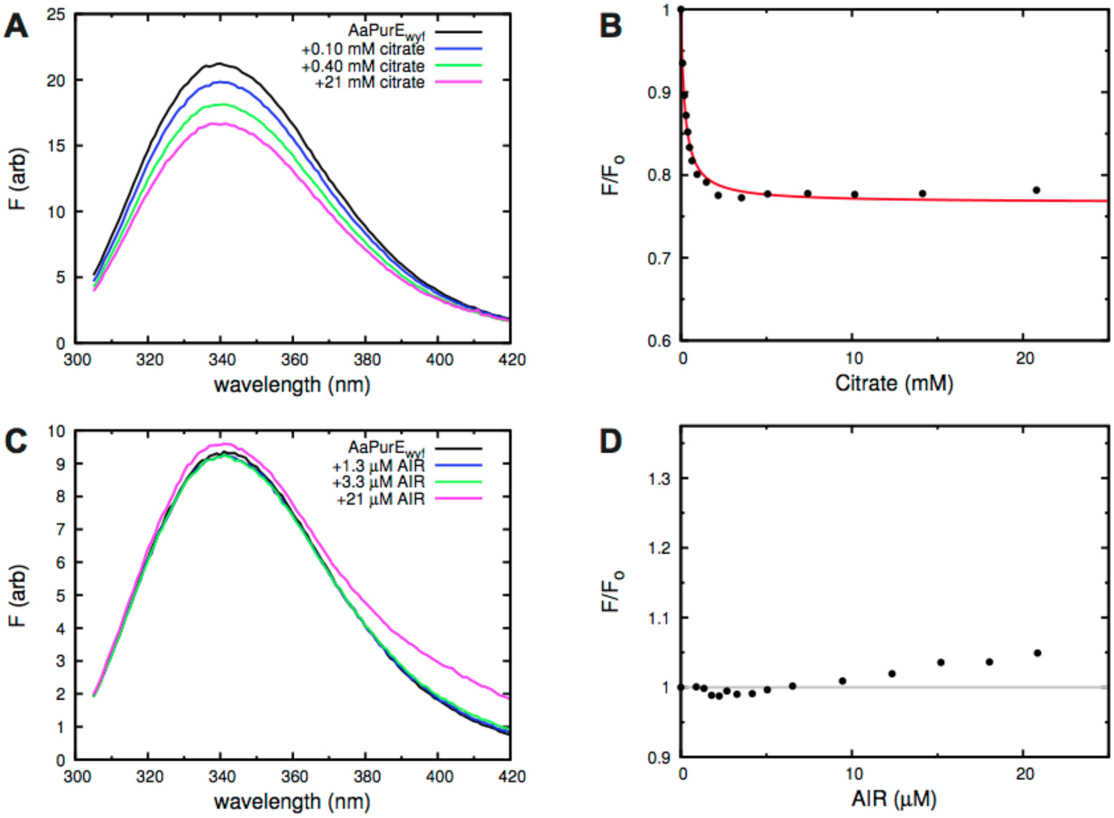

Figure A.13 Fluorescence titrations with AaPurE$_{wyf}$. Excitation wavelength was 295 nm. Citrate titrations were performed with 2.17 µM [subunit] in 50 mM Potassium acetate, 100 mM KCl, pH 4.6 at 25 °C and data were fit to equation 3.2. K_d values are given in Table 3.7. AIR titrations were performed with 0.89 µM [subunit] in 50 mM Tris-HCl, pH 8 at 30 °C. (A) Fluorescence emission spectra with increasing amounts of citrate. (B) Recorded emission at 320 nm upon citrate addition. (C) Fluorescence emission spectra with increasing amounts of AIR. (D) Recorded emission at 320 nm upon AIR addition.

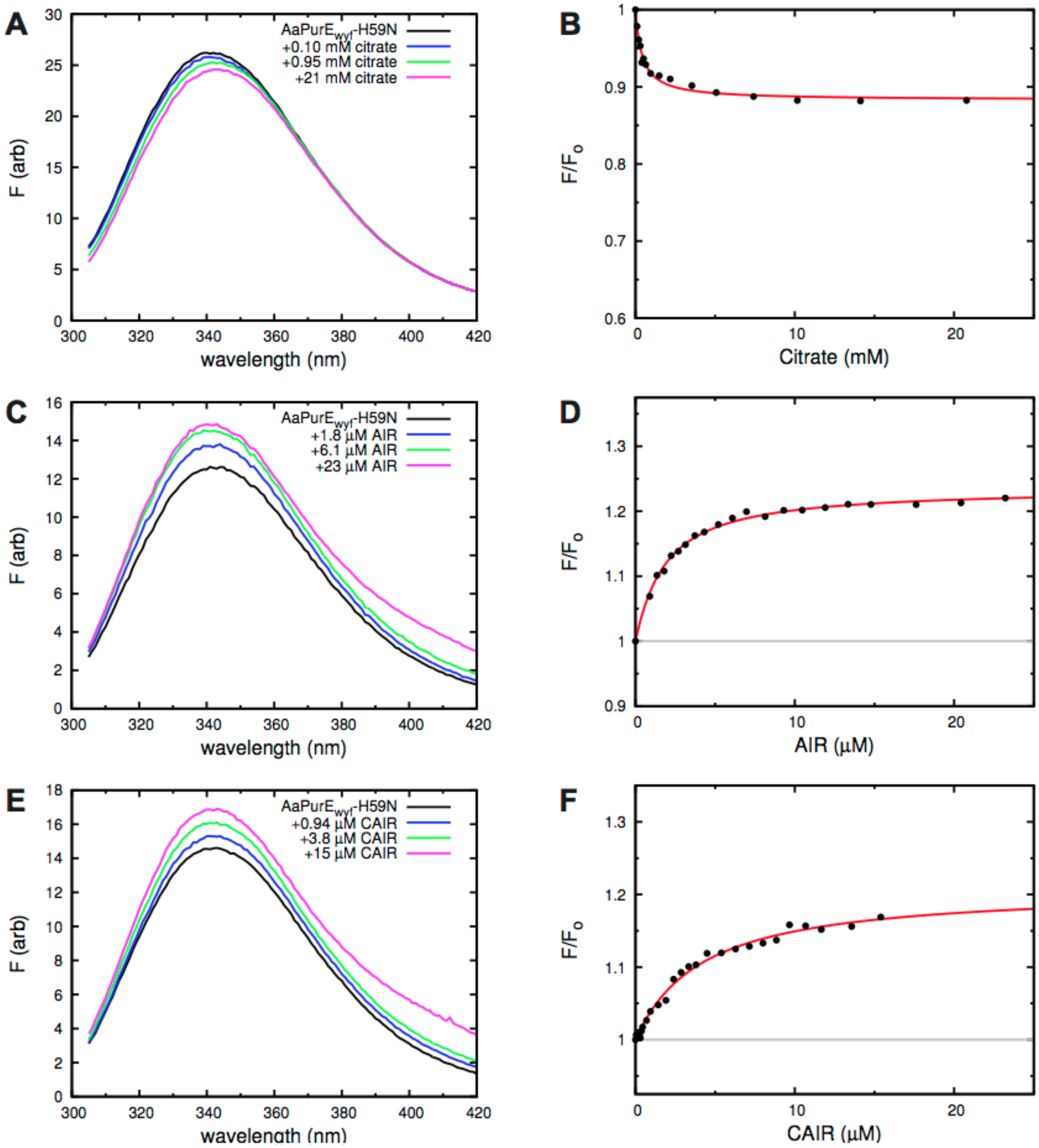

Figure A.14 Fluorescence titrations with AaPurE$_{\text{wyf}}$-H59N. Excitation wavelength was 295 nm. Citrate titrations were performed with 2.98 μM [subunit] in 50 mM Potassium acetate, 100 mM KCl, pH 4.6 at 25 °C and data were fit to equation 3.2. AIR and CAIR titrations were performed with 1.00 μM [subunit] and 1.00 μM [subunit] in 50 mM Tris-HCl, pH 8 at 30 °C and data were fit to equation 3.3. K_d values are given in Table 3.7. (A) Fluorescence emission spectra for titration with increasing amounts of citrate. (B) Recorded emission at 320 nm upon citrate addition. (C) Fluorescence emission spectra with increasing amounts of AIR. (D) Recorded emission at 320 nm upon AIR addition. (E) Fluorescence emission spectra with increasing amounts of CAIR. (F) Recorded emission at 320 nm upon CAIR addition.

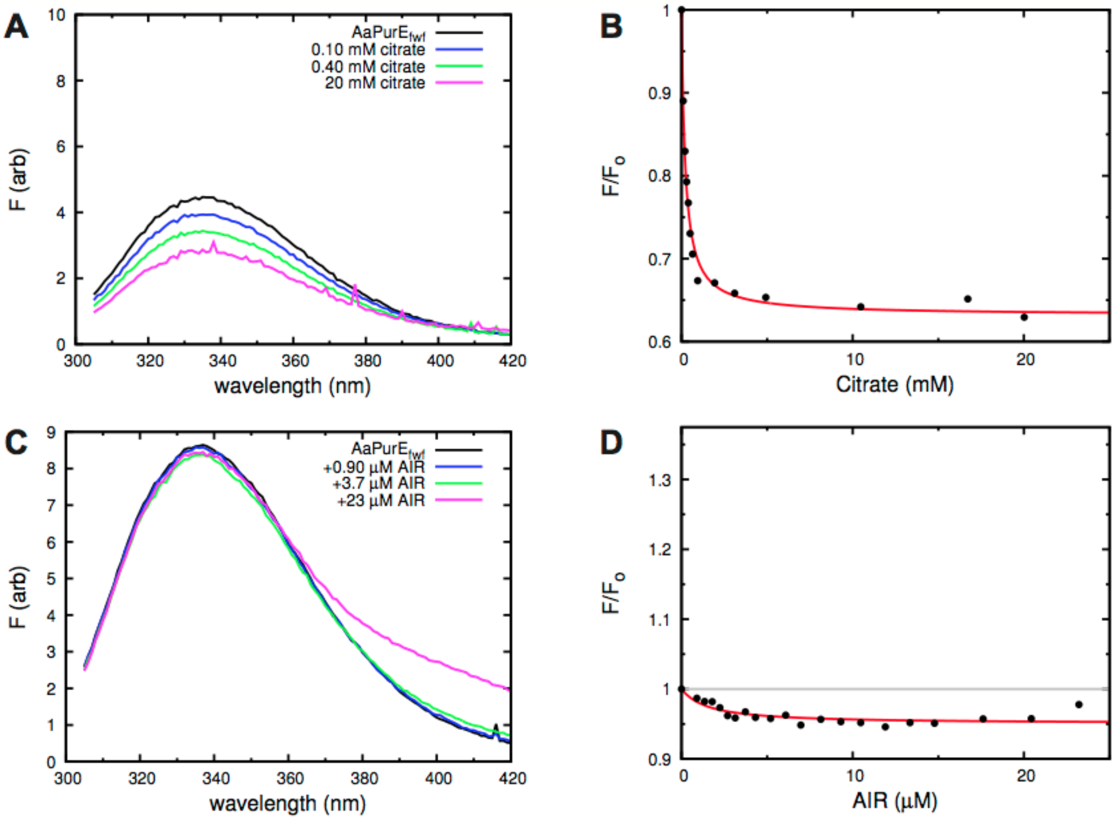

Figure A.15 Fluorescence titrations with AaPurE$_{fwf}$. Excitation wavelength was 295 nm. Citrate titrations were performed with 0.12 µM [subunit] in 50 mM Potassium acetate, 100 mM KCl, pH 4.6 at 25 °C and data were fit to equation 3.2. AIR titrations were performed with 0.29 µM [subunit] in 50 mM Tris-HCl, pH 8 at 30 °C and data were fit to equation 3.3. K_d values are given in Table 3.7. (A) Fluorescence emission spectra with increasing amounts of citrate. (B) Recorded emission at 320 nm upon citrate addition. (C) Fluorescence emission spectra with increasing amounts of AIR. (D) Recorded emission at 320 nm upon AIR addition.

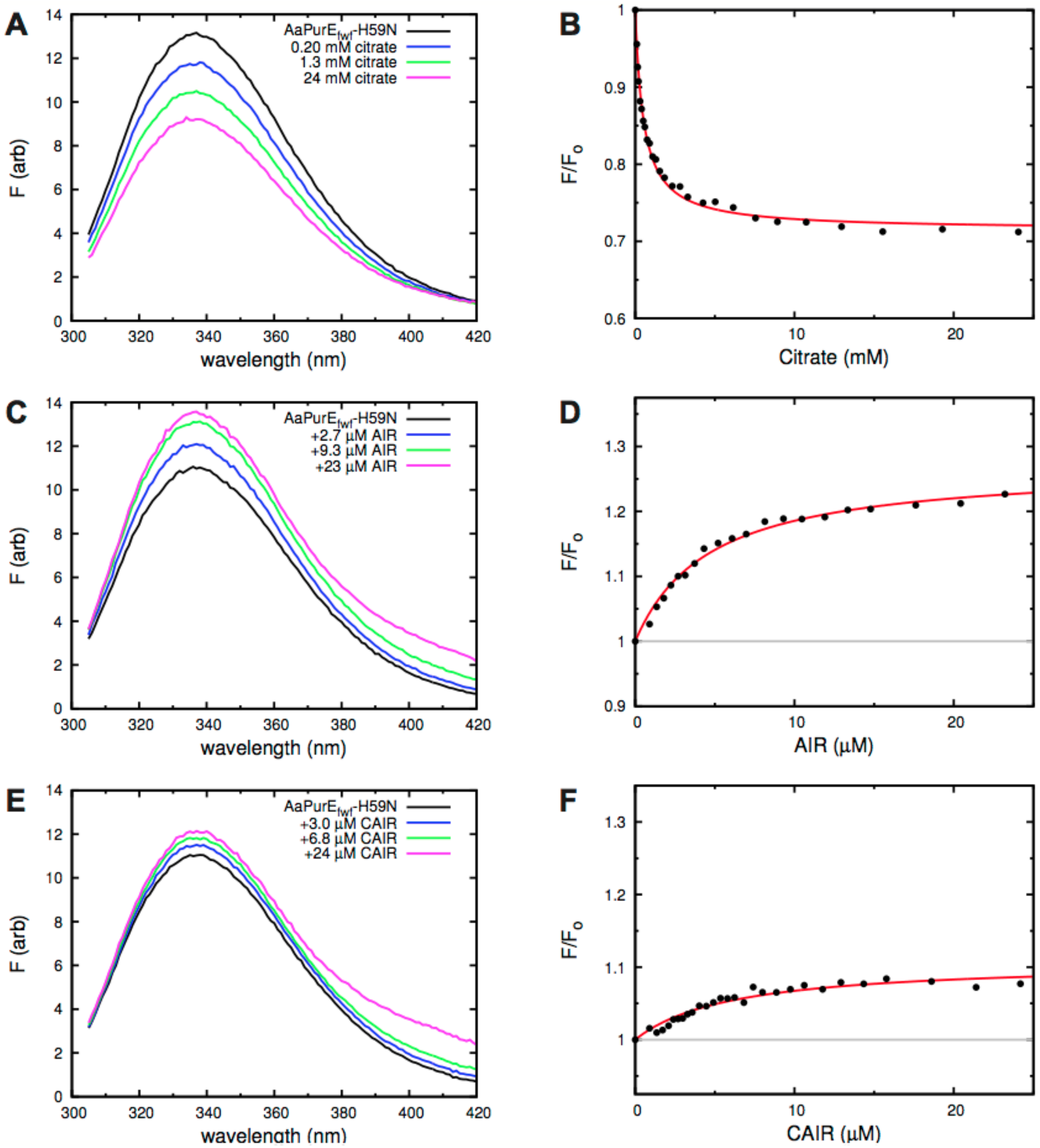

Figure A.16 Fluorescence titrations with AaPurE$_{fwf}$-H59N. Excitation wavelength was 295 nm. Citrate titrations were performed with 0.79 μM [subunit] in 50 mM Potassium acetate, 100 mM KCl, pH 4.6 at 25 °C and data were fit to equation 3.2. AIR and CAIR titrations were performed with 0.79 μM [subunit] and 0.79 μM [subunit] in 50 mM Tris-HCl, pH 8 at 30 °C and data were fit to equation 3.3. K_d values are given in Table 3.7. (A) Fluorescence emission spectra for titration with increasing amounts of citrate. (B) Recorded emission at 320 nm upon citrate addition. (C) Fluorescence emission spectra with increasing amounts of AIR. (D) Recorded emission at 320 nm upon AIR addition. (E) Fluorescence emission spectra with increasing amounts of CAIR. (F) Recorded emission at 320 nm upon CAIR addition.

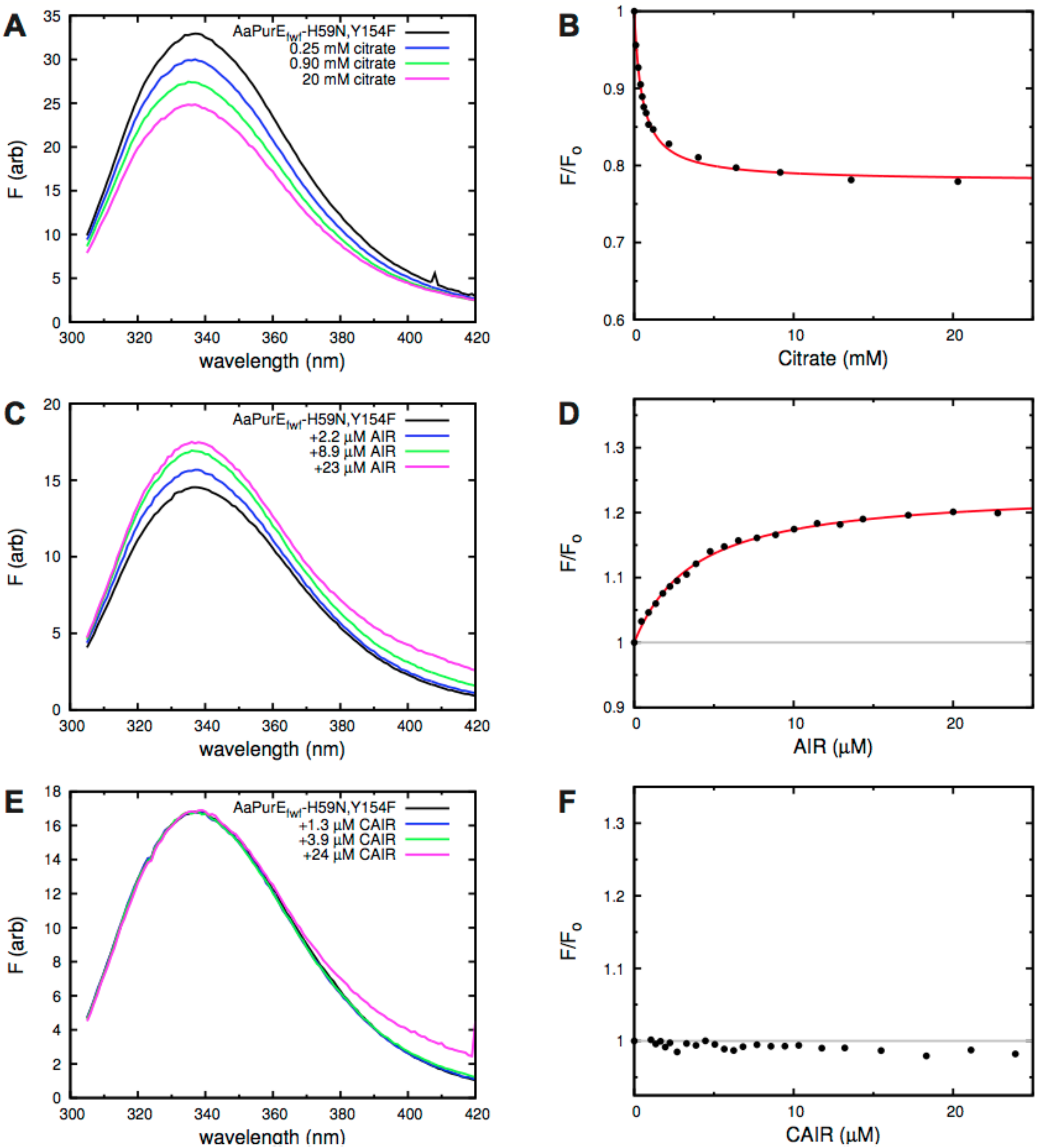

Figure A.17 Fluorescence titrations with AaPurE$_{fwf}$-H59N,Y154F. Excitation wavelength was 295 nm. Citrate titrations were performed with 1.65 μM [subunit] in 50 mM Potassium acetate, 100 mM KCl, pH 4.6 at 25 °C and data were fit to equation 3.2. AIR and CAIR titrations were performed with 1.01 μM [subunit] and 1.01 μM [subunit] in 50 mM Tris-HCl, pH 8 at 30 °C and data for the AIR titration was fit to equation 3.3. K_d values are given in Table 3.7. (A) Fluorescence emission spectra for titration with increasing amounts of citrate. (B) Recorded emission at 320 nm upon citrate addition. (C) Fluorescence emission spectra with increasing amounts of AIR. (D) Recorded emission at 320 nm upon AIR addition. (E) Fluorescence emission spectra with increasing amounts of CAIR. (F) Recorded emission at 320 nm upon CAIR addition.

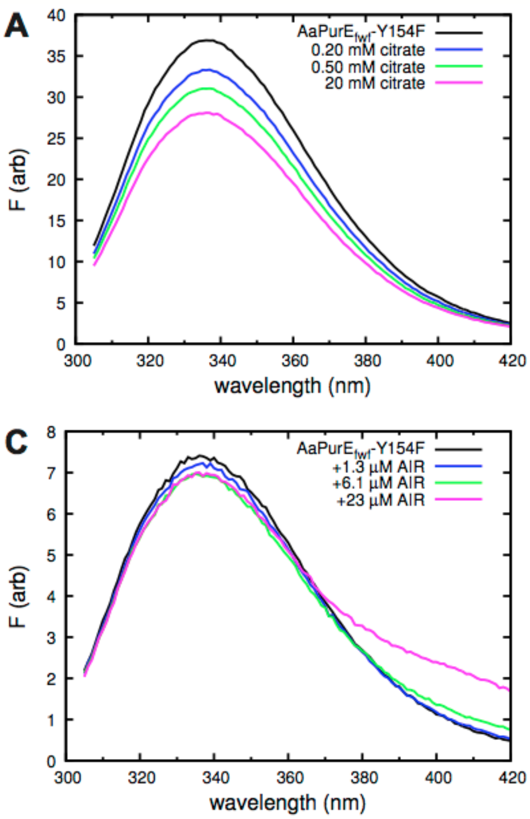

Figure A.18 Fluorescence titrations with AaPurE$_{fwf}$-Y154F. Excitation wavelength was 295 nm. Citrate titrations were performed with 2.01 µM [subunit] in 50 mM Potassium acetate, 100 mM KCl, pH 4.6 at 25 °C and data were fit to equation 3.2. AIR titrations were performed with 0.61 µM [subunit] in 50 mM Tris-HCl, pH 8 at 30 °C and data were fit to equation 3.3. K_d values are given in Table 3.7. (A) Fluorescence emission spectra with increasing amounts of citrate. (B) Recorded emission at 320 nm upon citrate addition. (C) Fluorescence emission spectra with increasing amounts of AIR. (D) Recorded emission at 320 nm upon AIR addition.

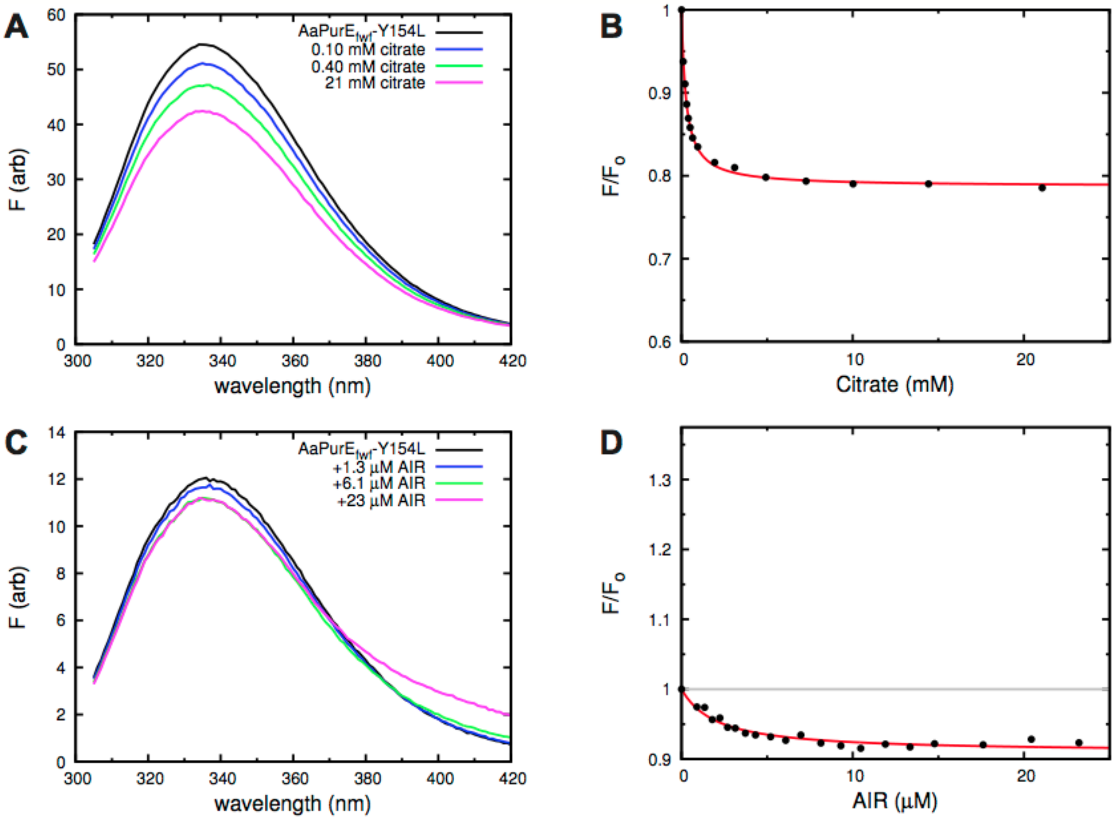

Figure A.19 Fluorescence titrations with AaPurE$_{\text{fwf}}$-Y154L. Excitation wavelength was 295 nm. Citrate titrations were performed with 2.62 µM [subunit] in 50 mM Potassium acetate, 100 mM KCl, pH 4.6 at 25 °C and data were fit to equation 3.2. AIR titrations were performed with 0.69 µM [subunit] in 50 mM Tris-HCl, pH 8 at 30 °C and data were fit to equation 3.3. K_d values are given in Table 3.7. (A) Fluorescence emission spectra with increasing amounts of citrate. (B) Recorded emission at 320 nm upon citrate addition. (C) Fluorescence emission spectra with increasing amounts of AIR. (D) Recorded emission at 320 nm upon AIR addition.

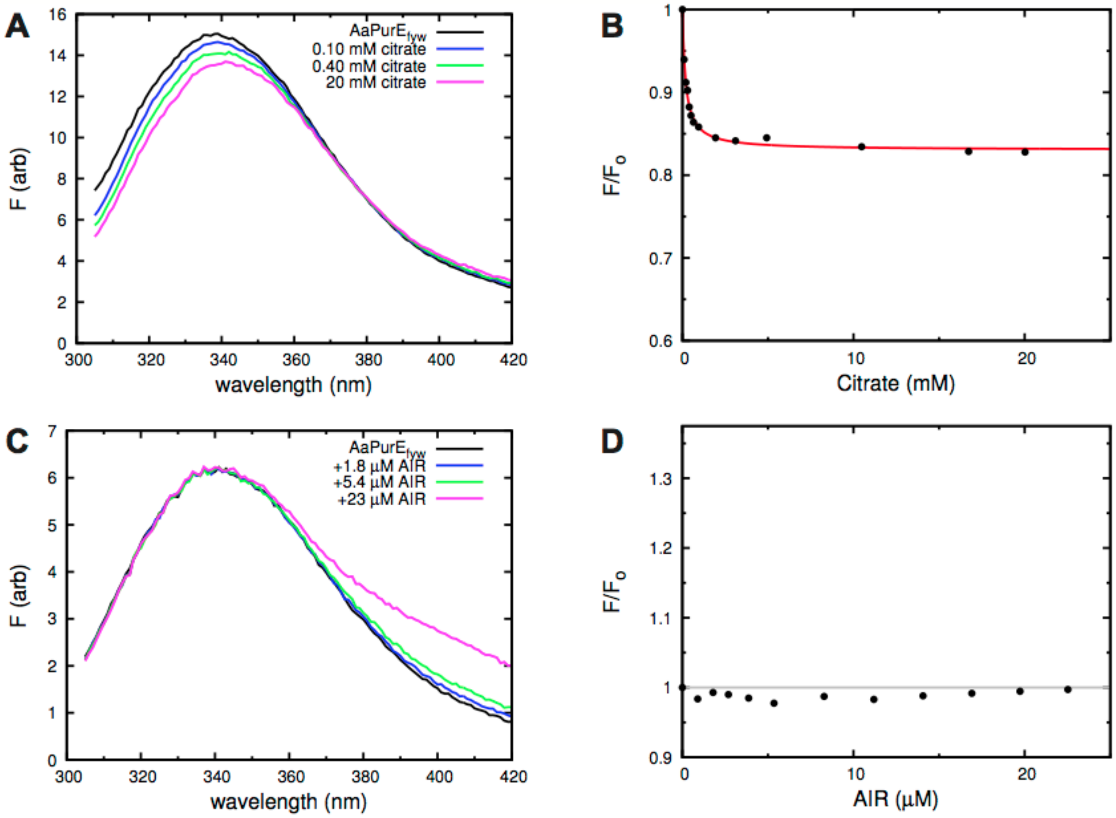

Figure A.20 Fluorescence titrations with AaPurE$_{fyw}$. Excitation wavelength was 295 nm. Citrate titrations were performed with 9.85 µM [subunit] in 50 mM Potassium acetate, 100 mM KCl, pH 4.6 at 25 °C and data were fit to equation 3.2. K_d values are given in Table 3.7. AIR titrations were performed with 4.25 µM [subunit] in 50 mM Tris-HCl, pH 8 at 30 °C. (A) Fluorescence emission spectra with increasing amounts of citrate. (B) Recorded emission at 320 nm upon citrate addition. (C) Fluorescence emission spectra with increasing amounts of AIR. (D) Recorded emission at 320 nm upon AIR addition**.**

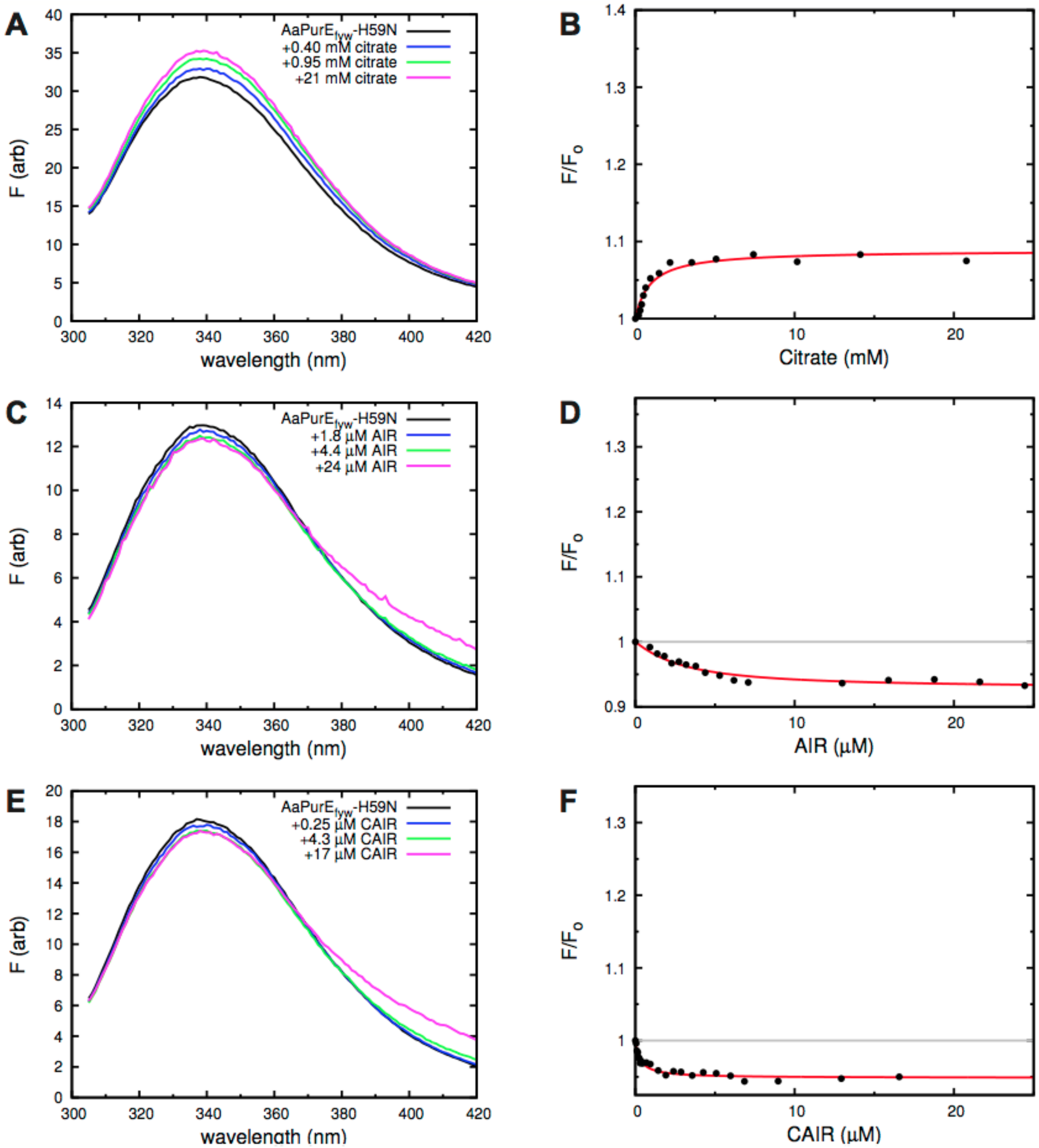

Figure A.21 Fluorescence titrations with AaPurE$_{fyw}$-H59N. Excitation wavelength was 295 nm. Citrate titrations were performed with 10.66 μM [subunit] in 50 mM Potassium acetate, 100 mM KCl, pH 4.6 at 25 °C and data were fit to equation 3.2. AIR and CAIR titrations were performed with 5.21 μM [subunit] and 5.21 μM [subunit] in 50 mM Tris-HCl, pH 8 at 30 °C and data were fit to equation 3.2. K_d values are given in Table 3.7. (A) Fluorescence emission spectra with increasing amounts of citrate. (B) Recorded emission at 320 nm upon citrate addition. (C) Fluorescence emission spectra with increasing amounts of AIR. (D) Recorded emission at 320 nm upon AIR addition.

VITA

VITA

Kelly Lorraine Sullivan was born in Binghamton, NY. After graduating from Vestal Senior High School in Vestal in 2002, Kelly took a year off to work and then enrolled at Tompkins Cortland Community College in Dryden, NY. She received an Associate Degree in General Studies in May 2006. She then entered Cornell University in Ithaca, NY and received a Bachelor of Science in Molecular and Cell Biology in May 2008. Kelly took a year off to travel and in August 2009 she entered Graduate School at Purdue University.